Journal of Mechanics of Materials and Structures

Volume 15, No. 1 January 2020

msp

JOURNAL OF MECHANICS OF MATERIALS AND STRUCTURES

msp.org/jomms

Founded by Charles R. Steele and Marie-Louise Steele

EDITORIAL BOARD

ADAIR R. AGUIAR	University of São Paulo at São Carlos, Brazil
KATIA BERTOLDI	Harvard University, USA
DAVIDE BIGONI	University of Trento, Italy
MAENGHYO CHO	Seoul National University, Korea
HUILING DUAN	Beijing University
YIBIN FU	Keele University, UK
IWONA JASIUK	University of Illinois at Urbana-Champaign, USA
DENNIS KOCHMANN	ETH Zurich
MITSUTOSHI KURODA	Yamagata University, Japan
CHEE W. LIM	City University of Hong Kong
ZISHUN LIU	Xi'an Jiaotong University, China
THOMAS J. PENCE	Michigan State University, USA
GIANNI ROYER-CARFAGNI	Università degli studi di Parma, Italy
DAVID STEIGMANN	University of California at Berkeley, USA
PAUL STEINMANN	Friedrich-Alexander-Universität Erlangen-Nürnberg, Germany
KENJIRO TERADA	Tohoku University, Japan

ADVISORY BOARD

J. P. CARTER	University of Sydney, Australia
D. H. HODGES	Georgia Institute of Technology, USA
J. HUTCHINSON	Harvard University, USA
D. PAMPLONA	Universidade Católica do Rio de Janeiro, Brazil
M. B. RUBIN	Technion, Haifa, Israel

PRODUCTION production@msp.org

SILVIO LEVY Scientific Editor

Cover photo: Ev Shafrir

See msp.org/jomms for submission guidelines.

JoMMS (ISSN 1559-3959) at Mathematical Sciences Publishers, 798 Evans Hall #6840, c/o University of California, Berkeley, CA 94720-3840, is published in 10 issues a year. The subscription price for 2020 is US $660/year for the electronic version, and $830/year (+$60, if shipping outside the US) for print and electronic. Subscriptions, requests for back issues, and changes of address should be sent to MSP.

JoMMS peer-review and production is managed by EditFLOW® from Mathematical Sciences Publishers.

PUBLISHED BY

mathematical sciences publishers

nonprofit scientific publishing

http://msp.org/

© 2020 Mathematical Sciences Publishers

JOURNAL OF MECHANICS OF MATERIALS AND STRUCTURES
Vol. 15, No. 1, 2020
dx.doi.org/10.2140/jomms.2020.15.1

STRESS-MINIMIZING HOLES WITH A GIVEN SURFACE ROUGHNESS IN A REMOTELY LOADED ELASTIC PLANE

SHMUEL VIGDERGAUZ AND ISAAC ELISHAKOFF

We proposed a new form of modeling the boundary roughness effects on the stress distribution and stress concentration around a single hole in a loaded thin elastic plate. The shape irregularities are simulated as periodic patterns of notch-like deviations from an "ideal" shape (mostly from a circle). These are assessed with two relative measures: their maximum peak-to-valley height and the average slope. At given hole shape, all expressions for stress fields are derived in explicit form. This analysis serves as a basis to formulate and numerically solve the optimization problem of finding the stress-minimizing hole shape under fixed irregularities levels. In doing so, the surface topography need not be shallow as was supposed in previous studies.

Methodologically, this study continues the previous work of the authors in detecting the "worst" hole shape under certain extremizing conditions [Vigdergauz and Elishakoff 2019]. The performance of the proposed scheme is verified via instructive numerical examples. The results obtained are presented graphically and may be analyzed visually. They have a practical relevance for optimal design problems in mechanical engineering.

1. Introduction

The problem of determining stress distributions and reducing the stress concentration factor (SCF) around holes in thin flat elastic plates occurs in numerous design situations. The SCF is defined here as the (dimensionless) ratio between the maximum hoop stress and unit applied stresses.

Stress concentrations are highly localized effects which are functions of loading mode and geometry. At given shape, the direct problem of finding SCF is solved, analytically or numerically, for a host of different cases together spanning a large range of possibilities as summarized, for instance, in [Pilkey and Pilkey 2007]. In addition to the SCF, a modern physical explanation of the influence of local shape irregularities on fatigue and fracture mechanical performance also includes the volumetric strain energy density approach (see, for instance, [Pluvinage 2003; Savruk and Kazberuk 2017]) which is beyond our scope.

The paper is focused on nonideal hole-shapes with technologically inevitable irregularities. These are well approximated by isolated notches which can be described by several geometric parameters: the notch peak-to-valley height ρ, the notch edge angle ϑ and the notch radius [Pluvinage 2003]. The latter is less important in the current context of the shape-smoothing SCF minimization, while the first two are chosen here as lower constraints on the shape roughness under which the SCF-minimizing hole is found numerically through a global optimization approach.

Vigdergauz is the corresponding author.

Keywords: 2D-elastostatic problem, Kolosov–Muskhelishvili potentials, shape optimization, stress concentration factor, shape irregularity, genetic algorithm.

This research, therefore, has three key novel aspects. First, we introduce easy-to-measure geometrical parameters well applicable separately or in combination to quantitatively assess the shapes irregularities. Second, together with the primary analytical findings from [Vigdergauz 2006; Vigdergauz and Elishakoff 2019], these are embedded into a stable and fast GA-based optimization scheme which can be handled by modern computers. Third, its efficient numerical implementation permits to identify the SCF-minimizing hole shape in an elastic plate over a wide variety of the governing parameters. Especially interesting here is the notch edge slope ϑ which has not received sufficient attention in the literature so far.

The findings of this study are in line with the earlier conducted studies [Vigdergauz and Cherkaev 1986; Cherkaev et al. 1998; Vigdergauz 2006; Vigdergauz and Elishakoff 2019].

The remainder of this paper is organized as follows: for reader's convenience, Section 2 summarizes the complex valued direct solver of the considered 2D model; Section 3 introduces and describes in detail the suggested geometrical constraints; in these terms the precise problem formulation is presented in Section 4; and then Section 5 gives the solution scheme and some computational hints for practical applications; Section 6 displays representative numerical examples to illustrate the use of the proposed approach and demonstrate its effectiveness and rationality. Concluding remarks are offered in Section 7.

2. Basic model: assumptions and notations

This whole section contains mainly classical material. We choose to include it nevertheless, since the novel parts of this works to be presented in the next sections, will refer to many of the equations in this section.

2.1. ***Problem setup.*** Consider Figure 1. Let a thin infinite linear elastic plate be weakened by a hole with a p-fold rotationally symmetric boundary L_p enclosing the origin of the plane E of a complex variable $z = x + iy \in E$. Suppose further that the plate is remotely loaded by uniform nontangential stresses

$$\sigma_{xx}^{\infty} = P, \quad \sigma_{yy}^{\infty} = Q, \quad \sigma_{xy}^{\infty} = 0, \tag{2-1}$$

while the hole is traction-free:

$$\sigma_{nn}(t), \sigma_{n\tau}(t) \equiv 0, \quad t \in L_p; \tag{2-2}$$

where $\sigma(t) = \{\sigma_{nn}, \sigma_{\tau\tau}, \sigma_{n\tau}\}$ denotes the stress tensor in a local system of curvilinear orthogonal coordinates (n, τ) at a point $t \in L_p$.

Let also the infinite material-filled domain S outside the hole be conformally mapped onto the exterior T of the unit circle γ in the auxiliary complex ζ-plane by the holomorphic function $\omega(\zeta)$, $\zeta \in T$ which has only finite number M of the Laurent terms:

$$L_p : t = \omega(\xi), \ t \in L_p; \quad \xi = \exp(i\phi) \in \gamma, \ |\xi| = 1; \quad \omega(\zeta) = \zeta + \sum_{m=1}^{M} \frac{d_m}{\zeta^{pm-1}}, \ |\zeta| \geq 1. \tag{2-3}$$

By the required mapping uniqueness the coefficients $\{d_m\}$ are necessarily bounded by the successfully narrowing intervals [Ahlfors 1953]

$$-\frac{1}{\sqrt{pm-1}} \leq d_m \leq \frac{1}{\sqrt{pm-1}}; \quad m = 1, 2, \ldots, M. \tag{2-4}$$

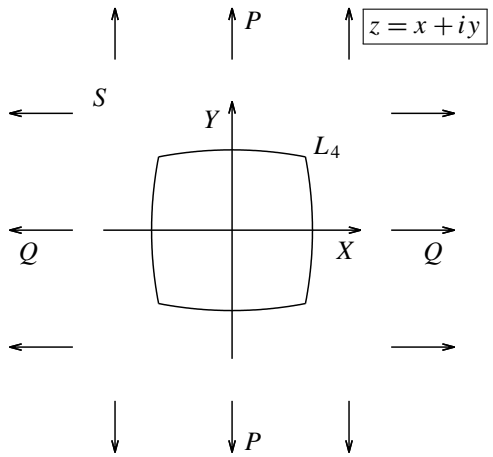

Figure 1. The problem schematic: an infinite plate with a traction-free hole under uniform stresses, the cases $P = Q$ and $P = -Q$ correspond to remote bulk and shear, respectively. The piecewise smooth hole boundary possesses a certain p-fold rotational symmetry as exemplified here for $p = 4$.

For $M = 1$, the equal sign in (2-4) defines (up to rigid rotation) the limiting case of a p-cusped hypocycloid identified in the optimization context in [Givoli and Elishakoff 1992; Shahzad et al. 2017; Vigdergauz and Elishakoff 2019].

Equation (2-3) provides, in effect, a finite parametrization of an arbitrary closed curve $L_p = L_p(d_1, d_2, \ldots, M)$, which is approximated as a point in an M-dimensional rectangular parallelepiped Π_M with the edges of the length (2-4). This is further used as a searching space to find the globally optimal hole shape (Section 4) with taking $\{d_m\}$ as the design variables. In view of the loading symmetry (2-1) they can be taken as real-valued quantities without loss of generality.

The integers $p = 2, 3, 4, \ldots$ and $M = 1, 2, 3, \ldots$ are governing parameters determining the behavior of the numerical simulations and their convergence to a stable solution (Section 6).

2.2. ***Kolosov–Muskhelishvili formalism for 2D linear elasticity.*** This widely known approach replaces the biharmonic real-valued Airy function with two complex-valued functions $\Phi_0(\zeta)$, $\Psi_0(\zeta)$, $\zeta \in T$ [Muskhelishvili 1963] commonly referred to as the KM potentials. They are analytic functions in T and continuously extendible on γ.The loading conditions (2-1), (2-2) are then equivalently expressed as

$$\Phi_0(\zeta) = B + \Phi(\zeta); \quad \Psi_0(\zeta) = \Gamma + \Psi(\zeta), \ \zeta \in \Sigma; \quad \Phi(\zeta), \Psi(\zeta) = O(|\zeta|^{-2}); \tag{2-5a}$$

$$4B = \mathrm{Tr}\{\sigma^\infty\} = Q + P; \quad 2\Gamma = \mathrm{Dev}\{\sigma^\infty\} = Q - P; \quad \mathrm{Im}\, B, \mathrm{Im}\, \Gamma = 0; \tag{2-5b}$$

and

$$-\frac{2}{\xi^2}\overline{\omega'(\xi)}[\mathrm{Re}\, \Phi(\xi) + B] + \overline{\omega(\xi)}\Phi'(\xi) + \Gamma\omega'(\xi) = -\omega'(\xi)\Psi(\xi), \quad \xi \in \gamma; \tag{2-6}$$

respectively. The terms in (2-6) are rearranged specifically for later use [Kalandiya 1975].

At any given shape L_p, identities (2-5), (2-6) comprise together the direct boundary-value problem in $\Phi(\xi)$, $\Psi(\xi)$. This formulation allows to employ the rich machinery of the complex-variable theory.

Especially relevant here is to expand the KM potentials in the convergent Laurent series (the summation begins with $k = 2$ to match the asymptotic (2-5a))

$$\Phi(\zeta) = \sum_{k=2}^{\infty} a_k \zeta^{-k}, \quad \Psi(\zeta) = \sum_{k=2}^{\infty} b_k \zeta^{-k}, \quad \zeta \in \Sigma + \gamma. \tag{2-7}$$

The coefficients $\{a_k\}$, $\{b_k\}$ may partially vanish due to the adopted rotational symmetry. Nevertheless, one should keep in mind that both expansions are *infinite* even for a *finite*-term mapping $\omega(\zeta)$ [Muskhelishvili 1963].

2.3. ***Explicit closed form of the hoop stress.*** The left-hand side of (2-6) is the boundary value of an T-holomorphic function tending to zero at infinity. In turn, this means that its series expansion involves no nonnegative powers in ζ. Substitution of (2-3) and (2-7) in (2-6) with zeroing the resultant coefficients for ζ^n, $n \geq 0$ gives the infinite linear algebraic system in a_k, $k \geq 2$ [Kalandiya 1975]

$$a_{j+2} - \sum_{k=1}^{j} (j-k+1)\bar{d}_{j-k+1} a_k - (j+1) \sum_{k=1}^{\infty} \bar{d}_{j+k+1} \bar{a}_k = A_j, \quad j = 0, 1, \ldots, \tag{2-8a}$$

$$A_0 = 2B - \Gamma, \quad A_1 = 0, \quad A_j = -2B(j+1)\bar{d}_{j+1}, \quad j \geq 2. \tag{2-8b}$$

The first sum is omitted in (2-8a) when $j = 0, 1$. Again, by the symmetry arguments, the above equations may be eliminated partially from the system, thus facilitating the computations.

Actually, the second potential $\Psi(\zeta)$ remains outside the system thus allowing to separate out the coefficients $\{a_k\}$ only needed to compute the boundary hoop stress $\sigma_{\tau\tau}(\xi)$ [Muskhelishvili 1963]

$$\sigma_{\tau\tau}(\xi) = 4 \operatorname{Re} \Phi_0(\xi) \tag{2-9}$$

that are of our interest here. Note in passing that by the principle of maximum applied to harmonic function $\operatorname{Re} \Phi_0(\zeta)$ we have for the hoop stress average over an arbitrary hole shape (at $|P|, |Q| = 1$, for definiteness)

$$\overline{\sigma_{\tau\tau}} = \Phi_0(\infty) = 2 \Longrightarrow K = \max |\sigma_{\tau\tau}(\xi)| \geq 2, \tag{2-10}$$

where K stands for the SCF.

Remarkably, for the finite term mapping (2-3) system (2-8) breaks up into two subsystems

(a) the first M nonvanishing equations for the first M unknowns $\{a_k\}$ and

(b) the infinite remainder for the "tail" $\{a_k\}$, $k > M$.

The key feature of the subsystem (b)enumi is its finite-differences structure [Levy and Lessman 1958] by which the "tail" is expressed *analytically* through the first M unknowns as proved at length in [Vigdergauz 2006; Vigdergauz and Elishakoff 2019]. The resultant formula reads

$$\Phi_0(\xi) = B + \frac{R_M(\bar{\xi})}{\xi \omega'(\xi)}, \tag{2-11}$$

where $R_M(\xi)$ is a polynomial of degree M in ξ:

$$R_M(\xi) = r_M \xi^M + r_{M-1} \xi^{M-1} + \cdots + r_0 \tag{2-12}$$

with the coefficients

$$r_0 = a_1 = 0, \quad r_1 = a_2, \quad r_m = a_{m+1} - \sum_{k=2}^{m} (-1)^k k d_k a_{m+k+1}, \quad m \geq 2. \tag{2-13}$$

In other words, equations (2-11)–(2-13) are *exact* up to negligible errors caused by numerically solving the subsystem (a)enumi at moderate values of M. When, for example, $p = 4$, the numerical simulations gives stable results at most for $M = 8 \div 12$.

Note that just this (almost) analytical solution of the direct problem provides the numerical effectiveness of the SCF local optimization.

3. Geometrical constraints

The question here is how to quantitatively assess the deviations of real holes surfaces $R(\theta)$ from the nominally "ideal" shape with no local disturbances or spikes, like, say, a circle ($R(\theta) = \text{constant}$). We advance the following two easy-to-measure dimensionless factors:

(1) The maximum peak-to-valley normalized height,

$$\rho[L_p] = \frac{R_{\max} - R_{\min}}{R_{\max}}, \quad 0 \leq \rho \leq 1, \quad R_{\max} = \max R(\theta), \quad R_{\min} = \min R(\theta), \quad \theta \in \lambda_p, \tag{3-1}$$

which equals to zero only for a circle. Here $\lambda_p = [0; \pi/p]$ is the irreducible angular interval along L_p. Any given $\rho > 0$ corresponds to a variety of curves from an ellipse with eccentricity $\sqrt{\rho(2-\rho)}$ to a highly irregular shape with many notches around the perimeter as exemplified in Section 6 (Figure 8, left).

(2) The normalized variation of $R(\theta)$

$$V[L_p] = \frac{\text{var}[L_p]}{R_{\max}} \geq 0. \tag{3-2}$$

In conformity with the theory of real-valued functions [Natanson 1955], the (bounded) variation $\text{var}[L_p]$ is here defined through the nonnegative discrete sums of absolute values of the differences of the radii between each two adjacent points on the irreducible part L

$$\text{var}[L_p] = \sup \sum_{i=0}^{n} |R(\arg(\theta_{i+1})) - R(\arg(\theta_i))| \geq 0, \quad \{t_i\} \in L, \quad \{\arg(t_i)\} \in \lambda_p. \tag{3-3}$$

The supremum is taken over all possible partitions of L_p with an arbitrary set of points $t_0, t_1, \ldots, t_n$ ordered by a chosen direction of traversing. Clearly, only one such set is used in numerically evaluating the variations.

The variations are nontrivially bounded below [Natanson 1955] as

$$\text{var}[L_p] \geq R_{\max} - R_{\min}, \tag{3-4}$$

where the equal sign is true for only monotonic functions so that

$$V[L_p] \geq \rho[L_p]. \tag{3-5}$$

Say, the shape shown in the above-mentioned Figure 8 (left) has a small ratio $\rho = 0.019$ and a markedly larger variation $V = 2\rho = 0.038$ by which the function $R(\theta)$ is forced to oscillate along the hole perimeter.

For a differentiable function $R(\theta)$ one has with (3-2)

$$V[L_p] = R_{\max}^{-1} \int_0^{\pi/p} |R'(\theta)|\, d\theta. \tag{3-6}$$

Again, as before, $V[L_p]$ is zero only on a circle $R(\theta) = \text{constant}$.

Remark. For an arbitrary one-term mapping (2-3) $\omega(\zeta) = \zeta + d_m \zeta^{1-pm}$ both parameters take the same value thus reaching the equal sign in (3-5). Indeed, in view of (3-6),

$$R^2(\theta) = 1 + 2d_m \cos p\theta + d_m^2; \tag{3-7a}$$

$$R_{\max} = 1 + |d_m| \quad \text{and} \quad R_{\min} = 1 - |d_m|, \quad \text{therefore} \quad \rho = \frac{2|d_m|}{1 + |d_m|}; \tag{3-7b}$$

$$V[L_p] = \frac{2pd_m}{1 + |d_m|} \int_0^{\pi/p} \frac{|\sin p\theta|}{\sqrt{1 + 2d_m \cos p\theta + d_m^2}}\, d\theta = \frac{2|d_m|}{1 + |d_m|} = \rho[L_p]. \tag{3-7c}$$

With (3-4) the last identity is however evident: function $R(\theta)$ is monotonic in each irreducible part of L_p since $\operatorname{sgn}(R'(\theta)) = -\operatorname{sgn}(d_n)$, $\theta \in \lambda_p$.

Generally speaking, ρ and V are not interrelated for $M > 1$. On the contrary, they basically complement each other in that ρ defines the maximal relative height of the notches while V is, through (3-6), proportional to the tangent of the average slope angle $\bar{\vartheta}$ of the notches edges. These are precisely the parameters used in [Palmov 1963; Sheinin 1972] in developing a probabilistic risk evaluation of the surface roughness, thus possibly bridging the gap between deterministic and stochastic uncertainty assessments. In the current optimization context, their interplay becomes all the more intimate (Section 6) returning us again to the equal sign in (3-5).

Before leaving this section we note the following useful features of the proposed approach:

- Neglecting the V-factor may adversely affect the accuracy of some previous published results [Medina and Hinderliter 2014; Chang et al. 2017] where the restriction of very small slopes $\vartheta \ll 1$ was involved. Taking into account irregularities tilts substantially expands the practicability of this study.
- Mathematically, an integral-type assessment V of the slopes provides a numerically stable optimization scheme and requires less computational efforts than direct angular differentiation of $R(\vartheta)$ between closely spaced points.
- Both parameters do not need to be as small as frequently supposed in the literature.

4. One-side constraining inequalities and problem statement

Our aim is to numerically minimize the SCF at given ρ and V in a representative interval of their values. For embedding these constraints into the minimization framework it is desirable to reformulate them as one-side inequalities. For this purpose we recall the previous result in [Vigdergauz 2006], which states that the unconstrained K-minimizing shape is always a circle with one exception of the four-fold

symmetric hole under remote shear. In this case (named S_4 for brevity) the optimal shape looks as a smoothed quadrangle with

$$\rho^* = V^* = 0.23, \quad K = 2.78, \tag{4-1}$$

in contrast to the circle-related value $K = 4$. Keeping this in mind, we intuitively conjecture that here the SCF is a monotonically decreasing function of either of these two quantities from zero to ρ^* and an increasing one afterward while in all other cases it increases monotonically everywhere. Then one can introduce the following constraining inequalities:

$$\rho \le \rho_0, \quad \rho_0 \in [0, \rho*], \quad \rho \ge \rho_0, \quad \rho_0 \ge \rho^*, \qquad S_4 \text{ case;} \tag{4-2a}$$

$$\rho \ge \rho_0, \quad \rho_0 \ge 0, \qquad \text{any other case;} \tag{4-2b}$$

and analogously for V. These are tailored especially to fix *a priori* the intervals of monotonicity of the functions $K(\rho)$, $K(V)$. Both ρ- and V-types can be applied either separately or together. For the case (4-2b) they are used directly while for (4-2a), their appropriate combination is given and explained in Section 6.

It is hoped that the adequate choice of the inequality sign within each interval will make the $K(\rho)$ minimum occur exactly at the boundary point ρ_0. This presumption is fully justified by the numerical simulations for a set of ρ^* and V values in the representative interval $[0, 0.75]$ (Section 6).

Remark. Noteworthy is that the SCF-minimizing ρ and V values coincide not only for S_4 as indicated by (4-1) but also for the general minimization case as revealed by the numerical simulations.

With these preliminaries we are now in a position to quantitatively formulate the following optimization problem:

> *Given an external loading type to find, over all admissible set of the design variables* $\{d_m\}$, *the* p*-symmetrical hole shape* $L_p \in \Pi_M$ *which minimizes the stress concentration factor* K *under either or both* (ρ *and* V) *constraint types* (4-2)

$$K(L_p, M, c^*) \underset{\{d_m\}}{\longrightarrow} \min(p, M, c^*). \tag{4-3}$$

Here c^* abstractly denotes given thresholds ρ^*, V^*.

5. Numerical solution procedure

Computationally, (4-3) is a rather standard optimization problem whose numerical solution is conveniently obtained by an iterative loop over successively modified shapes with computing the criterion K (fitness function) of each candidate. For this purpose, we apply the approach developed and validated in the first author's previous paper [Vigdergauz 2006]. It includes three main ingredients: an enhanced direct solver (2-11)–(2-13), a standard GA-based global searching engine (see, for instance, [Goldberg and Sastry 2007]) and an efficient shape encoding scheme (2-3) within the GA framework. The use of a global scheme rather than a gradient-type scheme is intended to avoid being trapped by the highly nonlinear and sensitive cost function K.

The GA starts with randomly generating an initial population of individual binary strings that might be possible solutions. Each string concatenates M randomly generated two-byte signed integers I_m :

$-W \le I_m \le W$, $W = 2^{15} - 1$, $m = \overline{1, M}$. In view of (2-4), this encodes a shape L_p within the searching space Π_M as

$$d_m = \frac{I_m}{W\sqrt{m}}, \quad m = 1, 2, \ldots, M. \tag{5-1}$$

Substitution of (5-1) into (2-3) decodes the corresponding shape. However, in doing so, self-intersecting shapes may appear, since the inequalities (2-4) are only necessary, but not sufficient to guarantee their absence. To the author's best knowledge, no conditions imposed on the Laurent terms (2-3) to effectively trim out any self-intersection are known thus far. Therefore, we check each decoded curve for possibly breaking the monotonicity

$$\frac{d \arg \omega(\theta)}{d\theta} \ge 0, \quad \theta \in \lambda_p, \tag{5-2}$$

which provides the more restrictive shape property of star-shapedness. It is clear, physically, that only star-shaped holes are promising for optimization. In the numerical simulations (Section 6) this is attested to by the fact that the optimal values of $\{d_m\}$ are rather distant from the intervals limiting values (2-4).

After decoding each string into the corresponding shape its fitness K is then computed through (2-11)–(2-13) at a large number of the unit circle points. Whenever the current shape violates any imposed constraint, including (5-2), a significant constant penalty is assigned as its fitness value without further computation of K. After that, all strings are subject to the GA binary operations of 1-point crossover and mutations performed with certain predefined probability levels to obtain offspring.

This is repeated many times (typically several hundreds) up to achieving a stable solution which is believed to be close to the global optimum.

The stopping criterion is a problematic issue in GA iterations as there are no practical means to assess the actual error in real applications. Instead, the optimization is stopped after some N_{iter} iterations — in belief that the process really converges. However, at specific stochastic combinations, GAs may become "stuck" quite far from the global optimum. This is prevented by multiple GA runs carried out for every result point. Practically, N_{iter} is chosen in such a way that the optimization criterion remains unchanged in successive iterations well in advance of termination. For the problem at hand, we averaged five runs per point with $N_{\text{iter}} = 200 \div 500$ depending on specific values of the governing parameters.

6. Numerical results

This constrained optimization scheme is tested numerically in the most informative case of square symmetry ($p = 4$) except for the case $p = 64$ in Section 6.3. For comparison convenience, the results obtained are displayed and commented (wherever possible) in parallel for both bulk and shear loading modes. They are further grouped into three subsections according to constraints combinations preimposed on the shape geometry.

6.1. ***The ρ-inequality constraint alone.*** Our first set of computations is carried out with no V-constraint when the minimization problem (4-3) is treated only under ρ-inequalities (4-2). The resultant curves in Figure 2 visualize the attainable lower bound on $K(\rho)$ as yielded by the GA searching.

The corresponding K-minimizing hole shapes (normalized to the unit area) are exemplified in Figure 3. Here the attention is drawn to the resultant smoothly shaped "arms", which are gradually lengthening in an attempt to match the growing constraint ρ. Notice that in the shear (antisymmetric) mode the

GA optimizes also the shapes orientation by aligning the "arms" along the diagonals $y = \pm x$ where the (continuous) hoop stress $\sigma_{\tau\tau}(\theta)$ must change its sign. This is of no concern in the isotropic bulk mode but we rotate them through the same angle for easier comparison to their shear-related counterparts.

Figure 4 illustrates the shape convergence to the stable solution with increasing number M of the mapping terms at a given ρ. One can see that the bulk mode exhibits faster convergence ($M \geq 8$ against $M \geq 12$). This can directly be attributed to the higher local curvature occurring near the diagonal since this is the only substantial difference between the shapes.

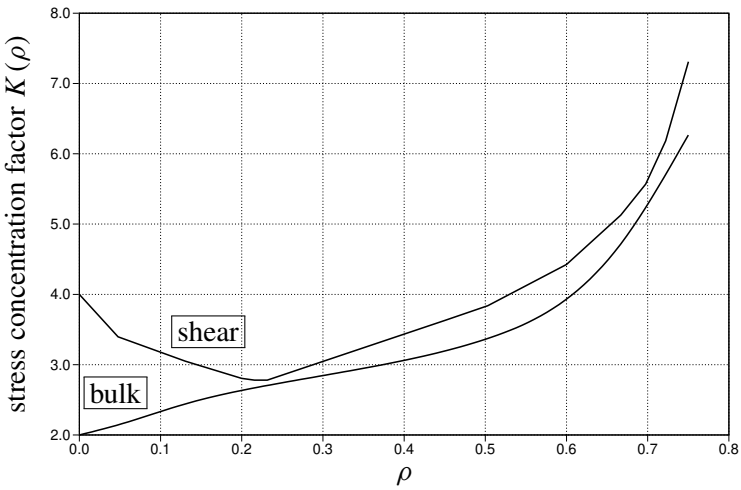

Figure 2. The minimal attainable $K(\rho)$ for the basic loads.

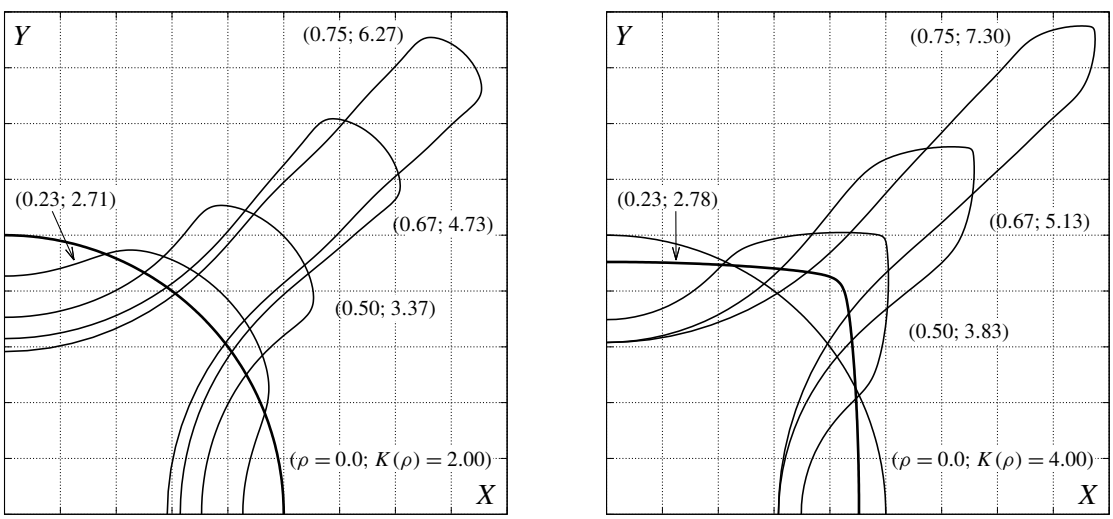

Figure 3. The upper-right quarter of K-optimal hole: the shape evolution with increasing ρ for bulk load (left) and pure shear (right). The globally optimal shapes at $\rho = 0.0$ and $\rho = 0.23$, respectively (Equation (4-1)), are emboldened for better comparison.

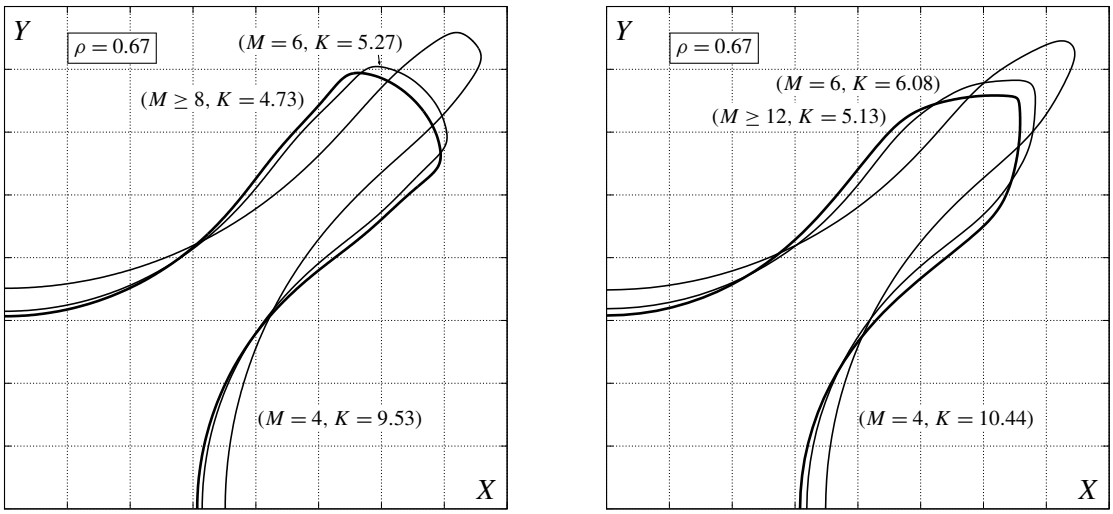

Figure 4. The upper-right quarter of K-optimal hole: the shape convergence to the stable state (bolded lines) at $\rho = 0.67$ with increasing number M of nonzero mapping terms for bulk load (left) and pure shear (right).

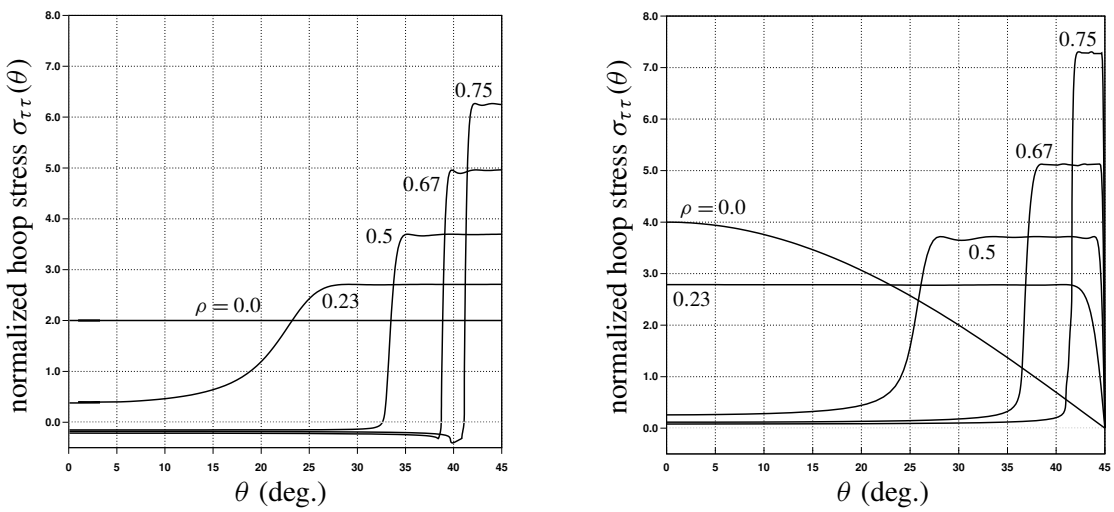

Figure 5. The upper-right quarter of K-optimal hole: the hoop stress angular distribution in the physical plane E for bulk load (left) and pure shear (right).

The angular stress distributions $\sigma_{\tau\tau}(\theta)$ (normalized by the unit load) along the K-minimal shapes in the physical plane E is depicted by Figure 5. Interestingly, with the increasing ρ, the distributions form a distinct step near the diagonal while remaining almost zero along the rest of the shape. To avoid confusion, note that the bulk-related nonzero stress average (2-10) holds only in the auxiliary ζ-plane as shown in explanatory Figure 6.

Such piecewise constant pattern is consistent with two others obtained previously in the similar context:

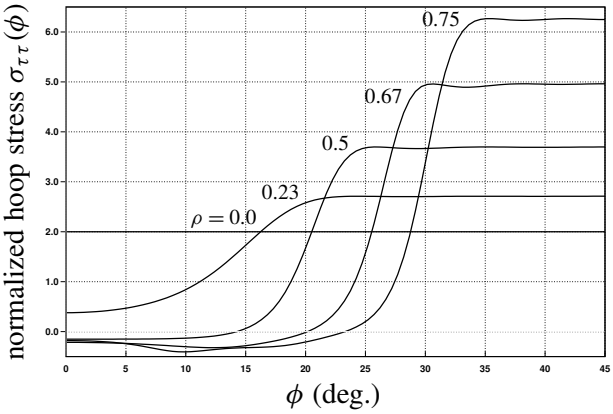

Figure 6. The bulk case: the hoop stress from the left-side of Figure 4 depicted along the unit circle γ in the auxiliary complex plane.

(a) the unrestricted minimization of K under pure shear [Vigdergauz 2006];

(b) the stress-smoothing optimization in perforated checkerboard structures [Vigdergauz 2012].

This numerically found smoothing-minimization relationship should be studied also analytically in the future. This is more so relevant since combination of the equistress concept advanced in [Cherepanov 1974] and the maximum principle [Ahlfors 1953] for harmonic function $\Phi(z)$ proves directly that both criteria are equivalent at least for the unconstrained shape optimization of several holes under bulk-dominating remote load [Vigdergauz 1976].

Figure 7 presents a typical dependence of the K-minimum stress distribution on the number of held mapping terms. As this shows, the stress peak and attendant oscillations are progressively being smoothed by larger M.

We see, therefore, that the bulk- and shear-related K-minimum hole shapes have exactly the same *integral* measures ρ and V but differ *locally* as clearly seen in Figure 3.

Finally, of special importance is that *a posteriori* computed normalized variation $V(\rho)$ of the K-minimum shapes appear, in numerical fact, to attain the smallest possible values everywhere for $\rho \in [0, 0.75]$ by saturating the nonzero lower bound for monotonous functions (3-5): $V(\rho) = V_{\min}(\rho) = \rho$. To put it differently, the ρ-constrained minimization of the SCF has the nice property of minimizing the optimal shape variation as well:

$$K_{\rho}^{(0)} \equiv \min K(\rho_0) \leftrightarrow V_{\min}(\rho_0) \equiv V_{\rho}^{(0)} = \rho_0, \tag{6-1}$$

endowing the function $R(\theta)$ with the monotonicity property in the irreducible interval λ_p. However, the exact explanation of this remains unclear.

6.2. ***The V-inequality constraint alone.*** Here, the limitations are obtained from (4-2) by the evident substitution of ρ, ρ_0, $\rho*$ with V, V_0, V^*, respectively. With the established monotonicity of the functions $\min K(\rho)$ and $V_{\min}(\rho)$, one can write analogously to (6-1),

$$K_{V}^{(0)} \equiv \min K(V_0) \leftrightarrow \min \rho(V_0) \equiv \rho_{V}^{(0)} = V_0, \tag{6-2}$$

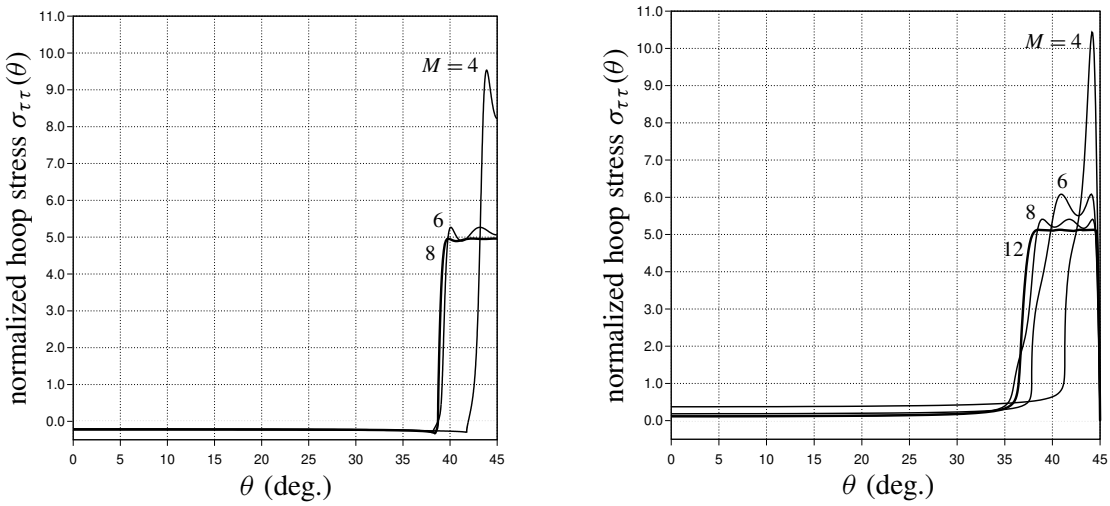

Figure 7. The upper-right quarter of K-optimal hole: hoop stress convergence to the stable state (bolded lines) at $\rho = 0.67$ with increasing number M of nonzero mapping terms for bulk load (left) and pure shear (right).

so that if $K_V^{(0)} = K_\rho^{(0)}$ then $\rho_V^{(0)} = \rho_0$, $V_\rho^{(0)} = V_0$. Therefore, taken separately, both ρ- and V-constraints return the same optimal results already detailed in the previous subsection, as expected.

6.3. ***Both constraints combined.*** Taken together, they have a nontrivial sense only as the following inequality constraints

$$\rho \le \rho_0, \quad V \ge V_0, \quad V_0 > \rho_0, \tag{6-3}$$

where the last one is introduced to conform with the general relation (3-5). The evident modification of (6-3) for the exceptional S_4 case is omitted here to save space.

The first two opposite-sided bounds are intended to detect the K-minimizing shapes with $V > \rho$ (and hence with $K(V) > K(\rho)$) which appear to be unattainable by applying these constraints separately as before. The stronger this inequality is and the larger p is, the more wavy is the K-optimal hole shape with increasing number of smoothed notches as exemplified in Figure 8 (left). Again, as before, the resultant optimal shapes tend to avoid the hoop stress jumps or singularities with a step-like pattern of the tangential stresses (Figure 8, right). The oscillations observed along the step's top side are caused by the local nature of the K-minimum criterion. These are small (with the valley-to-peak ratio greater than 96.5%) and may be further diminished with increasing M. More extended numerical results are too bulky to be presented here. We will analyze this case in the future.

7. Concluding remarks

We advanced two possible parameters with clear engineering meaning for geometrically measuring hole-shape irregularities. These are maximum height and average steepness of the shape deviations easily embedded into the stable and highly accurate numerical scheme of the constrained minimization of the stress concentration factor. The results obtained give a good indication of the SCF attainable lower limit

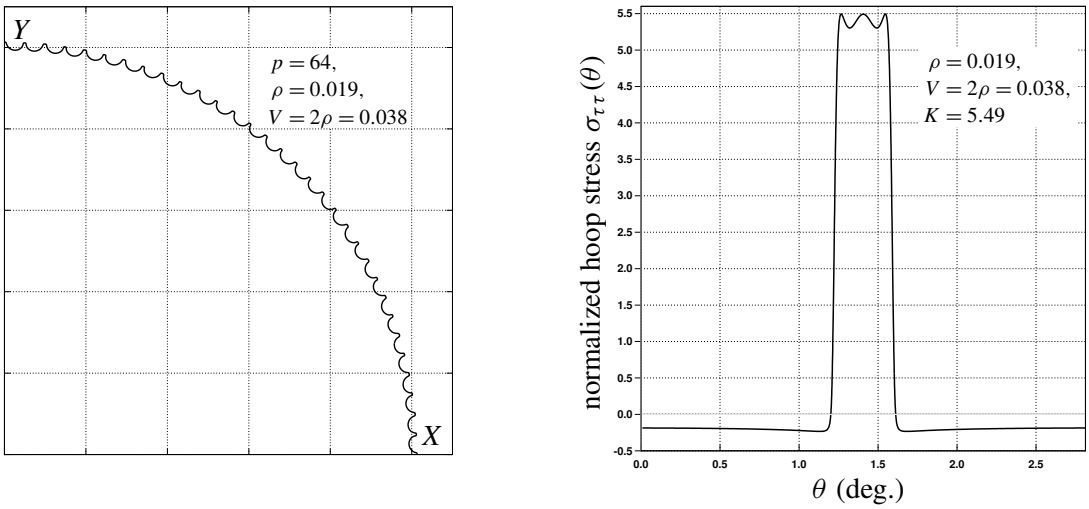

Figure 8. Both constraints together for bulk load and $p = 64$: the upper-right quarter of K-optimal hole (left) and the corresponding hoop stress (right) at $V > \rho$.

and the corresponding hole shapes. Fascinatingly, the K-minimum hoop stress distributions tend to be piecewise constant with a distinctive step along strongly rounded notches and a very small stress value and gradient in all other locations.

It should be emphasized that the analytical direct solver ((2-11)–(2-13)) cannot be extended to the next in complexity cases of a single elastic inclusion or several interacting holes. Here, new approaches are required for a stable and accurate minimization of the local K-criterion.

References

[Ahlfors 1953] L. V. Ahlfors, *Complex analysis: an introduction to the theory of analytic functions of one complex variable*, McGraw-Hill, New York, 1953.

[Chang et al. 2017] Z. Chang, R. Liao, and W. Lu, "Surface stress concentration factor via Fourier representation and its application for machined surfaces", *Int. J. Solids Struct.* **113-114** (2017), 108–117.

[Cherepanov 1974] G. P. Cherepanov, "Inverse problems of the plane theory of elasticity", *Prikl. Mat. Mekh.* **38**:6 (1974), 963–979. In Russian; translated in *J. Appl. Math. Mech.* **38**:6 (1974) 915–931.

[Cherkaev et al. 1998] A. V. Cherkaev, Y. Grabovsky, A. B. Movchan, and S. K. Serkov, "The cavity of the optimal shape under the shear stresses", *Int. J. Solids Struct.* **35**:33 (1998), 4391–4410.

[Givoli and Elishakoff 1992] D. Givoli and I. Elishakoff, "Stress concentration at a nearly circular hole with uncertain irregularities", *J. Appl. Mech.* **59**:25 (1992), S65–S71.

[Goldberg and Sastry 2007] D. E. Goldberg and K. Sastry, *Genetic algorithms: the design of innovation*, 2nd ed., Springer, 2007.

[Kalandiya 1975] A. I. Kalandiya, *Mathematical methods of two-dimensional elasticity*, Mir, Moscow, 1975.

[Levy and Lessman 1958] H. Levy and F. Lessman, *Finite difference equations*, Pitman, London, 1958.

[Medina and Hinderliter 2014] H. Medina and B. Hinderliter, "The stress concentration factor for slightly roughened random surfaces: analytical solution", *Int. J. Solids Struct.* **51**:10 (2014), 2012–2018.

[Muskhelishvili 1963] N. I. Muskhelishvili, *Some basic problems of the mathematical theory of elasticity*, Noordhoff, Groningen, Netherlands, 1963.

[Natanson 1955] I. P. Natanson, *Theory of functions of a real variable*, Ungar, New York, 1955.

[Palmov 1963] V. A. Palmov, "State of stress in the neighborhood of a rough surface of elastic bodies", *Prikl. Mat. Mekh.* **27**:5 (1963), 963–969. In Russian; translated in *J. Appl. Math. Mech.* **27**:5 (1963), 1479–1489.

[Pilkey and Pilkey 2007] W. D. Pilkey and D. F. Pilkey, *Peterson's stress concentration factors*, 3rd ed., Wiley, New York, 2007.

[Pluvinage 2003] G. Pluvinage, *Fracture and fatigue emanating from stress concentrators*, Springer, 2003.

[Savruk and Kazberuk 2017] M. P. Savruk and A. Kazberuk, *Stress concentration at notches*, Springer, 2017.

[Shahzad et al. 2017] S. Shahzad, F. Dal Corso, and D. Bigoni, "Hypocycloidal inclusions in nonuniform out-of-plane elasticity: stress singularity vs. stress reduction", *J. Elasticity* **126**:2 (2017), 215–229.

[Sheinin 1972] V. I. Sheinin, "On the asymptotic method for calculating stress near rough surface of elastic solids", *Izv. Akad. Nauk SSSR Mekh. Tverd. Tela* **2** (1972), 94–102. In Russian; translated in *Mech. Solids* **7**:2 (1972), 94–102.

[Vigdergauz 1976] S. B. Vigdergauz, "Integral equation of the inverse problem of the plane theory of elasticity", *Prikl. Mat. Mekh.* **40** (1976), 566–569. In Russian; translated in *J. Appl. Math. Mech.* **40**:3 (1976), 518–522.

[Vigdergauz 2006] S. Vigdergauz, "The stress-minimizing hole in an elastic plate under remote shear", *J. Mech. Mater. Struct.* **1**:2 (2006), 387–406.

[Vigdergauz 2012] S. Vigdergauz, "Stress-smoothing holes in an elastic plate: from the square lattice to the checkerboard", *Math. Mech. Solids* **17**:3 (2012), 289–299.

[Vigdergauz and Cherkaev 1986] S. B. Vigdergauz and A. V. Cherkaev, "A hole in a plate, optimal for its biaxial extension-compression", *Prikl. Mat. Mekh.* **50**:3 (1986), 524–528. In Russian; translated in *J. Appl. Math. Mech.* **50**:3 (1986), 401–404.

[Vigdergauz and Elishakoff 2019] S. Vigdergauz and I. Elishakoff, "Energy-maximizing holes in an elastic plate under remote loading", *J. Mech. Mater. Struct.* **14**:1 (2019), 139–154.

Received 28 Jun 2019. Revised 27 Aug 2019. Accepted 28 Sep 2019.

SHMUEL VIGDERGAUZ: shmuelvigdergauz@gmail.com
R&D Division, The Israel Electric Corp. Ltd., Haifa, Israel

ISAAC ELISHAKOFF: elishako@fau.edu
Department of Mechanical Engineering, Florida Atlantic University, Boca Raton, FL, United States

JOURNAL OF MECHANICS OF MATERIALS AND STRUCTURES
Vol. 15, No. 1, 2020
dx.doi.org/10.2140/jomms.2020.15.15

ANALYTICAL MODELING AND COMPUTATIONAL ANALYSIS ON TOPOLOGICAL PROPERTIES OF 1-D PHONONIC CRYSTALS IN ELASTIC MEDIA

MUHAMMAD AND C. W. LIM

The topological interface state governed by topological phononic crystals (PnC) can potentially host one-way, backscattering free nontrivial edge modes, immune to defects and sharp edges. We study here 1D topological phononic crystals with interface modes/states generated by an exchange of wave mode polarization and geometric phases, using the spectral element method with Timoshenko beam model for flexural wave propagation. The constitutive relations for the longitudinal wave, and modeling and formulation are derived for theoretical band structure and frequency response studies. The analysis is validated by finite element numerical simulations. The geometric phases of the Bloch bands are determined by numerical Zak phase analysis. As the geometric properties of the PnC vary, a band transition resulting from an exchange in wave mode polarization is observed and the symmetry characteristics of the Bloch bands are determined. The geometric phases provide useful information about the interface mode that is generated when the mode transition frequency is common between the bandgaps of topological PnC. We further conduct theoretical and numerical studies on the presence of interface state and excellent agreement observed between both models is reported. The theoretical details of the topological PnC with protected interface mode can be helpful for better understating of research in phononic crystals.

A list of symbols can be found on page 32.

1. Introduction

Recent advances in the study of the quantum Hall effect [Haldane 1988], valley Hall effect [Dong et al. 2017; Zhou et al. 2019a] and quantum spin Hall effect [Bernevig et al. 2006; Kane and Mele 2005] in classical wave physics have paved the way for novel discoveries in the photonic and phononic research community. Analogous to the quantum theory presented, physicists explored the realm of periodic structures in solids supported by theory [Kushwaha et al. 1993; Sigalas and Economou 1993], observation [Martínez-Sala et al. 1995] and experimental work [Liu et al. 2000]; those authors investigated the propagation of acoustic and elastic waves in a periodic array of scatterers that revealed frequency bandgap characteristics where no wave propagation occurs. The discovery of topological insulators [Hasan and Kane 2010; Huber 2016; Moore 2010], which exhibit topological properties with nontrivial geometric phases in the electronic system and counterpart photonic [Khanikaev et al. 2013] and phononic crystals (PnCs) in both acoustic [Xiao et al. 2015; Zhao et al. 2018] and elastic [Muhammad et al. 2019; Zhou et al. 2019b] media has opened up an active research area for the study of new physical phenomena related

Muhammad's ORCID is 0000-0003-3492-0123.

Keywords: geometric phase, interface mode, spectral element, topological phononic crystals, Zak phase, geometric phase, interface mode, spectral element, topological phononic crystals, Zak phase.

to topological phases. Topology as a tool has been recently explored in conventional band theories and marvelous wave characteristics in hexagonal lattices [Chen et al. 2018b; Chen et al. 2018a; Jia et al. 2018; Khanikaev et al. 2015; Pal et al. 2018; Reda et al. 2016; Xia et al. 2018], beams [Kim et al. 2018; Li et al. 2018; Muhammad et al. 2019; Zhou et al. 2019b] and plate structures [Brendel et al. 2018; Foehr et al. 2018; Jin et al. 2018; Miniaci et al. 2018] have been reported.

Spatially, the topological properties illustrate the quantized behavior of the wavefunctions over an associated band structure and they greatly influence the transportation behavior of phonons and photons. Furthermore, they also preserve certain symmetry against the local perturbation and the symmetric properties are retained unless the perturbation is not strong enough to close the bandgap of topological PnCs [Ma et al. 2019]. The topological characteristics is governed either by actively breaking time reversal symmetry, mimicking the quantum Hall effect [Haldane 1988; Mei et al. 2016] or nucleation and coupling of degenerate modes [Cha and Daraio 2018; Miniaci et al. 2018; Susstrunk and Huber 2015], and analogues to the quantum spin Hall effect. They are demonstrated through the Dirac cone dispersion plot. The peculiar characteristics of the topologically distinct PnCs include the generation of topologically protected interface mode (TPIM) at the junction of topologically protected unit cells. The primary characteristics of TPIM include robustness and backscattering immune single way wave transport without any loss of energy. Furthermore, TPIMs have a maximum amount of energy that concentrates at the interface of topological PnCs with decaying energy fields away from it. Such TPIMs can also control, divert, confine and enhance the propagation of elastic waves in solid structures [Miniaci et al. 2018; Muhammad et al. 2019; Xia et al. 2018; Zhang et al. 2019]. The recently proposed idea of reprogrammable TPIMs in acoustic [Xia et al. 2018] and elastic media [Zhang et al. 2019; Zhou et al. 2019a; Zhou et al. 2019c] is also intriguing. These modes also govern different characteristics with reference to passband and bandgap frequencies as explained by [Muhammad et al. 2019]. Nonlinear nanobeam vibration with surface effects [Chen et al. 2019a], auxetic metamaterials [Andrade et al. 2018] and topological optimization of spatially continuum structure [Czubacki et al. 2015] has also been reported.

The geometric phases of Bloch bands are determined by topological invariants such as Zak phase [Delplace et al. 2011; Muhammad et al. 2019; Xiao et al. 2015; Zhou et al. 2019b] or Berry phase [Chen et al. 2019b; Wang et al. 2015; Xiao et al. 2010] for 1D and 2D PnCs respectively. For the details of theoretical and experimental observation of the Zak phase, one may refer to [Xiao et al. 2015]. The Zak phase provides information about the symmetry characteristics of Bloch bands and help distinguish the symmetric and unsymmetric edge modes of topological PnCs that further helps in the derivation of TPIMs. A detailed analysis on the geometric phases is given in Section 4. As is today, the reported works like one-way elastic edge state [Wang et al. 2015; Yu et al. 2018], topological valley transport [Huo et al. 2017; Zhang et al. 2013; Zhang et al. 2019], helical edge modes [Miniaci et al. 2018; Susstrunk and Huber 2015] and topological insulators [He et al. 2016; Huber 2016; Yu et al. 2018] etc are well recognized. Although multiple studies have investigated topological properties in photonics, electromagnetic and acoustic systems yet due to complex medium characteristics, the propagation of elastic waves in solids is still an open challenge. Furthermore, as already explored for the other wave media, TPIM in an elastic system may have more far-reaching applications in engineering vibration problems in civil, mechanical and aerospace engineering.

The present study extends and generalizes the reported work of [Muhammad et al. 2019] with a more generalize Timoshenko beam model to investigate the topological characteristics of 1D PnC beam. Using

the spectral element method, the dispersion relation and frequency response spectra for the longitudinal and bending elastic waves are established. In this study, a commercial finite element method (FEM) simulation code COMSOL Multiphysics is applied to validate the theoretical research findings and both theoretical and numerical results do show excellent agreement. A 1D PnC with varying cross-sectional area is proposed and the geometric phases of the Bloch band is determined by analyzing the Zak phase. The symmetry characteristics of the edge modes are determined and through the Dirac cone dispersion analysis the band transition and exchange in wave mode polarization are studied. The Dirac cone for the longitudinal wave is related to a symmetric band inversion as compared to bending waves where unsymmetric band transition due to nonlinear wave dispersion behavior is observed [Muhammad et al. 2019]. Two topologically distinct PnCs with different edge modes symmetry characteristic induces an interface mode provided that the mode transition frequency (band transition point) is present inside the bandgap of topological PnCs. We also perform a study on the finite unit cell based frequency response to reveal the existence of TPIM by both theoretical and numerical analyses. This theoretical and numerical model may help phononic community to better understand the physical phenomenon. The robustness with confinement of the wave energy at the interface of PnCs can be useful for solving vibration related engineering problems.

The paper is organized as follow. The topological beam model is explained in Section 2. Section 3 develops the theoretical formulation for a finite and an infinite unit cell model. Numerical formulation and Zak phase are explained in Section 4. The results are discussed in Section 5, and Section 6 presents conclusions.

2. Problem definition and physical modeling

A thick beam model as illustrated in Figure 1 is considered here. The model consists of a piecewise continuous periodic circular beam with two thinner sections sandwiching a thicker section. The lattice length of the periodic structure is a and L_A, D_A are length and diameter of the thicker beam while, L_B, d_B designate the length and diameter of the thinner beam. The material properties and geometric parameters are as follows:

$$L = 40\,\text{mm}; \quad D_A = 8\,\text{mm}; \quad d_B = 4\,\text{mm}; \quad \text{density } \rho = 2700\,\text{kg/m}^3;$$
$$\text{Young's modulus } E = 70\,\text{GPa}; \quad \text{Posson's ratio } \nu = 0.33.$$

In general, for any elastic beam structure, longitudinal and bending waves coexist with distinct wave dispersion characteristic. The propagation of longitudinal waves is linearly dispersive that is governed by $\omega^2 = k^2 E/\rho$, however, flexural waves show nonlinear dispersion behavior. To ensure the decoupling of longitudinal and flexural waves, the unit cell of the PnC is arranged symmetrically with respect to the xy-plane. A topological shape parameter $\delta = (L_A + 2L_B)/L$ is introduced to characterize a topologically distinct unit cell.

The spectral element method with Timoshenko beam model is applied here to derive the band structure and frequency response spectra for bending waves. A constitutive relation for dispersion spectra of longitudinal wave is also derived (see Section 3.1). The symmetry properties of the edge modes are determined by the Zak phase (see Section 4). The theoretical findings are validated by numerical simulations of COMSOL Multiphysics.

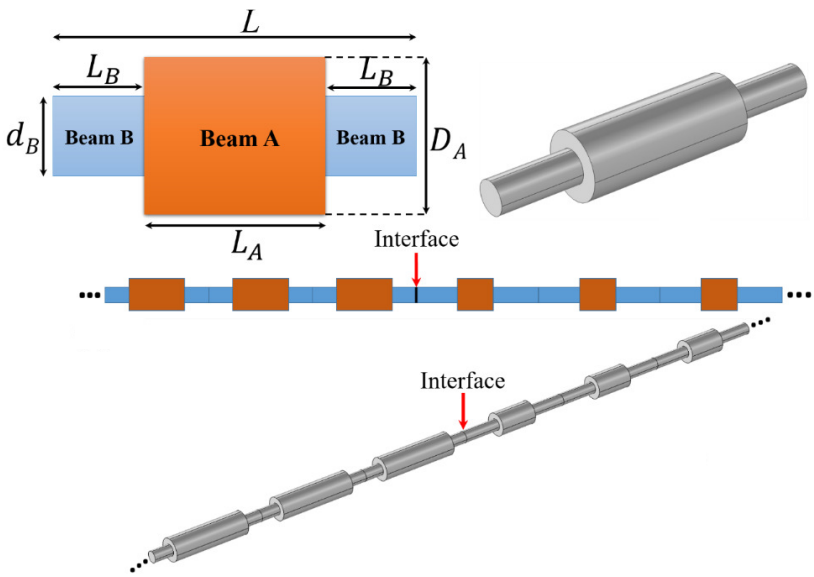

Figure 1. Top: geometry of the PnC beam units. Bottom: finite length PnC beam with interface highlighted by red arrows.

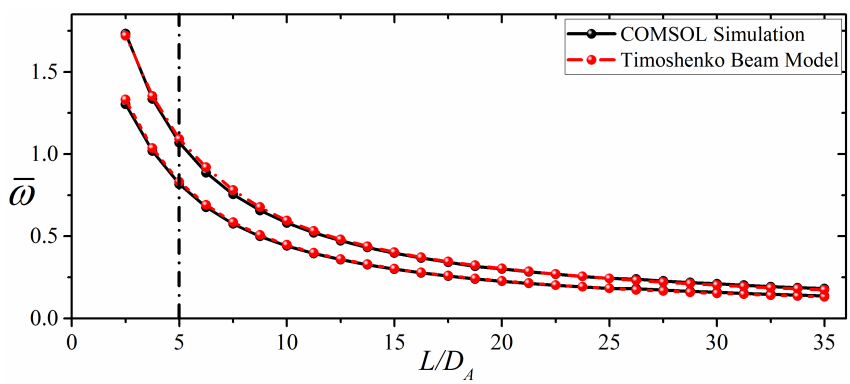

Figure 2. Comparison of the theoretical and numerical models for flexural wave propagation with varying slenderness ratio L/D_A. Black dashed line for $L/D_A = 5$ represents geometric parameter adopted in the present study.

3. Governing equations and solution methodology

3.1. ***Flexural waves.*** For flexural wave propagation in a beam with a considerable thickness-to-length ratio (significantly shear deformable), the characteristic equation of motion can be expressed as follows [Gao et al. 2018; Yu et al. 2006; Zhou et al. 2019b]:

$$\frac{EI_z}{\rho S}\frac{\partial^4 w(x,t)}{\partial x^4} - \frac{I_z}{S}\left(1+\frac{E}{\kappa G}\right)\frac{\partial^4 w(x,t)}{\partial x^2 \partial t^2} + \frac{\partial^2 w(x,t)}{\partial t^2} + \frac{\rho I_z}{\kappa G S}\frac{\partial^4 w(x,t)}{\partial t^4} = 0, \tag{1}$$

where EI_z, G and κ are flexural rigidity, shear modulus and shear correction factor for the beam, while S, ρ are cross-sectional area, mass density and $w(x,t) = W(x)e^{i\omega t}$ is lateral displacement of the beam with $W(x)$ being mode shape function and ω is angular frequency. For a circular or rectangular beam, the following expressions apply:

$$I_z = \begin{cases} \dfrac{wh^3}{12} & \text{(rectang.)} \\ \dfrac{\pi D^4}{64} & \text{(circular)} \end{cases} \qquad EI_z = \begin{cases} \dfrac{Ewh^3}{12} & \text{(rectang.)} \\ \dfrac{\pi E D^4}{64} & \text{(circular)} \end{cases} \qquad \kappa = \begin{cases} \dfrac{5(1+\nu)}{6+5\nu} & \text{(rectang.)} \\ \dfrac{6(1+\nu)^2}{7+12\nu+4\nu^2} & \text{(circular)} \end{cases} \tag{2}$$

For such a shear deformable beam, the Timoshenko beam model is applicable. The governing equation for bending moment and shear force is, respectively,

$$M = EI_z \frac{\partial \psi}{\partial x}, \quad V = \kappa GS\left(\frac{\partial w}{\partial x} - \psi\right), \tag{3}$$

where ψ is the angular rotation of circular beam that is related to $w(x)$ by

$$\psi = \frac{EI_z}{\kappa GS - \rho I_z \omega^2}\frac{\partial^3 w(x)}{\partial x^3} + \frac{1}{\kappa GS - \rho I_z \omega^2}\left(EI\frac{\rho}{\kappa G}\omega^2 + \kappa GS\right)\frac{\partial w(x)}{\partial x}. \tag{4}$$

For generality in formulation, the key quantities are made dimensionless by introducing the variables

$$\begin{gathered} \bar{w} = w/L, \quad \bar{x} = x/L, \quad \overline{\omega} = \omega L\sqrt{\rho_B/E_B} \quad \phi = EI_z/(E_B L^4), \bar{\rho} = \rho/\rho_B, \\ \bar{S} = S/L^2, \quad \bar{I}_z = I_z/L^4, \quad \overline{G} = G/E_B, \quad \overline{M} = M/(E_B L^3), \quad \overline{V} = V/(E_B L^2), \end{gathered} \tag{5}$$

where E_B and ρ_B are Young's modulus and density of beam B, respectively. By substituting (4) into (3), the normalized constitutive relations are

$$\psi = A\bar{w}''' + B\bar{w}', \quad \overline{M} = C\bar{w}''(\bar{x}) + Dw(\bar{x}),, \quad \overline{V} = \kappa\overline{G}\bar{S}((1-B)\bar{w}' - A\bar{w}'''). \tag{6}$$

The normalized bending moment using (6) becomes

$$\psi'(\bar{x}) = \bar{w}''(\bar{x}) + \frac{\overline{\rho\omega}^2}{\kappa\overline{G}}\bar{w}. \tag{7}$$

In (6) and (7)) the derivatives are with respect to $\bar{x}$ and A, B, C, D are given by

$$A = \frac{\phi}{\kappa\overline{G}\bar{S} - \bar{\rho}\bar{I}_z\overline{\omega}^2}, \quad B = \frac{1}{\kappa\overline{G}\bar{S} - \overline{\rho}\bar{I}_z\overline{\omega}^2}\left(\phi\frac{\bar{\rho}}{\kappa\overline{G}}\overline{\omega}^2 + \kappa\overline{G}\bar{S}\right), \quad C = \phi, \quad D = \phi\frac{\bar{\rho}\overline{\omega}^2}{\kappa\overline{G}}. \tag{8}$$

Using these dimensionless quantities, (1) can be rewritten as

$$\phi\frac{\partial^4\bar{w}}{\partial\bar{x}^4} + \left[\left(\frac{\phi}{\kappa\overline{G}} + \bar{I}_z\right)\bar{\rho}\overline{\omega}^2\right]\frac{\partial^2}{\partial\bar{x}^2}\bar{w} - \bar{\rho}\overline{\omega}^2\left(\bar{S} - \frac{\bar{\rho}\bar{I}_z\overline{\omega}^2}{\kappa\overline{G}}\right)\bar{w} = 0. \tag{9}$$

As in [Zhou et al. 2019b], the surface effect is neglected here. The harmonic solution to (9) is

$$\bar{w}(\bar{x}) = A_1 e^{i\zeta\bar{x}}. \tag{10}$$

Substituting this relation into (9) yields

$$S_1\zeta^4 + S_2\zeta^2 + S_3 = 0, \tag{11}$$

with

$$S_1 = \phi, \quad S_2 = -\bar{\rho}\overline{\omega}^2\left(\frac{\phi}{\kappa\overline{G}} + \bar{I}_z\right), \quad S_3 = -\bar{\rho}\overline{\omega}^2\left(\bar{S} - \frac{\bar{\rho}\bar{I}_z}{\kappa\overline{G}}\overline{\omega}^2\right). \tag{12}$$

Solving (11) in ζ yields four solutions:

$$\zeta_1 = -\zeta_2 = \sqrt{\frac{-S_2 + \sqrt{S_2^2 - 4S_1S_3}}{2S_1}}, \quad \zeta_3 = -\zeta_4 = \sqrt{\frac{-S_2 - \sqrt{S_2^2 - 4S_1S_3}}{2S_1}}. \tag{13}$$

Hence, the general solution of (11) can be expressed as

$$w(\bar{x}) = A_1 e^{i\chi_1\bar{x}} + A_2 e^{i\chi_2\bar{x}} + A_3 e^{i\chi_3\bar{x}} + A_4 e^{i\chi_4\bar{x}}, \tag{14}$$

where the A_j $(j = 1, 2, 3, 4)$ are unknown coefficients to be determined by the boundary conditions.

We introduce a nodal displacement vector $\boldsymbol{q} = (\boldsymbol{q}_L^T \ \boldsymbol{q}_R^T)^T$, which according to (6) can be written as

$$\boldsymbol{q} = \boldsymbol{P}\boldsymbol{b}. \tag{15}$$

Superscript T in the equations above means transposition, $\boldsymbol{q}_L = [\bar{w}(0)\ \psi(0)]^T$, $\boldsymbol{q}_R = \left[\bar{w}(\bar{L})\psi(\bar{L})\right]^T$, $\boldsymbol{b} = [A_1\ A_2\ A_3\ A_4]^T$ and

$$\boldsymbol{P} = \begin{bmatrix} 1 & 1 & 1 & 1 \\ iX_1 & iX_2 & iX_3 & iX_4 \\ e^{i\zeta_1\bar{L}} & e^{i\zeta_2\bar{L}} & e^{i\zeta_3\bar{L}} & e^{i\zeta_4\bar{L}} \\ iX_1e^{i\zeta_1\bar{L}} & iX_2e^{i\zeta_2\bar{L}} & iX_3e^{i\zeta_3\bar{L}} & iX_4e^{i\zeta_4\bar{L}} \end{bmatrix}, \tag{16}$$

where $X_j = \zeta_j(B - A\zeta_j^2)$ and $\bar{L} = L_B/2$ or L_A. The nodal force vector $\boldsymbol{f} = \left[\boldsymbol{f}_L^T \ \ \boldsymbol{f}_R^T\right]^T$ is written as

$$\boldsymbol{f} = \boldsymbol{R}\boldsymbol{b}, \tag{17}$$

in which $\boldsymbol{f}_L = \left[-\overline{M}(0) - \overline{V}(0)\right]^T$ and $\boldsymbol{f}_R = \left[\overline{M}(\bar{L})\overline{V}(\bar{L})\right]^T$. Here $\boldsymbol{R}$ is

$$\boldsymbol{R} = \begin{bmatrix} -Z_1 & -Z_2 & -Z_3 & -Z_4 \\ -iY_1 & -iY_2 & -iY_3 & -iY_4 \\ Z_1e^{i\zeta_1\bar{L}} & Z_2e^{i\zeta_2\bar{L}} & Z_3e^{i\zeta_3\bar{L}} & Z_4e^{i\zeta_4\bar{L}} \\ iY_1e^{i\zeta_1\bar{L}} & iY_2e^{i\zeta_2\bar{L}} & iY_3e^{i\zeta_3\bar{L}} & iY_4e^{i\zeta_4\bar{L}} \end{bmatrix}, \tag{18}$$

where $Y_j = \kappa\overline{G}\bar{S}\left(1 - B + A\zeta_j^2\right)\zeta_j$, $Z_j = D - C\zeta_j^2$ with $j = 1, 2, 3, 4$. Combining (16), (17) and (18), we get

$$\begin{bmatrix} \boldsymbol{f}_L^{(A,B)} \\ \boldsymbol{f}_R^{(A,B)} \end{bmatrix} = \begin{bmatrix} \boldsymbol{D}_{LL}^{(A,B)} & \boldsymbol{D}_{LR}^{(A,B)} \\ \boldsymbol{D}_{RL}^{(A,B)} & \boldsymbol{D}_{RR}^{(A,B)} \end{bmatrix} \begin{bmatrix} \boldsymbol{q}_L^{(A,B)} \\ \boldsymbol{q}_R^{(A,B)} \end{bmatrix}. \tag{19}$$

Superscript A, B denote the parameters calculated on the left and right sides of subbeams A and B. Also, we have

$$\boldsymbol{D}^{(A,B)} = \begin{bmatrix} \boldsymbol{D}_{LL}^{(A,B)} & \boldsymbol{D}_{LR}^{(A,B)} \\ \boldsymbol{D}_{RL}^{(A,B)} & \boldsymbol{D}_{RR}^{(A,B)} \end{bmatrix} = \boldsymbol{R}^{(A,B)}\left(\boldsymbol{P}^{(A,B)}\right)^{-1}, \tag{20}$$

which is the dynamic stiffness matrix. The dispersion relation and band structure study involve an infinite periodic unit cell structure. The equation of motion for each unit cell can be described by the dynamic stiffness matrix as follows:

$$\begin{bmatrix} \boldsymbol{f}_L^B \\ \boldsymbol{f}_R^A \end{bmatrix} = \begin{bmatrix} \boldsymbol{Q}_{LL} & \boldsymbol{Q}_{LR} \\ \boldsymbol{Q}_{RL} & \boldsymbol{Q}_{RR} \end{bmatrix} \begin{bmatrix} \boldsymbol{q}_L^B \\ \boldsymbol{q}_R^A \end{bmatrix}. \tag{21}$$

Furthermore,

$$\begin{aligned} \boldsymbol{f}_L^B &= \left[\boldsymbol{D}_{LL}^B - \boldsymbol{D}_{LR}^B\left(\boldsymbol{D}_{RR}^B + \boldsymbol{D}_{LL}^A\right)^{-1}\boldsymbol{D}_{LR}^B\right]\boldsymbol{q}_{LL}^B - \boldsymbol{D}_{LR}^B\left(\boldsymbol{D}_{RR}^B + \boldsymbol{D}_{LL}^A\right)^{-1}\boldsymbol{D}_{LR}^A\boldsymbol{q}_{RR}^A, \\ \boldsymbol{f}_R^A &= -\boldsymbol{D}_{LR}^A\left(\boldsymbol{D}_{RR}^B + \boldsymbol{D}_{LL}^A\right)^{-1}\boldsymbol{D}_{LR}^B\boldsymbol{q}_{LL}^B + \left[\boldsymbol{D}_{RR}^A - \boldsymbol{D}_{LR}^A\left(\boldsymbol{D}_{RR}^B + \boldsymbol{D}_{LL}^A\right)^{-1}\boldsymbol{D}_{LR}^A\right]\boldsymbol{q}_{RR}^A, \end{aligned}$$

where $\boldsymbol{Q} = \begin{bmatrix} \boldsymbol{Q}_{LL} & \boldsymbol{Q}_{LR} \\ \boldsymbol{Q}_{RL} & \boldsymbol{Q}_{RR} \end{bmatrix}$ is the dynamic stiffness matrix for each unit cell with

$$\begin{aligned} \boldsymbol{Q}_{LL} &= \boldsymbol{U}_{LL} - \boldsymbol{U}_{LR}\left(\boldsymbol{U}_{RR} + \boldsymbol{D}_{LL}^B\right)^{-1}\boldsymbol{U}_{RL}, \\ \boldsymbol{Q}_{LR} &= -\boldsymbol{U}_{LR}\left(\boldsymbol{U}_{RR} + \boldsymbol{D}_{LL}^B\right)^{-1}\boldsymbol{D}_{LR}^B, \\ \boldsymbol{Q}_{RL} &= -\boldsymbol{D}_{RL}^A\left(\boldsymbol{U}_{RR} + \boldsymbol{D}_{LL}^B\right)^{-1}\boldsymbol{U}_{RL}, \\ \boldsymbol{Q}_{RR} &= \boldsymbol{D}_{RR}^B - \boldsymbol{D}_{RL}^B\left(\boldsymbol{U}_{RR} + \boldsymbol{D}_{LL}^B\right)^{-1}\boldsymbol{D}_{LR}^B, \end{aligned} \tag{22}$$

$$\begin{aligned} \boldsymbol{U}_{LL} &= \boldsymbol{D}_{LL}^B - \boldsymbol{D}_{LR}^B\left(\boldsymbol{D}_{RR}^B + \boldsymbol{D}_{LL}^A\right)^{-1}\boldsymbol{D}_{RL}^A, \\ \boldsymbol{U}_{LR} &= -\boldsymbol{D}_{LR}^B\left(\boldsymbol{D}_{RR}^B + \boldsymbol{D}_{LL}^A\right)^{-1}\boldsymbol{D}_{LR}^A, \\ \boldsymbol{U}_{RL} &= -\boldsymbol{D}_{RL}^A\left(\boldsymbol{D}_{RR}^B + \boldsymbol{D}_{LL}^A\right)^{-1}\boldsymbol{D}_{RL}^B, \\ \boldsymbol{U}_{RR} &= \boldsymbol{D}_{RR}^A - \boldsymbol{D}_{RL}^A\left(\boldsymbol{D}_{RR}^B + \boldsymbol{D}_{LL}^A\right)^{-1}\boldsymbol{D}_{LR}^A. \end{aligned} \tag{23}$$

Using the expressions above and applying the continuity condition $\boldsymbol{f}_R^B = -\boldsymbol{f}_L^A$, $\boldsymbol{q}_R^B = \boldsymbol{q}_L^A$ at the interface between beams A and B, and further applying the Floquet–Bloch periodicity condition, the physical parameters at both ends of the unit cell become

$$\boldsymbol{q}_R^A = e^{ik}\boldsymbol{q}_L^B, \quad \boldsymbol{f}_R^A = -e^{ik}\boldsymbol{f}_L^B, \tag{24}$$

where k designates the dimensionless Bloch parameter. Combining (21) and (24) gives

$$\begin{aligned} \left[e^{2ik} - \boldsymbol{Q}_{LR}^{-1}\boldsymbol{Q}_{RR}e^{ik} + e^{ik}\boldsymbol{Q}_{LR}^{-1}\boldsymbol{Q}_{LL} - \boldsymbol{Q}_{LR}^{-1}\boldsymbol{Q}_{RL}\right]\boldsymbol{q}_{LL}^B = \boldsymbol{0}, \\ e^{2ik}\boldsymbol{q}_{LL}^B + e^{ik}\boldsymbol{Q}_{LR}^{-1}\left[\boldsymbol{Q}_{LL} + \boldsymbol{Q}_{RR}\right]\boldsymbol{q}_{LL}^B + \boldsymbol{Q}_{LR}^{-1}\boldsymbol{Q}_{RL}\boldsymbol{q}_{LL}^B = \boldsymbol{0}. \end{aligned} \tag{25}$$

By further modification, (25) can be reexpressed as follows [Zhou et al. 2019b]:

$$\begin{aligned} \begin{bmatrix} \boldsymbol{0} & \boldsymbol{I} \\ \boldsymbol{Q}_{LR}^{-1}\boldsymbol{Q}_{RL} & \boldsymbol{Q}_{LR}^{-1}(\boldsymbol{Q}_{RR} - \boldsymbol{Q}_{LL}) \end{bmatrix}\begin{pmatrix} \boldsymbol{q}_L^B \\ e^{ik}\boldsymbol{q}_L^B \end{pmatrix} - e^{ik}\begin{pmatrix} \boldsymbol{q}_L^B \\ e^{ik}\boldsymbol{q}_L^B \end{pmatrix} = \boldsymbol{0}, \\ \begin{bmatrix} \boldsymbol{0} & \boldsymbol{I} \\ -\boldsymbol{Q}_{LR}^{-1}\boldsymbol{Q}_{RL} & -\boldsymbol{Q}_{LR}^{-1}(\boldsymbol{Q}_{LL}+\boldsymbol{Q}_{RR}) \end{bmatrix}\begin{pmatrix} \boldsymbol{q}_L^B \\ e^{ik}\boldsymbol{q}_L^B \end{pmatrix} - e^{ik}\begin{pmatrix} \boldsymbol{q}_L^B \\ e^{ik}\boldsymbol{q}_L^B \end{pmatrix} = \boldsymbol{0}, \end{aligned} \tag{26}$$

where $\boldsymbol{I}$ is the 2×2 identity matrix. This is the generalized eigenvalue problem for dispersion relation. The solution of (26) yields four roots of e^{ik} for a specific value of the normalized frequency $\overline{\omega}$. If the complex root is $x+iy$ and the associated Bloch parameter k is $p+iq$, with x, y, p, q being real, according to [Han et al. 2012; Muhammad et al. 2019] the expression $x+iy$ can be written in the form of p and q as

$$q = -\ln(x^2+y^2), \tag{27}$$

$$p = \begin{cases} \arctan(y/x) & \text{if } x > 0, \\ \pi + \arctan(y/x) & \text{if } x < 0 \text{ and } y > 0, \\ -\pi + \arctan(y/x) & \text{if } x < 0 \text{ and } y < 0. \end{cases} \tag{28}$$

Next, we consider the propagation of flexural waves in finite number of unit cells as shown in Figure 1. An excitation force is applied at the left (right) end and the output response in the form of out-of-plane displacement is received at the right (left) end. The wave motion in finite length PnC can be described by expressing the global stiffness matrix as follows [Zhou et al. 2019b]:

$$\boldsymbol{f}_{\text{tot}} = \boldsymbol{Q}_{\text{tot}}\, \boldsymbol{q}_{\text{tot}}. \tag{29}$$

Here $\boldsymbol{f}_{\text{tot}}$, $\boldsymbol{q}_{\text{tot}}$ and $\boldsymbol{Q}_{\text{tot}}$ are global force, displacement and stiffness matrix respectively. In the case of an excitation signal induced at the left end of finite length PnCs and the out-of-plane displacement is recorded at the right end, the force, displacement and stiffness vectors are

$$\boldsymbol{q}_{\text{tot}} = \begin{Bmatrix} \boldsymbol{q}_{(0)} \\ \boldsymbol{q}_{(1)} \\ \vdots \\ \boldsymbol{q}_{(N)} \end{Bmatrix}, \quad \boldsymbol{f}_{\text{tot}} = \begin{Bmatrix} \boldsymbol{f}_{(0)} \\ \boldsymbol{0} \\ \vdots \\ \boldsymbol{0} \end{Bmatrix}, \quad \boldsymbol{f}_{(0)} = \begin{pmatrix} \bar{P}_I \\ 0 \end{pmatrix}, \quad \boldsymbol{q}_{(0)} = \begin{pmatrix} \bar{w}_I \\ \bar{\psi}_I \end{pmatrix}, \quad \boldsymbol{q}_{(N)} = \begin{pmatrix} \bar{w}_O \\ \bar{\psi}_O \end{pmatrix}, \tag{30}$$

$$\boldsymbol{Q}_{\text{tot}} = \begin{bmatrix} \boldsymbol{Q}_{(1)}^{LL} & \boldsymbol{Q}_{(1)}^{LR} & \boldsymbol{0} & \boldsymbol{0} & \cdots & \boldsymbol{0} & \boldsymbol{0} \\ \boldsymbol{Q}_{(1)}^{RL} & \boldsymbol{Q}_{(1)}^{RR} + \boldsymbol{Q}_{(2)}^{LL} & \boldsymbol{Q}_{(2)}^{LR} & \boldsymbol{0} & \vdots & \vdots & \boldsymbol{0} \\ \boldsymbol{0} & \boldsymbol{Q}_{(2)}^{RL} & \boldsymbol{Q}_{(2)}^{RR} + \boldsymbol{Q}_{(3)}^{LL} & \cdots & \cdots & \cdots & \vdots \\ \boldsymbol{0} & \boldsymbol{0} & \vdots & \ddots & \vdots & \boldsymbol{0} & \boldsymbol{0} \\ \vdots & \cdots & \cdots & \cdots & \boldsymbol{Q}_{(N-2)}^{RR} + \boldsymbol{Q}_{(N-1)}^{LL} & \boldsymbol{Q}_{(N-1)}^{LR} & \boldsymbol{0} \\ \boldsymbol{0} & \cdots & \ddots & \boldsymbol{0} & \boldsymbol{Q}_{(N-1)}^{RL} & \boldsymbol{Q}_{(N-1)}^{RR} + \boldsymbol{Q}_{(N)}^{LL} & \boldsymbol{Q}_{(N)}^{LR} \\ \boldsymbol{0} & \boldsymbol{0} & \boldsymbol{0} & \boldsymbol{0} & \boldsymbol{0} & \boldsymbol{Q}_{(N)}^{RL} & \boldsymbol{Q}_{(N)}^{RR} \end{bmatrix}. \tag{31}$$

The wave transmission ratio can be expressed as

$$FRF = 20 \log \frac{\bar{w}_0}{\bar{w}_I}, \tag{32}$$

where w_0 and w_I are the out-of-plane displacement at the output and input end of the finite length PnCs.

3.2. ***Longitudinal waves.*** Now we consider the propagation of longitudinal waves in an infinite PnC. The longitudinal wave propagation can be expressed by [Muhammad et al. 2019]

$$\rho \frac{\partial^2 u}{\partial t^2} = \frac{\partial}{\partial x}\left(E \frac{\partial u}{\partial x}\right), \tag{33}$$

where $\rho$and E are mass density and Young's modulus. The displacement in the n-th unit cell can be expressed written as

$$u_n^s(x,t) = U_n^{(s)} e^{i\omega t} = \left[A_n^{(s)+} e^{ikx} + A_n^{(s)-} e^{-ikx}\right] e^{i\omega t}. \tag{34}$$

By considering continuity of displacement and stress at the interface of topologically distinct PnCs and periodicity condition $U_{n+1}^{(s)}(x+h) = U_n^{(s)}(x) e^{ik\bar{L}}$, the unknown coefficients $\{A_n^{(1)+}, A_n^{(1)-}, A_n^{(2)+}, A_n^{(2)-}\}$ can be determined by

$$\begin{bmatrix} 1 & -1 & 1 & -1 \\ \frac{\omega}{c_{L_B}}\frac{Z_B^2}{\rho_B} & -\frac{\omega}{c_{L_A}}\frac{Z_A^2}{\rho_A} & -\frac{\omega}{c_{L_B}}\frac{Z_B^2}{\rho_B} & \frac{\omega}{c_{L_A}}\frac{Z_A^2}{\rho_A} \\ e^{i\left(kL-\frac{\omega}{c_{L_B}}L_B\right)} & -e^{i\frac{\omega}{c_{L_A}}L_A} & e^{i\left(kL+\frac{\omega}{c_{L_B}}L_B\right)} & -e^{-i\frac{\omega}{c_{L_A}}L_A} \\ \frac{\omega}{c_{L_B}}\frac{Z_B^2}{\rho_B} e^{i\left(kL-k_1L_B\right)} & -\frac{\omega}{c_{L_A}}\frac{Z_A^2}{\rho_A} e^{i\frac{\omega}{c_{L_A}}L_A} & -\frac{\omega}{c_{L_B}}\frac{Z_B^2}{\rho_B} e^{i\left(kL+\frac{\omega}{c_{L_B}}L_B\right)} & \frac{\omega}{c_{L_A}}\frac{Z_A^2}{\rho_A} e^{-i\frac{\omega}{c_{L_A}}L_A} \end{bmatrix} \begin{Bmatrix} A_n^{(1)+} \\ A_n^{(1)-} \\ A_n^{(2)+} \\ A_n^{(2)-} \end{Bmatrix} = 0, \tag{35}$$

where $Z = \rho c_L$ is the impedance, k is the wavenumber and c_L is the longitudinal wave velocity. Superscript A, B designate quantities for corresponding beams. From (35) the constitutive equation for the dispersion relation can be computed as

$$\cos(kL) = \cos\frac{2\omega L_B}{c_L}\cos\frac{\omega L_A}{c_L} - \frac{1}{2}\left(\frac{S_A}{S_B} + \frac{S_B}{S_A}\right)\sin\frac{2\omega L_B}{c_L}\sin\frac{\omega L_A}{c_L}. \tag{36}$$

Substituting $L = L_A + 2L_B$ leads to

$$\cos(k\bar{L}) = \cos(\frac{\overline{\omega}\bar{L}}{c_L}) - 0.5\left(\frac{\bar{S}_A}{\bar{S}_B} + \frac{\bar{S}_B}{\bar{S}_A} - 2\right)\sin\frac{2\overline{\omega}\bar{L}_B}{c_L}\sin\frac{\overline{\omega}\bar{L}_A}{c_L}, \tag{37}$$

which is the dispersion relation for longitudinal waves. For each ω, the wavenumber k can be determined accordingly.

The propagation of longitudinal waves in a finite length PnCs as shown in Figure 1(c-d) is further considered. The wave motion for a finite PnC can be expressed by the global stiffness matrix as

$$\boldsymbol{f}_{\text{tot}} = \boldsymbol{D}_{\text{tot}}\,\boldsymbol{q}_{\text{tot}}, \tag{38}$$

where $\boldsymbol{D}_{\text{tot}} = \boldsymbol{K} - \boldsymbol{M}\overline{\omega}^2$ is the dynamic stiffness matrix with $\boldsymbol{K}$ and $\boldsymbol{M}$ being the global stiffness and mass matrix, respectively. Besides, $\boldsymbol{f}_{\text{tot}}$ and $\boldsymbol{q}_{\text{tot}}$ are vectors of the global nodal force and displacement,

respectively, given by

$$\boldsymbol{q}_{\text{tot}} = \begin{Bmatrix} \boldsymbol{q}_{(0)} \\ \boldsymbol{q}_{(1)} \\ \vdots \\ \boldsymbol{q}_{(N)} \end{Bmatrix}, \quad \boldsymbol{f}_{\text{tot}} = \begin{Bmatrix} \boldsymbol{f}_{(0)} \\ \boldsymbol{0} \\ \vdots \\ \boldsymbol{0} \end{Bmatrix}, \quad \boldsymbol{f}_{(0)} = \begin{pmatrix} \bar{P}_I \\ 0 \end{pmatrix}, \quad \boldsymbol{q}_{(0)} = (\bar{u}_I), \quad \boldsymbol{q}_{(N)} = (\bar{u}_O), \tag{39}$$

$$\boldsymbol{D}_{\text{tot}} = \begin{bmatrix} \boldsymbol{D}_{(1)}^{LL} & \boldsymbol{D}_{(1)}^{LR} & \boldsymbol{0} & \boldsymbol{0} & \cdots & \boldsymbol{0} & \boldsymbol{0} \\ \boldsymbol{D}_{(1)}^{RL} & \boldsymbol{D}_{(1)}^{RR} + \boldsymbol{D}_{(2)}^{LL} & \boldsymbol{D}_{(2)}^{LR} & \boldsymbol{0} & \vdots & \vdots & \boldsymbol{0} \\ \boldsymbol{0} & \boldsymbol{D}_{(2)}^{RL} & \boldsymbol{D}_{(2)}^{RR} + \boldsymbol{D}_{(3)}^{LL} & \cdots & \cdots & \cdots & \vdots \\ \boldsymbol{0} & \boldsymbol{0} & \vdots & \ddots & \vdots & \boldsymbol{0} & \boldsymbol{0} \\ \vdots & \cdots & \cdots & \cdots & \boldsymbol{D}_{(N-2)}^{RR} + \boldsymbol{D}_{(N-1)}^{LL} & \boldsymbol{D}_{(N-1)}^{LR} & \boldsymbol{0} \\ \boldsymbol{0} & \cdots & \ddots & \boldsymbol{0} & \boldsymbol{D}_{(N-1)}^{RL} & \boldsymbol{D}_{(N-1)}^{RR} + \boldsymbol{D}_{(N)}^{LL} & \boldsymbol{D}_{(N)}^{LR} \\ \boldsymbol{0} & \boldsymbol{0} & \boldsymbol{0} & \boldsymbol{0} & \boldsymbol{0} & \boldsymbol{D}_{(N)}^{RL} & \boldsymbol{D}_{(N)}^{RR} \end{bmatrix}. \tag{40}$$

The wave transmission ratio can be expressed as

$$FRF = 20 \log \frac{\bar{u}_0}{\bar{u}_I}, \tag{41}$$

where u_0 and u_I are the displacements at the input and output ends.

4. Phononic crystal geometric phases

Pancharatnam [1956] introduced the idea of geometric phases while investigating light propagation through a sequence of polarizers. The study was latter extended to quantum mechanics in [Berry 1984]. See [Ma et al. 2019] for a detailed review of geometric phase in acoustic and mechanical lattices. The intersection of two bands at the Weyl point [Young et al. 2012] in a 3D system results in the variation of geometric phases. The Weyl point can be regarded as a source/drain of Berry flux, which is the surface integral of Berry curvature enhanced topological charge. For a 2D system, the Chern number is used to indicate the surface integral [Aidelsburger et al. 2014]. For a 1D model, the Zak phase is an integration of Berry connection [Ma et al. 2019]. Multiple studies have explained this characterization through the Su–Schrieffer–Heeger (SSH) model for acoustic and electronic system [Chiang et al. 1977; Li et al. 2018]. There are multiple studies [Chiang et al. 1977; Mei et al. 2016; Su et al. 1979] on the energy bandgap by electrons staggered hopping at the joint of unit cell. For a 1D system, the closing and reopening of bandgap depend upon the strength of intercell and intracell hopping. The topological nontrivial phase is induced when intercell hopping is stronger than intracell hopping. Stronger intracell hopping results in trivial topological phases. The interface mode is induced for lattices with nontrivial topological phases.

Apart from the SSH model, the similar concept can be applied in PnCs. The hopping strength can be controlled by adjusting the cross-sectional area of the unit cell. Variation in the cross-section of the unit cell lattice reveals band closing and reopening with an exchange of geometric phases determined by the Zak phase. The geometric phases of the bulk band are determined by integrating the Berry connection

over the Brillouin zone [Ma et al. 2019]. Due to inversion symmetry of the unit cell, the Zak phase has a quantized value of 0 or π. For a bulk band with $\theta_n^{\text{Zak}} = 0$, the symmetry at the center and edge of the Brillouin zone remains unchanged however for a bulk band with $\theta_n^{\text{Zak}} = \pi$, the symmetry of the edge mode at the center and edge of the Brillouin zone varies and it results in an antisymmetric edge mode.

As reported in [Li et al. 2018; Xiao et al. 2015; Zhao et al. 2018] for acoustic media and in [Muhammad et al. 2019; Yin et al. 2018; Zhou et al. 2019b] for elastic media, geometric phases provide important information about the symmetry characteristic of the edge states. The transition in the symmetry type of band edge for a topological PnCs results in the generation of an interface mode. If two PnCs with different topological properties (symmetric and antisymmetric edge states) are combined and the mode transition frequency is common between their bandgaps, an interface mode with robust energy field at the boundary of PnCs are induced. Thus, the knowledge of geometric phases is important for achieving a TPIM. Although the Zak phase has been extensively studied in the acoustic system in theory and experiment [Xiao et al. 2015], in this study the method reported by [Xiao et al. 2015] is adopted to numerically determine the Zak phase of the Bloch bands in elastic media.

The geometric phase of the n-th Bloch band in a 1D system can be expressed as

$$\theta_n^{\text{Zak}} = \int_{-\pi/a}^{\pi/a} \left[i \int_{\substack{\text{unit} \\ \text{cell}}} \frac{1}{2\rho c^2} dx \xi_{n,k}^*(x) \partial \xi_{n,k}(x) \right] dk, \tag{42}$$

where $\xi_{n,k}(x)$ is the Bloch eigenstate function of the periodic structure for a specific wavenumber k and $1/\left(2\rho c^2\right)$ is the factor for weight function of elastic medium. The Bloch eigenstate function in the n-th Bloch band is given by [Xiao et al. 2015]

$$U_{n,k}(x) \text{ or } W_{n,k}(x) = \xi_{n,k}(x) e^{ikx}. \tag{43}$$

Here $U_{n,k}(x)$ and $W_{n,k}(x)$ denote the longitudinal and flexural modes, respectively. COMSOL Multiphysics is used to discretize (43) and determine the Zak phase [Xiao et al. 2015], using

$$\theta_n^{\text{Zak}} = -\text{Im} \sum_{i=1}^{N} \ln \left[\int_{\substack{\text{unit} \\ \text{cell}}} \frac{1}{2\rho c^2} dx \xi_{n,k_i}^*(x) \partial \xi_{n,k_{i+1}}(x) \right]. \tag{44}$$

5. Result analysis and discussion

5.1. ***Flexural waves.*** To verify the validity and accuracy of this theoretical model, a COMSOL based numerical simulation study is conducted for the finite (frequency response) and infinite (band structure) models. For flexural waves, TB1 ($\delta = -0.9$), TB2 ($\delta = -0.71$) and TB3 ($\delta = -0.38$) are considered with band structure shown in Figure 3. For the first three Bloch bands, the geometric phases for the lower and higher edges of the second bandgap is determined. The geometric phase of the second Bloch band for TB1 is symmetric while for TB3 it is antisymmetric with respect to the central cross-sectional plane. The band inversion for TB2 is shown in Figure 3(b). The center and edge vibration modes of the Brillouin zone are shown at the inset of Figure 3. For TB1 since the center (yellow) and edge (red) vibration mode of Brillouin zone is symmetric with respect to the central cross-sectional plane, the Zak phase is 0 while for TB3 it is opposite.

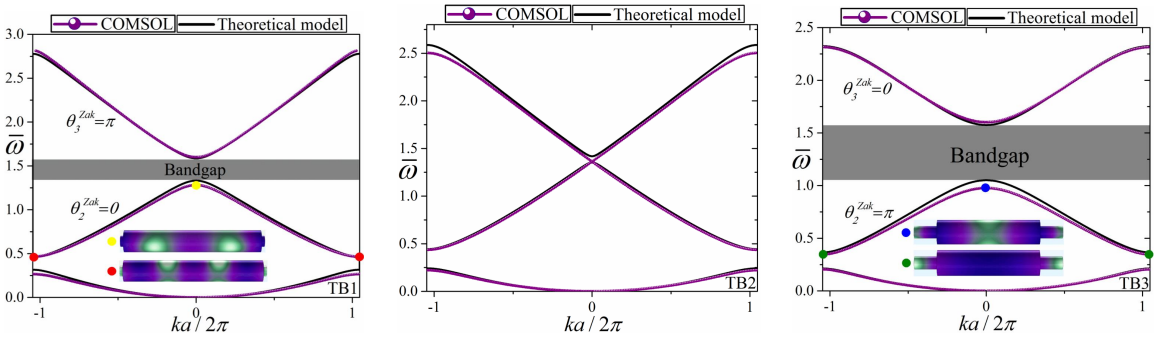

Figure 3. Flexural waves band structure with geometric phases of the band edge-state for (a) TB1, (b) TB2, and (c) TB3. An exchange in wave mode polarization with band inversion and accidental degeneracy can be observe for TB2. Mode shapes corresponding to center and edges of the Brillouin zone are shown at the inset of figures where symmetric and unsymmetric edge states can be distinguished. Solid black and dotted violet colors correspond to theoretical and numerical results, respectively.

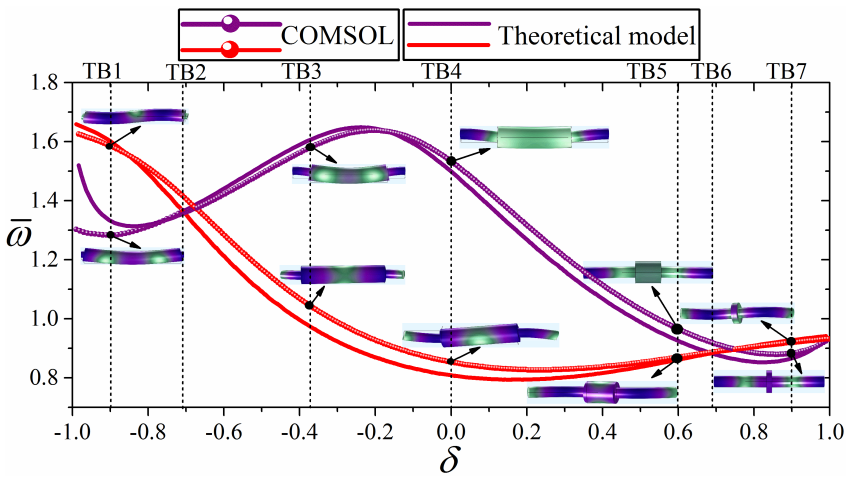

Figure 4. Dirac cone for flexural waves with bounding eigenfrequencies calculated for varying δ with band transition and accidental degeneracy point. Solid (theoretical) and dotted (numerical) red and violet colors correspond to antisymmetric and symmetric edge states, respectively. At the mode transition frequency, an exchange in wave mode polarization can be observed through the mode shapes.

Furthermore, the bounding eigenfrequencies for the second and third Bloch bands corresponding to varying δ at the center of the Brillouin zone ($k = 0$) are determined. The symmetric (purple) and antisymmetric (red) edge modes are highlighted with band inversion. An exchange in wave mode polarization is observed at TB2, the details are available in [Muhammad et al. 2019; Yin et al. 2018]. For $\delta > -0.9$, the difference in frequency for the lower edge of the second bandgap can be observed due to model dissimilarity between the spectral element method and FEM.

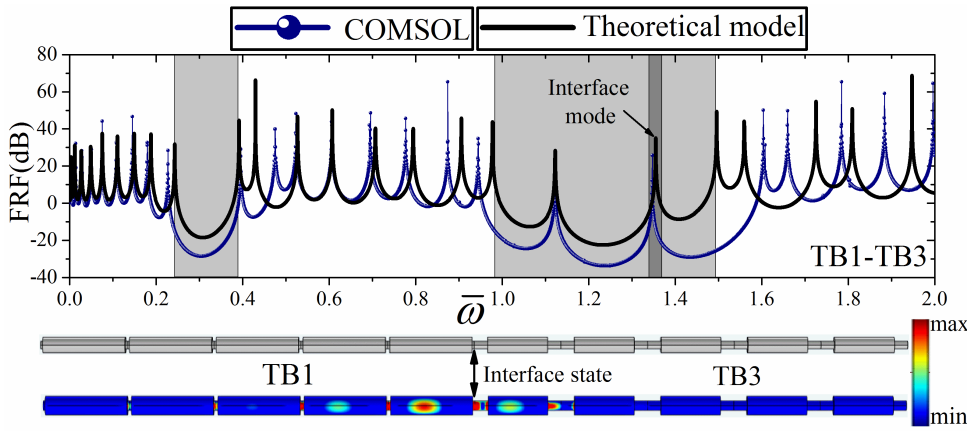

Figure 5. A finite unit cell based frequency response study with five unit cells of TB1 connecting five unit cells of TB3 with interface mode. An excitation force is applied at the left (right) end and displacement is recorded at the right (left) end. The existence of interface mode can be seen from the von Mises stress plot shown at the bottom. The interface mode frequency (black arrow) is identical to the mode transition frequency in Figure 4.

We consider ten unit cells of TB1-TB3 to analyze the presence and significance of TPIM. An excitation signal is applied at the left (right) end of the finite length model and out-of-plane displacement is recorded at the right (left) end. Since the mode transition frequency is common between the bandgaps of TB1-TB3 (Figure 4), an interface mode is generated as shown in Figure 5. The simple and von Mises stress figure of finite length PnCs with interface mode are shown for reference. From the von Mises stress figure, localization and confinement of wave energy at the interface of TB1-TB3 can be observed. The interface mode corresponds to mode transition frequency where an exchange in wave mode polarization occurs (see Figure 4), thus the accuracy of the finite unit cell model developed in this study is validated.

Furthermore, we also consider ten unit cells of TB1-TB3, TB1-TB4 and TB5-TB7 separately to further corroborate the claim for TPIM generation. As shown in Figure 6, for TB1-TB4 and TB5-TB7, no interface mode is obtained because the mode transition frequency is not common between the bandgaps of topologically distinct PnCs. Thus, it validates the statement that an interface state is induced when PnCs are topologically distinct and mode transition frequency is common between the bandgaps.

5.2. ***Longitudinal waves.*** In this section, we consider longitudinal wave propagation in topologically distinct PnCs shown in Figure 1. The response of the band inversion for TL2 ($\delta = 0$), band structures for TL1 ($\delta = -1/3$) and TL3 ($\delta = 1/3$) is presented in Figure 7. The geometric phases of the Block bands at the lower and upper edge of the bandgap are highlighted. For TL1 the edge state at the center and edges of the Brillouin zone is symmetric with respect to the center cross-sectional plane $\theta_2^{\text{Zak}} = 0$ while for TL3 it is antisymmetric $\theta_2^{\text{Zak}} = \pi$ where the bandgap closing and reopening can be observed for TL2. This conclusion is further confirmed by the vibration modes shown at the inset of the figures.

The symmetry characteristics of the bounding edge states are determined by scanning the geometric parameter δ at the center of the Brillouin zone ($k = 0$) as shown in Figure 8. Through the theoretical and

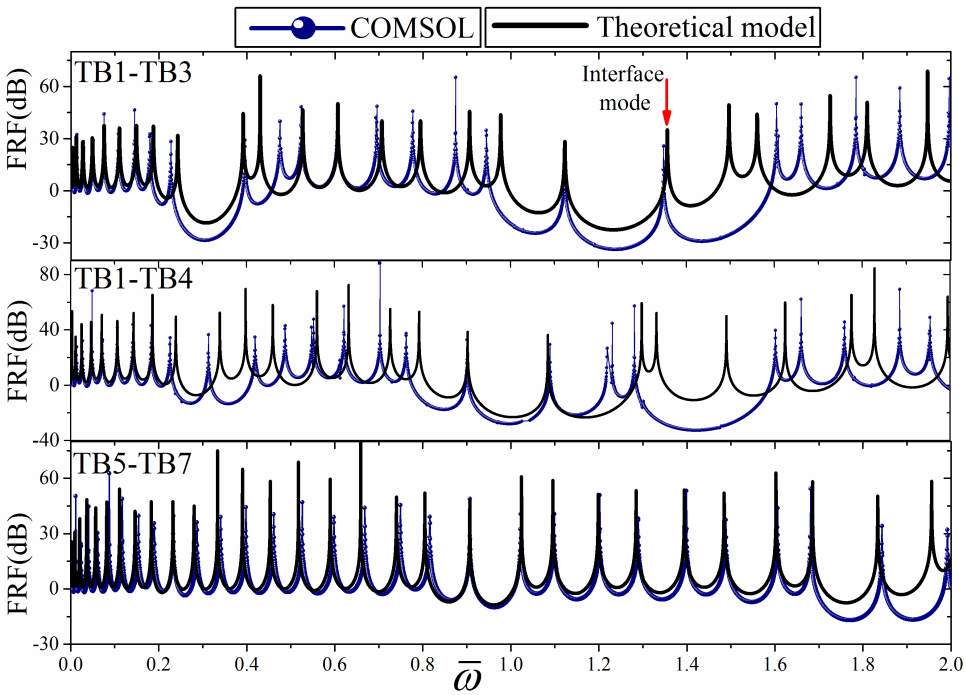

Figure 6. A finite unit cell based frequency response study. (a) Five unit cells of TB1 are connected with five cells of TB3 and the interface mode is shown with red arrow. (b) Similarly, five unit cells of TB1 are connected with five unit cells of TB4. (c) Five unit cells of TB5 are connected with five unit cells of TB7. For (b,c) no interface mode is observed as the mode transition frequency is not common between the bandgaps.

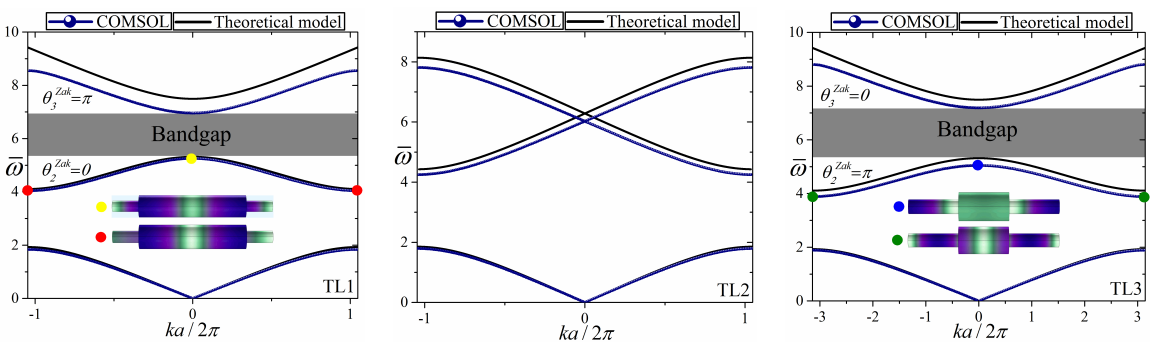

Figure 7. Longitudinal waves band structure of topologically distinct PnCs with (a) TL1 (b) TL2 (c) TL3 with geometric phases determined by the Zak phase analysis. An exchange in wave mode polarization with band inversion and accidental degeneracy can be observed for TL2. Mode shapes corresponding to center and edges of the Brillouin zone are shown at the inset of figures where symmetric and unsymmetric edge-mode states can be distinguished. Solid black and dotted violet colors correspond to theoretical and numerical solutions, respectively.

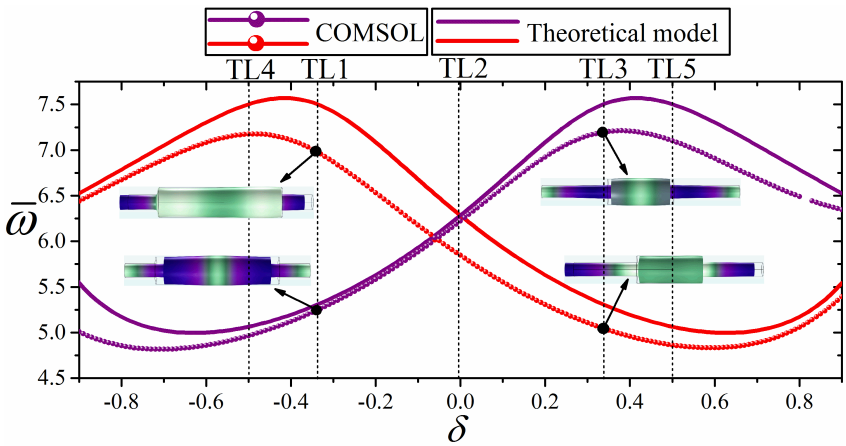

Figure 8. Longitudinal waves Dirac cone plot with bounding eigenfrequencies determined for varying δ with band transition and accidental degeneracy point. Solid (theoretical) and dotted (numerical) red and violet colors correspond to unsymmetric and symmetric edge-mode states, respectively. At the mode transition frequency, an exchange in wave mode polarization can be observed through the mode shapes shown.

numerical approaches developed here, the symmetric (purple) and antisymmetric (red) edge modes are successfully distinguished. For varying δ, the transition in the geometric phases and band inversion can be observed at TL2 where an exchange in the wave mode polarization occurs. Because longitudinal wave propagation is linearly dispersive in nature [Muhammad et al. 2019; Yin et al. 2018], thus comparing to flexural waves, a combination of any δ smaller or greater than 0 can induce an interface state, see Figure 10 for more details.

The result of an infinite unit cell model is validated by considering five unit cells of TL1 and TL3 connected together. A harmonic excitation force is applied at the left (right) end of the finite length PnCs and the displacement as output is recorded at the right (left) end. As shown in the Dirac cone plot (see Figure 8), the mode transition frequency is common between the bandgaps of TL1-TL3, thus the interface state exists. The frequency response study validates and reveals the existence of an interface mode as shown in Figure 9. The mode transition frequency reported in the Dirac cone plot is identical to the interface state frequency obtained from the theoretical and numerical models.

Similarly to Figure 6, an analysis by varying the geometric parameter array of unit cells to validate the existence of interface mode is attempted. For longitudinal wave, as demonstrated in Figure 8, any two geometric configurations with a mode transition frequency common between the bandgaps of topological distinct PnCs, can induce an interface state. In Figure 10, it shows the generation of an interface mode resulting from ten unit cells of TL1-TL3 and TL4-TL5. The interface mode is highlighted with black arrow. Both theoretical and numerical findings further validate the conclusion for TPIM.

The spatial distribution of the displacement field at the interface mode frequency for longitudinal and bending elastic waves is shown in Figure 11. At the boundary of topological PnCs ($x = 0$), the displacement is maximum and away from it, the wave energy decays. A similar conclusion can be observed from the von Mises stress plot shown in Figure 5 and Figure 9.

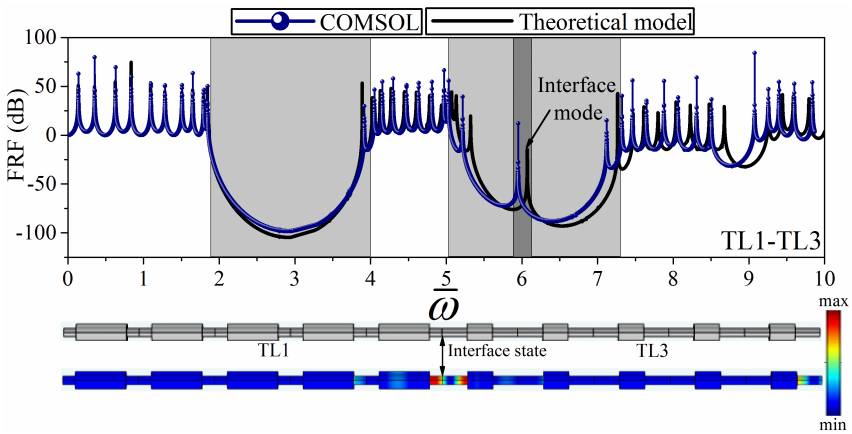

Figure 9. A finite unit cell based frequency response study with five unit cells of TL1 connecting five cells of TL3 with interface mode. An excitation force is applied at the left (right) end and displacement is recorded at the right (left) end. The existence of an interface mode can be seen from the von Mises stress plot shown at the bottom. The frequency of the interface mode is identical to the mode transition frequency in Figure 8.

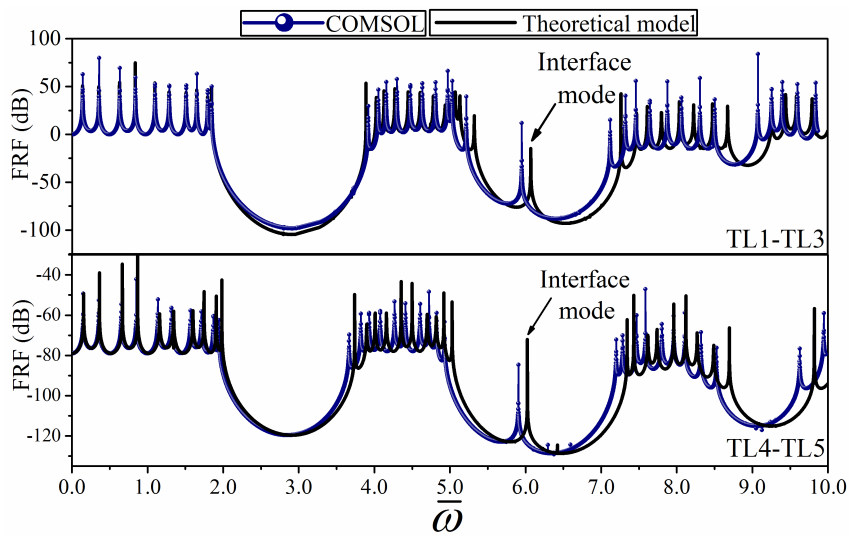

Figure 10. A finite unit cell based frequency response study. (a) Five unit cells of TL1 is connected with five unit cells of TL3. (b) Five unit cell of TL4 is connected to five unit cells of TL5. The interface state at mode transition frequency is shown with a black arrow.

6. Conclusions

In summary, a theoretical study with numerical simulation on the topological characteristics of the 1D PnC for longitudinal and bending elastic waves is presented. The interface modes are reported by spectral

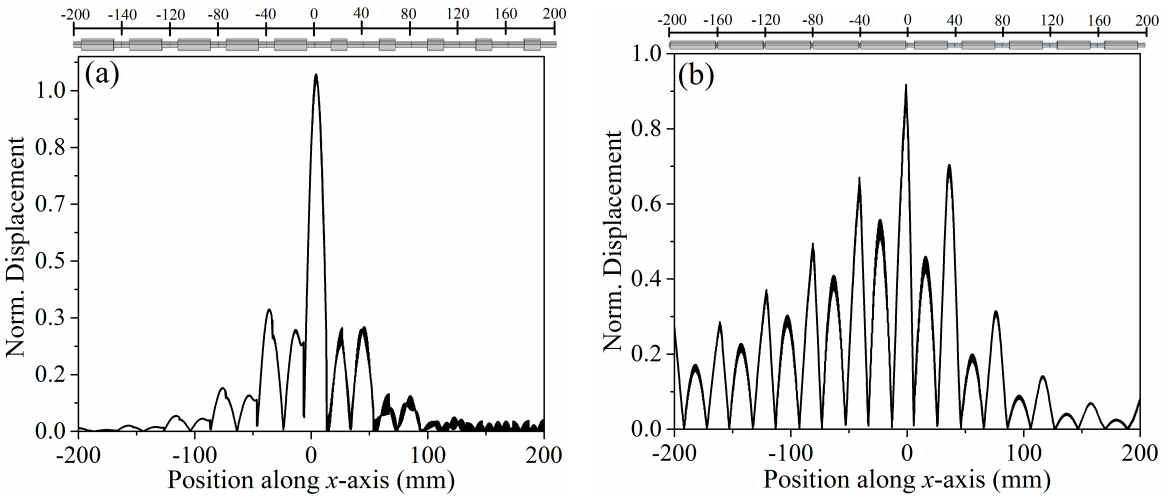

Figure 11. Spatial distribution of displacement field across the length of finite length PnC at the interface mode frequency for (a) longitudinal and (b) bending elastic waves.

element based theoretical and FEM based numerical techniques. The flexural wave dispersion relation is derived by using the Timoshenko beam model with the spectral element method. We also derived the constitutive relation for the longitudinal waves band structure with frequency response analyses. The geometric phases of the Block bands are determined by the Zak phase analysis. The symmetry characteristics of the edge modes are identified and the band inversion along with an exchange in wave mode polarization caused by topology is investigated. The Dirac cone plot for the flexural waves show distinct behavior due to nonlinear dispersive nature as compared to the longitudinal wave counterpart. The geometric phases provide useful information not only about the symmetry properties of the edge modes but also the presence of topologically protected interface modes. With the mode transition frequency being common between the bandgaps of topologically distinct PnCs, an interface mode with robust energy field at the interface with decaying energy field away from it can be observed. The robust nature, immune to backscattering and sharp edges properties of the interface mode, makes it a potential tool for solving vibration related engineering problem.

The conclusions here may contribute in the better understanding of topological phenomena of 1D PnCs. The results have been validated by comparing the theoretical and numerical solutions with excellent agreement achieved.

Acknowledgments

The work described in this paper was supported by Shenzhen Science and Technology Funding Fundamental Research Program (Project No. JCYJ20170413141248626) and General Research Grant from the Research Grants Council of the Hong Kong Special Administrative Region (Project Nos. CityU 11212017, 11216318).

List of symbols

a	lattice constant
$A_1 - A_4$	unknown constants
$\boldsymbol{B}$	unknown coefficient vector
A, B, C, D	coefficients for angular deflection, shear force and bending moments
c_L	longitudinal wave velocity
$\boldsymbol{D}$	dynamic stiffness matrix
d_B	diameter of thinner beam
D_A	diameter of thicker B
E	young's modulus
$\boldsymbol{f}$	nodal force vector
$G, \overline{G}$	shear modulus
$I_z, \bar{I}_z$	moment of inertia
$\boldsymbol{I}$	identity matrix
EI_z	flexural rigidity
k	wavenumber
$\boldsymbol{K}$	stiffness matrix
L, L_A, L_B	total length of beam with designated length for beam A-B
L/D_A	slenderness ratio
$M, \overline{M}$	bending moment
$\boldsymbol{M}$	mass matrix
P_I	input excitation force
$\boldsymbol{q}$	nodal displacement vector
$\boldsymbol{Q}$	dynamic stiffness matrix for each unit cell
$S, \bar{S}, S_A, S_B$	cross-section area
S_1, S_2, S_3	unknown coefficients
$u, \bar{u}$	in-plane displacement
$U_{n,k}$	longitudinal wave field
$V, \overline{V}$	shear force
$w, \bar{w}$	out-of-plane displacement
$W_{n,k}$	flexural wave field
$x, \bar{x}$	local coordinate
Z	impedance
0	symmetric edge mode
δ	geometric parameter
ζ_j	unknown roots
θ_n^{Zak}	Zak phase of nth Bloch band
i	iota
κ	shear correction factor
ν	poisson ratio
$\xi_{n,k}$	Bloch eigenfunction
π	antisymmetric edge mode
ρ, ρ_B	density
$\sum_{i=1}^{n}$	summation
ϕ	normalized flexure rigidity
ψ	angular rotation
$\omega, \overline{\omega}$	normalized angular frequency
$', '', '''$	first, second and third differentiation with respect to $\bar{x}$

References

[Aidelsburger et al. 2014] M. Aidelsburger, M. Lohse, C. Schweizer, M. Atala, J. T. Barreiro, S. Nascimbène, N. R. Cooper, I. Bloch, and N. Goldman, "Measuring the Chern number of Hofstadter bands with ultracold bosonic atoms", *Nature Phys.* **11** (2014), 162.

[Andrade et al. 2018] C. Andrade, C. S. Ha, and R. S. Lakes, "Extreme Cosserat elastic cube structure with large magnitude of negative Poisson's ratio", *J. Mech. Mater. Struct.* **13**:1 (2018), 93–101.

[Bernevig et al. 2006] B. A. Bernevig, T. L. Hughes, and S.-C. Zhang, "Quantum spin Hall effect and topological phase transition in HgTe quantum wells", *Science* **314** (2006), 1757–1761.

[Berry 1984] M. V. Berry, "Quantal phase factors accompanying adiabatic changes", *Proc. Roy. Soc. London Ser. A* **392**:1802 (1984), 45–57.

[Brendel et al. 2018] C. Brendel, V. Peano, O. Painter, and F. Marquardt, "Snowflake phononic topological insulator at the nanoscale", *Phys. Rev. B* **97** (2018), art. id. 014110.

[Cha and Daraio 2018] J. Cha and C. Daraio, "Electrical tuning of elastic wave propagation in nanomechanical lattices at MHz frequencies", *Nature Nanotechnol.* **13** (2018), 1016–1020.

[Chen et al. 2018a] Chen, H., Nassar, H., Huang, and G. L., "A study of topological effects in 1D and 2D mechanical lattices", *J. Mech. Phys. Solids* **117** (2018), 22–36.

[Chen et al. 2018b] H. Chen, H. Nassar, and G. Huang, "Topological mechanics of edge waves in Kagome lattices", 2018. arXiv

[Chen et al. 2019a] Chen, Wei, Wang, Lin, Dai, and Hu-Liang, "Nonlinear free vibration of nanobeams based on nonlocal strain gradient theory with the consideration of thickness-dependent size effect", *J. Mech. Mater. Struct.* **14**:1 (2019), 119–137.

[Chen et al. 2019b] Chen, Yi, Liu, Xiaoning, Hu, and Gengkai, "Topological phase transition in mechanical honeycomb lattice", *J. Mech. Phys. Solids* **122** (2019), 54–68.

[Chiang et al. 1977] C. K. Chiang, C. R. Fincher, Y. W. Park, A. J. Heeger, H. Shirakawa, E. J. Louis, S. C. Gau, and A. G. MacDiarmid, "Electrical Conductivity in Doped Polyacetylene", *Phys. Rev. Lett.* **39** (1977), 1098–1101.

[Czubacki et al. 2015] Czubacki, R. aw, Lewiński, and Tomasz, "Topology optimization of spatial continuum structures made of nonhomogeneous material of cubic symmetry", *J. Mech. Mater. Struct.* **10**:4 (2015), 519–535.

[Delplace et al. 2011] P. Delplace, D. Ullmo, and G. Montambaux, "Zak phase and the existence of edge states in graphene", *Phys. Rev. B* **84** (2011), art. id. 195452.

[Dong et al. 2017] J. W. Dong, X. D. Chen, H. Zhu, Y. Wang, and X. Zhang, "Valley photonic crystals for control of spin and topology", *Nature Mater.* **16** (2017), 298–302.

[Foehr et al. 2018] A. Foehr, O. R. Bilal, S. D. Huber, and C. Daraio, "Spiral-based phononic plates: from wave beaming to topological insulators", *Phys. Rev. Lett.* **120** (2018), art. id. 205501.

[Gao et al. 2018] R. Z. Gao, G. Y. Zhang, T. Ioppolo, and X.-L. Gao, "Elastic wave propagation in a periodic composite beam structure: A new model for band gaps incorporating surface energy, transverse shear and rotational inertia effects", *J. Micromech. Molec. Phys.* **03** (2018), art. id. 1840005.

[Haldane 1988] F. D. Haldane, "Model for a quantum Hall effect without Landau levels: Condensed-matter realization of the 'parity anomaly'", *Phys. Rev. Lett.* **61** (1988), 2015–2018.

[Han et al. 2012] L. Han, Y. Zhang, Z. Q. Ni, Z. M. Zhang, and L. H. Jiang, "A modified transfer matrix method for the study of the bending vibration band structure in phononic crystal Euler beams", *Physica B* **407** (2012), 4579–4583.

[Hasan and Kane 2010] M. Z. Hasan and C. L. Kane, "Colloquium: Topological insulators", *Rev Mod Phys* **82** (2010), 3045–3067.

[He et al. 2016] C. He, X. Ni, H. Ge, X. C. Sun, Y. B. Chen, M. H. Lu, X. P. Liu, and Y. F. Chen, "Acoustic topological insulator and robust one-way sound transport", *Nature Phys.* **12** (2016), 1124–.

[Huber 2016] S. D. Huber, "Topological mechanics", *Nature Phys.* **12** (2016), 621–623.

[Huo et al. 2017] S. Y. Huo, J. J. Chen, H. B. Huang, and G. L. Huang, "Simultaneous multi-band valley-protected topological edge states of shear vertical wave in two-dimensional phononic crystals with veins", *Sci. Rep.* **7** (2017), art. id. 10335.

[Jia et al. 2018] D. Jia, H. x. Sun, J. p. Xia, S. q. Yuan, X. j. Liu, and C. Zhang, "Acoustic topological insulator by honeycomb sonic crystals with direct and indirect band gaps", *New J. Phys.* **20** (2018), art. id. 093027.

[Jin et al. 2018] Y. Jin, D. Torrent, and B. Djafari-Rouhani, "Robustness of conventional and topologically protected edge states in phononic crystal plates", *Phys. Rev. B* **98** (2018), art. id. 054307.

[Kane and Mele 2005] C. L. Kane and E. J. Mele, "Quantum spin Hall effect in graphene", *Phys. Rev. Lett.* **95** (2005), art. id. 226801.

[Khanikaev et al. 2013] A. B. Khanikaev, S. H. Mousavi, W. K. Tse, M. Kargarian, A. H. MacDonald, and G. Shvets, "Photonic topological insulators", *Nature Mater.* **12** (2013), 233–239.

[Khanikaev et al. 2015] A. B. Khanikaev, R. Fleury, S. H. Mousavi, and A. Alù, "Topologically robust sound propagation in an angular-momentum-biased graphene-like resonator lattice", *Nature Comm.* **6** (2015), art. id. 8260.

[Kim et al. 2018] I. Kim, S. Iwamoto, and Y. Arakawa, "Topologically protected elastic waves in one-dimensional phononic crystals of continuous media", *Appl. Phys. Express* **11** (2018), art. id. 017201.

[Kushwaha et al. 1993] M. S. Kushwaha, P. Halevi, L. Dobrzynski, and B. Djafari-Rouhani, "Acoustic band structure of periodic elastic composites", *Phys. Rev. Lett.* **71** (1993), 2022–2025.

[Li et al. 2018] X. Li, Y. Meng, X. X. Wu, S. Yan, Y. Z. Huang, S. X. Wang, and W. J. Wen, "Su-Schrieffer-Heeger model inspired acoustic interface states and edge states", *Appl. Phys. Lett.* **113** (2018), art. id. 203501.

[Liu et al. 2000] Z. Liu, X. Zhang, Y. Mao, Y. Y. Zhu, Z. Yang, C. T. Chan, and P. Sheng, "Locally resonant sonic materials", *Science* **289** (2000), 1734–1736.

[Ma et al. 2019] G. Ma, M. Xiao, and C. T. Chan, "Topological phases in acoustic and mechanical systems", *Nature Rev. Phys.* **1** (2019), 281–294.

[Martínez-Sala et al. 1995] R. Martínez-Sala, J. Sancho, J. V. Sánchez, V. Gómez, J. Llinares, and F. Meseguer, "Sound attenuation by sculpture", *Nature* **378** (1995), 241–241.

[Mei et al. 2016] J. Mei, Z. Chen, and Y. Wu, "Pseudo-time-reversal symmetry and topological edge states in two-dimensional acoustic crystals", *Sci. Rep.* **6** (2016), art. id. 32752.

[Miniaci et al. 2018] M. Miniaci, R. K. Pal, B. Morvan, and M. Ruzzene, "Experimental observation of topologically protected helical edge modes in patterned elastic plates", *Phys. Rev. X* **8** (2018), art. id. 031074.

[Moore 2010] J. E. Moore, "The birth of topological insulators", *Nature* **464** (2010), 194–198.

[Muhammad et al. 2019] Muhammad, W. Zhou, and C. W. Lim, "Topological edge modeling and localization of protected interface modes in 1D phononic crystals for longitudinal and bending elastic waves", *Int. J. Mech. Sci.* **159** (2019), 359–372.

[Pal et al. 2018] R. K. Pal, J. Vila, M. Leamy, and M. Ruzzene, "Amplitude-dependent topological edge states in nonlinear phononic lattices", *Phys. Rev. E* **97** (2018), art. id. 032209.

[Pancharatnam 1956] S. Pancharatnam, "Generalized theory of interference and its applications, II: Partially coherent pencils", *Proc. Indian Acad. Sci. Sect. A* **44** (1956), 398–417.

[Reda et al. 2016] H. Reda, Y. Rahali, J. F. Ganghoffer, and H. Lakiss, "Wave propagation analysis in 2D nonlinear hexagonal periodic networks based on second order gradient nonlinear constitutive models", *Int J Nonlin Mech* **87** (2016), 85–96.

[Sigalas and Economou 1993] M. Sigalas and E. N. Economou, "Band structure of elastic waves in two dimensional systems", *Solid state communications* **86** (1993), 141–143.

[Su et al. 1979] W. P. Su, J. R. Schrieffer, and A. J. Heeger, "Solitons in polyacetylene", *Phys. Rev. Lett.* **42** (1979), 1698–1701.

[Susstrunk and Huber 2015] R. Susstrunk and S. D. Huber, "PHYSICS. Observation of phononic helical edge states in a mechanical topological insulator", *Science* **349** (2015), 47–50.

[Wang et al. 2015] P. Wang, L. Lu, and K. Bertoldi, "Topological Phononic Crystals with One-Way Elastic Edge Waves", *Phys. Rev. Let.* **115** (2015), art. id. 104302.

[Xia et al. 2018] J.-P. Xia, D. Jia, H.-X. Sun, S.-Q. Yuan, Y. Ge, Q.-R. Si, and X.-J. Liu, "Programmable coding acoustic topological insulator", *Adv. Mater.* **30** (2018), art. id. 1805002.

[Xiao et al. 2010] D. Xiao, M. C. Chang, and Q. Niu, "Berry phase effects on electronic properties", *Rev. Modern Phys.* **82**:3 (2010), 1959–2007.

[Xiao et al. 2015] M. Xiao, G. C. Ma, Z. Y. Yang, P. Sheng, Z. Q. Zhang, and C. T. Chan, "Geometric phase and band inversion in periodic acoustic systems", *Nature Phys.* **11** (2015), 240–244.

[Yin et al. 2018] J. Yin, M. Ruzzene, J. Wen, D. Yu, L. Cai, and L. Yue, "Band transition and topological interface modes in 1D elastic phononic crystals", *Sci. Rep.* **8** (2018), art. id. 6806.

[Young et al. 2012] S. M. Young, S. Zaheer, J. Y. Teo, C. L. Kane, E. J. Mele, and A. M. Rappe, "Dirac semimetal in three dimensions", *Phys. Rev. Lett.* **108** (2012), art. id. 140405.

[Yu et al. 2006] D. Yu, Y. Liu, G. Wang, H. Zhao, and J. Qiu, "Flexural vibration band gaps in Timoshenko beams with locally resonant structures", *J. Appl. Phys.* **100** (2006), art. id. 124901.

[Yu et al. 2018] S. Y. Yu, C. He, Z. Wang, F. K. Liu, X. C. Sun, Z. Li, H. Z. Lu, M. H. Lu, X. P. Liu, and Y. F. Chen, "Elastic pseudospin transport for integratable topological phononic circuits", *Nature Comm.* **9** (2018), art. id. 3072.

[Zhang et al. 2013] F. Zhang, A. H. MacDonald, and E. J. Mele, "Valley Chern numbers and boundary modes in gapped bilayer graphene", *Proc. Natl. Acad. Sci. USA* **110** (2013), 10546–10551.

[Zhang et al. 2019] Q. Zhang, Y. Chen, K. Zhang, and G. Hu, "Programmable elastic valley Hall insulator with tunable interface propagation routes", *Extreme Mech. Lett.* **28** (2019), 76–80.

[Zhao et al. 2018] D. G. Zhao, M. Xiao, C. W. Ling, C. T. Chan, and K. H. Fung, "Topological interface modes in local resonant acoustic systems", *Phys. Rev. B* **98** (2018), art. id. 014110.

[Zhou et al. 2019a] W. Zhou, Y. Su, Muhammad, W. Chen, and C. W. Lim, "Voltage-controlled quantum valley Hall effect in dielectric membrane-type acoustic metamaterials", *Int. J. Mech. Sci.* (online publication December 2019), art. id. 105368.

[Zhou et al. 2019b] W. J. Zhou, W. Q. Chen, Muhammad, and C. W. Lim, "Surface effect on the propagation of flexural waves in periodic nano-beam and the size-dependent topological properties", *Compos Struct* **216** (2019), 427–435.

[Zhou et al. 2019c] W. J. Zhou, B. Wu, Z. Chen, W. Chen, C. W. Lim, and J. N. Reddy, "Actively controllable topological phase transition in homogeneous piezoelectric rod system", 2019. Submitted.

Received 29 Jul 2019. Revised 7 Nov 2019. Accepted 29 Nov 2019.

MUHAMMAD: fmuhammad6-c@my.cityu.edu.hk
City University of Hong Kong Shenzhen Research Institute, Shenzhen 518057, China

C. W. LIM: bccwlim@cityu.edu.hk
Department of Architecture and Civil Engineering, Kowloon, Hong Kong SAR, China

JOURNAL OF MECHANICS OF MATERIALS AND STRUCTURES
Vol. 15, No. 1, 2020
dx.doi.org/10.2140/jomms.2020.15.37

DYNAMICS AND STABILITY ANALYSIS OF AN AXIALLY MOVING BEAM IN AXIAL FLOW

YAN HAO, HULIANG DAI, NI QIAO, KUN ZHOU AND LIN WANG

The present study focuses on investigating dynamics and stability of an axially moving beam subjected to axial flows. The axially moving beam is simply-supported at both ends. The added mass of fluid attached to the beam and the nonlinear additional deflection-dependent axial force are considered in deriving the governing equation of motion. Firstly, the stability analysis is performed with consideration of the effects of parameters such as axial flow velocity, the speed of axially moving beam and slenderness ratio of the beam. It is indicated that the beam loses stability via buckling or flutter at a critical speed of moving beam which is associated with variations of system parameters. Subsequently, the nonlinear dynamic responses of the beam for increasing moving speed under different axial flow velocities are investigated in detail. Results show that the beam can successively experience buckling and flutter behaviors. In addition, effects of system parameters like mass ratio, slenderness ratio, and pretension on instability mode, buckling displacement and flutter amplitude of the beam are explored to obtain their sensitivity to dynamics of the moving beam. These findings provide an important guidance for designing axially moving structures in engineering applications.

1. Introduction

Axially moving structures (e.g., axially moving beams [Ghayesh et al. 2013a], belts [Hedrih 2007], strings [Chen et al. 2009], plates [Ghayesh et al. 2013b] can be applied in many engineering devices, such as magnetic tapes, aerial cables, power transmission belts and band saw blades. Owing to the widespread applications, the dynamics of elastic or viscoelastic beams axially moving at a certain speed have attracted increasing attention in the past decades from both academic and engineering realms. Hitherto, a great deal of research works on the dynamical behavior of axially moving material has been reported. One can get a general understanding of this field in [Mote Jr. 1968; Wickert and Mote 1988; Chen 2005; Marynowski and Kapitaniak 2014; Païdoussis and Li 1993].

Problems of interaction between axially moving structures and fluid have significant applications in shipping and ocean engineering, underwater equipment and aeronautical industries. Acoustic streamers used in ocean exploration [Telford et al. 1976], steel strip in continuous hot-dip galvanizing process [Li et al. 2013; Wang et al. 2016] and the underwater towed slender structures [Brown 2006; Kyriakides and Corona 2007] are typical examples. There are many fluid forces applied on structures and they have a great effect on the dynamics and stability of the axially moving structure system. In recent decades, many researches about axially moving structures like plates or beams under flow conditions have been conducted. Frondelius et al. [2006] investigated the interaction of an axially moving band and

Ni Qiao is the corresponding author.
Keywords: axially moving beam, axial flow, stability analysis, buckling, flutter.

surrounding fluid through boundary layer theory. Their results are significantly different from the earlier work. The dynamic behavior of axially moving plates and membranes immersed in axially flowing ideal fluid was investigated in [Banichuk et al. 2010; 2011]. Taleb and Misra [1981] investigated the dynamics of an axially deploying beam submerged in dense fluid, and Gosselin et al. [2007] improved Taleb's work by taking the axial added mass coefficient into account. Inspired by their works, Yan et al. [2016] investigated the dynamics of an extending beam attached to an axially moving base immersed in dense fluid. They found that the increase of velocity of the moving base can stabilize the system. Huo and Wang [2016] developed a theoretical model for an axially deploying/retracting cantilevered pipe conveying fluid and carried out a linear analysis. Then, Yan et al. [2018] tackled the same problem as Huo and Wang [2016]. They investigated the nonlinear dynamics of a sliding pipe conveying fluid. Wang and Ni [2008] conducted a linear study on the vibration and stability of an axially moving beam immersed in fluid using the differential quadrature method (DQM). The natural frequencies of the system were obtained for three different boundary conditions, i.e., hinged-hinged, fixed-fixed and hybrid supports with torsion spring. Afterwards, Ni et al. [2014] investigated the linear vibration and stability of a cantilevered beam attached to an axially moving base which was immersed in fluid. In this work, a transformation between absolute and moving coordinates was introduced to construct the theoretical model. In addition, a study on an underwater slender beam with two axially moving supports has been done in [Li et al. 2015b]. By utilizing the same modeling method as in their previous work, nonlinear governing equations are obtained and rich dynamic behaviors are detected. Païdoussis [1968; 1970] conducted some experiments and constructed linear theoretical model to study the dynamics and stability of towed cylinders. Qualitative agreement between experiment and theory was reached. Moreover, Païdoussis et al. [2002], Lopes et al. [2002] and Semler et al. [2002] conducted a fully nonlinear analytical investigation on the dynamics of a beam in axial flow. De Langre et al. [2007] proposed a simple model for the dynamical behaviour of long flexible cylinders in axial flow. Numerical results and experimental data show that flutter may exist for very long cylinders. Kheiri et al. [2013a; 2013b] derived three-dimensional linear equations of motion with consideration of cross-current effect to investigate the dynamics of long pipes towed underwater. Results show that the pipe may lose stability by divergence and at higher flow velocities by flutter. It should be noted that Kheiri et al. [2013c; 2015] developed a nonlinear model for a towed flexible slender cylinder via Hamilton's principle and conducted an experiment. The numerical results agree well with experimental observations, which show that a sufficiently blunt tail end-piece has a significant stabilizing effect.

In addition, Wang and Zu [2017a] investigated the instability of a viscoelastic plate, which moves longitudinally at variable velocity and is in contact with ideal liquid, by using multiple-scale method. Considering a plate made of functionally graded materials, Wang and Zu [2017b] and Wang [2018] investigated the multifield coupled dynamics of an axially moving system. Li et al. [2015a] studied the internal resonance of an axially moving unidirectional plate which is partially immersed in fluid and under foundation displacement excitation. More recently, Li et al. [2018] tackled a similar problem as that in their previous work [Li et al. 2015a], while this latest work was mainly concerned with the characteristics of combination resonances and its stability of this fluid-structure coupling system under two frequency excitations.

However, the previous studies on axially moving structures in fluid did not consider the flow velocity in the axial direction (i.e., the axial flow velocity equals to zero). Although some researches [Dowling 1988; Kim and Perkins 2002] mentioned the axial flow, the axial flow effect in their researches is actually

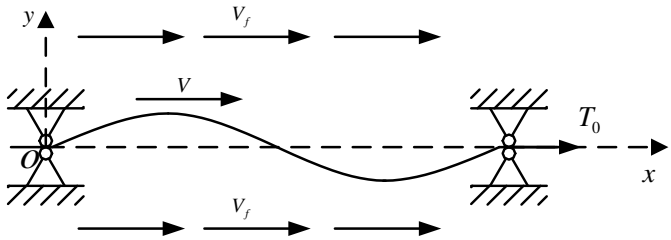

Figure 1. Schematic of an axially moving beam in axial flow.

due to the underwater structures being towed or axially moving themselves. That's to say, the external axial flow velocity is indeed zero. And it is noted that an axially moving beam in external axial flow with nonzero velocity is a common problem in ocean engineering and other applications. Hence, it is significant to take the axial flow into account when investigating the dynamic behaviors of axially moving structures. Motivated by this, the present study focuses on investigating the dynamics of axially moving beams in axial flow with nonzero velocity.

In this paper, we consider an axially flexible beam moving at the speed of V with both ends supported. The axially moving beam is simultaneously subjected to axial flow with velocity V_f, as shown in Figure 1. A nonlinear governing equation of motion will be derived by using Newtonian method and discretized via Galerkin's technique. Based on Runge–Kutta numerical method, the dynamical behavior and vibration responses of the beam are obtained.

2. Theoretical modeling

2.1. ***Assumptions and kinetic description.*** The axially moving beam indicated in Figure 1 has length l, diameter D, area moment of inertia I, and mass per unit length m. A complex elasticity modulus of material is utilized, $E_0 I(1 + \gamma\partial/\partial t)$, where γ is a coefficient of internal dissipation assumed to be viscoelastic and of the Kelvin–Voigt type. The simply-supported beam is travelling at a speed of V. It is subjected to a pretension T_0 and an axial flow velocity V_f. The density of the fluid is ρ. In the present study, we assume the fluid is incompressible and the mean flow velocity is constant. Although the deflections of the beam may be large, the strains are small. Furthermore, the influences of pressure drop, gravity, shear deformation and rotary inertia of the beam are ignored for a simplified analysis.

In this work, the longitudinal and transverse displacements of the beam element are denoted by $u(x, t)$ and $w(x, t)$, respectively. Moreover, it should be noted that longitudinal displacements are one order of magnitude smaller than the lateral ones, hence $u(x, t)$ can be ignored in the Newtonian approach. Then, the velocity and acceleration of the same element can be easily obtained [Ghayesh 2012; Yan et al. 2016]:

$$V_{bx} \approx V, \quad a_{bx} \approx \dot{V}, \quad B_{by} = \frac{\partial w}{\partial t} + V\frac{\partial w}{\partial x}, \quad a_{by} \approx \left(\frac{\partial}{\partial t} + V\frac{\partial}{\partial x}\right)^2 w, \tag{1}$$

where the subscripts bx and by stand for components of the velocity or acceleration of the beam element along the x- and y-direction, respectively. The over-dot denotes the derivative with respect to time.

2.2. ***Added mass and inviscid hydrodynamic forces.*** For this system, the lateral virtual mass per unit length is considered and defined as $m_v = \rho(\frac{1}{4}\pi D^2)$. However, in the axial direction of the beam, according to Païdoussis [2016] and Gosselin et al. [2007], the mass of the fluid attached to the beam is smaller than that of the lateral-direction virtual mass. Therefore, an "axial added mass coefficient" β is introduced to modify axial virtual mass as βm_v, where β varies between 0 and 1.

In the lateral direction, the resultant relative velocity between beam and fluid flowing past it can be expressed as [Lighthill 1960]

$$V_r = \frac{\partial w}{\partial t} + (V + V_f)\frac{\partial w}{\partial x}. \tag{2}$$

We suppose that this flow has momentum $m_v V_r$ per unit length of beam [Païdoussis 1998], the rate of change of this momentum per unit length is $[\partial/\partial t + (V + V_f)\cdot\partial/\partial x]\, m_v V_r$ and brings about an equal and opposite lateral force on the beam [Lighthill 1960]. According to Gosselin et al. [2007], this lateral inviscid hydrodynamic force can be rewritten as

$$F_{AL} = m_v\left(\frac{\partial}{\partial t} + \beta(V_f + V)\frac{\partial}{\partial x}\right)^2 w. \tag{3}$$

According to Païdoussis [2016], the dynamics of cylinder in axial flow is principally controlled by the inviscid force, which can be expressed as $m_v(\partial/\partial t + \beta V_f \cdot \partial/\partial x)^2 w$. Thus, it is supposed that the effect of V is simply to change V_f to $V_f + V$, and its effect on the dynamics of axially moving beam in axial flow can be expected to be quantitative rather than qualitative, as compared to a stationary cylinder in axial flow.

Owing to the fact that the beam is axially moving with speed V and immersed in fluid, the momentum per unit length of the fluid attached on the beam in the axial direction is $\beta m_v V$. Hence the axial inviscid hydrodynamic force F_{AD} can be obtained as

$$F_{AD} = \beta m_v \dot{V}. \tag{4}$$

2.3. ***Viscous forces.*** According to Taylor's work [Taylor 1952], the viscous forces per unit length of the beam along normal and longitudinal directions are

$$F_N = \frac{1}{2}\rho D U^2\big(C_{D_p}\sin^2 i + C_f \sin i\big), \tag{5}$$

$$F_L = \frac{1}{2}\rho D U^2 C_f \cos i, \tag{6}$$

where C_f and C_{D_p} are frictional and form drag coefficients, and i is the angle of incidence of the beam.

After straightforward but tedious manipulations and a linearization procedure, one can get the viscous forces in their simplest form as

$$F_L = \frac{1}{2}\frac{m_v}{D}(V_f - V)^2 c_f \operatorname{sgn}(V_f - V), \tag{7}$$

$$F_{Ny} = \frac{1}{2}\frac{m_v}{D}\left[c_f |V_f - V|\left(\frac{\partial w}{\partial t} + V_f\frac{\partial w}{\partial x}\right) + c_d\left(\frac{\partial w}{\partial t} + V\frac{\partial w}{\partial x}\right)\right], \tag{8}$$

where F_{Nx} can be neglected for its high order, and $\mathrm{sgn}(V_f - V)$ is a sign function, i.e., $\mathrm{sgn}(V_f - V) = 1$ if $V_f > V$; $\mathrm{sgn}(V_f - V) = -1$ if $V_f < V$; $\mathrm{sgn}(V_f - V) = 0$ if $V_f = V$. Details for derivation of the above expressions of (7) and (8) are given in Appendix A.

It is obvious that the dynamics of structures in axial flow also depends on the viscous forces. However, viscous forces do not control the stability behaviour and just modify it [Païdoussis 2016]. One can find that the expressions of viscous force shown above contain terms with $V_f - V$, which just shows that the model of an axially moving beam in axial flow is quite different from that of a stationary cylinder in axial flow, i.e., the case of $V = 0$.

2.4. ***Newtonian approach.*** An element δx of beam is chosen for modeling the dynamic equations, as shown in Figure 2. Let the shear force, axial tension and bending moment be denoted as Q, T and M, respectively. The inertia forces along the x- and y-directions are denoted as F_{Ix} and F_{Iy}. Summing forces in the x- and y-directions and the moment in the out-plane direction, yielding

$$F_{Ix} - \frac{\partial T}{\partial x} - F_L - F_{Nx} + F_{AD} = 0, \tag{9}$$

$$F_{Iy} + F_{Ny} + F_{AL} - F_L \frac{\partial w}{\partial x} - \frac{\partial}{\partial x}\left(Q + T\frac{\partial w}{\partial x}\right) = 0, \tag{10}$$

$$Q = -E_0 I\left(1 + \gamma\frac{\partial}{\partial t}\right)\frac{\partial^3 w}{\partial x^3}, \tag{11}$$

where F_{Nx} and F_{Ny} denote projections of normal viscous force on x- and y-directions, respectively.

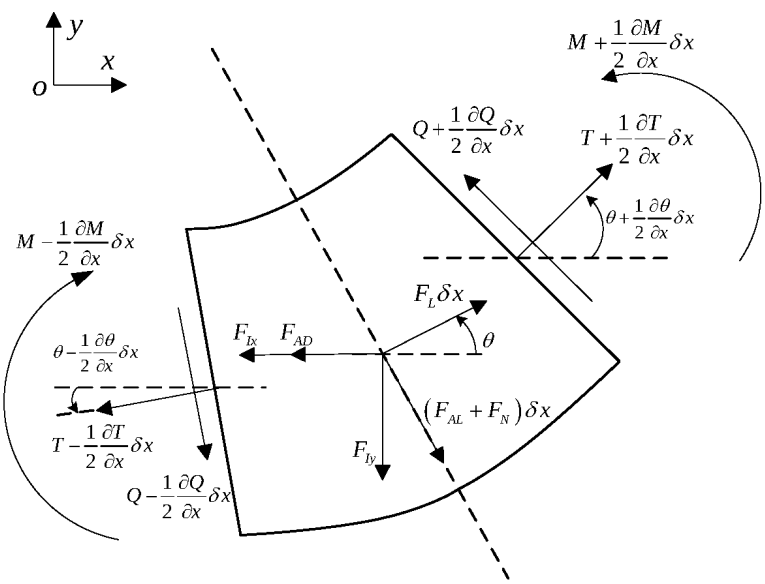

Figure 2. An element δx of the beam with forces and moments acting on it.

By substituting (3), (4), (7) and (8) into (9) to (11), and using the relationships $F_{Ix} = ma_{bx}$ and $F_{Iy} = ma_{by}$, the following equations can be obtained:

$$m\dot{V} + \beta m_v \dot{V} - \frac{1}{2} c_f \frac{m_v}{D} (V_f - V)^2 \operatorname{sgn}(V_f - V) - \frac{\partial T}{\partial x} = 0, \tag{12}$$

$$\begin{aligned} E_0 I \left(1 + \gamma \frac{\partial}{\partial t}\right) \frac{\partial^4 w}{\partial x^4} + m \left(\frac{\partial}{\partial t} + V \frac{\partial}{\partial x}\right)^2 w + m_v \left(\frac{\partial}{\partial t} + \beta (V_f + V) \frac{\partial}{\partial x}\right)^2 w \\ + \frac{1}{2} \frac{m_v}{D} \left[c_f |V_f - V| \left(V_f \frac{\partial w}{\partial x} + \frac{\partial w}{\partial t} \right) + c_d \left(\frac{\partial w}{\partial t} + V \frac{\partial w}{\partial x} \right) \right] \\ - \frac{1}{2} c_f \frac{m_v}{D} (V_f - V)^2 \frac{\partial w}{\partial x} \operatorname{sgn}(V_f - V) - \frac{\partial}{\partial x} \left(T \frac{\partial w}{\partial x} \right) = 0. \end{aligned} \tag{13}$$

By integrating (12) from x to l, and replacing the integration constant by the value of pretension T_0 at the end of the beam [Wang and Ni 2008], the axial tension can be obtained as

$$T(x) = -\left[(m + \beta m_v) \dot{V} - \frac{1}{2} c_f \frac{m_v}{D} (V_f - V)^2 \operatorname{sgn}(V_f - V) \right] (l - x) + T_0. \tag{14}$$

Substituting (12) and (14) into (13), the linear equation of motion can be obtained as

$$\begin{aligned} E_0 I \left(1 + \gamma \frac{\partial}{\partial t}\right) \frac{\partial^4 w}{\partial x^4} \\ + \left(m_v \beta^2 (V_f + V)^2 + m V^2 + \left[(m + \beta m_v) \dot{V} - \frac{1}{2} c_f \frac{m_v}{D} (V_f - V)^2 \operatorname{sgn}(V_f - V) \right] (l - x) - T_0 \right) \frac{\partial^2 w}{\partial x^2} \\ + 2 \left(m_v \beta V_f + (m + \beta m_v) V \right) \frac{\partial^2 w}{\partial t \, \partial x} + \frac{1}{2} \frac{m_v}{D} (c_f |V_f - V| V_f + c_d V) \frac{\partial w}{\partial x} \\ + \beta m_v \dot{V}_f \frac{\partial w}{\partial x} + \frac{1}{2} \frac{m_v}{D} (c_f |V_f - V| + c_d) \frac{\partial w}{\partial t} + (m + m_v) \frac{\partial^2 w}{\partial t^2} = 0. \end{aligned} \tag{15}$$

It is noted that this equation of motion can simplify into the governing equation for a cylindrical structure in axial fluid derived by Païdoussis [1998] when $V = 0$; also, it becomes the equation of motion for an axially moving beam if one removes the terms related to the fluid.

Moreover, the axial tension caused by the bending deflection should be taken into account if the order of amplitude of the transverse displacement is close to the order of the diameter of the beam [Li et al. 2015b]. Thus the additional nonlinear deflection-dependent axial force can be represented as

$$E_0 \left(1 + \gamma \frac{\partial}{\partial t}\right) \frac{A}{2l} \left(\frac{\partial w}{\partial x} \right)^2.$$

Then, an integral term

$$E_0 \left(1 + \gamma \frac{\partial}{\partial t}\right) \frac{A}{2l} \frac{\partial^2 w}{\partial x^2} \int_0^l \left(\frac{\partial w}{\partial x} \right)^2 dx,$$

should be added into (15) and the nonlinear governing equation for the beam system can be obtained as

$$\begin{aligned} &E_0 I\left(1+\gamma\frac{\partial}{\partial t}\right)\frac{\partial^4 w}{\partial x^4} \\ &\quad+\left(m_v\beta^2(V_f+V)^2+mV^2+\left[(m+\beta m_v)\dot{V}-\frac{1}{2}c_f\frac{m_v}{D}(V_f-V)^2\operatorname{sgn}(V_f-V)\right](l-x)\right. \\ &\qquad\left.-T_0-E_0\left(1+\gamma\frac{\partial}{\partial t}\right)\frac{A}{2l}\int_0^l\left(\frac{\partial w}{\partial x}\right)^2 dx\right)\frac{\partial^2 w}{\partial x^2} \\ &\qquad+2\big(m_v\beta V_f+(m+\beta m_v)V\big)\frac{\partial^2 w}{\partial t\,\partial x}+\frac{1}{2}\frac{m_v}{D}(c_f|V_f-V|V_f+c_d V)\frac{\partial w}{\partial x} \\ &\qquad+\beta m_v\dot{V}_f\frac{\partial w}{\partial x}+\frac{1}{2}\frac{m_v}{D}(c_f|V_f-V|+c_d)\frac{\partial w}{\partial t}+(m+m_v)\frac{\partial^2 w}{\partial t^2}=0. \end{aligned} \tag{16}$$

2.5. ***Nondimensionalization.*** After the following dimensionless variables and parameters:

$$\begin{gathered} \eta=\frac{w}{l},\quad \xi=\frac{x}{l},\quad \tau=\left(\frac{E_0 I}{m+m_v}\right)^{1/2}\frac{t}{l^2}=\alpha t,\quad v_f=\left(\frac{m_v}{E_0 I}\right)^{1/2}V_f l,\quad v=\left(\frac{m_v}{E_0 I}\right)^{1/2}Vl, \\ \varphi=\frac{m_v}{m+m_v},\quad \phi=\frac{m}{m_v},\quad \varepsilon=\frac{l}{D},\quad \bar{c}_d=\frac{c_d}{\alpha l},\quad \Gamma=\frac{T_0 l^2}{E_0 I},\quad \bar{\gamma}=\alpha\gamma, \\ \mu=\frac{Al^2}{I}=16\left(\frac{l}{D}\right)^2=16\varepsilon^2, \end{gathered} \tag{17}$$

are introduced in (16), the nonlinear equation of motion is obtained as

$$\begin{aligned} &\eta''''+\bar{\gamma}\dot{\eta}''''+\left(\phi v^2+\beta^2(v_f+v)^2+\left[(\phi+\beta)\varphi^{1/2}\dot{v}-\frac{1}{2}c_f\varepsilon(v_f-v)^2\operatorname{sgn}(v_f-v)\right](1-\xi)\right. \\ &\qquad\left.-\Gamma-\frac{\mu}{2}\int_0^1\eta'^2\,d\xi-\bar{\gamma}\mu\int_0^1\eta'\dot{\eta}'\,d\xi\right) \\ &\qquad+2\big((\phi+\beta)v+\beta v_f\big)\varphi^{1/2}\dot{\eta}'+\left[\frac{1}{2}\varepsilon(c_f|v_f-v|v_f+\bar{c}_d\varphi^{1/2}v)+\beta\varphi^{1/2}\dot{v}_f\right]\eta' \\ &\qquad+\frac{1}{2}\varepsilon(\varphi^{1/2}c_f|v_f-v|+\bar{c}_d\varphi)\dot{\eta}+\ddot{\eta}=0, \end{aligned} \tag{18}$$

where the over-dot and the prime denote the derivative with respect to τ and ξ, respectively.

3. Solutions via Galerkin's technique

The governing equation can be transformed into a set of ordinary equations (ODEs) via applying the Galerkin procedure, such that

$$\eta(\xi,\tau)=\sum_{j=1}^{N}\phi_j(\xi)\,q_j(\tau), \tag{19}$$

where N is the number of terms for Galerkin truncation. In this study, the eigenfunctions of a pinned-pinned beam are elected to be the admissible functions, i.e., $\phi_j(\xi)=\sqrt{2}\sin j\pi\xi$.

Substituting the above expression into (18), multiplying by $\phi_i(\xi)$ and integrating from 0 to 1 leads to

$$\boldsymbol{M}\ddot{\boldsymbol{q}} + \boldsymbol{C}\dot{\boldsymbol{q}} + \boldsymbol{K}\boldsymbol{q} + \boldsymbol{N}(\boldsymbol{q}) = 0, \tag{20}$$

where $\boldsymbol{M}$, $\boldsymbol{C}$, $\boldsymbol{K}$, $\boldsymbol{N}$ represent the structural mass matrix, damping matrix, stiffness matrix and nonlinear vector, respectively. The elements of these matrices are

$$\begin{aligned}
M_{ij} &= e_{ij} = \int_0^1 \phi_i\,\phi_j\,d\xi = \delta_{ij},\\
C_{ij} &= \frac{1}{2}\varepsilon(\varphi^{1/2}c_f|v_f - v| + \bar{c}_d\varphi)\,e_{ij} + \overline{\gamma}a_{ij} + 2\big((\phi+\beta)v + \beta v_f\big)\,\varphi^{1/2}d_{ij},\\
K_{ij} &= a_{ij} + \big(\phi v^2 + \beta^2(v_f+v)^2 + \Theta - \Gamma\big)b_{ij} - \Theta c_{ij} + \left[\frac{1}{2}\varepsilon(c_f|v_f - v|v_f + \bar{c}_d\,\varphi^{1/2}v) + \beta\varphi^{1/2}\dot{v}_f\right]d_{ij},\\
N(\boldsymbol{q}) &= -\frac{\mu}{2}\alpha_{ijkl}\,q_j\,q_k\,q_l - \overline{\gamma}\mu\,\alpha_{ijkl}\,q_j\,q_k\,\dot{q}_l,
\end{aligned} \tag{21}$$

where δ_{ij} is Kronecker delta and $\Theta = (\phi+\beta)\varphi^{1/2}\dot{v} - \frac{1}{2}c_f\varepsilon(v_f - v)^2\,\mathrm{sgn}(v_f - v)$.

Other coefficients in (21) are obtained as follows [Païdoussis 1998]:

$$\begin{aligned}
a_{ij} &= \int_0^1 \phi_1\,\phi_j''''\,d\xi = (j\pi)^4\delta_{ij}, \quad b_{ij} = \int_0^1 \phi_i\,\phi_j''\,d\xi = -(j\pi)^2\delta_{ij},\\
c_{ij} &= \int_0^1 \xi\phi_i\,\phi_j''\,d\xi = \begin{cases} \frac{4ij^3}{(j^2-i^2)^2}[1-(-1)^{j+1}] & i \neq j,\\ -\frac{1}{2}(j\pi)^2 & i = j,\end{cases}\\
d_{ij} &= \int_0^1 \phi_i\,\phi_j'\,d\xi = \begin{cases} \frac{2ji}{j^2-i^2}[(-1)^{j+1}-1] & i \neq j,\\ 0 & i = j,\end{cases}\\
\alpha_{ijkl} &= \int_0^1 \phi_i\,\phi_j'' \int_0^1 \phi_k'\,\phi_l'\,d\xi\,d\xi,
\end{aligned} \tag{22}$$

4. Convergence analysis

Firstly, the number of modes (i.e., N) used in Galerkin technique should be determined to obtain convergent results. It should be mentioned that the required number to get convergent results is different for linear and nonlinear analyses. In the present study, $N = 4$ and $N = 8$ are chosen for linear and nonlinear analyses, respectively. The details for convergence analysis can be found in Appendix B.

Following the parameter values chosen in [Wang and Ni 2008] and [Li et al. 2015b], here we give $\varphi = 0.5$, $\beta = 0.2$, $\varepsilon = 50$, $\bar{c}_d = 0.002$, $c_f = 0.02$, $\overline{\gamma} = 0.002$, $\Gamma = 1$, $\dot{v} = 0$ for the present investigation. For the sake of simplicity, it should be noted that the parameter $\overline{\gamma}$ is given without over-bar in the following sections.

5. Linear dynamic analysis

In this section, numerical studies are performed to investigate the effects of moving speed, flow velocity and some parameters on stabilities and critical moving speed of the beam. Evolutions of the natural

frequency and damping of the beam system can be obtained through eigenvalue analysis and only the lowest three modes are presented here.

Before analyzing the results, three kinds of critical moving speed are defined:

v_{Bi}: the bifurcation critical moving speed at ith mode, at which the frequency of beam is decreased to zero.

v_{Di}: the divergence critical moving speed at ith mode, at which buckling behavior of the beam occurs.

v_{Fi}: the flutter critical moving speed at ith mode, at which flutter vibrations of the beam take place.

5.1. ***Effects of the flow velocity on stability of the beam system.*** Figure 3 shows the evolution of dimensionless damping (Im(ω)) and frequency (Re(ω)) varying with the moving speed of beam when the external flow velocity is $v_f = 5$. Inspecting Figure 3 (left), one can find that bifurcation and divergence (static buckling) behaviors of the beam in the first mode occur at $v_{B1} = 3.04$ and $v_{D1} = 3.05$, respectively. This indicates that the beam loses stability by buckling at the first mode when the moving speed is 3.05. Increasing the moving speed further, the beam loses stability by flutter at $v_{F1} = 5.96$ in the first mode and keeps this state of instability as v increases further. As to the second mode, the bifurcation behavior occurs at $v_{B2} = 8.71$ and the divergence occurs at $v_{D2} = 8.86$ where static buckling of the beam takes place. As the moving speed is increased to $v_{F2} = 11.73$, flutter of the beam occurs. In the third mode of the beam, it always maintains stability over the moving speed range. The corresponding frequency varying with the moving speed is displayed in Figure 3 (right), showing the bifurcation points at which the frequency is deceased to zero in the first and second mode of the beam.

In order to further understand variations of the critical moving speed of the beam with the external flow velocity (v_f), we plot in Figure 4 the variation for divergence and flutter critical moving speeds in the first and second modes. The flow velocity is in the range of $0 \le v_f \le 15$. Different kinds of critical moving speeds, namely, v_{D1}, v_{F1}, v_{D2} and v_{F2}, are shown. It is found that the critical moving speed (v_{D1} and v_{F1}) in the first mode is slightly increased first and then decreased, and finally it is slightly increased

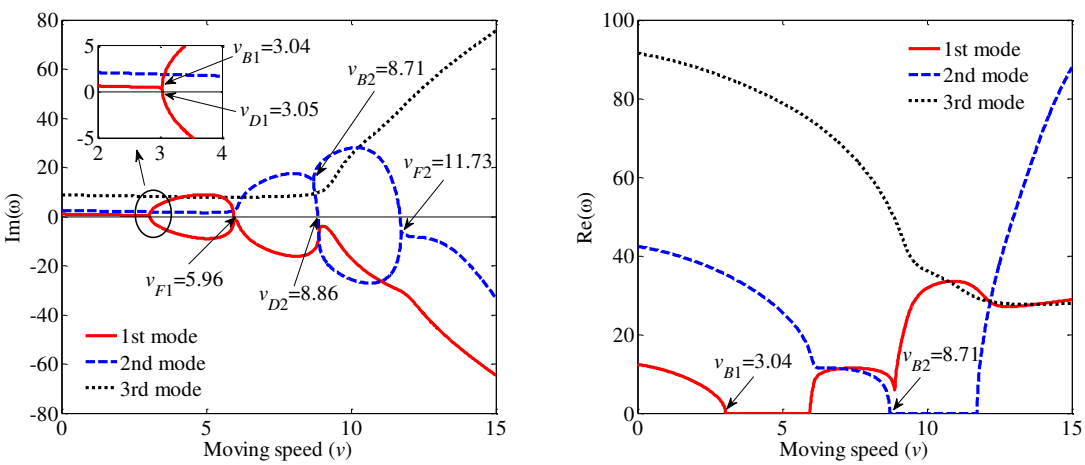

Figure 3. Evolutions of the damping (Im(ω)) and frequency (Re(ω)) of the beam with increasing the moving speed when $v_f = 5$.

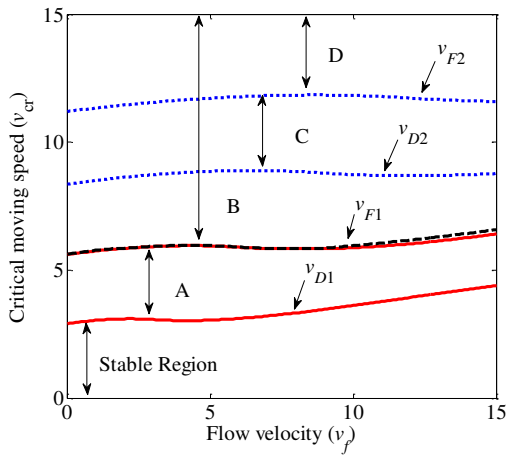

Figure 4. Stability diagram in the flow velocity-moving speed plane.

with the increase of flow velocity; while in the second mode, it changes a little with increasing the flow velocity. What is more, we offer the instability boundary varying with the flow velocity in Figure 4, which shows the instability characteristics of the beam.

In the considered flow velocity region from 0 to 15, when the moving speed is below the boundary of v_{D1}, the beam is stable. When the moving speed is beyond the boundary of v_{D1}, the beam displays several kinds of unstable modes. The instabilities involved can be divided into four regions which are described as follows:

Subregion A: in this region, between the two red lines, the beam loses stability by divergence, developing the static buckling in the first mode.

Subregion B: in this region, above the black dashed line, the beam loses stability by flutter in the first mode.

Subregion C: in this region, between the two blue dotted lines, the beam loses stability by divergence, developing static buckling in the second mode.

Subregion D: in this region, above the upper blue dotted line, the beam loses stability by flutter in the second mode.

5.2. ***Effects of other parameters on the first critical moving speed.*** In this subsection, the effects of parameters like the axial added mass coefficient β, slenderness ratio ε, mass ratio φ and pretension Γ on the critical moving speed are investigated. It should be pointed out that the instability of moving beam first occurs in the first mode via buckling, thus, v_{D1} is the critical moving speed v_{cr} when performing parametric analysis.

Four 3D plots are presented in Figure 5 to show the influences of β, ε, φ and Γ on the critical moving speed v_{cr}. Inspecting Figure 5 (top left), we can see that large flow velocity and small β gives a high critical moving speed of the beam. Specifically, the critical moving speed v_{cr} is reduced as β is increased, and the rate of reduction in the critical speed is faster as the flow velocity increased. By looking at Figure 5 (top right), one can find that the corner in the high values of ε and flow velocity region is high up, while the corner in the region of high flow velocity and low ε drops down. This indicates that

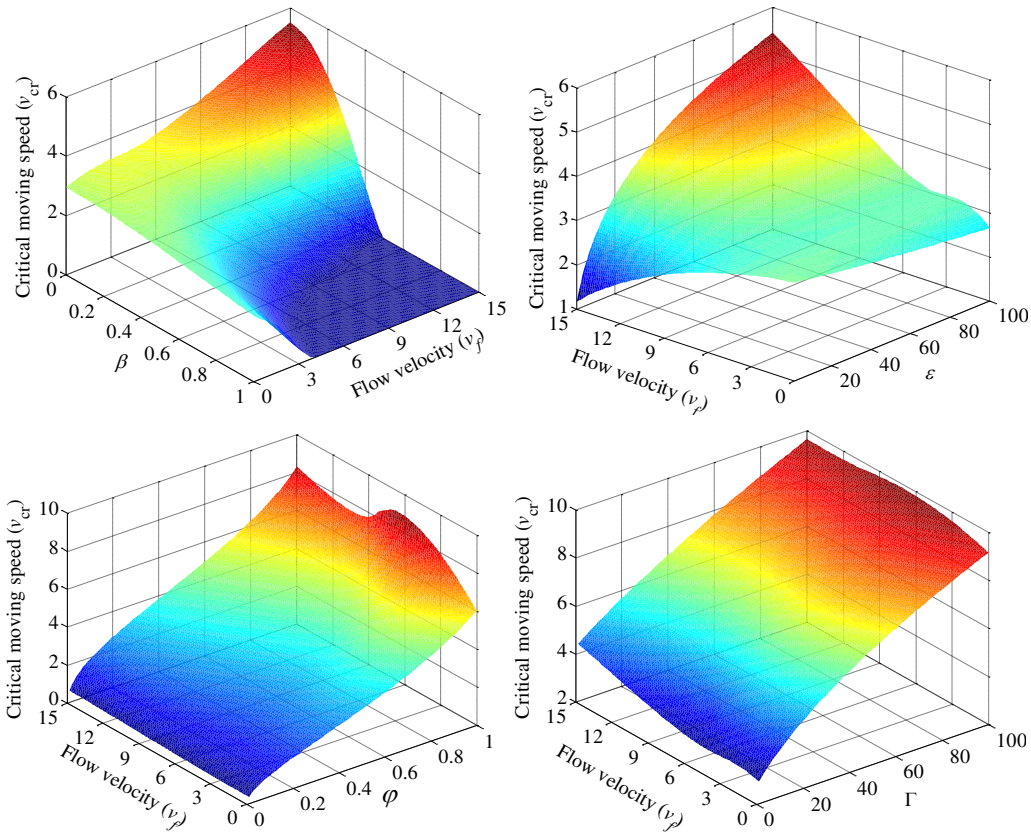

Figure 5. Critical moving speed v_{cr} as a function of the axial added mass coefficient β (top left); slenderness ratio ε (top right); mass ratio φ (bottom left); pretension Γ (bottom right) when varying the flow velocity (v_f) .

when the flow velocity (v_f) is high enough, a small slenderness ratio (ε) results in a low critical moving speed, while large slenderness ratio produces a high critical moving speed of the beam. The results in Figure 5 (bottom left and bottom right) respectively show that v_{cr} is increased for higher values of φ and Γ, while increasing the flow velocity gives a small increase in v_{cr}. In addition, the Kelvin–Voigt damping coefficient γ has no influence on the critical moving speed v_{cr}.

6. Nonlinear dynamic analysis

According to the linear analysis, it is noted that the beam can experience buckling and flutter with increasing moving speed. And parameters such as the axial added mass coefficient, slenderness ratio, mass ratio and pretension have a significant effect on the critical moving speed. However, linear analysis can only predict the dynamic behavior of the beam system, but cannot forecast its vibration response. So, nonlinear analysis is necessary to obtain the nonlinear vibration response of the beam.

6.1. ***General vibration response of the beam.*** Firstly, we focus on predicting vibration response of the beam with increasing moving speed for different values of the flow velocity. The Galerkin truncation

number is $N = 8$ to obtain convergent results (see Appendix B). The vibration response of the beam gained through nonlinear analysis is summarized via bifurcation diagrams where the vibration amplitude of the midpoint of the beam is recorded as a function of the moving speed v.

In the case of $v_f = 1$, the bifurcation diagram is shown in Figure 6 (top left). One can see that the beam system remains stable until $v = 3.0$ and the static buckling starts to occur at $v = 3.1$, as predicted by linear analysis. However, as the moving speed is increased to $v = 10.5$, the static buckling is transformed to flutter. At that time, the beam undergoes periodic or nonperiodic motions. Then the flutter instability ceases and the beam system is returned to static buckling at $v = 14.3$. The corresponding buckling and flutter responses can be found in the regions shown in the figure.

As the flow velocity is increased to $v_f = 2$, the bifurcation diagram is plotted in Figure 6 (top right). It is noted that the beam is stable for $v \leq 3.0$. However, with further increment of moving speed, static buckling instability occurs at $v = 3.1$, which is in conformity with linear theory. Then, the static buckling and flutter instability occur sequentially: static buckling instability for $3.1 \leq v \leq 10.6$ and flutter instability for $10.7 \leq v \leq 14.5$. When the flow velocity is equal to 3, we can find that buckling of the beam also occurs when the moving speed is between 3.1 and 10.6 and flutter occurs between 10.7 and 15.1. In summary, by inspecting Figure 6, we note that the buckling region of moving speed changes

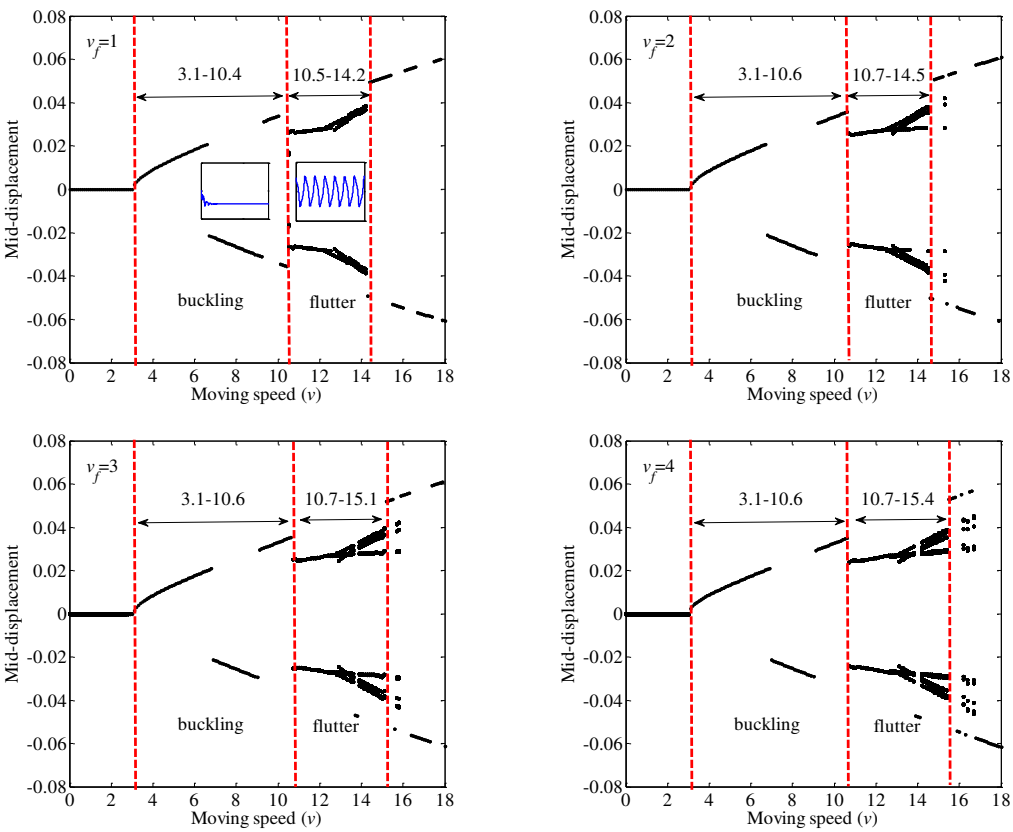

Figure 6. Bifurcation diagrams for the vibration amplitude of the beam when $v_f = 1$ (top left), $v_f = 2$ (top right), $v_f = 3$ (bottom left) and $v_f = 4$ (bottom right).

little while the flutter region of moving speed is a little increased when the flow velocity is increased from 1 to 4. In addition, for higher moving speeds, after the flutter region, it is noted that the responses are complex including flutter and buckling responses; also the flutter becomes clearer with the increase of flow velocity.

It is interesting to investigate how the dynamic responses of the beam vary with moving speed when the axial flow velocity is large enough (e.g., when v_f is beyond 7), as plotted in Figure 7. It is indicated that when flow velocity is increased to 7, the buckling moving speed is increased to 3.3, and the flutter responses occur at 11.7 till 14. Increasing the moving speed further, beyond 14, the beam then returns to buckling response. As the flow velocity is further increased to 8 and 9, we note that the critical moving speed is slightly increased to 3.4 and 3.5, and the buckling region is widened to 3.4–12.5 and 3.5–13.3, respectively. However, the flutter region is respectively decreased to 12.6–14.1 and 13.4–14.2. This indicates that increasing the flow velocity can eliminate the flutter response of the beam. Interestingly, as the flow velocity is increased to 11, the beam experiences totally a buckling response over the considered moving speed region.

It is concluded from figures 6 and 7 that the beam can undergo buckling and flutter motions with increasing moving speed v for different values of the axial flow velocity. However, when the flow

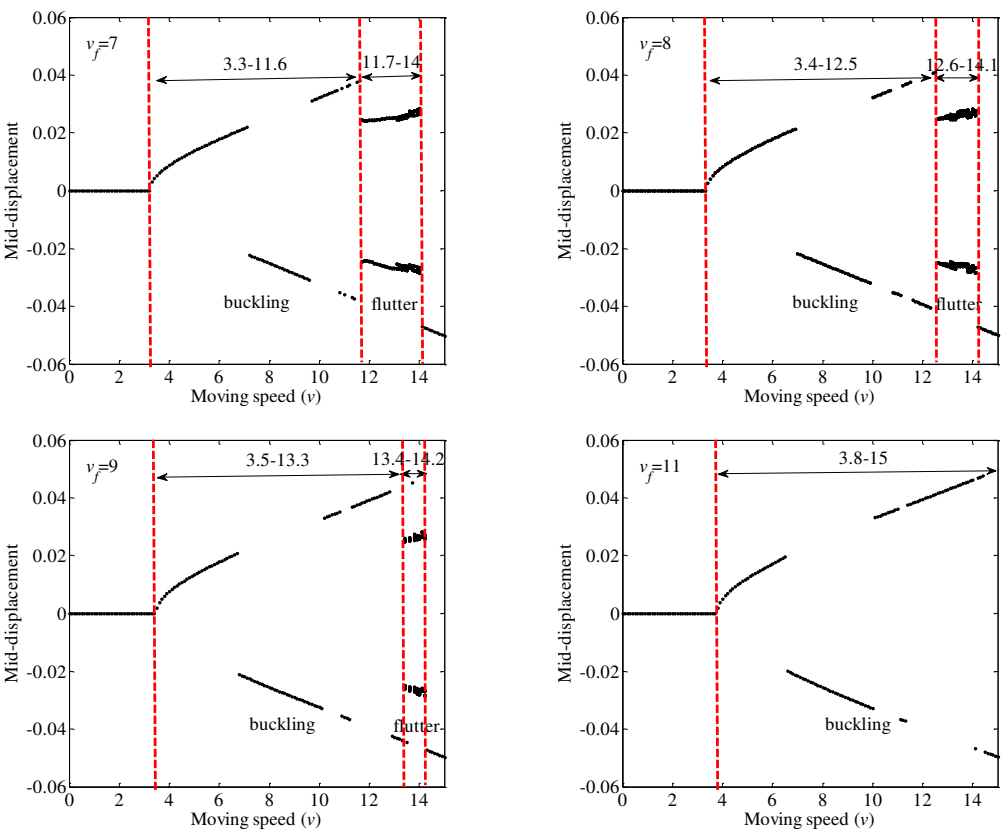

Figure 7. Bifurcation diagrams for the vibration amplitude of the beam when $v_f = 7$ (top left), $v_f = 8$ (top right), $v_f = 9$ (bottom left) and $v_f = 11$ (bottom right).

velocity is low (e.g., v_f is below 4), it has little effect on the buckling region but can increase the flutter region with the increase of flow velocity. In the case of large flow velocity (e.g., v_f beyond 7), the buckling region can be increased while the flutter region is decreased with increasing flow velocity.

6.2. ***Parametric analysis on buckling and flutter responses.*** In this subsection, the effects of several key parameters on the buckling and flutter responses of the beam system are examined and results are shown in figures 8–10. Figure 8 (top left) shows the bifurcation diagram of the beam for different values of the axial added mass coefficient β. It is seen that with increasing β the divergence point decreases, which agrees with the conclusion obtained by linear analysis. Also at a fixed moving speed, the amplitude of buckling is increased with larger values of axial added mass coefficient. Figure 8 (top right, bottom left and bottom right) show the bifurcation diagrams of the beam system for different values of the slenderness ratio ε , the mass ratio φ and the dimensionless pretension Γ, respectively. All these three figures show that, the larger the values of these three parameters are, the smaller the amplitudes of buckling become. As predicted by linear analysis, one can find that the critical moving speed at which divergence occurs increases with the increase of ε, φ, Γ, respectively.

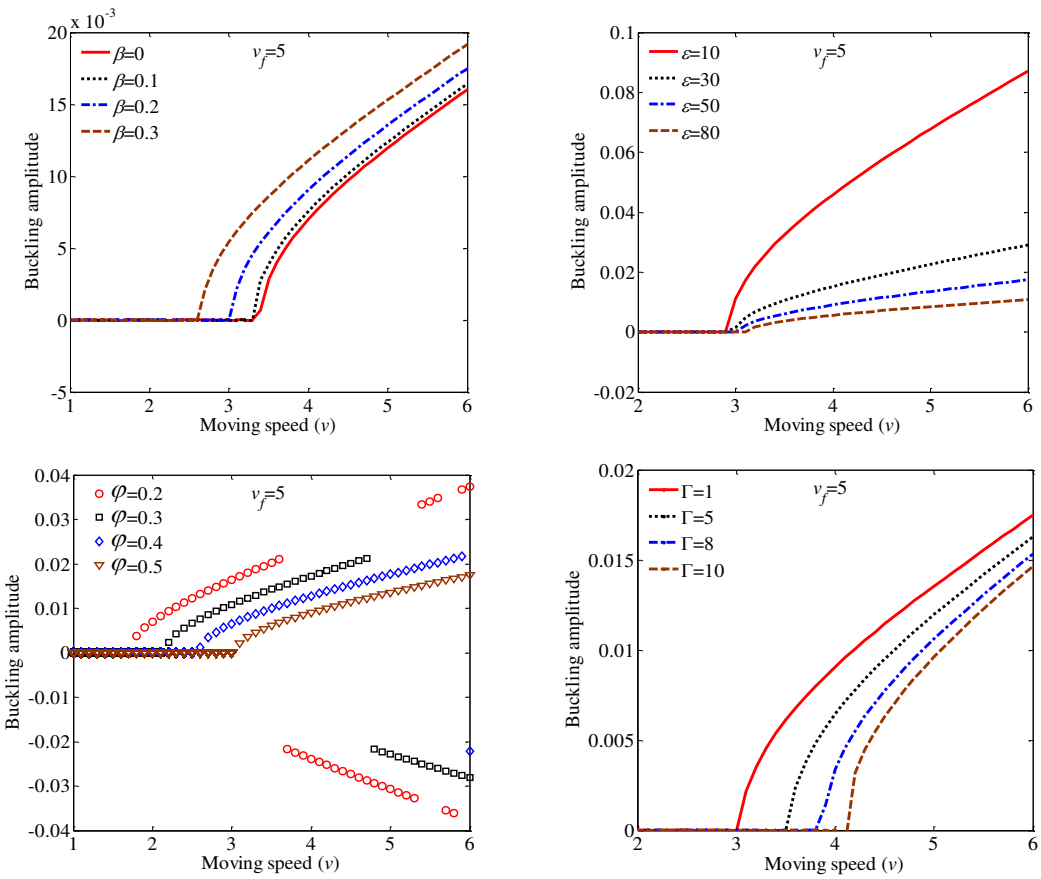

Figure 8. Bifurcation diagrams of the beam varying with β (top left); ε (top right); φ (bottom left); Γ (bottom right).

For fixed values of axial flow velocity and moving speed, Figure 9 shows the bifurcation diagrams of the beam as these key parameters are varied, for $v_f = 5$ and $v = 11$. We note the beam can experience buckling and flutter responses with increasing the axial added mass coefficient β and the slenderness ratio ε, as indicated in Figure 9 (top row). For example, when β is below 0.18, the beam is subjected to buckling. For β beyond 0.18, flutter responses of the beam occurs, but the vibration amplitude changes little. The instability type is transferred from buckling to flutter at $\varepsilon = 45$. The corresponding amplitudes are decreased with the increase of ε. It is noted from Figure 9 (bottom left) that the mass ratio φ has a great impact on the vibration amplitude of the moving beam, resulting in a clear reduction of amplitude with increasing the mass ratio. As to the effect of the pretension Γ, we note that the beam undergoes flutter over the considered region and the vibration amplitude is a little decreased with the increase of Γ.

The Kelvin–Voigt damping γ has no influence on the critical moving speed, as mentioned in the previous section. Here we study whether it has an effect on the vibration amplitude of the beam, as plotted in Figure 10. Indeed, γ has no effect on the buckling amplitude, as seen in Figure 10 (left). This can be expected from the equation of motion, showing that γ is always associated with time-dependent terms. By looking at Figure 10 (right), one can find that the beam system jumps from periodic responses

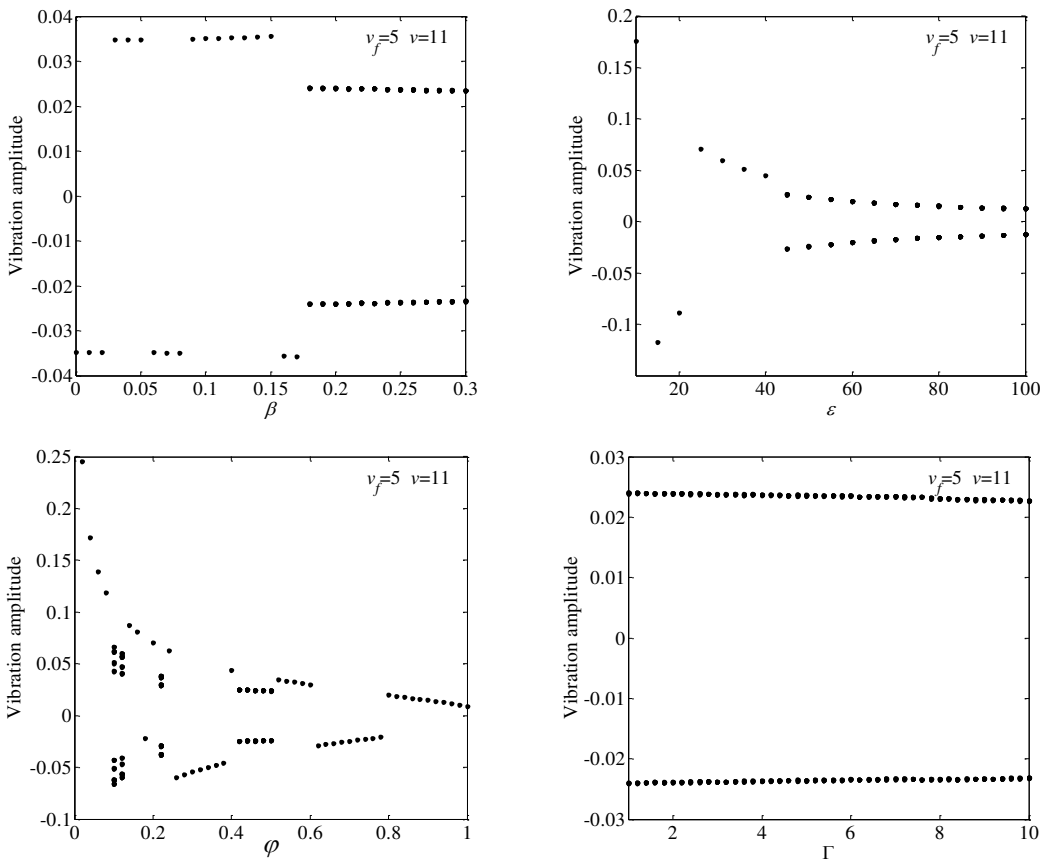

Figure 9. Bifurcation diagrams of the beam varying with β (top left); ε (top right); φ (bottom left); Γ (bottom right) when $v_f = 5$ and $v = 11$ throughout.

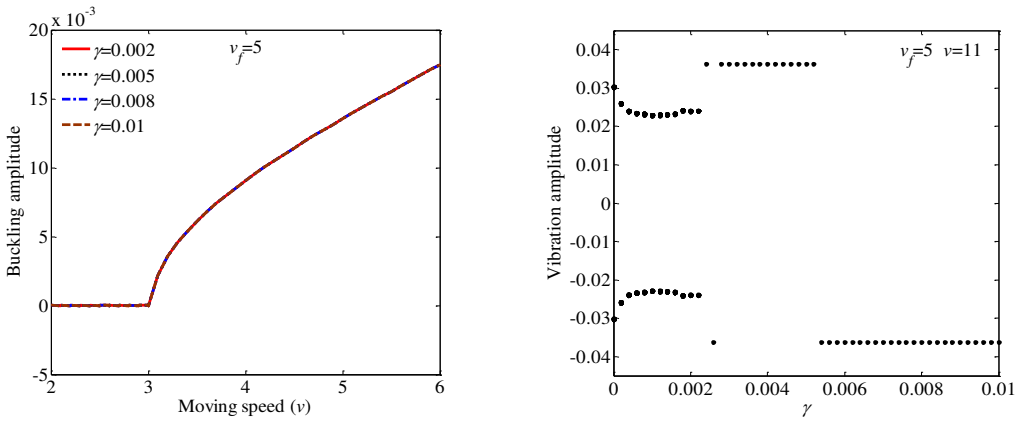

Figure 10. Bifurcation diagrams of the beam for different values of γ when $v_f = 5$ (left) and with increasing γ when $v_f = 5$ and $v = 11$ throughout (right).

to buckling when γ is increased to 0.0022. Moreover, the flutter amplitude is decreased as γ increases, while the buckling amplitude remains unchanged with increasing γ. The performed parametric analysis offers a significant insight into the sensitivity of the dynamic responses of the axially moving beam system on the parameters considered.

7. Conclusions

In this work, a nonlinear dynamic model for an axially moving beam subjected to external axial flow was established. The nonlinear vibrations and stability analysis of the moving beam were investigated in detail, considering the effects of system parameters such as the flow velocity, axial added mass coefficient, mass ratio, slenderness ratio, pretension and the Kelvin–Voigt damping. Results show that the critical moving speed where the instability of beam occurs is obviously affected by the system parameters for different values of flow velocity. The vibration characteristics of the moving beam can also be significantly affected by variation of the system parameters, showing a transition behavior between buckling and flutter responses. Some important conclusions can be drawn out as follows:

(1) It is noted that parameters such as axial added mass coefficient and slenderness ratio have great effects on the critical moving speed of beam, and their influences vary with flow velocity. However, increasing the mass ratio and pretension leads to an increase of the critical moving speed, which can be slightly affected by the flow velocity.

(2) When the flow velocity is low, it has little impact on the buckling region of moving speed, while the flutter region can be widened for increasing flow velocity. When the flow velocity is large enough, the flutter region of moving speed is gradually decreased and the beam may only undergo buckling over the moving speed with increasing flow velocity.

(3) The vibration responses of the beam are sensitive to the axial added mass coefficient, slenderness ratio, mass ratio and pretension. However, Kelvin–Voigt damping has no influence on the buckling response of the beam.

Appendix A. The derivation of the general expressions for the viscous forces

In this section, the general expressions for the F_N and F_L are derived in detail. Owing to the axial external flow is in x-direction, the free-stream velocity and the beam velocity can be expressed as [Kheiri et al. 2013a]

$$\vec{V}_{f,\infty} = V_f \boldsymbol{i}, \tag{A.1}$$

$$\vec{V}_b = V_{bx}\,\boldsymbol{i} + V_{by}\,\boldsymbol{j} = (\dot{v} + V + V u')\boldsymbol{i} + (\dot{w} + V w')\,\boldsymbol{j}, \tag{A.2}$$

where V_{bx} and V_{by} are components of $\vec{V}_b$ along the x- and y-directions, and the over-dot and the prime denote the derivative with respect to time and x. And w, $\dot{w}$, $w' \sim O(\varepsilon)$ and u, $\dot{u}$, $u' \sim O(\varepsilon^2)$.

The relative velocity between the free-stream and the beam can be easily obtained as

$$\vec{V}_{f/b} = (V_f - V_{bx})\boldsymbol{i} - V_{by}\,\boldsymbol{i}. \tag{A.3}$$

Therefore, the magnitude of the relative fluid-beam velocity can be written as

$$|\vec{V}_{f/b}| = V_f\left[\left(1 - \frac{V_{bx}}{V_f}\right)^2 + \left(\frac{V_{by}}{V_f}\right)^2\right]^{1/2}. \tag{A.4}$$

From Figure 11, the relative fluid-beam velocity $\vec{V}_{f/b}$ can be decomposed into an axial component $\vec{V}_a$ and a normal component $\vec{V}_c$; i is the angle of incidence angle; θ is the angle between the longitudinal axis of the beam with the x-axis. The axial and normal components of $\vec{V}_{f/b}$ may be expressed as

$$\vec{V}_a = |\vec{V}_a|\big((1+u')\boldsymbol{i} + w'\boldsymbol{j}\big), \tag{A.5}$$

$$\vec{V}_c = |\vec{V}_c|(a\boldsymbol{i} + b\boldsymbol{j}), \tag{A.6}$$

where the vectors given in bars are unit tangential vectors, hence $(1+u')^2 + w'^2 = 1$ and $a^2 + b^2 = 1$.

By using (A.3), (A.5) and (A.6), one obtains

$$|\vec{V}_a|(1+u') + |\vec{V}_c|a = V_f - V_{bx}, \quad |\vec{V}_a|w' + |\vec{V}_c|b = -V_{by}. \tag{A.7}$$

Adding the squares of the equations in (A.7) and using the relationship $|\vec{V}_{f/b}|^2 = |\vec{V}_a|^2 + |\vec{V}_c|^2$, the magnitude of axial flow velocity can be obtained as

$$|\vec{V}_a| = (1+u')(V_f - V_{bx}) - w' V_{by}. \tag{A.8}$$

According to Figure 11, one can write

$$|\cos i| = \frac{|\vec{V}_a|}{|\vec{V}_{f/b}|}, \quad |\sin i| = \frac{|\vec{V}_c|}{|\vec{V}_{f/b}|}. \tag{A.9}$$

From (A.4), (A.8) and $(A.9)_1$, using $(1+u') = 1 - \frac{1}{2}w'^2 + O(\varepsilon^4)$ and after neglecting the high-order terms, one can get

$$|\cos i| = 1 - \frac{1}{2}\left(w' + \frac{\dot{w} + V w'}{V_f - V_{bx}}\right)^2 + O(\varepsilon^4). \tag{A.10}$$

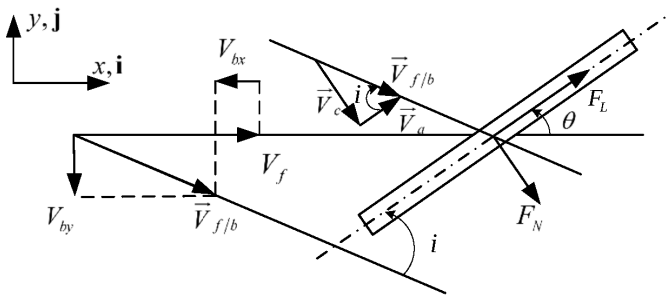

Figure 11. The beam element subjected to viscous forces.

According to Taylor's work, F_N and F_L can be expressed by (5) and (6). It is worth to point that the U in (5) and (6) is the axial external flow velocity in the stationary beam case. For this particular case (i.e., with the beam axially moving in axial external flow), one should consider the effect both of the axial external flow and the axial moving speed of the beam itself, hence U can be considered as the relative velocity between fluid and beam, i.e., $\vec{V}_{f/b}$. Then the viscous forces can be rewritten as

$$F_L = \frac{1}{2}\rho D(\vec{V}_{f/b})^2 C_f \cos i, \quad F_N = \frac{1}{2}\rho D(\vec{V}_{f/b})^2 (C_f \sin i + C_{D_p} \sin^2 i). \tag{A.11}$$

Substituting (A.10) into $(A.11)_1$, one can obtain

$$F_L = \frac{1}{2}\rho D(\vec{V}_{f/b})^2 C_f \left[1 - \frac{1}{2}\left(w' + \frac{\dot{w} + V w'}{V_f - V_{bx}}\right)^2\right]. \tag{A.12}$$

In order to derive the expression for normal viscous force conveniently, F_N is decomposed into two parts: the friction drag term $F_{N,f}$ and the form drag term $F_{N,fd}$ which can be expressed as

$$F_{N,f} = \frac{1}{2}\rho D(\vec{V}_{f/b})^2 C_f |\sin i|, \quad F_{N,fd} = \frac{1}{2}\rho D(\vec{V}_{f/b})^2 C_{D_p} \sin^2 i. \tag{A.13}$$

The y-component and x-component of $F_{N,f}$ become

$$(F_{N,f})_y = F_{N,f}\left(\frac{\vec{V}_c}{|\vec{V}_c|} \cdot \boldsymbol{j}\right), \quad (F_{N,f})_x = F_{N,f}\left(\frac{\vec{V}_c}{|\vec{V}_c|} \cdot \boldsymbol{i}\right). \tag{A.14}$$

From (A.4), $(A.7)_2$, (A.8), $(A.9)_2$, $(A.13)_1$, $(A.14)_1$ and after many tedious manipulations, we can obtain

$$(F_{N,f}) = -\frac{1}{2}\rho D(\vec{V}_{f/b})^2 C_f \left[w' + \frac{\dot{w} + V w'}{V_f - V_{bx}} - w'^2\left(\frac{\dot{w} + V w'}{V_f - V_{bx}}\right) - \frac{1}{2}w'\left(\frac{\dot{w} + V w'}{V_f - V_{bx}}\right)^2 - \frac{1}{2}w'^3 - \frac{1}{2}\left(\frac{\dot{w} + V w'}{V_f - V_{bx}}\right)^3\right]. \tag{A.15}$$

The minus sign in (A.15) arises because the force was considered to be generally in the positive direction. The minus sign can be removed if F_N is considered with the sign convention shown in Figure 11.

In the same spirit as (A.15) for $(F_{N,f})_y$, from (A.4), (A.7)$_1$, (A.8), (A.9)$_2$, (A.13)$_1$, (A.14)$_2$, $(F_{N,f})_x$ can be expressed as

$$(F_{N,f})_x = \frac{1}{2}\rho D(\vec{V}_{f/b})^2 C_f\left[w'^2 + \frac{w'(\dot{w}+Vw')}{V_f - V_{bx}}\right]. \tag{A.16}$$

From (A.10), one can obtain

$$\sin^2 i = 1 - \cos^2 i \approx \left(w' + \frac{\dot{w}+Vw'}{V_f - V_{bx}}\right)^2. \tag{A.17}$$

Substituting (A.17) into (A.13)$_2$, $F_{N,fd}$ can be expressed as

$$F_{N,fd} = \frac{1}{2}\rho D(\vec{V}_{f/b})^2 C_{D_p}\left(w' + \frac{\dot{w}+Vw'}{V_f - V_{bx}}\right)^2. \tag{A.18}$$

The y-component and x-component of $F_{N,fd}$ can be easily obtained:

$$(F_{N,fd})_y = F_{N,fd}\cos\theta \approx \frac{1}{2}\rho D(\vec{V}_{f/b})^2 C_{D_p}\left(w' + \frac{\dot{w}+Vw'}{V_f - V_{bx}}\right)^2, \tag{A.19}$$

$$(F_{N,fd})_x = F_{N,fd}\sin\theta \approx \frac{1}{2}\rho D(\vec{V}_{f/b})^2 C_{D_p} w'\left(w' + \frac{\dot{w}+Vw'}{V_f - V_{bx}}\right)^2. \tag{A.20}$$

Then, the expressions for the y-component and x-component of F_N, denoted by F_{Ny} and F_{Nx}, respectively, can be expressed as

$$\begin{aligned} F_{Ny} = {} & \frac{1}{2}\rho D(\vec{V}_{f/b})^2 \\ & \times \left\{ C_f\left[w' + \frac{\dot{w}+Vw'}{V_f - V_{bx}} - w'^2\left(\frac{\dot{w}+Vw'}{V_f - V_{bx}}\right) - \frac{1}{2}w'\left(\frac{\dot{w}+Vw'}{V_f - V_{bx}}\right)^2 - \frac{1}{2}w'^3 - \frac{1}{2}\left(\frac{\dot{w}+Vw'}{V_f - V_{bx}}\right)^3\right]\right. \\ & \left. + C_{D_p}\left(w' + \frac{\dot{w}+Vw'}{V_f - V_{bx}}\right)\right\}, \end{aligned} \tag{A.21}$$

$$F_{Nx} = \frac{1}{2}\rho D(\vec{V}_{f/b})^2\left[C_f\left(w'^2 + \frac{w'(\dot{w}+Vw')}{V_f - V_{bx}}\right) + C_{D_p} w'\left(w' + \frac{\dot{w}+Vw'}{V_f - V_{bx}}\right)^2\right]. \tag{A.22}$$

The component of $\vec{V}_{f/b}$ along y-axis is small compared with the component along x-axis and the axial displacement of beam $u(x,t)$ is of order $O(\varepsilon^2)$, hence we can write $\vec{V}_{f/b}^2 = (V_f - V_{bx})^2 + V_{by}^2 \approx (V_f - V_{bx})^2$ and $V_{bx} \approx V$. Recalling $V_{by} = \dot{w} + Vw'$ and according to Gosselin et al. [2007], the $V_{by\max}$ is given by the relationship $V_{by}^3 \cong V_{by}^2 V_{by\max}(8/3\pi)$. Substituting these relationships into (A.12), (A.21) and (A.22), and after some linearization procedures, one obtains

$$F_L = \frac{1}{2}\frac{m_v}{D}(V_f - V)^2 c_f, \quad F_{Ny} = \frac{1}{2}\frac{m_v}{D}c_f(V_f - V)(\dot{w} + V_f w') + \frac{1}{2}\frac{m_v}{D}c_d(\dot{w} + Vw'), \tag{A.23}$$

where $c_f = (4/\pi)C_f$, $c_d = (4/\pi)(8V_{by\max}/3\pi)C_{D_p}$ and $m_v = \frac{1}{2}\rho D^2\pi$. Furthermore, $F_{Nx} \sim O(\varepsilon^2)$ can be neglected.

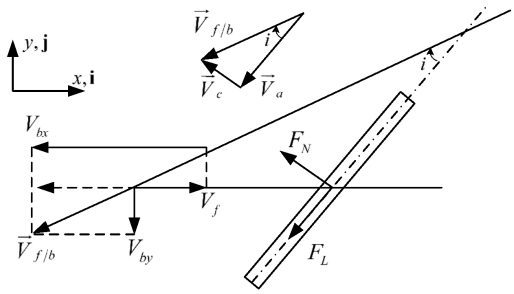

Figure 12. The beam element subjected to viscous forces when $V_f < V_{bx}$.

Considering the condition of $V_f < V_{bx}$, which is shown in Figure 12, the directions of F_L and F_N turn opposite. Recalling (A.15), the minus sign can be kept under this situation. Hence, the general linearized expressions for the viscous forces can be obtained:

$$F_L = \frac{1}{2}\frac{m_v}{D}(V_f - V)^2 c_f \,\mathrm{sgn}(V_f - V), \quad F_{Ny} = \frac{1}{2}\frac{m_v}{D}\big(c_f|V_f - V|(\dot{w} + V_f w') + c_d(\dot{w} + V w')\big), \tag{A.24}$$

where $\mathrm{sgn}(V_f - V)$ is a sgn function, i.e., $\mathrm{sgn}(V_f - V) = 1$ if $V_f > V$; $\mathrm{sgn}(V_f - V) = -1$ if $V_f < V$; $\mathrm{sgn}(V_f - V) = 0$ if $V_f = V$.

Appendix B. The determination of Galerkin truncation number N

In linear analysis, the critical speeds v_{cr} for different flow velocities are checked in the convergence tests to be discussed. Figure 13 shows the critical values of the moving speed v_{cr} as a function of the axial flow velocity, and the four curves represent results which are obtained with $N = 3, 4, 5$ and 6, respectively. One can find that these four curves are highly coincident with each other. Thus, $N = 4$ is an optimal choice from the point of a view of reliability and computational efficiency.

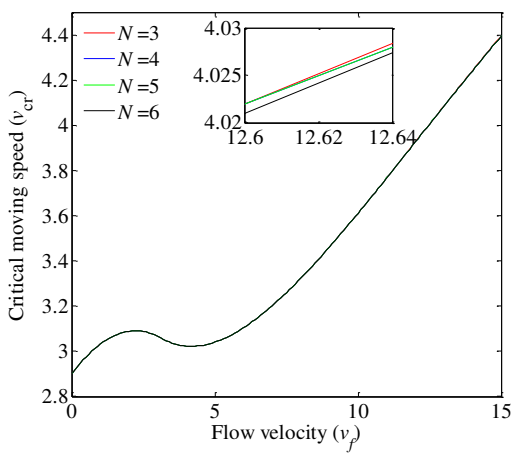

Figure 13. Critical speed v_{cr} as function of the flow velocity for different Galerkin truncation numbers N.

Furthermore, the Galerkin truncation number N for obtaining reliable nonlinear dynamic responses can be determined by inspecting Figure 14. In the case of $v_f = 0$, we choose $N = 4, 6$ and 8 in the numerical calculations (see Figure 14, left column). In the case of $v_f = 5$, we choose $N = 6, 8$ and 10 (see Figure 14, right column). As can be observed, $N = 8$ can be chosen to ensure the reliability of results in the nonlinear analysis.

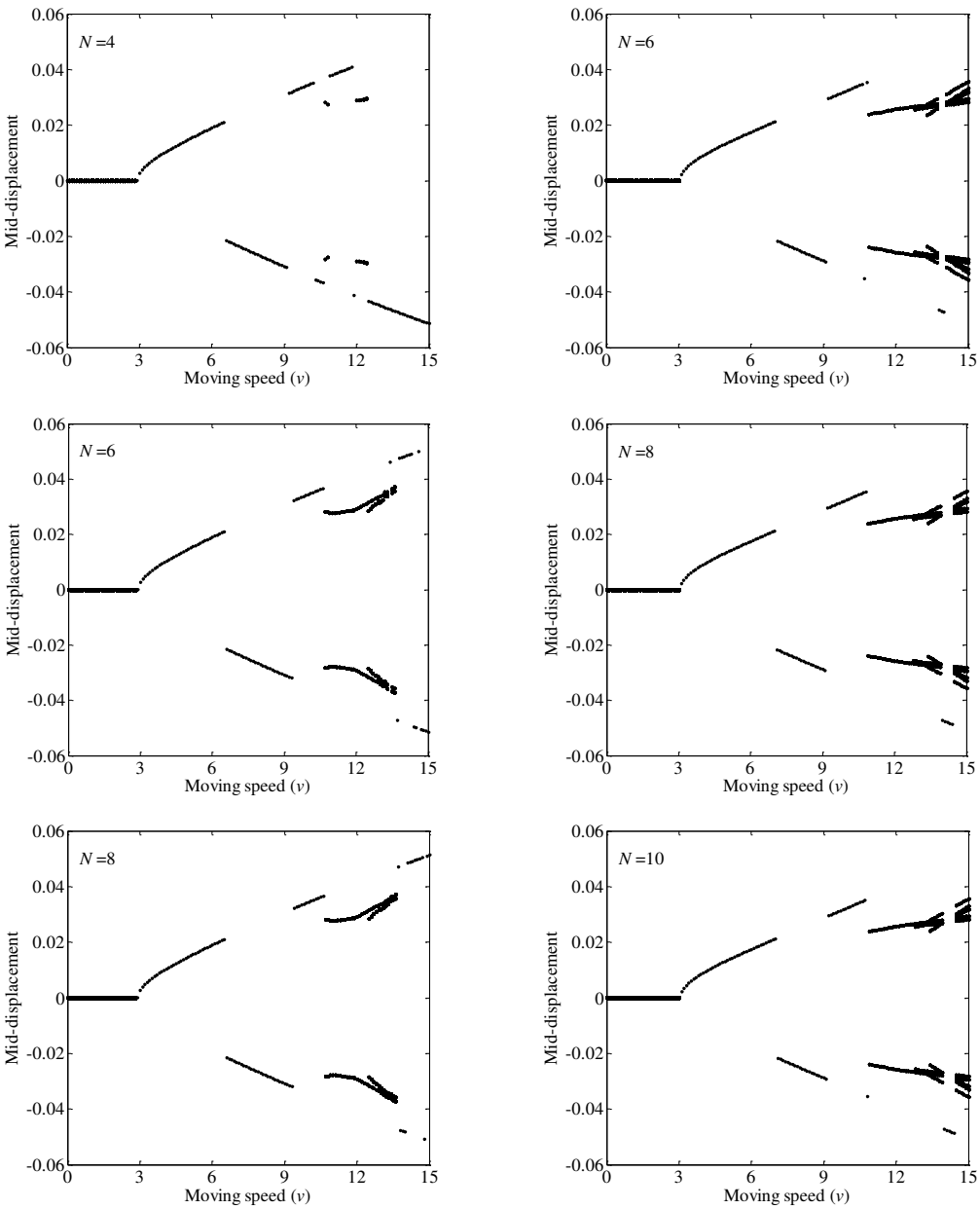

Figure 14. Bifurcation diagrams for the cases $v_f = 0$ (left column) and $v_f = 5$ (right column) by using different Galerkin truncation numbers N.

Acknowledgment

The financial support of the National Natural Science Foundation of China (No. 11672115, No. 11622216, No. 11602090 and No. 11902229) to this work is gratefully acknowledged.

References

[Banichuk et al. 2010] N. Banichuk, J. Jeronen, P. Neittaanmäki, and T. Tuovinen, "Static instability analysis for travelling membranes and plates interacting with axially moving ideal fluid", *J. Fluid. Struct.* **26**:2 (2010), 274–291.

[Banichuk et al. 2011] N. Banichuk, J. Jeronen, P. Neittaanmäki, and T. Tuovinen, "Dynamic behaviour of an axially moving plate undergoing small cylindrical deformation submerged in axially flowing ideal fluid", *J. Fluid. Struct.* **27**:7 (2011), 986–1005.

[Brown 2006] R. J. Brown, "Past, present, and future towing of pipelines and risers", pp. document id. OTC–18047–MS in *Offshore Technology Conference* (Texas), 2006.

[Chen 2005] L.-Q. Chen, "Analysis and control of transverse vibrations of axially moving strings", *Appl. Mech. Rev.* (*ASME*) **58**:2 (2005), 91–116.

[Chen et al. 2009] L.-Q. Chen, W. Zhang, and J. W. Zu, "Nonlinear dynamics for transverse motion of axially moving strings", *Chaos Solitons Fractals* **40**:1 (2009), 78–90.

[De Langre et al. 2007] E. De Langre, M. P. Païdoussis, O. Doaré, and Y. Modarres-Sadeghi, "Flutter of long flexible cylinders in axial flow", *J. Fluid Mech.* **571** (2007), 371–389.

[Dowling 1988] A. P. Dowling, "The dynamics of towed flexible cylinders, Part 1: neutrally buoyant elements", *J. Fluid Mech.* **187** (1988), 507–532.

[Frondelius et al. 2006] T. Frondelius, H. Koivurova, and A. Pramila, "Interaction of an axially moving band and surrounding fluid by boundary layer theory", *J. Fluid. Struct.* **22**:8 (2006), 1047–1056.

[Ghayesh 2012] M. H. Ghayesh, "Stability and bifurcations of an axially moving beam with an intermediate spring support", *Nonlinear Dyn.* **69** (2012), 193–210.

[Ghayesh et al. 2013a] M. H. Ghayesh, M. Amabili, and H. Farokhi, "Coupled global dynamics of an axially moving viscoelastic beam", *Int. J. Non-Linear Mech.* **51** (2013), 54–74.

[Ghayesh et al. 2013b] M. H. Ghayesh, M. Amabili, and M. P. Païdoussis, "Nonlinear dynamics of axially moving plates", *J. Sound Vib.* **332**:2 (2013), 391–406.

[Gosselin et al. 2007] F. Gosselin, M. P. Païdoussis, and A. K. Misra, "Stability of a deploying/extruding beam in dense fluid", *J. Sound Vib.* **299**:1-2 (2007), 123–142.

[Hedrih 2007] K. S. Hedrih, "Transversal vibrations of the axially moving sandwich belts", *Arch. Appl. Mech.* **77** (2007), 523–539.

[Huo and Wang 2016] Y. Huo and Z. Wang, "Dynamic analysis of a vertically deploying/retracting cantilevered pipe conveying fluid", *J. Sound Vib.* **360** (2016), 224–238.

[Kheiri et al. 2013a] M. Kheiri, M. P. Païdoussis, M. Amabili, and B. I. Epureanu, "Three-dimensional dynamics of long pipes towed underwater, Part 1: the equations of motion", *Ocean Eng.* **64** (2013), 153–160.

[Kheiri et al. 2013b] M. Kheiri, M. P. Païdoussis, M. Amabili, and B. I. Epureanu, "Three-dimensional dynamics of long pipes towed underwater, Part 2: linear dynamics", *Ocean Eng.* **64** (2013), 161–173.

[Kheiri et al. 2013c] M. Kheiri, M. P. Païdoussis, and A. M., "A nonlinear model for a towed flexible cylinder", *J. Sound Vib.* **332**:2 (2013), 1789–1806.

[Kheiri et al. 2015] M. Kheiri, M. P. Païdoussis, and M. Amabili, "An experimental study of dynamics of towed flexible cylinders", *J. Sound Vib.* **348** (2015), 149–166.

[Kim and Perkins 2002] W.-J. Kim and N. C. Perkins, "Two-dimensional vortex-induced vibration of cable suspensions", *J. Fluid. Struct.* **16**:2 (2002), 229–245.

[Kyriakides and Corona 2007] S. Kyriakides and E. Corona, *Mechanics of offshore pipelines: buckling and collapse*, vol. 1, Elsevier Science, 2007.

[Li et al. 2013] J. Li, X. H. Guo, J. Luo, and Y. Q. Li, H. Y. Wang, "Analytical study on inherent properties of a unidirectional vibrating steel strip partially immersed in fluid", *Shock Vib.* **20** (2013), 793–807.

[Li et al. 2015a] H. Y. Li, J. Li, and Y. J. Liu, "Internal resonance of an axially moving unidirectional plate partially immersed in fluid under foundation displacement excitation", *J. Sound Vib.* **358** (2015), 124–141.

[Li et al. 2015b] M. Li, Q. Ni, and L. Wang, "Nonlinear dynamics of an underwater slender beam with two axially moving supports", *Ocean Eng.* **108** (2015), 402–415.

[Li et al. 2018] H. Y. Li, J. Li, T. Y. Lang, and X. Zhu, "Dynamics of an axially moving unidirectional plate partially immersed in fluid under two frequency parametric excitation", *Int. J. Non-Linear Mech.* **99** (2018), 31–39.

[Lighthill 1960] M. J. Lighthill, "Note on the swimming of slender fish", *J. Fluid Mech.* **9**:2 (1960), 305–317.

[Lopes et al. 2002] J. L. Lopes, M. P. Païdoussis, and C. Semler, "Linear and nonlinear dynamics of cantilevered cylinders in axial flow, Part 2: the equations of motion", *J. Fluid. Struct.* **16**:6 (2002), 715–737.

[Marynowski and Kapitaniak 2014] K. Marynowski and T. Kapitaniak, "Dynamics of axially moving continua", *Int. J. Mech. Sci.* **81** (2014), 26–41.

[Mote Jr. 1968] C. D. Mote Jr., "Dynamic stability of an axially moving band", *J. Franklin Inst.* **285**:5 (1968), 329–346.

[Ni et al. 2014] Q. Ni, M. Li, M. Tang, and L. Wang, "Free vibration and stability of a cantilever beam attached to an axially moving base immersed in fluid", *J. Sound Vib.* **333**:9 (2014), 2543–2555.

[Païdoussis 1968] M. P. Païdoussis, "Stability of towed, totally submerged flexible cylinders", *J. Fluid Mech.* **34**:2 (1968), 273–297.

[Païdoussis 1970] M. P. Païdoussis, "Dynamics of submerged towed cylinders", pp. 981–1016 in *Eighth symposium on naval hydrodynamics: hydrodynamics in the ocean environment*, 1970.

[Païdoussis 1998] M. P. Païdoussis, *Fluid-structure interactions: slender structures and axial flow*, vol. 1, Academic Press, 1998.

[Païdoussis 2016] M. P. Païdoussis, *Fluid-structure interactions: slender structures and axial flow*, vol. 2, 2nd ed., Academic Press, 2016.

[Païdoussis and Li 1993] M. P. Païdoussis and G. X. Li, "Pipes conveying fluid: a model dynamical problem", *J. Fluid. Struct.* **7**:2 (1993), 137–204.

[Païdoussis et al. 2002] M. P. Païdoussis, E. Grinevich, D. Adamovic, and C. Semler, "Linear and nonlinear dynamics of cantilevered cylinders in axial flow, Part 1: physical dynamics", *J. Fluid. Struct.* **16**:6 (2002), 691–713.

[Semler et al. 2002] C. Semler, J. L. Lopes, N. Augu, and M. P. Païdoussis, "Linear and nonlinear dynamics of cantilevered cylinders in axial flow, Part 3: nonlinear dynamics", *J. Fluid. Struct.* **16**:6 (2002), 739–759.

[Taleb and Misra 1981] I. A. Taleb and A. K. Misra, "Dynamics of an axially moving beam submerged in a fluid", *J. Hydronautics* **15**:1 (1981), 62–66.

[Taylor 1952] G. I. Taylor, "Analysis of the swimming of long and narrow animals", *Proc. R. Soc. Lond. A* **214**:1117 (1952), 158–183.

[Telford et al. 1976] W. M. Telford, L. P. Geldart, R. E. Sheriff, and D. A. Key, *Applied geophysics*, Cambridge University Press, 1976.

[Wang 2018] Y. Q. Wang, "Electro-mechanical vibration analysis of functionally graded piezoelectric porous plates in the translation state", *Acta Astronaut.* **143** (2018), 263–271.

[Wang and Ni 2008] L. Wang and Q. Ni, "Vibration and stability of an axially moving beam immersed in fluid", *Int. J. Solids Struct.* **45**:5 (2008), 1445–1457.

[Wang and Zu 2017a] Y. Q. Wang and J. W. Zu, "Instability of viscoelastic plates with longitudinally variable speed and immersed in ideal liquid", *Int. J. Appl. Mech.* **9**:1 (2017), 1750005.

[Wang and Zu 2017b] Y. Q. Wang and J. W. Zu, "Vibration behaviors of functionally graded rectangular plates with porosities and moving in thermal environment", *Aerosp. Sci. Technol.* **69** (2017), 550–562.

[Wang et al. 2016] Y. Q. Wang, X. B. Huang, and J. Li, "Hydroelastic dynamic analysis of axially moving plates in continuous hot-dip galvanizing process", *Int. J. Mech. Sci.* **110** (2016), 201–216.

[Wickert and Mote 1988] J. A. Wickert and C. D. Mote, "Current research on the vibration and stability of axially-moving materials", *Shock Vib. Digest* **20**:5 (1988), 3–13.

[Yan et al. 2016] H. Yan, Q. Ni, H. L. Dai, L. Wang, M. Li, Y. Wang, and Y. Luo, "Dynamics and stability of an extending beam attached to an axially moving base immersed in dense fluid", *J. Sound Vib.* **383** (2016), 364–383.

[Yan et al. 2018] H. Yan, H. Dai, Q. Ni, L. Wang, and Y. Wang, "Nonlinear dynamics of a sliding pipe conveying fluid", *J. Fluid. Struct.* **81** (2018), 36–57.

Received 15 Apr 2019. Revised 25 Dec 2019. Accepted 29 Dec 2019.

YAN HAO: 824174017@qq.com
Wuhan Second Ship Design and Research Institute, Wuhan, 430205, China

HULIANG DAI: daihulianglx@hust.edu.cn
Department of Mechanics, Huazhong University of Science and Technology, Wuhan, 430074, China

NI QIAO: niqiao@hust.edu.cn
Department of Mechanics, Huazhong University of Science and Technology, Wuhan, 430074, China

KUN ZHOU: 2524642385@qq.com
Department of Mechanics, Huazhong University of Science and Technology, Wuhan, 430074, China

LIN WANG: wanglindds@hust.edu.cn
Department of Mechanics, Huazhong University of Science and Technology, Wuhan, 430074, China

JOURNAL OF MECHANICS OF MATERIALS AND STRUCTURES
Vol. 15, No. 1, 2020
dx.doi.org/10.2140/jomms.2020.15.61

AN APPROXIMATE FORMULA OF FIRST PEAK FREQUENCY OF ELLIPTICITY OF RAYLEIGH SURFACE WAVES IN AN ORTHOTROPIC LAYERED HALF-SPACE MODEL

TRUONG THI THUY DUNG, TRAN THANH TUAN, PHAM CHI VINH AND GIANG KIEN TRUNG

The propagation of Rayleigh surface waves in an orthotropic composite layer with fixed bottom is considered by using the transfer matrix method. By considering the critical frequency, an explicit approximate formula of the peak frequency of the fundamental mode of H/V ratio curve is derived. In case the impedance contrast between the half-space and the layer is high, the obtained formula is shown to be the limit of the formula of the resonance frequency of the layers under the excitement of SH body waves, which demonstrates that the peak frequency of the H/V ratio could be interpreted as the resonance frequency of the layer. Since Rayleigh surface waves are easier to be excited than SH body incident waves traveling from the half-space to the surface of the layer, and the H/V ratio is a dimensionless quantity and it is easier to be measured than the response function of SH body waves, the obtained formula is potentially useful in measuring the resonance frequency of thin films deposited on a thick layer of substantially higher rigidity. Finally, some numerical calculations are carried out to illustrate that the obtained approximate formula is a good one for the resonance frequency of a composite layer, especially of a periodic composite layer.

1. Introduction

In seismology, identifying the resonance frequency of a soft sediment layer is important and meaningful in evaluating the destruction to a city located over the zone of a sediment. Since the traditional methods such as borehole are costly and harmful to the surrounding environment, the H/V ratio technique has been used intensively in recent decades. This method uses the information of peak frequency of the recorded ratio of the horizontal to vertical displacements' amplitude spectra (H/V ratio) at the free surface to deduce the resonance frequency.

From the theoretical point of view and from the fact that the horizontal movement is the main reason to cause the destruction of the structures on the ground, the resonance frequency of the layer should be identified from the first peak of the SH body wave transfer function. This is the function of frequency showing the amplification of the magnitude of an SH body incident wave from the half-space to the surface of the layer. For the simple model of one layer over the half-space, the resonance frequency is [Nakamura 1989]

$$f_r = \frac{1}{4}\frac{\beta}{h}, \tag{1}$$

Keywords: Rayleigh waves, SH body waves, orthotropy, H/V technique, resonance frequency, transfer matrix.

where h is the thickness of the layer, and β is the SH wave speed in the layer. This formula is equivalent to

$$\frac{hf_r}{\beta} = \frac{h}{\lambda_\beta} = \frac{1}{4}, \tag{2}$$

where λ_β is the wavelength of SH wave at the resonance frequency. Therefore, this formula is called the quarter-wavelength law in determining the resonance frequency, meaning that the thickness of the layer is one quarter of the wavelength of the SH wave propagating at resonance frequency.

In practice, recording the transfer function of SH waves is only feasible in strong or moderate earthquakes in which the SH signal is dominated. But this data is not always available. Thus, the ambient noise is recorded instead. However, the composition of the recorded ambient noise is still controversial since it is believed to be composed of various types of waves such as surface waves, body waves, etc., and the different modes of surface waves other than the fundamental mode could interfere [Lunedei and Malischewsky 2015]. With many investigations based on the recorded data and on the synthetic data, scientists agree that to identify the resonance frequency the recorded ambient noise could be used as the data of the fundamental mode of Rayleigh waves when the impedance contrast of the layer and the half-space is big enough. Therefore, the first peak frequency of the fundamental mode of Rayleigh surface waves could be interpreted as the fundamental resonance frequency of the layer [Field and Jacob 1993; 1995; Lachetl and Bard 1994; Lermo and Chávez-García 1994; Bonnefoy-Claudet et al. 2006].

For a simple isotropic model of one layer over the half-space, the first H/V ratio peak frequency f_p of the fundamental mode of Rayleigh waves was shown to approach the resonance frequency of the layer f_r when the impedance contrast increases [Tuan et al. 2011]. For more complex models consisting of many isotropic layers over the half-space, this is also shown in [Tuan et al. 2016a].

In addition to being used in seismology to estimate the resonance frequency of a layer, the H/V ratio technique could be used in material science for orthotropic structures. It is because the H/V ratio is a dimensionless quantity and is easy to be measured [Junge et al. 2006], and Rayleigh waves could be actively excited in thin films over a thick layer structure, that the recorded H/V spectral ratio could contain only Rayleigh waves, not interfered by other waves as in seismology. The question addressed here is whether the orthotropy affects the estimation of the resonance frequency. It is shown in [Vinh et al. 2019] that although the orthotropy considerably affects the H/V ratio behavior, it does not greatly affect the peak frequency of the fundamental mode when the impedance contrast is high. However, this is the case for the model of a single orthotropic layer over a half-space.

This paper aims at proving that the resonance frequency of a stack of layers could be identified from the first peak frequency of the fundamental mode of Rayleigh surface waves not only for isotropic materials but also for orthotropic materials when the impedance contrast of the layers and the half-space is big enough. The paper uses the transfer matrix of an orthotropic layer to establish the dispersion equation and the H/V ratio formula of Rayleigh surface waves propagating in the model of a stack of layers with the bottom fixed and the top surface free. This model is the limiting case of the model layered half-space when the impedance contrast between the half-space and the layer goes to infinity. For the isotropic layer, the transfer matrix was introduced by [Thomson 1950; Haskell 1953] in explicit form, but the explicit form of this matrix for the orthotropic layer has just been given recently in [Vinh et al. 2015; 2016]. Then an explicit equation determining the first peak frequency of H/V ratio as the first singularity of the H/V ratio curve is obtained. Next, an approximate formula of the peak frequency is derived from this explicit

equation given in the form of the quarter-wavelength law. This formula is of the limiting form of the formula of first peak frequency of the SH-wave transfer function in the multilayered half-space model given in [Tuan et al. 2016b] when the impedance contrast goes to a high value. Finally, some numerical results are carried out to illustrate that the obtained approximate formula can estimate the resonance frequency of a composite layer well, especially of a periodic composite layer.

2. Rayleigh surface waves in a model of orthotropic multilayers with fixed bottom

2.1. ***The dispersion equation.*** Consider a composite layer composed of a stack of N homogeneous orthotropic layers. It is assumed that the N-th (last) layer has its bottom clamped (fixed) and the first (top) layer has its surface free. The layers are in welded contact and the principal material directions of layers are identical. For layer m ($m = 1, \ldots, N$), and for the problem of plane waves, we denote by $c_{11}^{(m)}, c_{12}^{(m)}, c_{22}^{(m)}, c_{66}^{(m)}, \rho_m, h_m$ the material parameters in the $0x_1x_2$ plane (with $0x_1$ pointing along a principal material direction within the layer and $0x_2$ along the other principal material direction through the layer), the density of mass, and the thickness of the m-th layer, respectively. Assume that the Rayleigh waves propagate along the x_1-direction and decay in the x_2-direction. The thickness of the composite layer is the total thickness of N layers and is denoted by $h = h_1 + h_2 + \cdots + h_N$.

Consider the plane strain problems

$$u_i = u_i(x_1, x_2, t), \quad u_3 \equiv 0, \tag{3}$$

where u_i ($i = 1, 2$) are displacement components in the x_1- and x_2-directions and t is the time.

For a general orthotropic material, the strain-stress relations of the plane problems are [Ting 1996]

$$\begin{aligned} \sigma_{11} &= c_{11}u_{1,1} + c_{12}u_{2,2}, \\ \sigma_{22} &= c_{12}u_{1,1} + c_{22}u_{2,2}, \\ \sigma_{12} &= c_{66}(u_{1,2} + u_{2,1}), \end{aligned} \tag{4}$$

where c_{ij} are material constants of the layer.

In the absence of body forces the equations of motion are

$$\begin{aligned} \sigma_{11,1} + \sigma_{12,2} &= \rho\ddot{u}_1, \\ \sigma_{12,1} + \sigma_{22,2} &= \rho\ddot{u}_2, \end{aligned} \tag{5}$$

where σ_{ij} are the stress components, commas indicate differentiation with respect to spatial variable x_k ($k = 1, 2$), and a dot shows differentiation with respect to the time t.

If we consider plane waves propagating in the x_1-direction with apparent velocity c, apparent wave number k, and decaying in the x_2-direction, the displacements and stresses are of forms [Vinh et al. 2016]

$$u_1 = U_1(x_2)e^{ik(x_1 - ct)}, \qquad u_2 = U_2(x_2)e^{ik(x_1 - ct)}, \tag{6}$$

$$\sigma_{12} = k\Sigma_1(x_2)e^{ik(x_1 - ct)}, \quad \sigma_{22} = k\Sigma_2(x_2)e^{ik(x_1 - ct)}. \tag{7}$$

Consider the layer j of thickness h_j; the transfer matrix which relates the displacement-stress vector $\boldsymbol{\xi}(x_2) = \begin{bmatrix} U_1 & U_2 & \Sigma_1 & \Sigma_2 \end{bmatrix}^T (x_2)$ at the top ($x_2 = 0$) and at the bottom ($x_2 = h_j$) of the layer is

$$\boldsymbol{\xi}(\text{top}) = \boldsymbol{T}^{(j)}\boldsymbol{\xi}(\text{bottom}), \tag{8}$$

where matrix $\boldsymbol{T}^{(j)}$ is given in [Vinh et al. 2016] as

$$\boldsymbol{T}^{(j)} = \begin{pmatrix} \boldsymbol{T}_1^{(j)} & \boldsymbol{T}_2^{(j)} \\ \boldsymbol{T}_3^{(j)} & \boldsymbol{T}_4^{(j)} \end{pmatrix} \tag{9}$$

with the elements given in the Appendix in explicit forms depending on the parameters of the layer, the apparent velocity, and the frequency.

The relation of the displacement-stress vector at the free top surface and at the fixed bottom of the composite layer could be obtained by applying the relation (8) successively for all layers $j = 1, \ldots, N$ in the form

$$\boldsymbol{\xi}(0) = \boldsymbol{T}\boldsymbol{\xi}(h), \tag{10}$$

where $\boldsymbol{T}$ is the global transfer matrix and is the product of all the local matrices of N layers and is expressed in the form

$$\boldsymbol{T} = \boldsymbol{T}^{(\mathrm{N})} \cdots \boldsymbol{T}^{(2)}\boldsymbol{T}^{(1)}. \tag{11}$$

Due to the traction-free condition at the surface, the displacement-stress vector at the top surface of the composite layer is

$$\boldsymbol{\xi}(0) = \begin{bmatrix} U_1(0) & U_2(0) & 0 & 0 \end{bmatrix}^T. \tag{12}$$

And due to the clamped condition at the bottom, the displacement-stress vector at the fixed bottom of the composite layer is

$$\boldsymbol{\xi}(h) = \begin{bmatrix} 0 & 0 & \Sigma_1(h) & \Sigma_2(h) \end{bmatrix}^T. \tag{13}$$

Substituting these two vectors of displacement-stress into (10), we obtain two equations for the traction-free conditions at $x_2 = 0$ as

$$\begin{aligned} T_{33}\Sigma_1(h) + T_{34}\Sigma_2(h) &= 0, \\ T_{43}\Sigma_1(h) + T_{44}\Sigma_2(h) &= 0. \end{aligned} \tag{14}$$

The condition for this system of equations having nontrivial solutions is that the determinant of the system of coefficients vanishes. This is the dispersion equation of Rayleigh surface waves which helps determine the phase velocity c in terms of frequency and it is of form

$$T_{33}T_{44} - T_{34}T_{43} = 0, \tag{15}$$

where T_{ij} $(i, j = 3, 4)$ are the entries (i, j) of the global transfer matrix $\boldsymbol{T}$.

The H/V ratio (or ellipticity) of the Rayleigh surface waves is defined as the ratio of the horizontal displacement to the vertical displacement of particles at the free surface of the composite plate and therefore is of form

$$\chi = \frac{U_1(0)}{U_2(0)} = \frac{T_{13}\Sigma_1(h) + T_{14}\Sigma_2(h)}{T_{23}\Sigma_1(h) + T_{24}\Sigma_2(h)}. \tag{16}$$

By using (14) we have

$$\chi = \frac{-T_{13}T_{44} + T_{14}T_{43}}{-T_{23}T_{44} + T_{24}T_{43}}. \tag{17}$$

The asymptotic form of the dispersion equation (15) and the formula of H/V ratio (17) will be expressed in explicit form in terms of the explicit form of the local transfer matrix of an orthotropic layer given in

[Vinh et al. 2016]. The asymptotic form will be used to establish an approximate formula of the peak frequency of H/V ratio curve.

2.2. ***The cutoff and singularity frequency equation.*** Equation (15) is an implicit equation showing the relation of the phase velocity of Rayleigh waves c depending on frequency f. As shown in [Tolstoy and Usdin 1953; Tuan et al. 2016a], the solution of the dispersion equation (15) consists of many modes corresponding to many separate curves of phase velocity c as a function of frequency f. Each mode exists if the frequency is greater than a certain value of frequency f_c which is called the critical frequency or cutoff frequency. At the cutoff frequencies, both the phase velocity c and the H/V ratio go to infinity. Therefore, to identify the sharp peak (singularity) frequency of the ellipticity of Rayleigh waves of the fundamental mode, we find the cutoff frequency of the fundamental mode by identifying the lowest frequency at which the phase velocity goes to infinity.

The local transfer matrix of the m-th layer is given in the Appendix. Its elements depend on the parameters of the layer m and the phase velocity c and frequency f. When $c \to \infty$, the asymptotic form of this local transfer matrix, with explanation given in the Appendix, is

$$\boldsymbol{T}_m = \begin{pmatrix} \cos\bar{\varepsilon}_{2m} & \dfrac{ic_2^{(m)}}{c}(\alpha_{12}^{(m)}\sin\bar{\varepsilon}_{1m} + \beta_{12}^{(m)} e_3 \sin\bar{\varepsilon}_{2m}) \\ -\dfrac{ic_2^{(m)}}{c}(\alpha_{21}^{(m)}\sin\bar{\varepsilon}_{1m} - \beta_{21}^{(m)}\sin\bar{\varepsilon}_{2m}) & \cos\bar{\varepsilon}_{1m} \\ \dfrac{cc_{66}^{(m)}}{c_2^{(m)}}\sin\bar{\varepsilon}_{2m} & ic_{66}^{(m)}\alpha_{32}^{(m)}(\cos\bar{\varepsilon}_{1m} - \cos\bar{\varepsilon}_{2m}) \\ ic_{66}^{(m)}\alpha_{41}^{(m)}(\cos\bar{\varepsilon}_{1m} - \cos\bar{\varepsilon}_{2m}) & \dfrac{cc_{66}^{(m)}}{c_2^{(m)}}\alpha_{42}^{(m)}\sin\bar{\varepsilon}_{1m} \end{pmatrix}$$

$$\begin{pmatrix} -\dfrac{c_2^{(m)}}{cc_{66}^{(m)}}\sin\bar{\varepsilon}_{2m} & \dfrac{ic_2^{(m)2}}{c^2c_{66}^{(m)}}\alpha_{14}^{(m)}(\cos\bar{\varepsilon}_{1m} - \cos\bar{\varepsilon}_{2m}) \\ -\dfrac{ic_2^{(m)2}}{c^2c_{66}^{(m)}}\alpha_{23}^{(m)}(\cos\bar{\varepsilon}_{1m} - \cos\bar{\varepsilon}_{2m}) & -\dfrac{c_2^{(m)}}{cc_{66}^{(m)}}\alpha_{24}^{(m)}\sin\bar{\varepsilon}_{1m} \\ \cos\bar{\varepsilon}_{2m} & -\dfrac{ic_2^{(m)}}{c}(\alpha_{34}^{(m)}\sin\bar{\varepsilon}_{1m} + \beta_{34}^{(m)}\sin\bar{\varepsilon}_{2m}) \\ -\dfrac{ic_2^{(m)}}{c}(\alpha_{43}^{(m)}\sin\bar{\varepsilon}_{1m} - \beta_{43}^{(m)}\sin\bar{\varepsilon}_{2m}) & \cos\bar{\varepsilon}_{1m} \end{pmatrix}, \quad (18)$$

in which each element is expressed as the dominant term in c. The $\alpha_{ij}^{(m)}$, $\beta_{ij}^{(m)}$, and $\bar{\varepsilon}_{im}$ are given in the Appendix.

From the form of global transfer matrix given in (11), it is straightforward to prove that the global transfer matrix has a similar asymptotic form as the local transfer matrix where the elements T_{11}, T_{22}, T_{33}, T_{44}, T_{32}, T_{41} are finite terms (do not depend on c), the elements T_{21}, T_{12}, T_{13}, T_{24}, T_{34}, T_{43} are of degree $1/c$, the elements T_{31}, T_{42} are of degree c, and the elements T_{14}, T_{23} are of degree $1/c^2$. Therefore, when $c \to \infty$, the dispersion equation becomes

$$T_{33}T_{44} = 0 \quad (19)$$

since the term $T_{34}T_{43}$ is of degree of $1/c^2$ and is eliminated. This equation is now used to determine the cutoff frequencies which are also the singularity frequencies.

Simple model of one layer. In the case of a simple model with one layer only, the global transfer matrix is the local transfer matrix of that layer and is of the form (18). In this case, the cutoff frequency equation of Rayleigh waves is

$$T_{33}T_{44} = \cos\bar{\varepsilon}_2 \cos\bar{\varepsilon}_1 = 0. \tag{20}$$

The solutions of $T_{33} = \cos\bar{\varepsilon}_2 = 0$ are

$$\frac{fh}{c_2} = \frac{1}{4} + \frac{n}{2}, \quad n = 0, 1, 2, \ldots, \tag{21}$$

where $c_2 = \sqrt{c_{66}/\rho}$ is the velocity of an SH-type wave propagating in the layer. These solutions are the cutoff frequencies of symmetric modes as classified in [Tolstoy and Usdin 1953]. The solutions of $T_{44} = \cos\bar{\varepsilon}_1 = 0$ are

$$\frac{fh}{c_2\sqrt{e_2}} = \frac{1}{4} + \frac{l}{2}, \quad l = 0, 1, 2, \ldots, \tag{22}$$

which are cutoff frequencies of asymmetric modes. Since $e_2 = c_{22}/c_{66} > 1$, the cutoff frequency of the fundamental mode belongs to the solution class of symmetric modes with $n = 0$ in (21). This solution corresponds to the quarter-wavelength law for the isotropic models stated in (1)–(2). The other cutoff frequencies of the asymmetric modes and symmetric modes are of the higher modes.

We can see from the asymptotic form of the transfer matrix in (18) that the H/V ratio given by (17) has the asymptotic form proportional to c. Hence, it goes to infinity as $c \to \infty$. Therefore, the singularity of the H/V ratio of the model layer with bottom fixed is at the cutoff frequency.

The case of many layers. If the composite layer is composed of N different layers, the element T_{33} of the global transfer matrix is computed from the product in (11) by the recursive equations

$$\begin{aligned} T_{33}^{(n+1)} &= \cos\bar{\varepsilon}_{2(n+1)} T_{33}^{(n)} - \frac{c_2^{(n+1)}}{cc_{66}^{(n+1)}} \sin\bar{\varepsilon}_{2(n+1)} T_{31}^{(n)}, \\ T_{31}^{(n+1)} &= \frac{cc_{66}^{(n+1)}}{c_2^{(n+1)}} \sin\bar{\varepsilon}_{2(n+1)} T_{33}^{(n)} + \cos\bar{\varepsilon}_{2(n+1)} T_{31}^{(n)}, \end{aligned} \tag{23}$$

where n runs from 1 to $N-1$. The matrix form of this system of equations is

$$\begin{pmatrix} T_{33}^{(n+1)} \\ T_{31}^{(n+1)} \end{pmatrix} = \begin{pmatrix} \cos\bar{\varepsilon}_{2(n+1)} & -\dfrac{c_2^{(n+1)}}{cc_{66}^{(n+1)}} \sin\bar{\varepsilon}_{2(n+1)} \\ \dfrac{cc_{66}^{(n+1)}}{c_2^{(n+1)}} \sin\bar{\varepsilon}_{2(n+1)} & \cos\bar{\varepsilon}_{2(n+1)} \end{pmatrix} \times \begin{pmatrix} T_{33}^{(n)} \\ T_{31}^{(n)} \end{pmatrix}. \tag{24}$$

This recursive equation has the same form as the recursive equation for the isotropic models given in (18) in [Tuan et al. 2016a] in which c_{66} and c_2 are replaced by shear modulus μ and shear wave speed β, respectively. Therefore, using the same steps carried out in [Tuan et al. 2016a] we obtain the equation

determining the cutoff frequencies of the orthotropic models as

$$1+\sum_{j=1}^{\infty}(-1)^j I_j(2\pi f)^{2j} = 1 - I_1(2\pi f)^2 + I_2(2\pi f)^4 - \cdots = 0, \tag{25}$$

which is in the same form as (27) with coefficients I_j given in (28) in [Tuan et al. 2016a], in which β_i is replaced by $c_2^{(i)}$.

For the composite layer, the approximate equation of (25) is obtained in the same manner as in [Tuan et al. 2016a] and has the form

$$1 - I_1(2\pi f)^2 = 0, \tag{26}$$

where I_1 is

$$I_1 = \sum_{i=1}^{N-1}\sum_{j=i+1}^{N}\frac{\rho_i}{\rho_j c_2^{(j)2}}h_i h_j + \frac{1}{2}\sum_{i=1}^{N}\frac{h_i^2}{c_2^{(j)2}}, \tag{27}$$

where $c_2^{(j)} = \sqrt{c_{66}^{(j)}/\rho_j}$ is the velocity of SH-type waves in orthotropic layer j.

Since the recursive equation determining the asymptote global transfer matrix (24) is in a similar form as that of the isotropic case, and in order to get the similar form of the quarter-wavelength law, we define the average shear-wave velocity of the composite layer in the same wave for the isotropic case [Tuan et al. 2016a] as

$$\overline{V} = \frac{h}{\sqrt{2\sum_{i=1}^{N-1}\sum_{j=i+1}^{N}(\rho_i/\rho_j c_2^{(j)2})h_i h_j + \sum_{i=1}^{N}(h_i^2/c_2^{(j)2})}}. \tag{28}$$

Then, the solution of the approximate equation (26) is

$$f_p = \frac{1}{4}\frac{\overline{V}}{h}. \tag{29}$$

In dimensionless form, the obtained approximate formula of the first peak of H/V ratio of Rayleigh surface waves in layered half-space is

$$\bar{f}_p = \frac{hf_p}{\overline{V}} = \frac{1}{4}. \tag{30}$$

Note that a factor of $2\sqrt{2}/\pi$ has been removed with the same argument due to the error of the approximation process given in [Tuan et al. 2016b]. In that paper, the dimensionless resonance frequency of the orthotropic composite layer is given as

$$\bar{f}_r = \frac{hf_r}{\overline{V}} = \frac{1}{4}\sqrt{1 - \frac{I_{(\mathrm{N})}^2}{I_{(\mathrm{HS})}^2}}, \tag{31}$$

where $I_{(\mathrm{N})}$ and $I_{(\mathrm{HS})}$ are the impedance values of the composite layer and the half-space defined as

$$I_{(\mathrm{N})} = \bar{\rho}\overline{V}, \quad I_{(\mathrm{HS})} = \rho^{(\mathrm{HS})}c_2^{(\mathrm{HS})}, \tag{32}$$

in which $\bar{\rho} = (1/h)\sum_{i=1}^{N}\rho_i h_i$ is the average density of mass of the composite layer and $\rho^{(\mathrm{HS})}$ and $c_2^{(\mathrm{HS})}$ are the density of mass and the SH-type wave velocity of the half-space. We can see that while (30) is

obtained from the problem of the Rayleigh surface wave, (31) is the result of the problem of SH body waves. Although the two formulas are derived from different approaches, they are of the same form. The only difference is the factor $\sqrt{1 - I_{(\mathrm{N})}^2/I_{(\mathrm{HS})}^2}$. This factor goes to 1 when the impedance value of the half-space is much more than impedance value of the composite layer. That means the resonance frequency f_r of the layer in (31) tends to the peak frequency of H/V ratio curve f_p in (30) when the impedance contrast between the half-space and the layer is big enough and we can therefore approximate the peak frequency of the H/V ratio of the recorded noise for the resonance frequency of the orthotropic layer.

3. Illustrative examples

This section is to numerically show that the first peak frequency of the H/V ratio of Rayleigh waves can be interpreted as the fundamental resonance frequency of a composite layer over a rigid half-space when the impedance contrast between the layer and the half-space is large enough. This has practical meaning since a Rayleigh surface wave propagating on the surface of the composite layer is easier to be excited and measured than an SH body wave traveling from within the half-space to the surface of the layer. The first part of this section is for a composite layer made from two orthotropic layers. The second part is for a periodic composite layer consisting of many unit cells made of the same two orthotropic layers as in the first part.

3.1. ***Composite layer.*** Consider a model of two orthotropic layers deposited on a half-space. The two layers are made of beryl rock and layered soil (called a composite layer) which are assumed to be of the same thickness. The half-space is assumed to be isotropic. The material constants of this model are given in Table 1, which are extracted from [Wang and Rajapakse 1994, Table 1].

The average shear velocity of the two layers is computed by (28) as $\overline{V} = 0.7977$ (km/s), while the SH-type wave velocity of the half-space is $c_2^{(\mathrm{HS})} = \sqrt{c_{66}^{(\mathrm{HS})}/\rho^{(\mathrm{HS})}} = 2$. Therefore, the impedance contrast between the half-space and the layers of this model computed from (32) is about 2.5. The exact H/V ratio curve of Rayleigh waves depending on frequency is computed numerically by a modified program for orthotropic layered half-space models given in [Tuan and Trung 2016]. The value 2.5 of impedance contrast is classified as low in [Bonnefoy-Claudet et al. 2006]. Therefore, the H/V ratio curve of this model only shows a broad peak at the dimensionless frequency $\bar{f}_p = 0.2248$ where $\bar{f}_p$ is defined in (30). The exact fundamental dimensionless resonance frequency of the composite layer computed by the explicit formula given in [Tuan et al. 2016b] is $\bar{f}_r = 0.2558$. The obtained approximate formula for the dimensionless resonance frequency always gives the value 0.25 due to the way it is expressed. We can see that in this low-impedance-contrast case, the peak frequency $\bar{f}_p$ is rather far from 0.25 but the resonance frequency $\bar{f}_r$ is close to 0.25 with a relative error of 2.3%. It indicates that the obtained approximate formula estimates the exact resonance frequency well.

material	c_{11}	c_{22}	c_{12}	c_{66}	ρ (g/cm^3)
beryl rock	4.13	3.62	1.01	1.0	2
layered soil	6.25	4.57	1.74	1.40	2
half-space	24	24	8	8	2

Table 1. Material constants ($\times 10^9$ N/m^2).

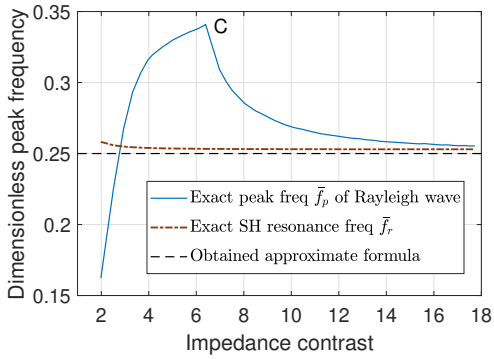

Figure 1. The exact peak frequency of H/V ratio curve and the resonance frequency of the composite layer of the orthotropic layered half-space given in Table 1.

To examine the obtained formula, we let the rigidity of the half-space (i.e., $c_{66}^{(\mathrm{HS})}$) vary such that the impedance contrast between the half-space and the composite layer varies from about 2 to 18, which spans from the low range to the high range of impedance contrast. By this variation of impedance contrast, we examine the change of the first peak frequency of ellipticity of Rayleigh surface waves and the change of resonance frequency and compare them to the obtained approximate formula. Figure 1 shows the change of the dimensionless peak frequency of the model with the above change of impedance contrast. In this figure, the continuous line is the exact peak frequency of the H/V ratio of Rayleigh waves and the dash-dotted line is the exact resonance frequency. By expressing the peak frequency in the dimensionless form (30), the obtained formula always gives $\bar{f}_p = \frac{1}{4}$, which is represented by a horizontal dashed line.

We can see from Figure 1 that the exact value of resonance frequency is always between the exact peak frequency of the H/V ratio of Rayleigh waves and the value of the obtained approximate formula. The obtained approximate formula is derived from the Rayleigh surface waves problem and it only approximates the peak frequency of H/V ratio well for high value of impedance contrast. However, it provides a good approximation of the resonance frequency in the whole impedance contrast range. For low impedance contrast, the H/V curves only show a broad peak frequency and its value can be far from the value of the quarter-wavelength law (the first part of the continuous line). When the impedance contrast is big enough, which is greater than a critical value (about 6 for this model and denoted by point C in the figure), the H/V ratio curves show a sharp peak (singularity point). The point C has already been reported in [Malischewsky and Scherbaum 2004]. The sharp peak frequency approaches the resonance frequency, which in turns approaches the value given by the quarter-wavelength law when the impedance contrast goes large. In this case, the peak frequency of the H/V ratio curve can therefore be interpreted as the resonance frequency of the layers.

3.2. ***Periodic composite layer.*** We consider now a composite layer with a periodical structure of n cells. Each cell is made of two orthotropic layers given in Table 1. The half-space is the same one given in Table 1. As shown in [Tuan et al. 2016b], the average shear velocity of the layers depends strongly on the position of the layer. If this average is taken in a traditional way such as the harmonic mean, the average value is constant despite the number of cells. However, the average formula given in (28) shows the different average value as it should be since the H/V ratio curve of the new model (with more layers)

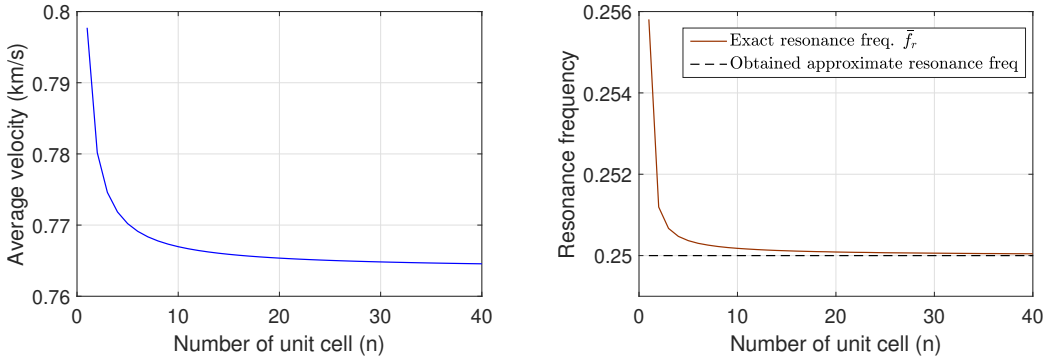

Figure 2. The average shear velocity (left) and the exact and approximate dimensionless resonance frequency (right) of the periodic composite layer depending on the number of cells n.

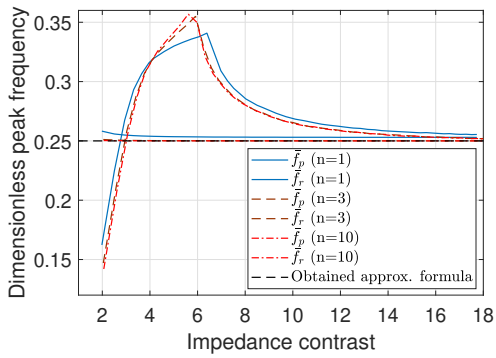

Figure 3. The exact peak frequency of the H/V ratio curve and the exact resonance frequency of the periodic composite layer.

should be different from the H/V ratio curve of the original model. This fact is illustrated in Figure 2, left, showing the value of average shear velocity of the periodic composite layer depending on the number of cells n. When the number n increases to about 40, the average value tends to a steady value of about 0.7641 (km/s).

Figure 2, right, shows the exact dimensionless resonance frequency of the periodic composite layer depending on the number of cells. When the composite layer has only a single cell, the exact dimensionless resonance frequency is $\bar{f}_r = 0.2558$ as mentioned above. When the number of cells is $n = 3$, that frequency is 0.2507, and when $n = 10$ it is 0.2502, which is almost equal to the prediction from the obtained approximate formula $\bar{f}_r = 0.25$. From this figure, we can see that the obtained approximate formula is substantially good for the periodic structure even for this model of low impedance contrast.

Figure 3 shows similar curves as in Figure 1 but for models of periodic composite layer deposited on the half-space. In this figure, we consider two more models of periodic composite layer with the number of cells $n = 3$ and $n = 10$. The total thicknesses of the layers of the three models are different, but note that the peak and resonance frequencies are given in dimensionless form. We can see that the shapes of the peak frequency curves of the three models are similar and close to each other's despite the considered

number of layers. When the number of cells is greater than 3, the shapes of the exact peak frequency curves of H/V ratios of Rayleigh waves are almost identical and the exact resonance frequency curves almost coincide with the approximate resonance frequency curves. That means the obtained formula is very good for the periodic structure.

4. Conclusions

An explicit approximate formula of the first peak frequency of the H/V ratio curve for the model of a stack of orthotropic layers underlain by a half-space has been derived using the transfer matrix method with the assumption that the impedance contrast between the half-space and the layers is high. It is shown that the obtained formula is the limiting result of the first peak frequency of the transfer function of SH body waves propagating from the half-space. This peak frequency is considered as the resonance frequency of the composite layer. Therefore, the paper has shown for the orthotropic models that when the impedance contrast between the half-space and the layers is high enough, the first peak frequency of the H/V ratio of the Rayleigh surface waves (the singularity) could be used to identify the first peak frequency of the transfer function of SH body waves (the resonance frequency). Although the approximate formula is obtained with the assumption of high impedance contrast between the composite layer and the half-space, it is numerically shown to be a good approximation of the resonance frequency of the composite layer even for moderate values of impedance contrast, especially in the case of periodic composite layer. Since orthotropic materials are widely used in the field of material and the data of Rayleigh surface waves is easier to be measured than the data of SH body waves, the obtained formula is potentially useful in determining the resonance frequency of orthotropic thin films deposited on a hard thick layer.

Appendix: Entries of matrix $\boldsymbol{T_m}$

The components of the transfer matrix $\boldsymbol{T}_m$ of the layer are given in [Vinh et al. 2016] as

$$\boldsymbol{T}_m = \begin{pmatrix} \dfrac{[\gamma_m;\cosh\varepsilon_m]}{[\gamma_m]} & \dfrac{-i[\beta_m;\sinh\varepsilon_m]}{[\alpha_m;\beta_m]} & \dfrac{-[\alpha_m;\sinh\varepsilon_m]}{[\alpha_m;\beta_m]} & \dfrac{-i[\cosh\varepsilon_m]}{[\gamma_m]} \\ \dfrac{-i[\gamma_m;\alpha_m\sinh\varepsilon_m]}{[\gamma_m]} & \dfrac{-ic[\alpha_m\cosh\varepsilon_m;\beta_m]}{[\alpha_m;\beta_m]} & \dfrac{-i\alpha_{1m}\alpha_{2m}[\cosh\varepsilon_m]}{[\alpha_m;\beta_m]} & \dfrac{-[\alpha_m\sinh\varepsilon_m]}{[\gamma_m]} \\ \dfrac{-[\gamma_m;\beta_m\sinh\varepsilon_m]}{[\gamma_m]} & \dfrac{-i\beta_{1m}\beta_{2m}[\cosh\varepsilon_m]}{[\alpha;\beta]} & \dfrac{[\gamma_m;\cosh\varepsilon_m]}{[\gamma_m]} & \dfrac{i[\beta_m\sinh\varepsilon_m]}{[\gamma_m]} \\ \dfrac{-i\gamma_{1m}\gamma_{2m}[\cosh\varepsilon_m]}{[\gamma_m]} & \dfrac{-[\beta_m;\gamma_m\sinh\varepsilon_m]}{[\alpha_m;\beta_m]} & \dfrac{-i[\alpha_m;\gamma_m\sinh\varepsilon_m]}{[\alpha_m;\beta_m]} & \dfrac{[\gamma_m\cosh\varepsilon_m]}{[\gamma_m]} \end{pmatrix}. \tag{33}$$

In this matrix, we use the notations

$$[f;g] := f_2g_1 - f_1g_2, \quad [f] = f_2 - f_1. \tag{34}$$

The other notations depend on the parameters of the layers $c_{ij}^{(m)}$, ρ_m, h_m, the phase velocity c, and the wave number k as

$$
\begin{aligned}
\alpha_i^{(m)} &= -\frac{(e_3^{(m)}+1)b_i^{(m)}}{e_2^{(m)}b_i^{(m)2}-1+x_m}, \quad i=1,2, & x_m &= \frac{\rho_m c^2}{c_{66}^{(m)}},\\
b_1^{(m)} &= \sqrt{\frac{S^{(m)}+\sqrt{S^{(m)2}-4P^{(m)}}}{2}}, & b_2^{(m)} &= \sqrt{\frac{S^{(m)}-\sqrt{S^{(m)2}-4P^{(m)}}}{2}},\\
S^{(m)} &= \frac{e_2^{(m)}(e_1^{(m)}-x_m)+1-x_m-(e_3^{(m)}+1)^2}{e_2^{(m)}}, & P^{(m)} &= \frac{(e_1^{(m)}-x_m)(1-x_m)}{e_2^{(m)}},\\
\beta_i^{(m)} &= c_{66}^{(m)}(b_i^{(m)}-\alpha_i^{(m)}), & \gamma_i^{(m)} &= e_3^{(m)}+e_2^{(m)}b_i^{(m)}\alpha_i^{(m)},\\
\varepsilon_{1m} &= b_1^{(m)}kh_m, & \varepsilon_{2m} &= b_2^{(m)}kh_m,
\end{aligned}
\tag{35}
$$

in which the dimensionless parameters $e_i^{(m)}$ are defined as

$$
e_1^{(m)} = \frac{c_{11}^{(m)}}{c_{66}^{(m)}}, \quad e_2^{(m)} = \frac{c_{22}^{(m)}}{c_{66}^{(m)}}, \quad e_3^{(m)} = \frac{c_{12}^{(m)}}{c_{66}^{(m)}}.
$$

For example, we have $[\cosh\varepsilon_m] = \cosh\varepsilon_{2m} - \cosh\varepsilon_{1m}$, $[\gamma_m;\cosh\varepsilon_m] = \gamma_2^{(m)}\cosh\varepsilon_{1m} - \gamma_1^{(m)}\cosh\varepsilon_{2m}$, and $[\alpha_m\sinh\varepsilon_m] = \alpha_2^{(m)}\sinh\varepsilon_{2m} - \alpha_1^{(m)}\sinh\varepsilon_{1m}$.

When $c\to\infty$, the asymptotic values of ε_{1m} and ε_{2m} are

$$
\varepsilon_{1m} \sim \frac{i2\pi f h_m}{c_2^{(m)}\sqrt{e_2^{(m)}}} := i\bar{\varepsilon}_{1m}, \quad \varepsilon_{2m} \sim \frac{i2\pi f h_m}{c_2^{(m)}} := i\bar{\varepsilon}_{2m}. \tag{36}
$$

Since $\cosh(ix) = \cos(x)$ and $\sinh(ix) = i\sin(x)$, the asymptotic values of elements of the transfer matrix $\boldsymbol{T}_m$ in (33) are

$$
\begin{aligned}
(T_m)_{11} &\sim \cos\bar{\varepsilon}_{2m}, & (T_m)_{21} &\sim -\frac{ic_2^{(m)}}{c}(\alpha_{21}^{(m)}\sin\bar{\varepsilon}_{1m} - \beta_{21}^{(m)}\sin\bar{\varepsilon}_{2m}),\\
(T_m)_{12} &\sim \frac{ic_2^{(m)}}{c}(\alpha_{12}^{(m)}\sin\bar{\varepsilon}_{1m} + \beta_{12}^{(m)}e_{3m}\sin\bar{\varepsilon}_{2m}), & (T_m)_{22} &\sim \cos\bar{\varepsilon}_{1m},\\
(T_m)_{13} &\sim \frac{-cc_{66}^{(m)}}{c_2^{(m)}}\sin\bar{\varepsilon}_{2m}, & (T_m)_{23} &\sim -\frac{ic_2^{(m)2}}{c^2c_{66}^{(m)}}\alpha_{23}(\cos\bar{\varepsilon}_{1m} - \cos\bar{\varepsilon}_{2m}),\\
(T_m)_{14} &\sim \frac{ic_2^{(m)2}}{c^2c_{66}^{(m)}}\alpha_{14}^{(m)}(\cos\bar{\varepsilon}_{1m} - \cos\bar{\varepsilon}_{2m}), & (T_m)_{24} &\sim \frac{-c_2^{(m)}}{cc_{66}^{(m)}}\alpha_{24}^{(m)}\sin\bar{\varepsilon}_{1m},\\
(T_m)_{31} &\sim \frac{cc_{66}^{(m)}}{c_2^{(m)}}\sin\bar{\varepsilon}_{2m}, & (T_m)_{32} &\sim ic_{66}^{(m)}\alpha_{32}^{(m)}(\cos\bar{\varepsilon}_{1m} - \cos\bar{\varepsilon}_{2m}),\\
(T_m)_{33} &= (T_m)_{11}, & (T_m)_{34} &\sim -\frac{ic_2^{(m)}}{c}(\alpha_{34}^{(m)}\sin\bar{\varepsilon}_{1m} + \beta_{34}^{(m)}\sin\bar{\varepsilon}_{2m}),\\
(T_m)_{41} &\sim ic_{66}^{(m)}\alpha_{41}^{(m)}(\cos\bar{\varepsilon}_{1m} - \cos\bar{\varepsilon}_{2m}), & (T_m)_{42} &\sim \frac{cc_{66}^{(m)}}{c_2^{(m)}}\alpha_{42}^{(m)}\sin\bar{\varepsilon}_{1m},\\
(T_m)_{43} &\sim -\frac{ic_2^{(m)}}{c}(\alpha_{43}^{(m)}\sin\bar{\varepsilon}_{1m} - \beta_{43}^{(m)}\sin\bar{\varepsilon}_{2m}), & (T_m)_{44} &= (T_m)_{22}
\end{aligned}
$$

with

$$\alpha_{12}^{(m)} = -\frac{\sqrt{e_2^{(m)}}}{1+e_3^{(m)}}, \qquad \beta_{12}^{(m)} = -\alpha_{32}^{(m)} = -\frac{e_3^{(m)}}{1+e_3^{(m)}}, \qquad \alpha_{14}^{(m)} = \beta_{34}^{(m)} = \frac{1}{1+e_3^{(m)}},$$

$$\alpha_{21}^{(m)} = \frac{e_2^{(m)}+e_3^{(m)}}{\sqrt{e_2^{(m)}}(e_2^{(m)}-1)}, \qquad \beta_{21}^{(m)} = \alpha_{23}^{(m)} = \frac{1+e_3^{(m)}}{e_2^{(m)}-1}, \qquad \alpha_{24}^{(m)} = \frac{1}{\sqrt{e_2^{(m)}}},$$

$$\alpha_{34}^{(m)} = \frac{e_3^{(m)}}{\sqrt{e_2^{(m)}}(1+e_3^{(m)})},$$

$$\alpha_{41}^{(m)} = \beta_{43}^{(m)} = \frac{e_2^{(m)}+e_3^{(m)}}{e_2^{(m)}-1}, \qquad \alpha_{42}^{(m)} = \sqrt{e_2^{(m)}}, \qquad \alpha_{43}^{(m)} = \frac{\sqrt{e_2^{(m)}}(1+e_3^{(m)})}{e_2^{(m)}-1}.$$

Acknowledgments

This research is funded by Vietnam National Foundation for Science and Technology Development (NAFOSTED) under grant number 107.02–2019.06.

References

[Bonnefoy-Claudet et al. 2006] S. Bonnefoy-Claudet, F. Cotton, P.-Y. Bard, M. Cornou, C. Ohrnberger, and M. Wathelet, "Robustness of the H/V ratio peak frequency to estimate 1D resonance frequency", pp. 361–370 in *Third International Symposium on the Effects of Surface Geology on Seismic Motion* (Grenoble, 2006), edited by P.-Y. Bard et al., Laboratoire Central des Ponts et Chaussées, Paris, 2006.

[Field and Jacob 1993] E. Field and K. Jacob, "The theoretical response of sedimentary layers to ambient seismic noise", *Geophys. Res. Lett.* **20**:24 (1993), 2925–2928.

[Field and Jacob 1995] E. H. Field and K. H. Jacob, "A comparison and test of various site-response estimation techniques, including three that are not reference-site dependent", *B. Seismol. Soc. Am.* **85**:4 (1995), 1127–1143.

[Haskell 1953] N. A. Haskell, "The dispersion of surface waves on multi-layered media", *B. Seismol. Soc. Am.* **43** (1953), 17–34.

[Junge et al. 2006] M. Junge, J. Qu, and L. J. Jacobs, "Relationship between Rayleigh wave polarization and state of stress", *Ultrasonics* **44**:3 (2006), 233–237.

[Lachetl and Bard 1994] C. Lachetl and P.-Y. Bard, "Numerical and theoretical investigations on the possibilities and limitations of Nakamura's technique", *J. Phys. Earth* **42**:5 (1994), 377–397.

[Lermo and Chávez-García 1994] J. Lermo and F. J. Chávez-García, "Are microtremors useful in site response evaluation?", *B. Seismol. Soc. Am.* **84**:5 (1994), 1350–1364.

[Lunedei and Malischewsky 2015] E. Lunedei and P. Malischewsky, "A review and some new issues on the theory of the H/V technique for ambient vibrations", pp. 371–394 in *Perspectives on European earthquake engineering and seismology*, vol. 2, edited by A. Ansal, Geotechnical, Geological and Earthquake Engineering **39**, Springer, 2015.

[Malischewsky and Scherbaum 2004] P. G. Malischewsky and F. Scherbaum, "Love's formula and H/V-ratio (ellipticity) of Rayleigh waves", *Wave Motion* **40**:1 (2004), 57–67.

[Nakamura 1989] Y. Nakamura, "Method for dynamic characteristics estimation of subsurface using microtremor on the ground surface", *Q. Report RTRI* **30**:1 (1989), 25–33.

[Thomson 1950] W. T. Thomson, "Transmission of elastic waves through a stratified solid medium", *J. Appl. Phys.* **21** (1950), 89–93.

[Ting 1996] T. C. T. Ting, *Anisotropic elasticity: theory and applications*, Oxford Engineering Science Series **45**, Oxford University, 1996.

[Tolstoy and Usdin 1953] I. Tolstoy and E. Usdin, "Dispersive properties of stratified elastic and liquid media: A ray theory", *Geophysics* **18** (1953), 844–870.

[Tuan and Trung 2016] T. T. Tuan and T. N. Trung, "The dispersion of Rayleigh waves in orthotropic layered half-space using matrix method", *Vietnam J. Mech.* **38**:1 (2016), 27–38.

[Tuan et al. 2011] T. T. Tuan, F. Scherbaum, and P. G. Malischewsky, "On the relationship of peaks and troughs of the ellipticity (H/V) of Rayleigh waves and the transmission response of single layer over half-space models", *Geophys. J. Int.* **184**:2 (2011), 793–800.

[Tuan et al. 2016a] T. T. Tuan, P. C. Vinh, P. Malischewsky, and A. Aoudia, "Approximate formula of peak frequency of H/V ratio curve in multilayered model and its use in H/V ratio technique", *Pure Appl. Geophys.* **173**:2 (2016), 487–498.

[Tuan et al. 2016b] T. T. Tuan, P. C. Vinh, M. Ohrnberger, P. Malischewsky, and A. Aoudia, "An improved formula of fundamental resonance frequency of a layered half-space model used in H/V ratio technique", *Pure Appl. Geophys.* **173**:8 (2016), 2803–2812.

[Vinh et al. 2015] P. C. Vinh, N. T. K. Linh, and V. T. N. Anh, "On a technique for deriving explicit transfer matrices of orthotropic layers", *Vietnam J. Mech.* **37**:4 (2015), 303–315.

[Vinh et al. 2016] P. C. Vinh, V. T. N. Anh, and N. T. K. Linh, "On a technique for deriving the explicit secular equation of Rayleigh waves in an orthotropic half-space coated by an orthotropic layer", *Waves Random Complex Media* **26**:2 (2016), 176–188.

[Vinh et al. 2019] P. C. Vinh, T. T. Tuan, L. T. Hue, V. T. N. Anh, T. T. T. Dung, N. T. K. Linh, and P. Malischewsky, "Exact formula for the horizontal-to-vertical displacement ratio of Rayleigh waves in layered orthotropic half-spaces", *J. Acoust. Soc. Am.* **146**:2 (2019), 1279–1289.

[Wang and Rajapakse 1994] Y. Wang and R. K. N. D. Rajapakse, "An exact stiffness method for elastodynamics of a layered orthotropic half-plane", *J. Appl. Mech.* **61**:2 (1994), 339–348.

Received 23 May 2019. Revised 27 Dec 2019. Accepted 29 Jan 2020.

TRUONG THI THUY DUNG: dungttt@hus.edu.vn
Faculty of Mathematics, Mechanics and Informatics, VNU University of Science, Vietnam, Hanoi, Vietnam

TRAN THANH TUAN: tranthanhtuan@hus.edu.vn
Faculty of Mathematics, Mechanics and Informatics, VNU University of Science, Vietnam, Hanoi, Vietnam

PHAM CHI VINH: pcvinh@gmail.com
Faculty of Mathematics, Mechanics and Informatics, VNU University of Science, Vietnam, Hanoi, Vietnam

GIANG KIEN TRUNG: trunggk@hus.edu.vn
Faculty of Physics, VNU University of Science, Vietnam, Hanoi, Vietnam

JOURNAL OF MECHANICS OF MATERIALS AND STRUCTURES
Vol. 15, No. 1, 2020
dx.doi.org/10.2140/jomms.2020.15.75

EFFECT OF NUMBER OF CROWNS ON THE CRUSH RESISTANCE IN OPEN-CELL STENT DESIGN

GIDEON PRAVEEN KUMAR, KEPING ZUO, LI BUAY KOH, CHI WEI ONG, YUCHENG ZHONG, HWA LIANG LEO, PEI HO AND FANGSEN CUI

Our group is developing novel preferential covered carotid stents aimed at preventing friable parts from atherosclerotic plaques from dislodging into the cerebral blood flow, and also preserving external carotid artery (ECA) perfusion through slits on the membrane. Enhanced ECA flow rates can be achieved by designing bare metal stents with larger cells that can accommodate more slits for enhanced blood flow to the ECA where the stents have fewer crowns in the circumferential direction. The general perception is that the stent stiffness and thereby the crush resistance will decrease with fewer crowns in the circumferential direction. However, we observed the opposite effect. To study the effect of crown number on crush resistance of stents, finite element analysis (FEA) was used to evaluate the crush resistance of open-cell stent designs by varying the number of crowns. From FEA simulation results, it was found that the crush resistance of the open-cell stent design actually increases with fewer crowns. To verify this effect, three stent designs with different crown numbers were fabricated and subjected to crush resistance experimental testing. The experimental testing further confirmed the effect observed by FEA. Finally, a simplified analytical model was proposed to explain why the crush resistance of stent increases with a reduction in the number of stent crowns. From this study, we can infer that the stent's crush resistance increases with reduction in the number of stent crowns in the circumferential direction.

1. Introduction

Our group [Kabinejadian et al. 2013; 2015a; 2015b; Kumar et al. 2016] has been actively developing novel covered stents for preventing small friable parts of atherosclerotic plaques from dislodging into the cerebral blood circulation, and at the same time, preserving external carotid artery (ECA) blood flow. The device comprises of a bare metal stent coated with a biocompatible polymer membrane which has several arrays of cut slits. The main purpose of the slits on the covered membrane was to let blood through the membrane into ECA while confining the plaques along vessel wall and prevent them from dislodging. In one of our earlier in-vitro investigations [Kabinejadian et al. 2015a] we showed that our covered stent design is more efficient in emboli prevention than its corresponding bare metal stent, and at the same time, preserves more than 83% of the original flow of the ECA in carotid artery bifurcation models. Our group evaluated this covered stent design [Kabinejadian et al. 2013; 2015b] (with slit openings on ePTFE membrane) in various models of arteries with different arterial diameters, curvatures, and side-branch angles. We aimed to design new bare metal stents with bigger cell size which can provide higher ECA flow rates through enhanced perfusion to the side-branch as they can accommodate higher number of slits. Larger stent cell size thereby contributes to enhanced slit distribution on the membrane (and

Keywords: stent crown, nitinol, membrane, carotid, stent crush resistance finite element analysis.

thereby better side-branch flow preservation) and desirable crimpability [Kumar and Cui 2016; Kumar et al. 2014]. As part of our stent design-iteration process, we reduced the number of crowns of our open-cell stents in the circumferential direction to get bigger cells and put them through finite element analysis (FEA) to evaluate their crush resistance. Crush resistance can be defined as the ability of a stent to withstand crush loading and therefore prevention of stent collapse is crucial for stent development especially for superficial locations like carotid arteries [García et al. 2012; Timaran et al. 2011; Duerig and Wholey 2002] and peripheral indications as per Food and Drug Administration (FDA) standards [Dhruva et al. 2009; US Food and Drug Administration 2010]. The aim of this study is to evaluate the effect of the number of stent crowns in the circumferential direction on the stent crush resistance through the following steps: (a) analysis of this effect by FEA based modeling and simulation for three different stent designs; (b) fabrication of the stent designs followed by experimental compression tests; (c) providing some explanations with simplified analytical study.

2. Materials & methods

2.1. ***Stent design.*** In this study we took reference from the commercial stent E-Luminexx® stent (Bard Peripheral Vascular Inc., Tempe, AZ) to model the stent which has 12 crowns in the circumferential direction. Additionally, we designed two more stents by reducing their crown numbers to 9 and 6, respectively in the circumferential direction. Figure 1 shows the models of all the three stents. SOLIDWORKS (Dassault Systemes, MA) was used to model the stent geometries and ABAQUS (Dassault Systemes, MA) to conduct FEA. The stents had an outer diameter of 6 mm, a length of 40 mm and struts with uniform thickness of 0.15 mm. These are hybrid stents with combined [Timaran et al. 2011] open- and closed-cell sections (Figure 3). The open-cell sections improve flexibility and enhance stent-vessel conformability without injuring the vessel [Pierce et al. 2009; Carnelli et al. 2011; Tadros et al. 2012]. The closed-cell sections provide sufficient radial strength and in the case of lesions, to secure plaques and hold the plaque in position [Tadros et al. 2012; Hart et al. 2006; Bosiers et al. 2007]. The specifications of stent models considered in this study are given in Table 1. All the three stents were laser-cut from a nitinol tubes of 2.0 mm outer diameter (OD) and 0.18 mm thickness. They were then expanded and shape set using a cylindrical mandrel to 6 mm $\times$ 40 mm (OD $\times$ length) following which electropolishing was done to get a final strut thickness of 0.15 mm. The fabricated nitinol stents for testing are shown in Figure 4.

2.2. ***Material model.*** Nitinol has been used as a stent material as it possesses excellent properties like superelasticity, shape memory, corrosion resistance, biocompatibility, radiopacity, and fatigue resistance [Hansen 2008; Duerig et al. 1999]. When cooled to a very low temperature, nitinol transforms fully to martensite and becomes easily deformable and hence can be effortlessly crimped into a small catheter. When the stent is released into the artery, it recovers to its predetermined, original diameter when exposed to the body temperature which is higher than the Austenite finish (Af) temperature. The built-in Nitinol UMAT was used for our stent simulations. In this model [Auricchio and Taylor 1997; Auricchio et al. 1997] the total strain is the sum of the elastic, transformation and the plastic strain. The mechanical properties of nitinol used in this work are partly from our previous work [Kumar et al. 2013; 2014] and partly based on the information given by our stent fabrication partner and are shown in Table 2.

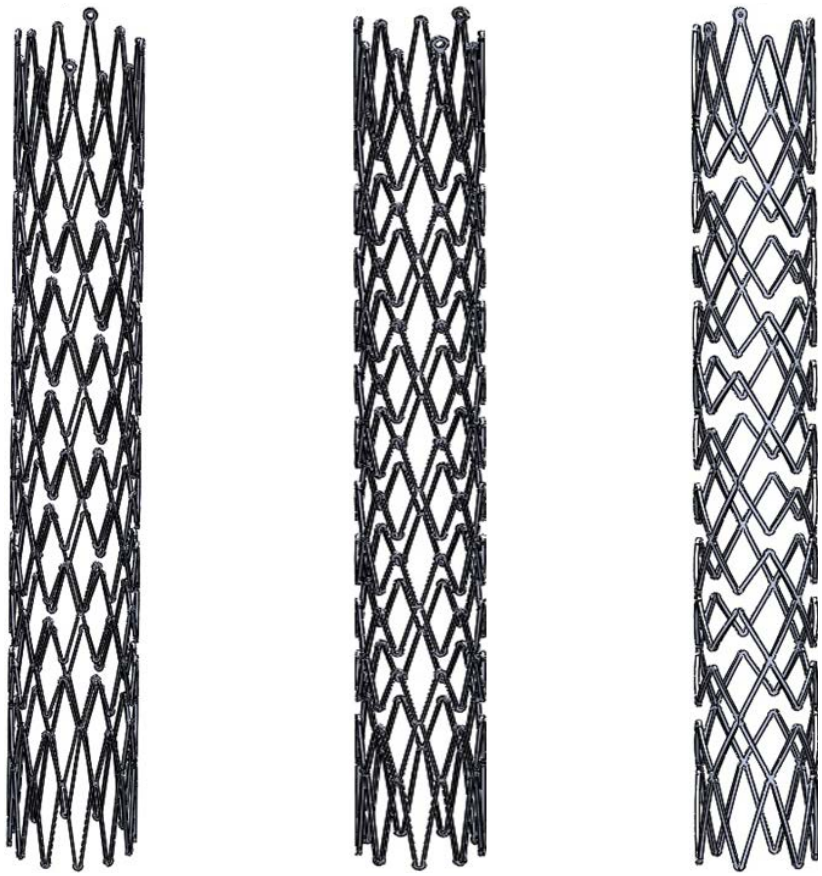

Figure 1. Stent designs investigated in the study: 12 crown design (left), 9 crown design (middle) and 6 crown design (right).

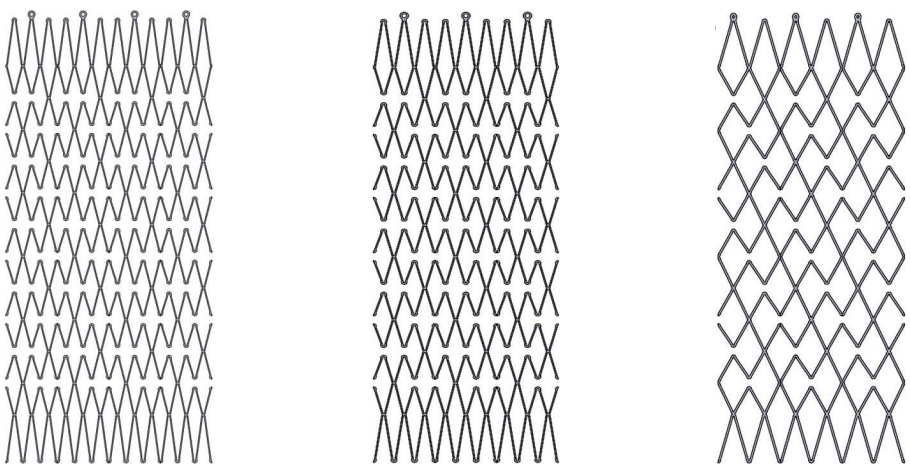

Figure 2. Stent designs with different crown numbers shown in their planar form: 12 crown design (left), 9 crown design (middle) and 6 crown design (right).

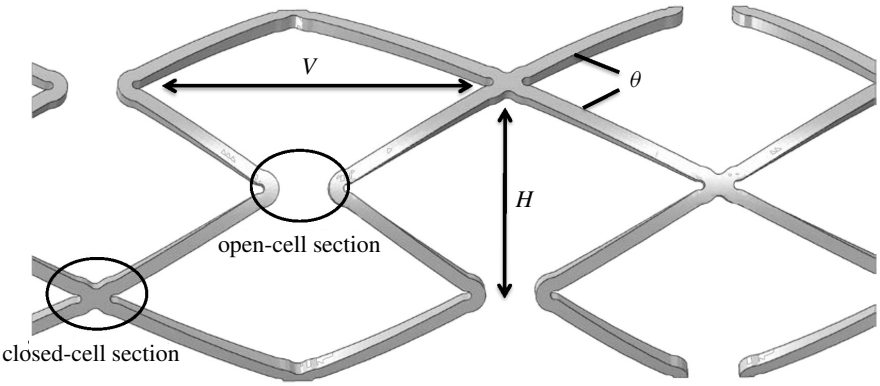

Figure 3. Representation of the stent cell specifications of the stents used in this work (V stands for the distance in axial direction, H the distance in circumferential direction and θ the inter-strut angle).

Figure 4. The three fabricated stents with varying crown numbers in the circumferential direction: 12 crown design (left), 9 crown design (middle) and 6 crown design (right).

stent	12 crown design	9 crown design	6 crown design
outer diameter, OD (mm)	6	6	6
length (mm)	40	40	40
number of crowns	12	9	6
vertical inter-strut distance, V (mm)	5	5	5
inter-crown distance, H (mm)	1.5	2.25	3
inter-strut angle, θ (degree)	21	33	45
strut thickness (mm)	0.15	0.15	0.15
strut width (mm)	0.15	0.15	0.15

Table 1. Specifications of stent models considered in this study.

variables	nitinol
Austenite elasticity, E_{A} (MPa)	40000
Austenite Poisson's ratio, ν_{A}	0.33
Martensite elasticity, E_{M} (MPa)	32000
Martensite Poisson's ratio, ν_{M}	0.33
transformation strain, ε^{l}	0.041
loading $(\delta\sigma/\delta T)_{\mathrm{l}}$ (MPa T^{-1})	6.7
start of transformation loading, $\sigma_{\mathrm{l}}^{\mathrm{s}}$ (MPa)	465
end of transformation loading, $\sigma_{\mathrm{l}}^{\mathrm{e}}$ (MPa)	480
reference temperature, T_0 (°C)	22
unloading, $(\delta\sigma/\delta T)_{\mathrm{u}}$	6.7
start of transformation unloading, $\sigma_{\mathrm{u}}^{\mathrm{s}}$ (MPa)	260
end of transformation unloading, $\sigma_{\mathrm{u}}^{\mathrm{e}}$ (MPa)	248
start of transformation stress in compression, $\sigma_{\mathrm{cl}}^{\mathrm{s}}$ (MPa)	−449
volumetric transformation strain, $\varepsilon_{\mathrm{v}}^{\mathrm{l}}$	0.041
Af temperature (°C)	37
strain limit, $\varepsilon_{\max}$	10%

Table 2. Nitinol material properties.

2.3. ***Computational simulation.*** The ABAQUS/Standard (v. 2017) FEA package was used to carry out the nonlinear FE analysis. The stents were modeled with eight-node linear brick elements with reduced integration and hourglass control. To make sure all the results were independent of further mesh refinements, mesh sensitivity studies were conducted. Mesh convergence was achieved by sequentially increasing the number of elements until there was no appreciable difference in the stress at the end of the analysis. The final mesh of the 6 crown, 9 crown and 12 crown stents comprised of 43,373, 72,481 and 103,845 elements, respectively. For the flat plate compression test, similar to an earlier work [García et al. 2012], each stent was placed between two rigid plates separated by a distance of 6.5 mm. The stents were then compressed by imposing a displacement of 3 mm to the upper plate, similar to the experimental test (described in Section 2.4), while constraining the lower plate in all degrees of freedom

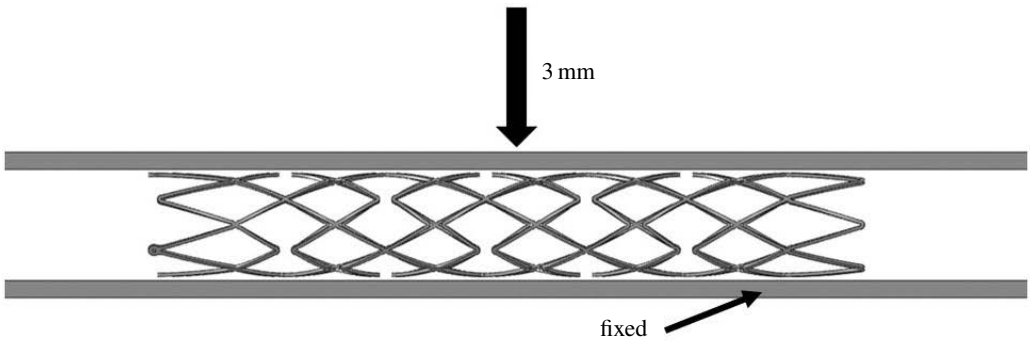

Figure 5. Boundary conditions used in the simulation for radial compression. The lower plate if fixed in to prevent rigid body translation in all three directions.

(see Figure 5). Contact between the plates and the stents was modeled with frictionless tangential and hard normal contact. A penalty interaction property was used to enforce impermeable boundaries. The reaction force after full loading was recorded.

2.4. ***Experimental setup.*** All tests were performed using an Instron 3345 machine (Instron, 825 University Avenue, Norwood, MA 02062, USA) at 20 °C–22 °C. For radial compression test which is similar to the experimental test [Petrini et al. 2005] developed to estimate the radial force of stents, the loads were applied over the full length of the stents with a plate 50 mm in diameter. All stents were placed between two flat plates. No external supports were used for the stents. Three samples were tested for each design (6, 9 and 12 crowns). For the individual stents, the test was repeated three times rotating the stent twice by 120° to negate the possible influence of the rotational orientation of stent. A displacement rate of 20 mm/min was used to start the test until a displacement of 3 mm was achieved. The force and displacement data were recorded using the Instron Bluehill 3 modular applications software for both loading and unloading processes. The experimental setup for the radial compression test is shown in Figure 6.

3. Results

3.1. ***Simulation.*** The results obtained from simulation for the three flat plate compression tests are presented in Figure 7. The results show that the force required to produce a displacement of 3 mm increases with a reduction in the number of crowns. These forces are 5.13 N, 1.03 N and 0.77 N for 6 crown, 9 crown and 12 crown stents, respectively. From the results it can be inferred that the 6 crown stent shows higher crush resistance among the three designs in comparison to the other designs whose crown number increases.

3.2. ***Experiment.*** Response to experimental compression tests is presented in Figure 8. The curves in the experimental results plots represent the mean of the three individual test data for each design. From the experiment, it is evident that the crush resistance of the 6 crown stent is the highest followed by the 9 crown and 12 crown stents. This trend is in agreement with the inference from our simulation results.

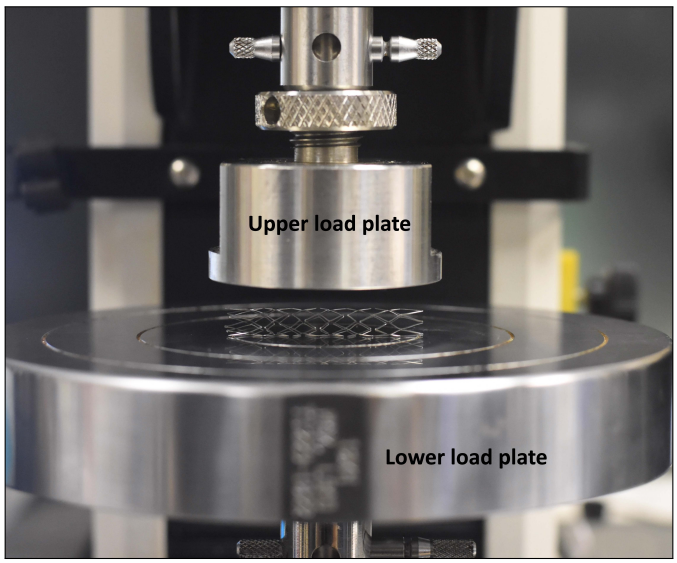

Figure 6. Experimental setup for radial compression test.

4. Discussion

From the simulation and experimental results it could be inferred that even though the metal density reduces as the crown number is reduced in the circumferential direction, surprisingly and contrary to the common observation, the crush resistance of stents increases. There could be a couple of reasons for this

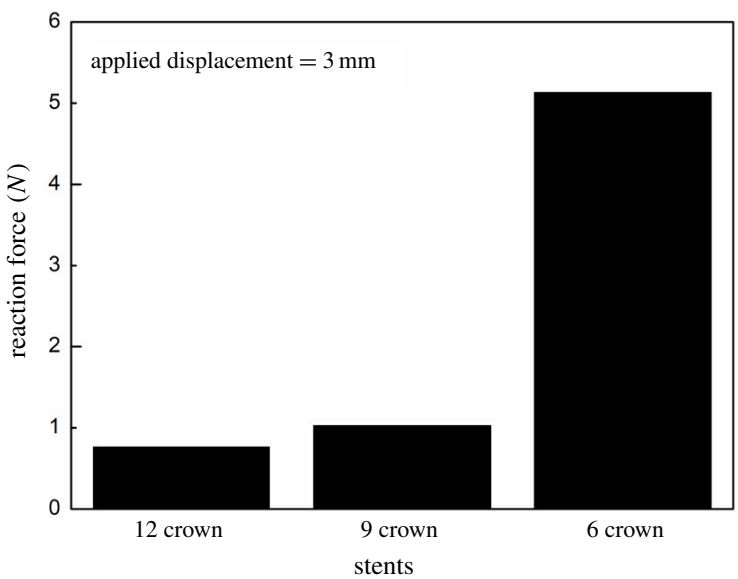

Figure 7. Results of the FEA study: 6 crown stent having maximum reaction force among the three designs in agreement with our experimental results.

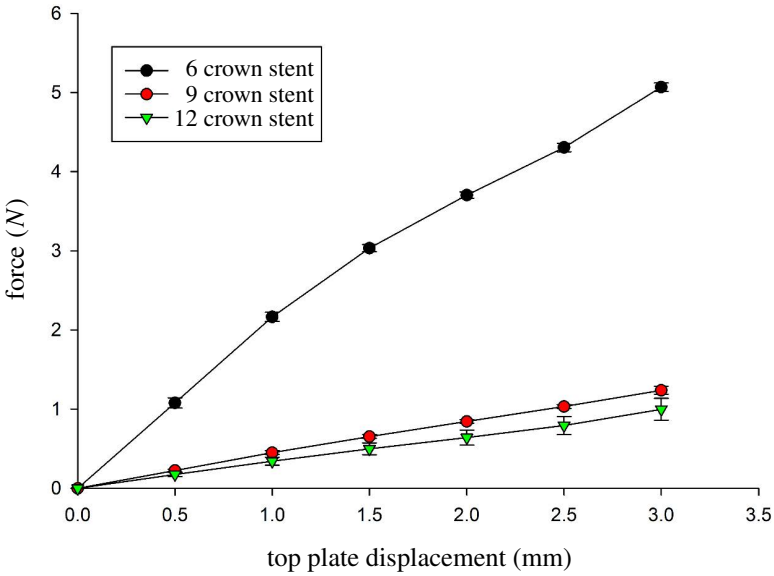

Figure 8. Results of the Experimental study. Force-displacement curve for the radial compression loading of the three stents.

trend. Firstly, when the number of crowns keeps getting reduced in the circumferential direction, there is also a proportional reduction in the open-cell sections which causes the stent to have high stiffness [Carnelli et al. 2011; Moore 2012; Hijazi et al. 2013] as open-cells offer lower stiffness. Secondly, the relationship between crown angle and the crush resistance contributing to the above trend has been explored below in details.

Each stent cell is made up of three basic elements: strut, link, and crown [Alaimo et al. 2017] responsible for crush resistance and crimpability. To understand the increase in the crush resistance with a reduction in the number of crowns, we can consider the stent crown as a simple ring as shown in Figure 9. The zoomed-in part shows one-half of the crown that is considered as a simple beam for the below analytical model.

Let H be the ring height, L the total length, n the number of rings, $\theta = (\text{crown angle})/2$. To obtain the stiffness, a force F is applied at two ends and thereby we have

$$\Delta D = \sum_{i=1}^{2n} \frac{F \cdot \cos\theta}{k_b} \cdot \cos\theta = \frac{F}{k_b} 2n \cos^2\theta, \tag{1}$$

where ΔD is the total displacement in the direction of the force F, and k_b is the beam stiffness. We can write the beam stiffness as

$$k_b = \frac{3EI}{l^3} = \frac{3EI}{(H/\cos\theta)^3},$$

where EI is the bending rigidity of stent strut. Thus the total stiffness k_{total} is

$$k_{\text{total}} = F/\Delta D = C(\cos\theta/n), \tag{2}$$

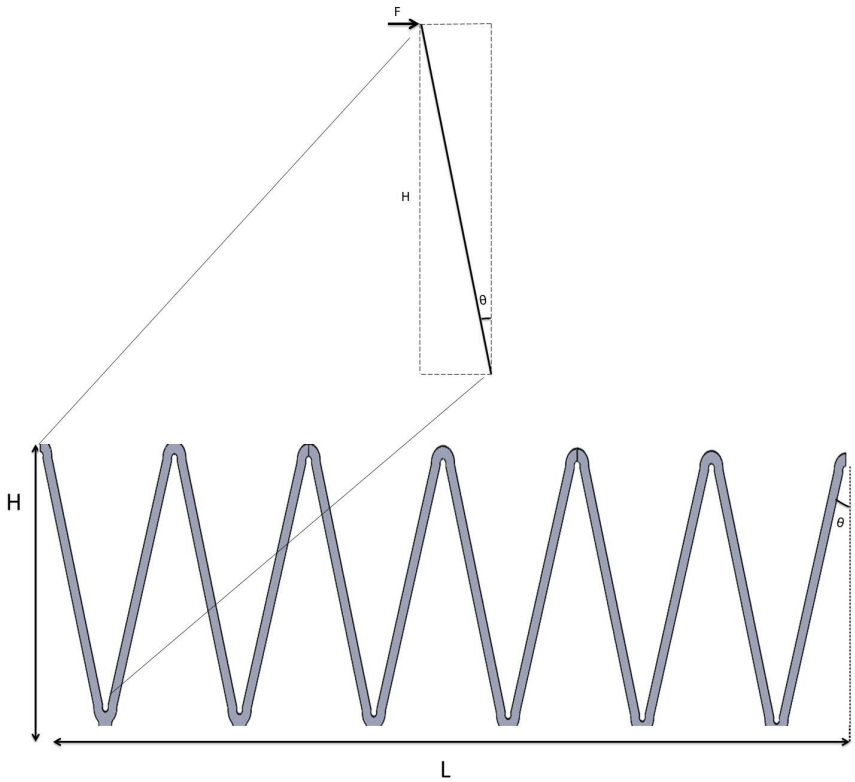

Figure 9. Stent cells being considered as a simple ring to study its stiffness behavior in relation to the number of crowns.

where $C = 3EI/2H^3$. The stiffness can be further expressed as

$$k_{\text{total}} = C \cdot \frac{1}{\sqrt{1 + (L/2nH)^2}} \cdot \frac{1}{n} = C \frac{1}{\sqrt{n^2 + L^2/4H^2}}. \tag{3}$$

Equation (3) shows that when the number of crowns increases, the crush resistance decreases due to a reduction in the total stiffness. When the number of crowns increases, the deformation per crown decreases for a given deformation, thus the load to produce the given total deformation reduces as illustrated in (3). The value of k_{total} as a function of n is plotted in Figure 10, which directly illustrates the relationship between the total stiffness (which determines the crush resistance) and the number of crowns.

5. Conclusion

In this paper the effect of number of crowns on the crush resistance of open-cell stents was studied using FEA and validated through experiment and analytical model. The conclusion made from the study is that the number of crowns in the circumferential direction was inversely proportional to crush resistance of open-cell stents. This is of particular importance especially when stents are designed for superficial locations like the carotid artery where high crush resistance is desirable due to the possibility of the application of external loads. So designing stents with lesser number of open-cells will render

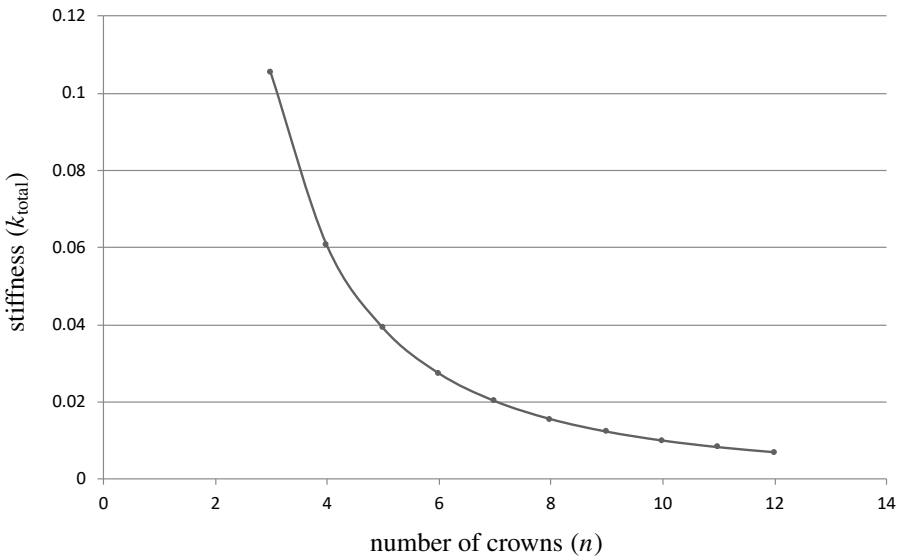

Figure 10. Total stiffness vs number of crowns with the value of k_{total} as a function of n according to (3).

them suitable for application in superficial blood vessels. This work will provide a guideline for stent design in different applications, especially at superficial locations such as carotid and femoral arteries and peripheral indications as per FDA standards where the stents are usually subjected to external loadings during the human activities of daily living.

Acknowledgements

This research is supported by the Singapore Ministry of Health's National Medical Research Council under its Clinician Scientist – Individual Research Grant (CS-IRG) Program (grant number NMRC/CIRG/1385/2014), A*STAR's BEP Program (SERC grant number 141 148 0016) and Singapore-China Joint Research Programme (grant number 1610500025).

References

[Alaimo et al. 2017] G. Alaimo, F. Auricchio, M. Conti, and M. Zingales, "Multi-objective optimization of nitinol stent design", *Med. Eng. Phys.* **47** (2017), 13–24.

[Auricchio and Taylor 1997] F. Auricchio and R. L. Taylor, "Shape-memory alloys: modelling and numerical simulations of the finite-strain superelastic behavior", *Comput. Methods Appl. Mech. Eng.* **143**:1-2 (1997), 175–194.

[Auricchio et al. 1997] F. Auricchio, R. L. Taylor, and J. Lubliner, "Shape-memory alloys: macromodelling and numerical simulations of the superelastic behavior", *Comput. Methods Appl. Mech. Eng.* **146**:3-4 (1997), 281–312.

[Bosiers et al. 2007] M. Bosiers, G. de Donato, K. Deloose, J. Verbist, P. Peeters, F. Castriota, A. Cremonesi, and C. Setacci, "Does free cell area influence the outcome in carotid artery stenting?", *Eur. J. Vasc. Endovasc. Surg.* **33**:2 (2007), 135–141.

[Carnelli et al. 2011] D. Carnelli, G. Pennati, T. Villa, L. Baglioni, B. Reimers, and F. Migliavacca, "Mechanical properties of open-cell, self-expandable shape memory alloy carotid stents", *Artif. Organs* **35**:1 (2011), 74–80.

[Dhruva et al. 2009] S. S. Dhruva, L. A. Bero, and R. F. Redberg, "Strength of study evidence examined by the FDA in premarket approval of cardiovascular devices", *JAMA* **302**:24 (2009), 2679–2685.

[Duerig and Wholey 2002] T. W. Duerig and M. Wholey, "A comparison of balloon- and self-expanding stents", *Minimal. Invasiv. Thera. All. Technol.* **11**:4 (2002), 173–178.

[Duerig et al. 1999] T. Duerig, A. Pelton, and D. Stöckel, "An overview of nitinol medical applications", *Mater. Sci. Eng. A* **273-275** (1999), 149–160.

[García et al. 2012] A. García, E. Peña, and M. Martínez, "Influence of geometrical parameters on radial force during self-expanding stent deployment. Application for a variable radial stiffness stent", *J. Mech. Behav. Biomed. Mater.* **10** (2012), 166–175.

[Hansen 2008] D. C. Hansen, "Metal corrosion in the human body: the ultimate bio-corrosion scenario", *Interface* **17** (2008), 31–34.

[Hart et al. 2006] J. P. Hart, P. Peeters, J. Verbist, K. Deloose, and M. Bosiers, "Do device characteristics impact outcome in carotid artery stenting?", *J. Vasc. Surg.* **44**:4 (2006), 725–730.

[Hijazi et al. 2013] Z. M. Hijazi, T. Feldman, J. Cheatham, and H. Sievert (editors), *Complications during percutaneous interventions for congenital and structural heart disease*, CRC Press, 2013.

[Kabinejadian et al. 2013] F. Kabinejadian, F. Cui, Z. Zhang, P. Ho, and H. L. Leo, "A novel carotid covered stent design: *in vitro* evaluation of performance and influence on the blood flow regime at the carotid artery bifurcation", *Ann. Biomed. Eng.* **41**:9 (2013), 1990–2002.

[Kabinejadian et al. 2015a] F. Kabinejadian, F. Cui, B. Su, A. Danpinid, P. Ho, and H. L. Leo, "Effects of a carotid covered stent with a novel membrane design on the blood flow regime and hemodynamic parameters distribution at the carotid artery bifurcation", *Med. Biol. Eng. Comput.* **53**:2 (2015), 165–177.

[Kabinejadian et al. 2015b] F. Kabinejadian, M. Kaabi Nezhadian, F. Cui, P. Ho, and H. L. Leo, "Covered stent membrane design for treatment of atheroembolic disease at carotid artery bifurcation and prevention of thromboembolic stroke: an in vitro experimental study", *Artif. Organs* **40**:2 (2015), 159–168.

[Kumar and Cui 2016] G. P. Kumar and F. Cui, "Stent design parameters and crimpability", *Int. J. Cardiol.* **223** (2016), 552–553.

[Kumar et al. 2013] G. P. Kumar, F. Cui, A. Danpinid, B. Su, J. K. F. Hon, and H. L. Leo, "Design and finite element-based fatigue prediction of a new self-expandable percutaneous mitral valve stent", *Comput.-Aided Des.* **45**:10 (2013), 1153–1158.

[Kumar et al. 2014] G. P. Kumar, F. Cui, H. Q. Phang, B. Su, H. L. Leo, and J. K. F. Hon, "Design considerations and quantitative assessment for the development of percutaneous mitral valve stent", *Med. Eng. Phys.* **36**:7 (2014), 882–888.

[Kumar et al. 2016] G. P. Kumar, F. Kabinejadian, J. Liu, P. Ho, H. L. Leo, and F. Cui, "Simulated bench testing to evaluate the mechanical performance of new carotid stents", *Artif. Organs* **41**:3 (2016), 267–272.

[Moore 2012] W. S. Moore, *Vascular and endovascular surgery: a comprehensive review expert consult*, Elsevier Health Sciences, 2012.

[Petrini et al. 2005] L. Petrini, F. Migliavacca, P. Massarotti, S. Schievano, G. Dubini, and F. Auricchio, "Computational studies of shape memory alloy behavior in biomedical applications", *J. Biomech. Eng.* (*ASME*) **127**:4 (2005), 716–725.

[Pierce et al. 2009] D. S. Pierce, E. B. Rosero, J. G. Modrall, B. Adams-Huet, R. J. Valentine, G. P. Clagett, and C. H. Timaran, "Open-cell versus closed-cell stent design differences in blood flow velocities after carotid stenting", *J. Vasc. Surg.* **49**:3 (2009), 602–606.

[Tadros et al. 2012] R. O. Tadros, C. T. Spyris, A. G. Vouyouka, C. Chung, P. Krishnan, M. W. Arnold, M. L. Marin, and P. L. Faries, "Comparing the embolic potential of open and closed cell stents during carotid angioplasty and stenting", *J. Vasc. Surg.* **56**:1 (2012), 89–95.

[Timaran et al. 2011] C. H. Timaran, E. B. Rosero, A. Higuera, A. Ilarraza, J. G. Modrall, and G. P. Clagett, "Randomized clinical trial of open-cell vs closed-cell stents for carotid stenting and effects of stent design on cerebral embolization", *J. Vasc. Surg.* **54**:5 (2011), 1310–1316.e1.

[US Food and Drug Administration 2010] US Food and Drug Administration, "Non-clinical engineering tests and recommended labeling for intravascular stents and associated delivery systems", Guidance for industry and FDA staff, U.S. Department of Health and Human Services, 2010, Available at https://www.fda.gov/media/71639/download.

Received 11 Jun 2019. Revised 16 Dec 2019. Accepted 20 Dec 2019.

GIDEON PRAVEEN KUMAR: vijayagpk@ihpc.a-star.edu.sg
Institute of High Performance Computing, Singapore 138632, Singapore

KEPING ZUO: keping.zuo@gmail.com
National University of Singapore, Singapore 119077, Singapore

LI BUAY KOH: maykoh88@gmail.com
National University of Singapore, Singapore 119077, Singapore

CHI WEI ONG: bieocw@nus.edu.sg
National University of Singapore, Singapore 119077, Singapore

YUCHENG ZHONG: zhong_yucheng@ihpc.a-star.edu.sg
Institute of High Performance Computing, Singapore 138632, Singapore

HWA LIANG LEO: bielhl@nus.edu.sg
National University of Singapore, Singapore 119077, Singapore

PEI HO: pei_ho@nuhs.edu.sg
National University of Singapore, Singapore 119077, Singapore

FANGSEN CUI: cuifs@ihpc.a-star.edu.sg
Institute of High Performance Computing, Singapore 138632, Singapore

JOURNAL OF MECHANICS OF MATERIALS AND STRUCTURES
Vol. 15, No. 1, 2020
dx.doi.org/10.2140/jomms.2020.15.87

A DIELECTRIC BREAKDOWN MODEL FOR AN INTERFACE CRACK IN A PIEZOELECTRIC BIMATERIAL

YURI LAPUSTA, ALLA SHEVELEVA, FRÉDÉRIC CHAPELLE AND VOLODYMYR LOBODA

A mode III electrically conductive crack between two piezoelectric semi-infinite spaces under the action of anti-plane mechanical loading and in-plane electrical field parallel to the crack faces is considered. All electromechanical quantities are presented as piecewise analytic vector functions. The problem is solved analytically, revealing an oscillating singularity at the crack tips in the stress and electric fields. To eliminate the electric field singularity the dielectric breakdown (DB) model is applied. According to this model, the electric field along some zone of the crack continuation is initially assumed to be equal to the electric breakdown strength and the length of this zone remains still unknown. A nonhomogeneous combined Dirichlet–Riemann boundary value problem for the crack with DB zone is formulated. An exact analytical solution of this problem is presented and the DB zone length is found from the electric field finiteness at the end point of this zone. The simple transcendental equation with respect to DB zone length is solved numerically and all required electromechanical quantities are found in closed analytical form. The DB model for a crack in a homogeneous material is also considered and compared with known results.

1. Introduction

Ferroelectric ceramics are widely used in piezoelectric devices, such as sensors, resonators and actuators, due to their distinctive piezoelectric propertyies. However, ferroelectric ceramics are brittle and susceptible to cracking at all scales. Their premature failure can be caused by high mechanical stresses or electrical fields. Therefore, it is very important to study the fracture behavior of piezoelectric ceramics under the combined action of mechanical stresses and electrical fields.

Consideration of a crack within the framework of linear fracture mechanics initiates singularities at the crack tips in stresses, deformations and, for piezoelectric materials, in electrical displacements and electric fields. Different ways of removing the crack tip singularities for cracks in homogeneous isotropic materials and modeling of fracture processes were initiated in [Leonov and Panasyuk 1959; Dugdale 1960; Barenblatt 1962].

Important problems of statics and dynamics of structural interfaces, which can be used for an interface crack investigation, were considered in [Bigoni and Movchan 2002; Bertoldi et al. 2007]. The mathematical modeling of the interface crack propagation was carried out in [Peride et al. 2009]. Mode III fracture propagation in prestressed and prepolarized piezoelectric crystals was studied in [Craciun et al. 2004]. Different crack models for interface cracks in piezoelectric bimaterials and in dielectric/piezoelectric ones were investigated in [Li and Chen 2008; Govorukha and Kamlah 2010; Sladek et al. 2012; Xu et al. 2015].

The way of eliminating the electrical displacement singularity for an electrically insulated crack in a homogeneous piezoelectric material was suggested in [Gao and Barnett 1996], due to the development

Keywords: dielectric breakdown model, electrically conductive interface crack, piezoelectric material.

of a polarization saturation (PS) model. It was assumed, similarly to [Dugdale 1960], that the electrical polarization reaches a saturation limit in a line segment in front of the crack. The length of this segment was found from the condition of finiteness of electrical displacement at the end point of the segment. The energy release rate (ERR) for this model was analyzed in [Gao et al. 1997]. A PS model for an electrically permeable crack was studied in [Ru and Mao 1999]. The saturation condition effects on the near-tip field and on the stress intensity factor, as well as the influence of the crack orientation with respect to the electrical polarization direction was investigated in [Ru 1999; Wang 2000] for an electrically impermeable crack. The electric saturation zone of circular and elliptical form in piezoelectric and electrostrictive materials was investigated in [Jeong et al. 2004; Beom et al. 2006a; 2006b]. Different variants of saturation zone for cracks in an interlayer between piezoelectric materials were studied in [Lapusta and Loboda 2009; Loboda et al. 2008; 2010]. A penny-shaped crack in an infinite piezoelectric and thermo-piezo-elastic medium was analyzed with use of PS model in [Fan et al. 2012; Li et al. 2017]. The electric-magnetic polarization saturation model is developed in [Zhao et al. 2015] for the numerical analysis of a nonlinear interfacial crack in three-dimensional transversely isotropic magneto-electro-elastic bimaterial.

The dielectric breakdown (DB) model was developed in [Zhang and Gao 2004], and used to study the problem of an impermeable crack in a piezoelectric material in [Zhang 2004; Zhang et al. 2005]. According to this model the electric field is assumed to be constant and equal to the dielectric breakdown strength in a strip ahead of the crack tip. For a conductive crack the DB model was developed in [Gao et al. 2006] and for a finite sized body it was applied in [Fan et al. 2009] using the boundary element method. The DB model was generalized to the investigation of a conductive crack in an electrostrictive solid in [Zhang and Gao 2012]. Electric and magnetic polarization saturation and breakdown models for penny shaped-cracks in magnetoelectroelastic media were developed in [Zhao et al. 2013]. A semipermeable penny-shaped crack in a piezoelectric media was studied in [Zhao et al. 2016] with use of the DB model. A comparison between the PS and DB models for a penny-shaped cracks in three-dimensional piezoelectric media was performed by [Fan et al. 2014].

It is worth mentioning that all results obtained in the framework of the DB model are related to cracks in homogeneous piezoelectric materials. To the authors' knowledge, no analytical investigations concerning this model have been presented for interface cracks in piezoelectric, piezoelectromagnetic or electrostrictive solids. This can be explained by complexity of the mathematical problem arising in this case. In the present paper the dielectric breakdown model is applied for the first time to the investigation of an interface crack in a piezoelectric bimaterial under anti-plane mechanical and inplane electric loadings. The problem is reduced to the nonhomogeneous combined Dirichlet–Riemann boundary value problem with a special right side. Although this problem appears mathematically more complicated than the Riemann–Hilbert problem, an exact analytical solution is found for an arbitrary length of DB zone. The actual length of this zone is obtained from the condition of electric field finiteness. All required electromechanical quantities are presented in analytical form.

2. Basic equations and motivation for DB model formulation

For a piezoelectric material the relationship between the main electromechanical characteristics are defined by the relations [Parton and Kudryavtsev 1988]

$$\sigma_{ij} = c_{ijks}\varepsilon_{ks} - e_{sij}E_s, \quad D_i = e_{iks}\varepsilon_{ks} + \alpha_{is}E_s,$$

where σ_{ij}, ε_{ij} are the components of stress and strain tensor; D_i, E_i are the components of the electric induction and the electric field, c_{ijks}, e_{sij} are elastic and piezoelectric constants and α_{is} are dielectric constants.

The equilibrium equations in the absence of body forces and free charges are:

$$\sigma_{ij,j} = 0, \quad D_{i,i} = 0.$$

The expressions for the deformation and electric field have the form:

$$\varepsilon_{ij} = \tfrac{1}{2}(u_{i,j} + u_{j,i}), \quad E_i = -\phi_{,i},$$

where u_i are the components of the displacement vector and ϕ is the electric potential.

For the anti-plane mechanical loading and in-plane electric loading assuming the material is transversely isotropic with the poling direction parallel to the x_3-axis one has

$$u_1 = u_2 = 0, \quad u_3 = u_3(x_1, x_2), \quad \phi = \phi(x_1, x_2).$$

Then the constitutive relations can be written in the form

$$\begin{Bmatrix} \sigma_{3i} \\ D_i \end{Bmatrix} = \boldsymbol{R} \begin{Bmatrix} u_{3,i} \\ \phi_{,i} \end{Bmatrix}, \tag{1}$$

where $i = 1, 2$ and $\boldsymbol{R} = \begin{bmatrix} c_{44} & e_{15} \\ e_{15} & -\alpha_{11} \end{bmatrix}$.

The functions u_3 and ϕ satisfy the equations $\Delta u_3 = 0$, $\Delta\phi = 0$; i.e., they are harmonic. Therefore, we present them in the form

$$\boldsymbol{u} = \begin{Bmatrix} u_3 \\ \phi \end{Bmatrix} = 2\,\mathrm{Re}\,\boldsymbol{\Phi}(z) = \boldsymbol{\Phi}(z) + \bar{\boldsymbol{\Phi}}(\bar{z}), \tag{2}$$

where $\boldsymbol{\Phi}(z) = [\Phi_1(z), \Phi_2(z)]^T$ is an arbitrary analytic vector function of the complex variable $z = x_1 + ix_2$ and an upper bar means complex conjugation.

Introducing the vectors

$$\boldsymbol{v}' = [u_3', D_2]^T, \quad \boldsymbol{P} = [\sigma_{32}, -E_1]^T, \tag{3}$$

and substituting (2) in (1) we obtain

$$\boldsymbol{v}' = \boldsymbol{A}\boldsymbol{\Phi}'(z) + \bar{\boldsymbol{A}}\bar{\boldsymbol{\Phi}}'(\bar{z}), \tag{4}$$

$$\boldsymbol{P} = \boldsymbol{B}\boldsymbol{\Phi}'(z) + \bar{\boldsymbol{B}}\bar{\boldsymbol{\Phi}}'(\bar{z}), \tag{5}$$

where

$$\boldsymbol{A} = \begin{bmatrix} 1 & 0 \\ Q_{21} & Q_{22} \end{bmatrix}, \quad \boldsymbol{B} = \begin{bmatrix} Q_{11} & Q_{12} \\ 0 & 1 \end{bmatrix}, \quad \boldsymbol{Q} = i\boldsymbol{R}.$$

Suppose further that the plane (x_1, x_2) is composed of two half-planes $x_1 > 0$ and $x_2 < 0$. The presentation (4), (5) can be written for regions $x_1 > 0$ and $x_2 < 0$ in the form

$$\boldsymbol{v}^{(m)} = \boldsymbol{A}^{(m)}\boldsymbol{\Phi}^{(m)}(z) + \bar{\boldsymbol{A}}^{(m)}\bar{\boldsymbol{\Phi}}^{(m)}(\bar{z}), \quad \boldsymbol{P}^{(m)} = \boldsymbol{B}^{(m)}\boldsymbol{\Phi}'^{(m)}(z) + \bar{\boldsymbol{B}}^{(m)}\bar{\boldsymbol{\Phi}}'^{(m)}(\bar{z}), \tag{6}$$

where $m = 1$ for the upper region and $m = 2$ for the lower one; $\boldsymbol{A}^{(m)}$ and $\boldsymbol{B}^{(m)}$ are the matrices $\boldsymbol{A}$ and $\boldsymbol{B}$ for the regions 1 and 2, respectively; $\boldsymbol{\Phi}^{(m)}(z)$ are arbitrary vector functions, analytic in the regions 1 and 2, respectively. Next we require that the equality $\boldsymbol{P}^{(1)} = \boldsymbol{P}^{(2)}$ holds true on the entire axis x_1. Then it follows from (6) that

$$\boldsymbol{B}^{(1)}\boldsymbol{\Phi}'^{(1)}(x_1 + i0) + \bar{\boldsymbol{B}}^{(1)}\bar{\boldsymbol{\Phi}}'^{(1)}(x_1 - i0) = \boldsymbol{B}^{(2)}\boldsymbol{\Phi}'^{(2)}(x_1 - i0) + \bar{\boldsymbol{B}}^{(2)}\bar{\boldsymbol{\Phi}}'^{(2)}(x_1 + i0). \tag{7}$$

Here $F(x_1 \pm i0)$ designates the limit value of a function $F(z)$ at $x_2 \to 0$ from above or below of the x_1-axis, respectively. The equation (7) can be rewritten as

$$\boldsymbol{B}^{(1)}\boldsymbol{\Phi}'^{(1)}(x_1 + i0) - \bar{\boldsymbol{B}}^{(2)}\bar{\boldsymbol{\Phi}}'^{(2)}(x_1 + i0) = \boldsymbol{B}^{(2)}\boldsymbol{\Phi}'^{(2)}(x_1 - i0) - \bar{\boldsymbol{B}}^{(1)}\bar{\boldsymbol{\Phi}}'^{(1)}(x_1 - i0).$$

The left and right sides of the last equation can be considered as the boundary values of the functions

$$\boldsymbol{B}^{(1)}\boldsymbol{\Phi}'^{(1)}(z) - \bar{\boldsymbol{B}}^{(2)}\bar{\boldsymbol{\Phi}}'^{(2)}(z) \quad \text{and} \quad \boldsymbol{B}^{(2)}\boldsymbol{\Phi}'^{(2)}(z) - \bar{\boldsymbol{B}}^{(1)}\bar{\boldsymbol{\Phi}}'^{(1)}(z), \tag{8}$$

which are analytic in the upper and lower half-planes, respectively. But it means that there is a function $\boldsymbol{M}(z)$, which is equal to the mentioned functions in each half-plane and is analytic in the entire plane.

Assuming that $\boldsymbol{M}(z)|_{z\to\infty} \to 0$, on the basis of the Liouville theorem we find that each of the functions (8) is equal to 0 for any z from the corresponding half-plane. Hence, we obtain

$$\bar{\boldsymbol{\Phi}}'^{(2)}(z) = (\bar{\boldsymbol{B}}^{(2)})^{-1}\boldsymbol{B}^{(1)}\boldsymbol{\Phi}'^{(1)}(z) \quad \text{for } x_2 > 0, \tag{9}$$

$$\bar{\boldsymbol{\Phi}}'^{(1)}(z) = (\bar{\boldsymbol{B}}^{(1)})^{-1}\boldsymbol{B}^{(2)}\boldsymbol{\Phi}'^{(2)}(z) \quad \text{for } x_2 < 0. \tag{10}$$

Further, we find the jump in the vector function

$$\langle \boldsymbol{v}'(x_1)\rangle = \boldsymbol{v}'^{(1)}(x_1 + i0) - \boldsymbol{v}'^{(2)}(x_1 - i0), \tag{11}$$

when passing through the interface. From $(6)_1$ we determine

$$\boldsymbol{v}'^{(m)}(z) = \boldsymbol{A}^{(m)}\boldsymbol{\Phi}'^{(m)}(z) + \bar{\boldsymbol{A}}^{(m)}\bar{\boldsymbol{\Phi}}'^{(m)}(\bar{z}),$$

or

$$\boldsymbol{v}'^{(m)}(x_1 \pm i0) = \boldsymbol{A}^{(m)}\boldsymbol{\Phi}'^{(m)}(x_1 \pm i0) + \bar{\boldsymbol{A}}^{(m)}\bar{\boldsymbol{\Phi}}'^{(m)}(x_1 \mp i0);$$

substituting in (11), one gets

$$\langle \boldsymbol{v}'(x_1)\rangle = \boldsymbol{A}^{(1)}\boldsymbol{\Phi}'^{(1)}(x_1 + i0) + \bar{\boldsymbol{A}}^{(1)}\bar{\boldsymbol{\Phi}}'^{(1)}(x_1 - i0) - \boldsymbol{A}^{(2)}\boldsymbol{\Phi}'^{(2)}(x_1 - i0) - \bar{\boldsymbol{A}}^{(2)}\bar{\boldsymbol{\Phi}}'^{(2)}(x_1 + i0).$$

Finding further $\boldsymbol{\Phi}'^{(2)}(x_1 - i0) = (\boldsymbol{B}^{(2)})^{-1}\bar{\boldsymbol{B}}^{(1)}\bar{\boldsymbol{\Phi}}'^{(1)}(x_1 - i0)$ from (10) and substituting this expression together with (9) in the latest formula at $x_2 \to +0$, leads to

$$\langle \boldsymbol{v}'(x_1)\rangle = \boldsymbol{D}\boldsymbol{\Phi}'^{(1)}(x_1 + i0) + \bar{\boldsymbol{D}}\bar{\boldsymbol{\Phi}}'^{(1)}(x_1 - i0),$$

where $\boldsymbol{D} = \boldsymbol{A}^{(1)} - \bar{\boldsymbol{A}}^{(2)}(\overline{\boldsymbol{B}}^{(2)})^{-1}\boldsymbol{B}^{(1)}$. Introducing a new vector function

$$\boldsymbol{W}(z) = \begin{cases} \boldsymbol{D}\boldsymbol{\Phi}'^{(1)}(z), & x_2 > 0, \\ -\overline{\boldsymbol{D}\boldsymbol{\Phi}'^{(1)}}(z), & x_2 < 0, \end{cases} \tag{12}$$

the last relation can be written as

$$\langle \boldsymbol{v}'(x_1)\rangle = \boldsymbol{W}^{+}(x_1) - \boldsymbol{W}^{-}(x_1), \tag{13}$$

where superscript + and − mean the limit values of $\boldsymbol{W}(z)$ as $z \to x + i0$ and $z \to x - i0$, respectively.

From $(6)_2$ we have

$$\boldsymbol{P}^{(1)}(x_1, 0) = \boldsymbol{B}^{(1)}\boldsymbol{\Phi}'^{(1)}(x_1 + i0) + \bar{\boldsymbol{B}}^{(1)}\bar{\boldsymbol{\Phi}}'^{(1)}(x_1 - i0). \tag{14}$$

It follows from (12) that

$$\boldsymbol{\Phi}'^{(1)}(x_1 + i0) = \boldsymbol{D}^{-1}\boldsymbol{W}(x_1 + i0), \quad \bar{\boldsymbol{\Phi}}'^{(1)}(x_1 - i0) = -(\bar{\boldsymbol{D}}^{-1})^{-1}\boldsymbol{W}(x_1 - i0);$$

substituting these relations into (14) leads to

$$\boldsymbol{P}^{(1)}(x_1, 0) = \boldsymbol{S}\boldsymbol{W}^{+}(x_1) - \bar{\boldsymbol{S}}\boldsymbol{W}^{-}(x_1), \tag{15}$$

where $\boldsymbol{S} = \boldsymbol{B}^{(1)}\boldsymbol{D}^{-1}$. Simple calculations show that

$$\boldsymbol{S} = [\boldsymbol{A}^{(1)}(\boldsymbol{B}^{(1)})^{-1} - \bar{\boldsymbol{A}}^{(2)}(\bar{\boldsymbol{B}}^{(2)})^{-1}]^{-1}. \tag{16}$$

The matrix $\boldsymbol{S}$ for the class of piezoelectric materials being considered has the structure

$$\boldsymbol{S} = \begin{bmatrix} is_{11} & s_{12} \\ s_{21} & is_{22} \end{bmatrix}, \tag{17}$$

where all the s_{kl} are real.

Further transformation of (13) and (15), performed similarly to [Lapusta et al. 2017], leads to

$$\sigma_{32}^{(1)}(x_1, 0) - im_j E_1^{(1)}(x_1, 0) = t_j[F_j^{+}(x_1) + \gamma_j F_j^{-}(x_1)], \tag{18}$$

$$\langle D_2(x_1, 0)\rangle + is_j\langle u_3'(x_1, 0)\rangle = F_j^{+}(x_1) - F_j^{-}(x_1), \tag{19}$$

where

$$F_j(z) = W_2(z) + is_j W_1(z) \quad (j = 1, 2). \tag{20}$$

and

$$s_j = -m_j, \quad t_j = s_{12} - m_j s_{22}, \quad m_j = \mp\sqrt{-\frac{s_{11}s_{12}}{s_{21}s_{22}}}, \quad \gamma_j = -(s_{12} + m_1 s_{22})/t_j \quad (j = 1, 2).$$

Let's assume further that an electrically conductive interface crack arises in the section $[c, a]$ of the material interface. The half-spaces are subjected to uniformly distributed shear stress σ_{23}^{∞} and electric field E_1^{∞} at infinity, which do not depend on coordinate x_3. The crack faces are free of loading. These kinds of external fields produce the anti-plane state, therefore, only the cross-section orthogonal to x_3 (Figure 1) can be considered.

The boundary conditions for the formulated problem for $x_2 = 0$ are

$$\sigma_{23}^{(1)} = \sigma_{23}^{(2)} = 0, \qquad E_1^{(1)} = E_1^{(2)} = 0 \quad \text{for } c < x_1 < a, \tag{21}$$

$$\langle\sigma_{23}\rangle = 0, \quad \langle D_2\rangle = 0, \quad \langle u_3'\rangle = 0, \quad \langle E_1\rangle = 0 \quad \text{for } x_1 \notin (c, a). \tag{22}$$

Satisfying conditions (21) and (22) with the use of (18), (19) for $j = 1$ provide the continuity of the function $F_1(z)$ over the segments $x_1 \notin (c, a)$ of the material interface and also leads to

$$F_1^{+}(x_1) + \gamma_1 F_1^{-}(x_1) = 0 \quad \text{for } c < x_1 < a. \tag{23}$$

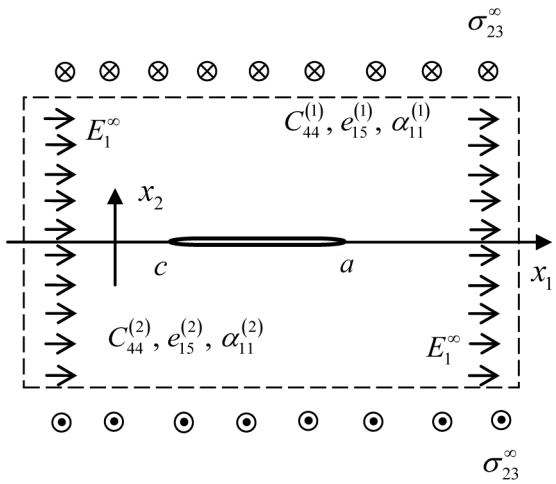

Figure 1. An electrically conducting crack between two piezoelectric materials.

Taking into account further that for $x_1 \notin (c, a)$ the relationships $F_1^+(x_1) = F_1^-(x_1) = F_1(x_1)$ are valid, it follows from (18) that

$$(1+\gamma_1)t_1 F_1(x_1) = \sigma_{23}^{(1)}(x_1, 0) - im_1 E_1^{(1)}(x_1, 0) \quad \text{as } x_1 \to \infty.$$

Using that the function $F_1(z)$ is analytic in the whole plane cut along (c, a) and applying the conditions at infinity, one gets from the last equation

$$F_1(z)|_{z\to\infty} = \tilde{\sigma}_{23} - i\tilde{E}_1, \tag{24}$$

where $\tilde{\sigma}_{23} = \sigma_{23}^{\infty}/r_1,\ \tilde{E}_1 = m_1 E_1^{\infty}/r_1,\ r_1 = (1+\gamma_1)t_1$.

The solution of (23) under the condition at infinity (24) was found with use of [Muskhelishvili 1977] in the form

$$F_1(z) = (\tilde{\sigma}_{23} - i\tilde{E}_1)\frac{z - (a+c)/2 - i\varepsilon l}{\sqrt{(z-c)(z-a)}}\left(\frac{z-c}{z-a}\right)^{i\varepsilon}, \tag{25}$$

where $\varepsilon = \frac{1}{2\pi}\ln\gamma_1$, $l = a - c$.

A similar analysis can be carried out for $j = 2$ in (18), (19) and the function $F_2(z)$ can be obtained.

The stress and electric fields at the interface are obtained from (18), (25) as follows:

$$\sigma_{23}^{(1)}(x_1, 0) - im_1 E_1^{(1)}(x_1, 0) = \pm(\sigma_{23}^{\infty} - im_1 E_1^{\infty})\frac{x_1 - (a+c)/2 - i\varepsilon l}{\sqrt{(x_1-c)(x_1-a)}}\left(\frac{x_1-c}{x_1-a}\right)^{i\varepsilon} \text{ for } x_1 > a, \tag{26}$$

where the upper sign corresponds to $x_1 > a$ and the lower sign to $x_1 < c$.

The electric induction and the derivative of the displacement jumps are found from the formula (19) in the form

$$\langle D_2(x_1, 0)\rangle + is_1\langle u_3'(x_1, 0)\rangle = -\frac{(\sigma_{23}^{\infty} i + m_1 E_1^{\infty})}{t_1\sqrt{\gamma_1}}\frac{(x_1 - (a+c)/2 - i\varepsilon l)}{\sqrt{(x_1-c)(a-x_1)}}\left(\frac{x_1-c}{a-x_1}\right)^{i\varepsilon} \text{ for } c < x_1 < a. \tag{27}$$

Integrating the last relation, we obtain

$$\langle \hat{D}_2(x_1,0)\rangle + is_1\langle u_3(x_1,0)\rangle = \sqrt{(x_1-c)(a-x_1)}\left\{\frac{\sigma_{23}^{\infty} i + m_1 E_1^{\infty}}{t_1\sqrt{\gamma_1}}\left(\frac{x_1-c}{a-x_1}\right)^{i\varepsilon}\right\} \quad \text{for } c < x_1 < a, \quad (28)$$

where $\langle \hat{D}_2(x_1,0)\rangle = \int \langle D_2(x_1,0)\rangle dx_1$.

It should be noted that for the case of a homogeneous material formulas (26) and (28) take the form

$$\sigma_{23}^{(1)}(x_1,0) - im_1 E_1^{(1)}(x_1,0) = \pm(\sigma_{23}^{\infty} - im_1 E_1^{\infty})\frac{x_1-(a+c)/2}{\sqrt{(x_1-c)(x_1-a)}} \quad \text{for} \begin{cases} x_1 > a \ (+\text{ sign}), \\ x_1 < c \ (-\text{ sign}), \end{cases} \quad (29)$$

$$\langle \hat{D}_2(x_1,0)\rangle + is_1\langle u_3(x_1,0)\rangle = t_1^{-1}(\sigma_{23}^{\infty} i + m_1 E_1^{\infty})\sqrt{(x_1-c)(a-x_1)} \quad \text{for } c < x_1 < a. \quad (30)$$

It is clearly seen from the formulas (29), (30) that mechanical and electrical components are independent for a homogeneous material, therefore, electrical characteristics at the whole interface are completely defined by external electric loading while mechanical – by mechanical one. Another situation takes place when considering the case of a bimaterial treated here. In this case mechanical and electrical components are coupled (see Equations (26)–(30)) and their mutual influence is demonstrated in Figures 2–5.

The calculations were performed for a bimaterial with the following characteristics:

$$c_{44}^{(1)} = 35.3\,\text{GPa}, \quad e_{15}^{(1)} = 17.0\ \text{C/m}^2, \quad \alpha_{11}^{(1)} = 15.1\times 10^{-9} \quad \text{C/(Vm)},$$
$$c_{44}^{(2)} = 42.5\,\text{GPa}, \quad e_{15}^{(2)} = -0.48\,\text{C/m}^2, \quad \alpha_{11}^{(2)} = 0.0757\times 10^{-9}\,\text{C/(Vm)},$$

and different values of mechanical and electric loadings.

The calculated tangential crack openings (sliding) $\langle u_3(x_1,0)\rangle$ for $c = -10$ mm, $b = 10$ mm, $\sigma_{23}^{\infty} = 10$ MPa, and different values of E_1^{∞} are presented in Figure 2 for the right vicinity of the left crack tip and for the left vicinity of the right tip. It is seen that for $E_1^{\infty} = 0$ the crack opening has the same behavior, but with different values of sliding, at the left and right crack tips. However an increase of E_1^{∞} leads to increasing the crack opening at the left crack tip and decreasing it at the right one.

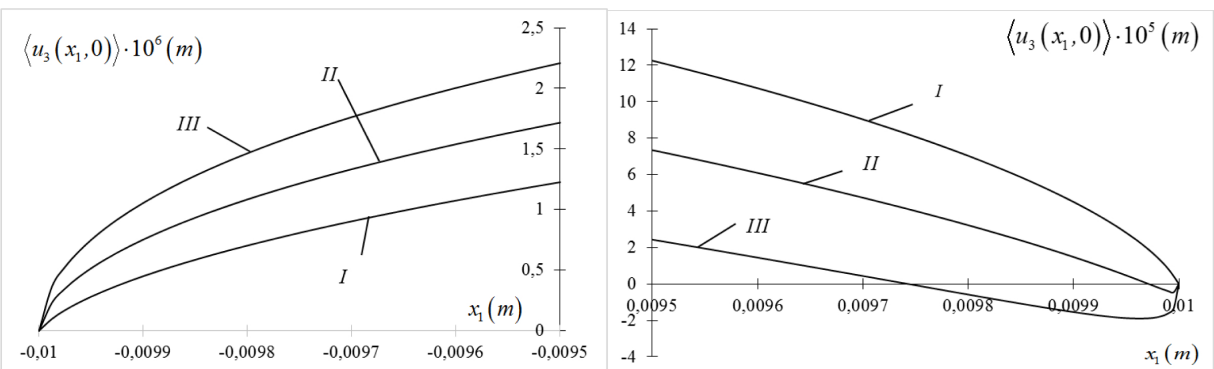

Figure 2. Dependence of the crack sliding $\langle u_3(x_1,0)\rangle$ at the left and right crack tips, respectively, on E_1^{∞} for $\sigma_{23}^{\infty} = 10$ MPa. Curves *I*, *II* and *III* correspond to $E_1^{\infty} = 0$, 300 kV/m and 600 kV/m, respectively.

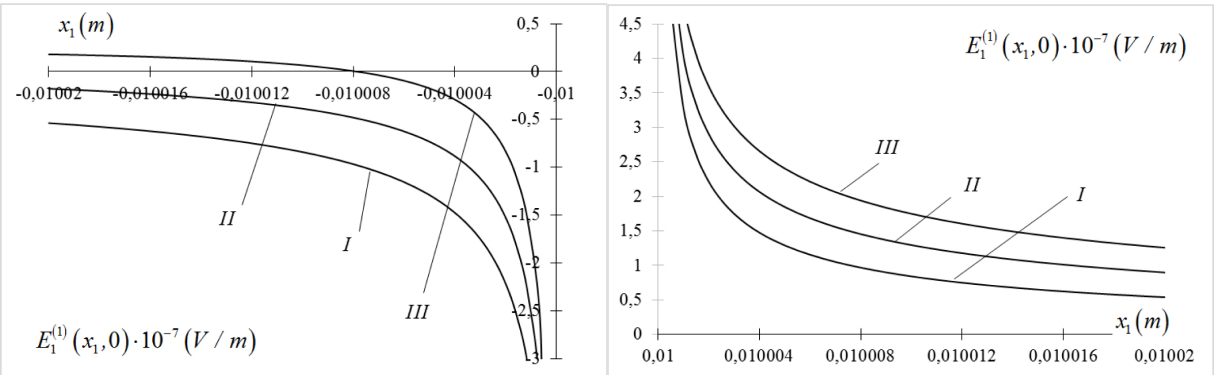

Figure 3. Variation of the electric field $E_1^{(1)}(x_1, 0)$ along the left crack continuation (left) and the right crack continuation for $\sigma_{23}^{\infty} = 10\,\text{MPa}$ and different values of E_1^{∞}.

The variation in electric field $E_1^{(1)}(x_1, 0)$ along the crack continuations for the same materials, crack length and loadings are given in Figure 3. These figures suggest that an increase in E_1^{∞} causes an increase in the intensity of the electric field at the right crack tip and a decrease in its absolute value at the left crack tip. Changing the E_1^{∞} sign leads to the same phenomenon, but with permutation of the crack tips. Thus, in contrast to the case of a crack in a homogeneous material, the electrical fields at the right and left crack tips of an interface crack become substantially different for nonzero external electric fields.

In some cases it is necessary to know the behavior of electromechanical quantities outside of the material interface. To define this behavior we obtain from $(6)_2$ and (12)

$$\boldsymbol{P}^{(m)} = 2\,\text{Re}\{\boldsymbol{K}^{(m)}\,\boldsymbol{W}(z)\}, \tag{31}$$

where $\boldsymbol{K}^{(1)} = \boldsymbol{B}^{(1)}\boldsymbol{D}^{-1}$, $\boldsymbol{K}^{(2)} = -\boldsymbol{B}^{(2)}\bar{\boldsymbol{D}}^{-1}$.

Considering $j = 1$ and $j = 2$ in (20) and solving the system obtained with respect to $W_1(z)$ and $W_2(z)$ one gets

$$W_1(z) = \frac{F_1(z) - F_2(z)}{i(s_1 - s_2)}, \qquad W_2(z) = \frac{s_2 F_1(z) - s_1 F_2(z)}{s_2 - s_1} \tag{32}$$

Formulas (31) and (32) define the shear stress and the electric field component at any point of the bimaterial domain via the functions $F_1(z)$ and $F_2(z)$ obtained above.

Figure 4 demonstrates the result of use of the formulas (31) and (32) for determination and presentation of electromechanical characteristics outside of the material interface. Namely, the shear stress distribution at the right crack tip in the upper part of the medium is shown in this figure. The curves with markers represent the level lines of the shear stress $\sigma_{32}^{(1)}(x_1, 0)$, which demonstrate its variation in the vicinity of the right crack tip. Similar fields can be drawn with use of (31) and (32) for other electromechanical components at any subdomain of the medium.

3. Formulation of the problem and dielectric breakdown model consideration for an interface crack

By separating the real and imaginary parts of (26) one can see that the mechanical stress and the electric

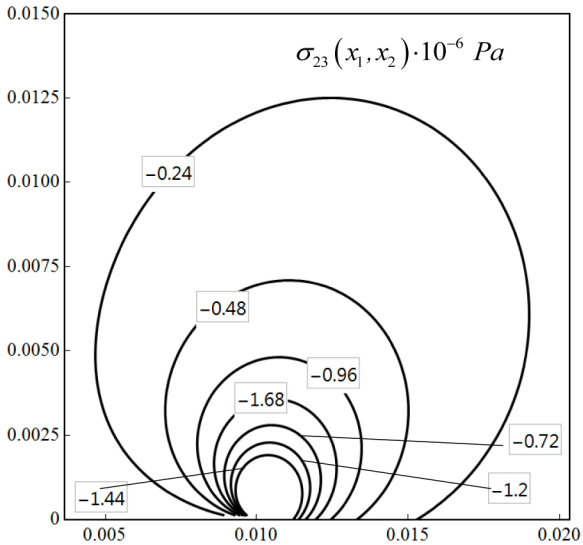

Figure 4. Variation of the shear stress $\sigma_{23}(x_1, x_2)$ distribution at the vicinity $0.004\,m \leq x_1 \leq 0.02\,m$, $0 \leq x_2 \leq 0.015\,m$ of the right crack tip.

field are singular at the crack tips. Moreover this singularity is oscillating. Square root singularity takes place at the crack tip also in a case of a homogeneous material. To remove the oscillation and to eliminate completely the singularity in the electric field the dielectric breakdown model (DB model) is applied. This model was suggested in papers by [Zhang and Gao 2004] for a conducting crack in a homogeneous piezoelectric material. In the present paper the generalization of this model to the interface crack is suggested. As follows from Figures 2 and 3, the DB zone lengths should be different at the left and right tips of an interface crack. Moreover, it will be shown later that these zones for an interface crack are either both very short (for $E_1^{\infty} = 0$) or one zone is substantially shorter than another one, therefore, their mutual influence can be neglected. Taking into account this circumstance we'll consider for simplicity only one zone paying the main attention to the longer one and assuming that it occurs at the right crack tip (Figure 5). If the longer zone occurs at another crack tip then this zone can be considered by simple transformation of half-spaces.

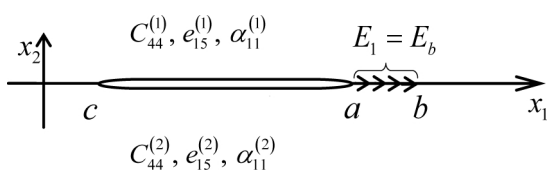

Figure 5. An electrically conducting interface crack with dielectric breakdown zone at the right crack tip.

Thus the boundary conditions for the considered model can be written as

$$\sigma_{23}^{(1)} = \sigma_{23}^{(2)} = 0, \quad E_1^{(1)} = E_1^{(2)} = 0 \text{ for } c < x_1 < a, \tag{33}$$

$$E_1^{(1)} = E_1^{(2)} = E_b, \quad \langle \sigma_{23} \rangle = 0, \quad \langle u_3' \rangle = 0, \text{ for } a < x_1 < b, \tag{34}$$

$$\langle \sigma_{23} \rangle = 0, \quad \langle D_2 \rangle = 0, \quad \langle u_3' \rangle = 0, \langle E_1 \rangle = 0 \text{ for } x_1 \notin (c, b), \tag{35}$$

where E_b is the dielectric breakdown strength, defined as a critical electric field at which partial discharge starts to occur around the crack tip [Gao et al. 2006].

Satisfying the interface conditions (33) with use of (18) one gets the equation (23), and the first and third conditions (34) together with (19) lead to

$$\begin{aligned} &\operatorname{Im}[F_1^+(x_1) + \gamma_1 F_1^-(x_1)] = -m_1 E_b / t_1, \\ &\operatorname{Im}[F_1^+(x_1) - F_1^-(x_1)] = 0 \text{ for } a < x_1 < b. \end{aligned} \tag{36}$$

Satisfaction of the boundary conditions (35) provides the analyticity of the function $F_1(z)$ outside of the interval (c, b). The relations (36) lead to the equation

$$\operatorname{Im} F_1^{\pm}(x_1) = E^* \text{ for } a < x_1 < b, \tag{37}$$

where $E^* = -m_1 E_b / r_1$.

Equations (23) and (37) present the nonhomogeneous combined Dirichlet–Riemann boundary value problem. The conditions at infinity (24) remain valid for this problem also. Following the paper by [Nakhmein and Nuller 1986] the general solution of the homogeneous problem corresponding to (23), (37) can be presented in the form

$$F_{1h}(z) = P(z) X_1(z) + Q(z) X_2(z), \tag{38}$$

where

$$P(z) = C_1 z + C_2, \quad Q(z) = D_1 z + D_2.$$

The functions

$$X_1(z) = i e^{i\chi(z)} / \sqrt{(z-c)(z-b)}, \quad X_2(z) = e^{i\chi(z)} / \sqrt{(z-c)(z-a)}, \tag{39}$$

are the canonical solutions of the homogeneous problem corresponding to (23), (37),

$$\chi(z) = 2\varepsilon \ln \frac{\sqrt{(b-a)(z-c)}}{\sqrt{(b-a)(z-a)} + \sqrt{(a-c)(z-b)}}, \quad z = x_1 + i\, x_2,$$

$i = \sqrt{-1}$ and $C_1,\ C_2,\ D_1,\ D_2$ are arbitrary real coefficients.

A particular solution of the nonhomogeneous problem (23), (37) we'll find in the form

$$F_{1p}(z) = \Phi(z) X_1(z), \tag{40}$$

where $\Phi(z)$ is assumed to be analytic in the whole complex plane with a cut $[a,\ b]$ along the x_1-axis. It is obvious that $F_{1p}(z)$ satisfies (23). Substituting (40) into (37) and taking into account that $\operatorname{Im} X_1^{\pm}(x_1) = 0$ on $(a,\ b)$ one gets the following equation

$$\operatorname{Im} \Phi^{\pm}(x_1) = \psi^{\pm}(x_1) \text{ for } a < x_1 < b, \tag{41}$$

where $\psi(x_1) = E^*/X_1(x_1)$.

A solution of the Dirichlet problem (41) has the following form [Gakhov 1966, formula (46.25)]:

$$\Phi(z) = \frac{Y(z)}{2\pi}\int_a^b \frac{\psi^+(t)+\psi^-(t)}{Y^+(t)(t-z)}\,dt + \frac{1}{2\pi}\int_a^b \frac{\psi^+(t)-\psi^-(t)}{t-z}\,dt, \tag{42}$$

where $Y(z) = \sqrt{(z-a)(z-b)}$ and $0 \le \arg(z-a) \le 2\pi$, $0 \le \arg(z-b) \le 2\pi$.

Taking into account that

$$\psi^+(t)+\psi^-(t) = -2E^*\sqrt{(t-c)(b-t)}\sinh\chi_0(t),$$
$$\psi^+(t)-\psi^-(t) = 2E^*\sqrt{(t-c)(b-t)}\cosh\chi_0(t),$$
$$\chi_0(x_1) = 2\varepsilon\tan^{-1}\sqrt{\frac{(a-c)(b-x_1)}{(b-c)(x_1-a)}}$$

and that $Y^+(t) = -i\sqrt{(t-a)(b-t)}$ on (a,b), the formula (42) takes the form

$$\Phi(z) = \frac{E^*}{\pi}[-iY(z)L_1(z) + L_2(z)], \tag{43}$$

where

$$L_1(z) = \int_a^b \sqrt{\frac{t-c}{t-a}}\,\frac{\sinh\chi_0(t)}{t-z}\,dt, \quad L_2(z) = \int_a^b \sqrt{(t-c)(b-t)}\,\frac{\cosh\chi_0(t)}{t-z}\,dt.$$

The general solution of the problem (23), (37) is the sum of the solutions (38), (40). Arbitrary constants C_1, C_2, D_1, D_2 can be found from the condition at infinity (24) together with condition of the displacement uniqueness and the absence of an electric charge in the crack region [Knysh et al. 2012], which due to (8) can be written in the form

$$\int_c^b (F_1^+(x_1) - F_1^-(x_1))dx_1 = 0.$$

Taking into account that for the validity of last equation the coefficient before z^{-1} in the expansion of $F_1(z)$ at infinity should be equal to zero [Herrmann and Loboda 2003] and also

$$X_1(z)|_{z\to\infty} = iz^{-2}e^{i\beta}\left(z + i\beta_1 + \frac{c+b}{2}\right) + o(z^{-3}),$$
$$X_2(z)|_{z\to\infty} = z^{-2}e^{i\beta}\left(z + i\beta_1 + \frac{c+a}{2}\right) + o(z^{-3}),$$
$$\Phi(z)|_{z\to\infty} = -iR + o(z^{-1}), \quad R = \frac{E^*}{\pi}\int_a^b \sqrt{\frac{t-c}{t-a}}\sinh\chi_0(t)\,dt,$$

one gets the following expressions for the unknown coefficients

$$C_1 = -\tilde{\sigma}_{23}\sin\beta - \tilde{E}_1\cos\beta, \quad D_1 = \tilde{\sigma}_{23}\cos\beta - \tilde{E}_1\sin\beta,$$
$$C_2 = -\frac{c+b}{2}C_1 - \beta_1 D_1, \quad D_2 = \beta_1 C_1 - \frac{c+a}{2}D_1 - R,$$

where

$$\beta = \varepsilon \ln \frac{1-\sqrt{1-\lambda}}{1+\sqrt{1-\lambda}}, \beta_1 = \varepsilon\sqrt{(a-c)(b-c)}, \quad \lambda = \frac{b-a}{b-c}. \tag{44}$$

From the exact analytical solution thus obtained,

$$F_1(z) = (P(z) + \Phi(z))X_1(z) + Q(z)X_2(z), \tag{45}$$

all required quantities at the material interface can be found. A similar analysis can be carried out for $j = 2$ in (18), (19), leading to the function $F_2(z)$.

4. Stress intensity factor and DB zone length

According to equation (18) stress and electric field on the right hand side from DB zone can be presented in the form

$$\sigma_{32}^{(1)}(x_1, 0) - im_1 E_1^{(1)}(x_1, 0) = r_1 F_1(x_1) = r_1\{(P(x_1) + \Phi(x_1))X_1(x_1) + Q(x_1)X_2(x_1)\}. \tag{46}$$

For an arbitrary position of the point b (defining the DB zone length) right hand side of (46) is singular for $x_1 \to b+0$ and besides $P(b) + \Phi(b)$ is real and $X_1(x_1)|_{x_1 \to b+0} = i/\sqrt{(b-c)(x_1-b)}$ is pure imaginary. Therefore, for any b the shear stress $\sigma_{32}^{(1)}(x_1, 0)$ is finite for $x_1 \to b+0$ whilst $E_1^{(1)}(x_1, 0)$ is singular. To remove this singularity the equation

$$P(b) + \Phi(b) = 0$$

should be satisfied. After some transformation this equation can be written in the form

$$m_1 E_1^{\infty} \cos\beta + \sigma_{23}^{\infty} \sin\beta + 2\varepsilon\sqrt{1-\lambda}(\sigma_{23}^{\infty} \cos\beta - m_1 E_1^{\infty} \sin\beta) - \frac{2m_1 E_b}{\pi(b-c)} \int_a^b \sqrt{\frac{t-c}{b-t}} \cosh\chi_0(t)\, dt = 0. \tag{47}$$

The obtained equation should be solved with respect to λ and then the point b can be found from the last of (44). As a rule (47) can be solved numerically and the largest root of this equation from the interval $(0,\ 1)$, which we denote λ_0, can be found.

In the particular case of homogeneous piezoelectric material one has $\varepsilon = 0$, $\chi_0(t) = 0$, $\beta = 0$, and equation (47) reduces to the form

$$\frac{2}{\pi(b-c)} \int_a^b \sqrt{\frac{t-c}{b-t}}\, dt = \frac{E_1^{\infty}}{E_b}.$$

After some transformations this can be written as

$$\frac{\sqrt{\lambda}}{\pi} \int_{-1}^{1} \sqrt{\frac{2+\lambda(\tau+1)}{1-\tau}} d\tau = \frac{E_1^{\infty}}{E_b}. \tag{48}$$

For a small λ this equation has the following asymptotic solution

$$\lambda \approx \lambda_0 = \left(\frac{\pi E_1^{\infty}}{4E_b}\right)^2. \tag{49}$$

For the case of two symmetrical DB zones $(-b, -a)$ and (a, b) at both crack tips in a homogeneous piezoelectric material the analysis similar to [Gao et al. 2006] leads to the following equation

$$\frac{a}{b} = \cos\frac{\pi E_1^\infty}{2E_b}. \tag{50}$$

Note that the asymptotic solution of this equation for small E_1^∞/E_b completely coincides with the solution (49).

The shear stress at (a, b) according to (18), (34) can be found in the form

$$\sigma_{32}^{(1)}(x_1, 0) = t_1[F_1^+(x_1) + \gamma_1 F_1^-(x_1)] + im_1 E_b.$$

Substituting the formula (45), taking into account that according to [Herrmann and Loboda 2003]

$$X_1^\pm(x_1) = \frac{\pm e^{\pm\chi_0(x_1)}}{\sqrt{(x_1-c)(b-x_1)}}, \quad X_2^\pm(x_1) = \frac{e^{\pm\chi_0(x_1)}}{\sqrt{(x_1-c)(x_1-a)}} \text{ for } x_1 \in (a, b)$$

and applying Plemeli's formulas [Muskhelishvili 1977] we arrive at the expression

$$\begin{aligned} t_1^{-1}\sigma_{32}^{(1)}(x_1, 0) = {} & P(x_1)\frac{e^{\chi_0(x_1)} - \gamma_1 e^{-\chi_0(x_1)}}{\sqrt{(x_1-c)(b-x_1)}} + Q(x_1)\frac{e^{\chi_0(x_1)} + \gamma_1 e^{-\chi_0(x_1)}}{\sqrt{(x_1-c)(x_1-a)}} \\ & + \frac{E^*}{\pi}\left\{-\sqrt{\frac{x_1-a}{x_1-c}}[e^{\chi_0(x_1)} + \gamma_1 e^{-\chi_0(x_1)}]L_1(x_1) + \frac{e^{\chi_0(x_1)} - \gamma_1 e^{-\chi_0(x_1)}}{\sqrt{(x_1-c)(b-x_1)}}L_2(x_1)\right\}, \end{aligned} \tag{51}$$

where the integrals $L_1(x_1)$ and $L_2(x_1)$ should be considered in sense of principal value on Cauchy [Muskhelishvili 1977].

Consider next the stress intensity factor (SIF) of the shear stress at the point a

$$K_3 = \lim_{x_1 \to a+0} \sqrt{2\pi(x_1-a)}\, \sigma_{23}^{(1)}(x_1, 0). \tag{52}$$

Taking into account that $L_1(x_1)$ has a square root singularity for $x_1 \to a+0$ and $L_2(x_1)$ has the logarithmic singularity at this point we arrive to the following formula

$$K_3 = 2t_1\sqrt{2\pi\gamma_1}\frac{Q(a)}{\sqrt{a-c}},$$

which after some transformations takes the form

$$K_3 = \frac{2t_1\sqrt{2\pi\gamma_1}}{\sqrt{a-c}}\left[\frac{b-c}{2}\sqrt{1-\lambda}(2\varepsilon C_1 + \sqrt{1-\lambda}D_1) - R\right]. \tag{53}$$

In the particular case of homogeneous piezoelectric material formula (53) reduces to

$$K_3 = \sqrt{\frac{\pi(a-c)}{2}}\sigma_{23}^\infty,$$

which completely coincides with the associated result of [Gao et al. 2006].

The derivative of the crack faces displacement jump at the interval (c, a) (crack sliding) can be found with use of (8) in the form

$$\langle u_3'(x_1, 0)\rangle = s_1^{-1}\,\mathrm{Im}[F_1^+(x_1) - F_1^-(x_1)].$$

$10^{-6}E_1^{\infty}$ [V/m]	0	1	2	3	4	5
λ_0	2.492×10^{-4}	7.285×10^{-3}	0.02571	0.05521	0.0947	0.1429
$10^{-6}K_3$ [Pa/m$^{3/2}$]	1.514	0.3850	−0.3448	−0.8656	−1.2375	−1.4879

Table 1. DB-zone length and SIF K_3 for $\sigma_{23}^{\infty} = 10$ MPa and different positive values of E_1^{∞}

$10^{-6}E_1^{\infty}$ [V/m]	−0.1	−0.2	−1	−2
λ_0	1.078×10^{-4}	3.522×10^{-5}	1.055×10^{-9}	2.419×10^{-11}
$10^{-6}K_3$ [Pa/m$^{3/2}$]	1.6739	1.852	4.061	7.531

Table 2. DB-zone length and SIF K_3 for $\sigma_{23}^{\infty} = 10$ MPa and different negative values of E_1^{∞}.

Substituting expression (31) one gets

$$\langle u_3'(x_1, 0)\rangle = \frac{\gamma_1 + 1}{s_1\sqrt{\gamma_1}} \operatorname{Im}\left\{\left[\frac{P(x_1) + \Phi(x_1)}{\sqrt{b - x_1}} - i\frac{Q(x_1)}{\sqrt{a - x_1}}\right]\frac{\exp[i\chi^*(x_1)]}{\sqrt{x_1 - c}}\right\} \text{ for } c < x_1 < a, \tag{54}$$

where

$$\chi^*(x_1) = 2\varepsilon \ln \frac{\sqrt{(b-a)(x_1-c)}}{\sqrt{(b-c)(a-x_1)} + \sqrt{(a-c)(b-x_1)}}$$

and the crack sliding can be found as

$$\langle u_3(x_1, 0)\rangle = \int_c^{x_1} \langle u_3'(t, 0)\rangle\, dt. \tag{55}$$

5. Numerical results and discussion

We performed calculations for a bimaterial composed of PZT-4 (upper material) and $BaTiO_3$ (lower one) having the following characteristics:

$$c_{44}^{(1)} = 25.6\,\text{GPa}, \quad e_{15}^{(1)} = 12.7\,\text{C/m}^2, \quad \alpha_{11}^{(1)} = 6.46\,\text{nC(V m)}^{-1},$$
$$c_{44}^{(2)} = 43.0\,\text{GPa}, \quad e_{15}^{(2)} = 11.6\,\text{C/m}^2, \quad \alpha_{11}^{(2)} = 11.2\,\text{nC(V m)}^{-1},$$

with $E_b = 10^7\ \frac{\text{V}}{\text{m}}$ [Fan et al. 2009], $c = -10$ mm, $b = 10$ mm and different values of mechanical and electric loadings.

In Table 1 the DB zone lengths and the SIF K_3 are presented for $\sigma_{23}^{\infty} = 10$ MPa and different positive values of E_1^{∞}. It can be seen from the results that increasing of E_1^{∞} leads to the increase of λ_0 and decrease of K_3 with resulting in its change of sign even. The reason for the change will be clear from the following graphs. Similar results, but for negative values of E_1^{∞} are presented in Table 2. It follows from this table that increasing of $|E_1^{\infty}|$ initiates the cardinal decreasing of the DB zone length to negligibly small values.

Results similar to Table 1, but for smaller values of σ_{23}^{∞}, are presented in Table 3. It is seen by comparison of these Tables that increase of σ_{23}^{∞} leads to an increase of λ_0 and K_3. However with increase of E_1^{∞} the difference in λ_0 for these two Tables almost disappear.

$10^{-6}E_1^{\infty}$ [V/m]	0	1	2	3	4	5
λ_0	8.036×10^{-5}	6.537×10^{-3}	0.0247	0.05412	0.09363	0.14188
$10^{-6}K_3$ [Pa/m$^{3/2}$]	0.7264	−0.4672	−1.211	−1.738	−2.113	−2.3659

Table 3. DB-zone length and SIF K_3 for $\sigma_{23}^{\infty} = 5$ MPa and different positive values of E_1^{∞}.

$10^{-6}E_1^{\infty}$ [V/m]	1	2	3	4	5
λ_0	6.144×10^{-4}	0.02428	0.05660	0.09295	0.1410
$\hat{\lambda}$	6.156×10^{-4}	0.02447	0.05449	0.09549	0.1464

Table 4. DB-zone lengths in case of homogenous material $BaTiO_3$ for $\sigma_{23}^{\infty} = 10$ MPa and different values of E_1^{∞}.

The results for the DB zone lengths in case of homogenous material $BaTiO_3$ for $\sigma_{23}^{\infty} = 10$ MPa and different values of E_1^{∞} are given in Table 4. Value λ_0 in this case is the root of (48) corresponding to one DB zone and $\hat{\lambda}$ is the root of (50) obtained for two symmetrical DB-zones at both crack tips. The SIF K_3 for all values of E_1^{∞} is equal to 1.772×10^6 Pa/m$^{3/2}$. It is clear that for relatively small magnitudes of E_1^{∞} the difference between λ_0 and $\hat{\lambda}$ is negligibly small, but it grows moderately as E_1^{∞} increases.

The calculated tangential crack opening (sliding) $\langle u_3(x_1, 0)\rangle$ for $c = -10$ mm, $b = 10$ mm, $\sigma_{23}^{\infty} = 10$ MPa is presented in Figure 6 for different values of E_1^{∞}. Lines *I*, *II* and *III* correspond to $E_1^{\infty} = 0$, 2×10^6 V/m and 4×10^6 V/m, respectively. It is clearly seen from these results that the crack sliding is almost symmetrical for $E_1^{\infty} = 0$, but increasing of E_1^{∞} leads to the distortion of the curve and a change of the sign of $\langle u_3(x_1, 0)\rangle$ in a region in the vicinity of the right crack tip (these explain the negative values of SIF in Table 1). However, the appearance of the negative $\langle u_3(x_1, 0)\rangle$ does not mean the crack faces interpenetration like in plane case and is quite admissible from physical point of view. It is worth to be mentioning also that the negative electric field will lead to mirror mapping of the obtained graphs with respect to the ordinate axis.

The behavior of the electric field in the DB zone and along its right continuation are presented in Figure 7 for the same crack geometry, mechanical loading and different E_1^{∞}. Here $E_1^{\infty} = 2 \times 10^6$ V/m (line *I*), 4×10^6 V/m (*II*) and 5×10^6 V/m (*III*). As it can be seen the DB-model eliminated the singularities of electric field at the right crack tip. Thus this model gives the possibility to get an electromechanical field at the point b free from singularities and to transform the oscillating singularity of the shear stress into conventional square root singularity at the point a. It is very important because it provides a possibility for the SIF to be used in a conventional way.

For an additional verification of the obtained analytical solution the independent methods based on finite element package has been used. The finite sized body composed of two piezoelectric parallelepipeds $-30\,\text{mm} \le x_1 \le 30\,\text{mm}$, $0 \le x_2 \le 20\,\text{mm}$, $0 \le x_3 \le 180\,\text{mm}$ and $-30\,\text{mm} \le x_1 \le 30\,\text{mm}$, $-20\,\text{mm} \le x_2 \le 0$, $0 \le x_3 \le 180\,\text{mm}$ with the same piezoelectric material parameters as presented at the beginning of this Section has been considered. An electrically conducting crack in the interface region $-10\,\text{mm} \le x_1 \le 10\,\text{mm}$, $x_2 = 0$, $0 \le x_3 \le 180\,\text{mm}$ is situated. The lower boundary $x_2 = -20$ mm was fixed while to the upper one $x_2 = 20$ mm the uniformly distributed shear stress $\sigma_{32}^{(1)}(x_1,20) = 10$ MPa was applied. Assuming the external electric field $E_1 = 0$ the DB zone in this case is defined by the second column of Table 1.

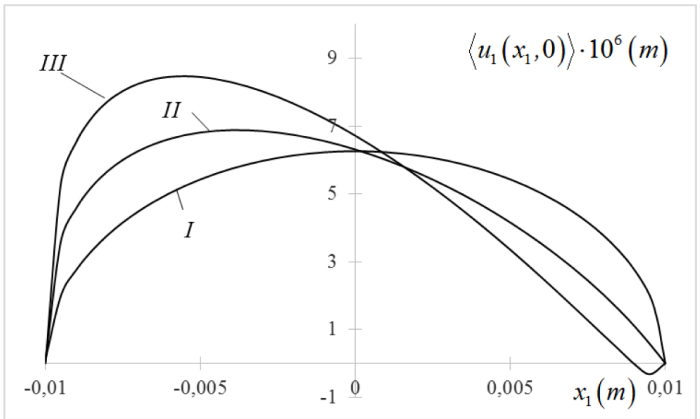

Figure 6. Tangential crack sliding $\langle u_3(x_1, 0)\rangle$ for $\sigma_{23}^{\infty} = 10\,\text{MPa}$ and different values of E_1^{∞}.

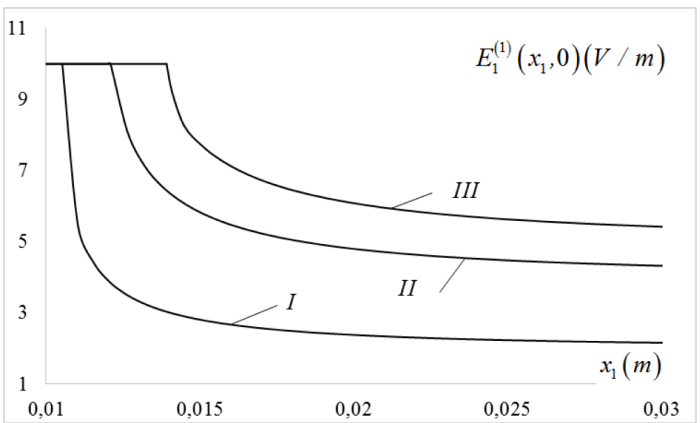

Figure 7. The electric field in DB zone and at it continuation for $\sigma_{23}^{\infty} = 10\,\text{MPa}$ and different values of E_1^{∞}.

The finite element ABAQUS code was used for the solution of this problem. The mesh refinement at the crack tips was done. As a result of this solution the maximum value of the crack sliding at the point $x_1 = x_2 = 0$, $x_3 = 90\,\text{mm}$ turned out to be $6.771 \times 10^{-3}\,\text{mm}$. Analytical analysis performed for the same geometrical and mechanical parameters gave the result $6.260 \times 10^{-3}\,\text{mm}$ for the crack sliding at the same point. Taking into account that we compared the results for finite size domain (with a crack 3 times shorter than the width of the compound) and for an infinite domain, the obtained error in 7.54% can be considered as quite satisfactory. Therefore, the presented numerical analysis confirms the validity of the analytical approach developed in this paper.

6. Conclusions

The mode III interface crack problem for a transversely isotropic dissimilar piezoelectric bimaterial media under the action of anti-plane mechanical loading and in-plane electrical field parallel to the crack faces is considered.

To eliminate the electric field singularity, which occurs at the crack tips, the dielectric breakdown model is applied. According to this model the electric field along some zone of the crack continuation is assumed to be equal to the electric breakdown strength E_b and the length of this zone remain unknown for a time being. A nonhomogeneous combined Dirichlet–Riemann boundary value problem (23), (37) is formulated. This problem is much more complicated than the problem (23) nevertheless an exact analytical solution (45) of this problem is presented. The transcendental equation for the determination of the DB zone length is obtained from the condition of the electric field finiteness at the boundary point of this zone. Analytical formulas for the shear stress in DB zone, the stress intensity factor at the crack tip and for the crack sliding are obtained.

The variation of the DB zone length, crack sliding and the SIF with respect to external electric field is illustrated in tables and figures. In particular it is shown that the electric field essentially influences all electrical and also mechanical characteristics of the model. Namele, the increase of the electric field changes the sign of the displacement jump in some part of the crack region (see line *III* of Figure 5). It is seen from the last lines of Tables 1 and 3 that this increase cardinally vary the value of the SIF changing it sign even.

The particular case of identical physical properties of upper and lower domains is considered. This case is equivalent to the case of a crack in a homogeneous piezoelectric medium. Equation (47), determining the DB zone length, and the formula (53) for the SIF finding reduce to very simple equations which solutions are in good agreement with the associated results obtained for the crack with two DB zones by another method.

It's worth to be mentioning that the dissimilarity of the bulk properties essentially effects the electromechanical quantities of the considered problem. In particular, the SIF K_3 does not depend on the applied electric field for a homogeneous case whilst it changes its value quite substantially with respect to this field for a dissimilar piezoelectric material. Besides, as it is seen from Figure 6, the crack opening transforms its symmetrical form due to electric field for a dissimilar material what is not observed for a homogeneous one.

Comparison of the obtained analytical solution with the associated results obtained by finite element method has been performed and good agreement has been found.

The importance of the obtained solution is justified by the possibility of using the obtained results in electronic engineering for decreasing of the threat of failure of electronic devices produced from dissimilar piezoelectric materials and having internal electrodes, which can lead to the appearance of conducting interface cracks.

Acknowledgments

This work was sponsored by a public grant overseen by the French National Research Agency as part of the "Investissements d'Avenir" through the IMobS3 Laboratory of Excellence (ANR-10-LABX-0016) and through the IDEX-ISITE initiative CAP 20-25 (ANR-16-IDEX-0001) within the framework of the program WOW PhD Mentoring.

References

[Barenblatt 1962] G. I. Barenblatt, "The mathematical theory of equilibrium cracks in brittle fracture", *Adv. Appl. Mech.* **7** (1962), 55–129.

[Beom et al. 2006a] H. G. Beom, Y. H. Kim, C. Cho, and C. B. Kim, "A crack with an electric displacement saturation zone in an electrostrictive material", *Arch. Appl. Mech.* **76** (2006a), 19–31.

[Beom et al. 2006b] H. G. Beom, Y. H. Kim, C. Cho, and C. B. Kim, "Asymptotic analysis of an impermeable crack in an electrostrictive material subjected to electric loading", *Int. J. Solids Struct.* **43** (2006b), 6869–6886.

[Bertoldi et al. 2007] K. Bertoldi, D. Bigoni, and W. J. Drugan, "Structural interfaces in linear elasticity, part I: Nonlocality and gradient approximations", *J. Mech. Phys. Solids* **55** (2007), 1–34.

[Bigoni and Movchan 2002] D. Bigoni and A. B. Movchan, "Statics and dynamics of structural interfaces in elasticity", *Int. J. Solids Struct.* **39** (2002), 4843–4865.

[Craciun et al. 2004] E.-M. Craciun, E. Baesu, and E. Soós, "General solution in terms of complex potentials for incremental antiplane states in prestressed and prepolarized piezoelectric crystals: application to mode III fracture propagation", *IMA J. Appl. Math.* **70** (2004), 39–52.

[Dugdale 1960] D. S. Dugdale, "Yielding of steel sheets containing slits", *J. Mech. Phys. Solids* **8** (1960), 100–108.

[Fan et al. 2009] C. Y. Fan, M. H. Zhao, and Y. H. Zhou, "Numerical solution of polarization saturation/ dielectric breakdown model in 2D finite piezoelectric media", *J. Mech. Phys. Solids* **57** (2009), 1527–1544.

[Fan et al. 2012] C. Y. Fan, Y. F. Zhao, M. H. Zhao, and E. Pan, "Analytical solution of a semi-permeable crack in a 2D piezoelectric medium based on the PS model", *Mech. Res. Commun.* **40** (2012), 34–40.

[Fan et al. 2014] C. Y. Fan, Z. H. Guo, H. Y. Dang, and M. H. Zhao, "Extended displacement discontinuity method for nonlinear analysis of penny-shaped cracks in three-dimensional piezoelectric media", *Eng. Anal. Bound. Elem.* **38** (2014), 8–16.

[Gakhov 1966] F. D. Gakhov, *Boundary value problems*, Pergamon Press, 1966.

[Gao and Barnett 1996] H. Gao and D. M. Barnett, "An invariance property of local energy release rate in a strip saturation model of piezoelectric fracture", *Int. J. Fract.* **79** (1996), R25–R29.

[Gao et al. 1997] H. Gao, T. Y. Zhang, and P. Tong, "Local and global energy release rates for an electrically yielded crack in a piezoelectric ceramic", *J. Mech. Phys. Solids* **45** (1997), 491–510.

[Gao et al. 2006] C. F. Gao, N. Noda, and T. Y. Zhang, "Dielectric breakdown model for a conductive crack and electrode in piezoelectric materials", *Int. J. Eng. Sci.* **44:3–4** (2006), 256–272.

[Govorukha and Kamlah 2010] V. Govorukha and M. Kamlah, "On contact zone models for an electrically limited permeable interface crack in a piezoelectric bi-material", *Int. J. Fract.* **164(1)** (2010), 133–146.

[Herrmann and Loboda 2003] K. P. Herrmann and V. V. Loboda, "Fracture mechanical assessment of interface cracks with contact zones in piezoelectric bimaterials under thermoelectromechanical loadings, I: Electrically permeable interface cracks", *Int. J. Solids Struct.* **40** (2003), 4191–4217.

[Jeong et al. 2004] K. M. Jeong, I. O. Kim, and H. G. Beom, "Effect of electric displacement saturation on the stress intensity factor for a crack in a ferroelectric ceramic", *Mech. Res. Comm.* **31** (2004), 371–382.

[Knysh et al. 2012] P. Knysh, V. Loboda, F. Labesse-Jied, and Y. Lapusta, "An electrically charged crack in a piezoelectric material under remote electromechanical loading", *Lett. Fract. Micromech.* **175**:1 (2012), 87–94.

[Lapusta and Loboda 2009] Y. Lapusta and V. Loboda, "Electro-mechanical yielding for a limited permeable crack in an interlayer between piezoelectric materials", *Mech. Res. Commun.* **36** (2009), 183–192.

[Lapusta et al. 2017] Y. Lapusta, O. Onopriienko, and V. Loboda, "An interface crack with partially electrically conductive crack faces under antiplane mechanical and in-plane electric loadings", *Mech. Res. Commun.* **81** (2017), 38–43.

[Leonov and Panasyuk 1959] M. Y. Leonov and V. V. Panasyuk, "Development of the smallest cracks in a rigid body", *Appl. Mech.* **5:4** (1959), 391–401.

[Li and Chen 2008] Q. Li and H. Chen, "Solution for a semi-permeable interface crack in elastic dielectric/piezoelectric bimaterials", *J. Appl. Mech.* (*ASME*) **75(1)** (2008), 011010.

[Li et al. 2017] P.-D. Li, X.-Y. Li, G.-Z. Kang, C.-F. Gao, and R. Müller, "Crack tip electric polarization saturation of a thermally loaded penny-shaped crack in an infinite thermo-piezo-elastic medium", *Int. J. Solids Struct.* **117** (2017), 67–79.

[Loboda et al. 2008] V. Loboda, Y. Lapusta, and V. Govorukha, "Mechanical and electrical yielding for an electrically insulated crack in an interlayer between piezoelectric materials", *Int. J. Eng. Sci.* **46** (2008), 260–272.

[Loboda et al. 2010] V. Loboda, Y. Lapusta, and A. Sheveleva, "Limited permeable crack in an interlayer between piezoelectric materials with different zones of electric saturation and mechanical yielding", *Int. J. Solids Struct.* **47** (2010), 1796–1806.

[Muskhelishvili 1977] N. I. Muskhelishvili, *Some basic problems of mathematical theory of elasticity*, Noordhoff, 1977.

[Nakhmein and Nuller 1986] E. L. Nakhmein and B. M. Nuller, "Contact between an elastic half-plane and a partly separated stamp", *J. Appl. Math. Mech.* **50**:4 (1986), 507–515.

[Parton and Kudryavtsev 1988] V. Z. Parton and B. A. Kudryavtsev, *Electromagnetoelasticity*, Gordon and Breach Science Publishers, 1988.

[Peride et al. 2009] N. Peride, A. Carabineanu, and E.-M. Craciun, "Mathematical modelling of the interface crack propagation in a pre-stressed fiber reinforced elastic composite", *Comput. Mater. Sci.* **45(1)** (2009), 684–692.

[Ru 1999] C. Q. Ru, "Effect of electrical polarization saturation on stress intensity factors in a piezoelectric ceramics", *Int. J. Solids Struct.* **36** (1999), 869–883.

[Ru and Mao 1999] C. Q. Ru and X. Mao, "Conducting crack in a piezoelectric ceramics of limited electrical polarization", *J. Mech. Phys. Solids* **47** (1999), 2125–2146.

[Sladek et al. 2012] J. Sladek, V. Sladek, M. Wnsche, and C. Zhang, "Analysis of an interface crack between two dissimilar piezoelectric solids", *Eng. Fract. Mech.* **89** (2012), 114–117.

[Wang 2000] T. C. Wang, "Analysis of strip electric saturation model of crack problem in piezoelectric materials", *Int. J. Solids Struct.* **37** (2000), 6031–6049.

[Xu et al. 2015] C. H. Xu, Z. H. Zhou, X. S. Xu, and A. Y. T. Leung, "Electroelastic singularities and intensity factors for an interface crack in piezoelectric-elastic bimaterials", *Appl. Math. Model.* **39**:9 (2015), 2721–2739.

[Zhang 2004] T. Y. Zhang, "Dielectric breakdown model for an electrical impermeable crack in a piezoelectric material", *Comput. Mater. Continua* **1** (2004), 107–115.

[Zhang and Gao 2004] T. Y. Zhang and C. F. Gao, "Fracture behavior of piezoelectric materials", *Theor. Appl. Fract. Mech.* **41** (2004), 339–379.

[Zhang and Gao 2012] N. Zhang and C. F. Gao, "Effects of electrical breakdown on a conducting crack or electrode in electrostrictive solids", *Eur. J. Mech. A Solids* **32** (2012), 62–68.

[Zhang et al. 2005] T. Y. Zhang, M. H. Zhao, and C. F. Gao, "The strip dielectric breakdown model", *Int. J. Fract.* **132** (2005), 311–327.

[Zhao et al. 2013] M. H. Zhao, Z. H. Guo, C. Y. Fan, and E. Pan, "Electric and magnetic polarization saturation and breakdown models for penny shaped cracks in 3D magnetoelectroelastic media", *Int. J. Solids Struct.* **50** (2013), 1747–1754.

[Zhao et al. 2015] Y. F. Zhao, M. H. Zhao, and E. Pan, "Displacement discontinuity analysis of a nonlinear interfacial crack in three-dimensional transversely isotropic magneto-electro-elastic bi-materials", *Eng. Anal. Bound. Elem.* **61** (2015), 254–264.

[Zhao et al. 2016] M. Zhao, H. Dang, G. Xu, and C. Fan, "Dielectric breakdown model for an electrically semi-permeable penny-shaped crack", *Acta Mech. Solida Sin.* **29**:5 (2016), 536–546.

Received 15 Jun 2019. Revised 11 Nov 2019. Accepted 15 Nov 2019.

YURI LAPUSTA: yuri.lapusta@sigma-clermont.fr
Université Clermont Auvergne, CNRS, SIGMA Clermont, Institut Pascal, F-63000 Clermont-Ferrand, France

ALLA SHEVELEVA: allasheveleva@i.ua
Department of Theoretical and Computational Mechanics, Oles Honchar Dnipro National University, Dnipro, 49010, Ukraine

FRÉDÉRIC CHAPELLE: frederic.chapelle@sigma-clermont.fr
Université Clermont Auvergne, CNRS, SIGMA Clermont, Institut Pascal, F-63000 Clermont-Ferrand, France

VOLODYMYR LOBODA: loboda@dnu.dp.ua
Department of Theoretical and Computational Mechanics, Oles Honchar Dnipro National University, Dnipro, 49010, Ukraine

JOURNAL OF MECHANICS OF MATERIALS AND STRUCTURES
Vol. 15, No. 1, 2020
dx.doi.org/10.2140/jomms.2020.15.107

THERMAL BUCKLING AND FREE VIBRATION OF TIMOSHENKO FG NANOBEAMS BASED ON THE HIGHER-ORDER NONLOCAL STRAIN GRADIENT THEORY

GORAN JANEVSKI, IVAN PAVLOVIĆ AND NIKOLA DESPENIĆ

A size-dependent Timoshenko beam model is derived within the framework of the higher-order nonlocal strain gradient theory. Nonlocal equations of motion are derived through Hamilton's principle and solved by applying an analytical solution. The solution is obtained using the Navier solution procedure. The paper investigates the thermal effects on buckling and free vibrational characteristics of functionally graded (FG) size-dependent nanobeams subjected to various types of thermal loading. The influence of higher-order and lower-order nonlocal parameters and strain gradient scale on buckling and vibration are investigated for various thermal conditions. To validate the solutions, the obtained results are compared with previous research.

1. Introduction

Thermal buckling of beams, as major solid structural components, has been the topic of many studies for a number of years. The development of functionally graded materials, which are a new type of materials, has attracted increasing attention recently. Structural elements such as beams in the micro or nanolength scale are commonly used as components in electromechanical systems. Therefore, understanding the mechanical properties of a functionally graded nanobeam in a thermal environment is necessary for its practical application.

There are various methods for static and dynamic analysis of nanostructures, such as molecular dynamics simulations [Neek-Amal and Peeters 2010; Alshehri and Hill 2017] and nonclassical continuum mechanics. Eringen's nonlocal elasticity theory [Eringen 1983; 2002] is one of the nonclassical continuum methods, which includes size-dependent effects, i.e., where stress at a reference point depends not only on the strain in this point but also on the strain in other points in the nearby region. The gradient elasticity theories [Aifantis 1992; Mindlin 1964] are also examples of the nonclassical continuum theories that can predict the stiffness enhancement effect. Based on the gradient elasticity theories, materials should be considered as atoms with a higher-order deformation mechanism at a small scale.

Lim et al. [2015] presented the higher-order nonlocal strain gradient theory starting from the point of view that the length scale present in the nonlocal elasticity and the strain gradient theory describe two entirely different physical characteristics. The nonlocal elasticity theory does not include nonlocality of higher-order stress. On the other hand, the strain gradient theory only considers local higher-order strain gradients. The higher-order nonlocal strain theory is primarily based on the nonlocal effects of the strain gradient field, i.e., nonlocal effects in a global sense.

Keywords: Timoshenko beam theory, thermal buckling, vibration, functionally graded materials, higher-order strain gradient theory.

Ebrahimi and Salari [2015a] studied the free vibration of an FG nanobeam subjected to an in-plane thermal loading. Material properties of the FG nanobeam vary along the thickness of the beam with power law graduation in the transversal direction. Using the Timoshenko beam theory, the authors considered the influence of the thermal effect, material distribution profile and small-scale effect based on the nonlocal elasticity theory of Eringen. The Navier type solution for a simply supported nanobeam was given for the first time. Temperature varied linearly as a function of thickness. For the same beam, as in the previous case, Ebrahimi and Salari [2016] studied the free vibration of the FG nanobeam where the temperature changed uniformly and varied linearly and nonlinearly.

The influence of the material distribution profile, thermal effect, small-scale effect, mode number and boundary conditions on the normalized natural frequencies of the temperature-dependent FG Euler–Bernoulli nanobeams was investigated in [Ebrahimi and Salari 2015b], where the nonlocal equations were solved by applying the differential transform method. Based on the nonlocal elasticity theory of Eringen, the authors considered the influence of the thermal effect, material distribution profile and small-scale effect, where the FG nanobeam was subjected to an in-plane thermal loading, which varied linearly and nonlinearly.

Li et al. [2016] studied the free vibration of an FG Timoshenko and Euler–Bernoulli nanobeam based on the nonlocal strain gradient theory. Material properties of the FG nanobeam depended on the through-thickness power-law variation of the two materials. The authors investigated the effect of the power-law and small length-scaled effect on natural frequencies of a simply supported FG nanobeam. In this paper, comparisons of the natural frequencies of Timoshenko and Euler beams were performed.

Xu et al. [2017] studied the bending and buckling of Euler–Bernoulli beams using the nonlocal strain gradient theory and the von Kármán nonlinear geometric relation.

Lu et al. [2017] studied the free vibration of the sinusoidal shear deformation of a nanobeam model based on the nonlocal strain gradient theory. Navier's method was utilized to obtain analytical solutions for natural frequencies of simply supported nanobeams.

Trinh et al. [2016] presented an analytical method for vibration of a functionally graded beam under mechanical and thermal loads. The FG nanobeam was subjected to an in-plane thermal loading, where three types of temperature distribution through the thickness were taken into account: uniform temperature rise, linear temperature rise and nonlinear temperature rise. The effects of boundary conditions, temperature distributions and material parameters were investigated as well.

Chen et al. [2019] developed a nonlinear dynamical model for nonlocal strain gradient beams and analyzed its nonlinear free vibration. Based on the nonlocal strain gradient theory, the nonlinear governing equation of boundary conditions of the nanobeam was derived first. The effect of the slender ratio parameter, which might be also interpreted as the thickness-dependent size effect, was caused by the stress on account of the thickness-direction strain gradient. In the nonlinear free vibration analysis, an analytical solution for predicting the nonlinear free vibration frequencies was derived via the homotopy analysis method. It was shown that the nonlinear frequencies of the nanobeam display significant size-dependent phenomena for large values of the slender ratio parameter and either stiffness-softening or stiffness-hardening behavior might occur.

Based on the nonlocal strain gradient theory and various higher-order shear deformation theories, Alshujairi and Mollamahmutoğlua [2018] studied the buckling and free vibration of functionally graded sandwich microbeams resting on an elastic foundation. The authors reported on the effects of the nonlocal

parameter, the length scale parameter, gradient index, different cross-section shapes, temperature change and stiffnesses of Winkler and shear layer springs on the dimensionless critical buckling load and dimensionless frequencies.

In the manuscript [Ghazavi et al. 2018], the second strain gradient theory is applied to study the fluid-conveying Euler–Bernoulli nanotubes. Based on the high-order nonlocal strain gradient theory, Yang et al. [2018] studied the wave propagation behaviors of fluid-filled carbon nanotubes.

Ebrahimi and Haghi [2017] studied a rotating FG thermoelastic nanobeam under different temperature distributions. Based on the refined beam theory by using the nonlocal strain gradient theory, the authors analyzed the effects of temperature changes, angular velocity, nonlocal parameter, length scale parameter and material graduation on wave dispersion characteristics.

Pavlović et al. [2019a; 2019b] studied the stability and instability problem of a nanobeam subjected to the compressive axial load based on the higher-order nonlocal strain gradient theory. According to the direct Lyapunov method, the authors obtained the bounds of the almost sure asymptotic stability and instability, which was verified by numerical results using the Monte Carlo simulation method.

In this paper, size-dependent Timoshenko nanobeam models, which account for through-thickness power-law variation of two-constituent FG materials, will be deduced within the framework of the higher-order nonlocal strain gradient theory. This theory is employed to study effects of the buckling and vibrational behavior of nanobeams in different thermal environments. Equations of motion will be derived using Hamilton's principle. By employing an analytical solution procedure, the closed-form critical buckling temperature and frequency will be obtained for simply supported boundary conditions. The obtained results are compared with the literature to confirm the validity of the solution. The influence of higher-order and lower-order nonlocal parameters and strain gradient scale on buckling and vibration will be investigated. Finally, certain important conclusions will be summarized.

2. Mathematical model

2.1. ***Problem description.*** Consider a nanobeam of functionally graded material, where the graded properties are assumed to be in the through-thickness direction. The system of interest is a rectangular functionally graded nanobeam of length L, width b and thickness h (Figure 1). The beam is subjected to an in-plane thermal loading, where, according to the rule of mixture, the effective material properties P_f are distributed as [Şimşek and Yurtcu 2013]

$$P_f(T,z) = P_c(T)\,V_c(z) + P_m(T)\,V_m(z), \tag{1}$$

where the volume fraction of the ceramic $V_c(z)$ and the volume fraction of the metal $V_m(z)$ constituent of the beam may be expressed using the power-law distribution

$$V_c(z) = \left(\frac{1}{2} + \frac{z}{h}\right)^p, \quad V_m(z) = 1 - V_c(z), \quad -\frac{h}{2} \le z \le \frac{h}{2}. \tag{2}$$

The temperature-dependent material properties (such as Young's modulus E, thermal expansion coefficient α, mass density ρ, thermal conductivity κ and Poisson's ratio ν) can be written as [Touloukian 1967]

$$P(T) = P_0(P_{-1}T^{-1} + 1 + P_1T + P_2T^2 + P_3T^3), \tag{3}$$

Figure 1. Geometry and coordinates of the functionally graded beam.

material	properties	P_0	P_{-1}	P_1	P_2	P_3
Si_3N_4	E (Pa)	$348.4300 \cdot 10^9$	0	$-3.010 \cdot 10^{-4}$	$2.160 \cdot 10^{-7}$	$-8.946 \cdot 10^{-11}$
	α (K^{-1})	$5.8723 \cdot 10^{-6}$	0	$9.095 \cdot 10^{-4}$	0	0
	ρ (kg/m^3)	2370	0	0	0	0
	κ (W/mK)	13.723	0	$-1.032 \cdot 10^{-3}$	$5.466 \cdot 10^{-7}$	$-7.876 \cdot 10^{-11}$
	ν	0.24	0	0	0	0
SU 304	E (Pa)	$201.0400 \cdot 10^9$	0	$3.079 \cdot 10^{-4}$	$-6.534 \cdot 10^{-7}$	0
	α (K^{-1})	$12.3300 \cdot 10^{-6}$	0	$8.086 \cdot 10^{-4}$	0	0
	ρ (kg/m^3)	8166	0	0	0	0
	κ (W/mK)	15.3790	0	$-1.264 \cdot 10^{-3}$	$2.092 \cdot 10^{-6}$	$-7.223 \cdot 10^{-10}$
	ν	0.3262	0	$-2.002 \cdot 10^{-4}$	$3.797 \cdot 10^{-7}$	0

Table 1. Temperature-dependent coefficient of Young's modulus E, thermal expansion coefficient α, mass density ρ, thermal conductivity κ and Poisson's ratio ν for Si_3N_4 and SUS 304.

where P_0, P_{-1}, P_1, P_2 and P_3 are the coefficients that can be seen in the table of material properties for Si_3N_4 and SUS 304 (Table 1).

For the power-law distribution (2), the effective material properties are

$$P(z, T) = \big(P_c(T) - P_m(T)\big)\left(\frac{z}{h} + \frac{1}{2}\right)^p + P_m(T). \tag{4}$$

The bottom surface ($z = -h/2$) of the FG beam is pure metal (SUS 304) and the top surface ($z = h/2$) is pure ceramic (Si_3N_4).

2.2. ***The higher-order nonlocal strain gradient model for the FG nanobeam.*** Based on the higher-order nonlocal strain gradient theory [Lim et al. 2015], the nonlocal stress in a reference point x depends not only on the strain at that location but also on the strains in all other points in the nearby region. According to this theory, the internal strain energy density function can be expressed as

$$U_0 = \frac{1}{2} C_{ijkl}\, \varepsilon_{ij} \int_V \alpha_0(|x - x'|, e_0\, a)\, \varepsilon'_{kl}\, dV' + \frac{l^2}{2}\, C_{ijkl}\, \varepsilon_{ij,m} \int_V \alpha_1(|x - x'|, e_1 a)\, \varepsilon'_{kl,m}\, dV', \tag{5}$$

where C_{ijkl} is the elastic modulus tensor of classical elasticity, ε_{ij} and ε'_{ij} are the Cartesian components of the strain tensor in points x and x'; α_0 and α_1 are the kernel function related to the nonlocal effects

with respect to the strain field and the first order strain gradient field; e_0 and e_1 are the nonlocal material constants, a is the internal characteristic length and l is the strain gradient length scale parameter.

By using (5), the classical stress tensor $\boldsymbol{\sigma}$, the higher-order stress tensor $\boldsymbol{\sigma}^{(1)}$ and the total stress $\boldsymbol{t}$ can be written as

$$\boldsymbol{\sigma} = \int_V \boldsymbol{\alpha}_0(|x-x'|, e_0\, a)\, C : \boldsymbol{\varepsilon}'\, dV', \quad \boldsymbol{\sigma}^{(1)} = l^2 \int_V \boldsymbol{\alpha}_1(|x-x'|, e_0\, a)\, C : \nabla\boldsymbol{\varepsilon}'\, dV', \quad \boldsymbol{t} = \boldsymbol{\sigma} - \nabla\boldsymbol{\sigma}^{(1)}. \tag{6}$$

In (6) the symbol ":" is used to denote the double-dot product. For an elastic material in the one-dimensional case, the generalized nonlocal constitutive relations in a differential form based on the higher-order nonlocal strain gradient theory may be simplified as

$$\left(1-\mu_1\frac{\partial^2}{\partial x^2}\right)\left(1-\mu_0\frac{\partial^2}{\partial x^2}\right) t_{xx} = E\left[\left(1-\mu_1\frac{\partial^2}{\partial x^2}\right) - l^2\left(1-\mu_0\frac{\partial^2}{\partial x^2}\right)\frac{\partial^2}{\partial x^2}\right]\varepsilon_{xx}, \tag{7}$$

$$\left(1-\mu_1\frac{\partial^2}{\partial x^2}\right)\left(1-\mu_0\frac{\partial^2}{\partial x^2}\right) t_{xz} = G\left[\left(1-\mu_1\frac{\partial^2}{\partial x^2}\right)\frac{\partial^2}{\partial x^2} - l^2\left(1-\mu_0\frac{\partial^2}{\partial x^2}\right)\frac{\partial^2}{\partial x^2}\right]\gamma_{xz}, \tag{8}$$

where $\mu_0 = (e_0\, a)^2$ and $\mu_1 = (e_1 a)^2$. The normal and shear components of the total stress tensor of the nonlocal strain gradient theory are defined as

$$t_{xx} = \sigma_{xx} - \frac{\partial\sigma_{xx}^{(1)}}{\partial x}, \quad t_{xz} = \sigma_{xz} - \frac{\partial\sigma_{xz}^{(1)}}{\partial x}, \tag{9}$$

where σ_{xx} and σ_{xz} are the classical normal stress and classical shear stress components, $\sigma_{xx}^{(1)}$ and $\sigma_{xz}^{(1)}$ are the higher-order normal stress and higher-order shear stress components, ε_{xx} and γ_{xz} are the E normal strain and shear strain, E is Young's modulus, $G = E/2(1+\nu)$ is the shear modulus, ν is Poisson's ratio. It is worth mentioning that for certain cases, the effect of structural thickness on the constitutive behaviors of nanostructures is studied in [Tang et al. 2019; Li et al. 2018; Chen et al. 2019].

2.3. ***Kinematic relations.*** The displacement components of any material point in the x, y and z direction can be written as

$$q_x = u(x,t) + z\varphi(x,t), \tag{10}$$

$$q_z = w(x,t), \tag{11}$$

where u and w are the displacement components of the mid-plane in the x and z direction, φ is the total bending rotation of the cross-section and t is the time. Using (10) and (11), the nonzero components of the beam are obtained as

$$\varepsilon_{xx} = \frac{\partial u}{\partial x} + z\frac{\partial\varphi}{\partial x}, \tag{12}$$

$$\gamma_{xz} = \frac{\partial w}{\partial x} + \varphi. \tag{13}$$

The governing equations of motion are obtained based on Hamilton's principle, which is expressed as

$$\int_{t_1}^{t_2} (\delta U + \delta V - \delta K)\, dt = 0, \tag{14}$$

in a time interval $t_1 < t < t_2$; δU is the virtual strain energy:

$$\begin{aligned}\delta U &= \int_V \left(\sigma_{xx}\,\delta\varepsilon_{xx} + \sigma_{xz}\,\delta\gamma_{xz} + \sigma_{xx}^{(1)} \frac{\partial(\delta\varepsilon_{xx})}{\partial x} + \sigma_{xz}^{(1)} \frac{\partial(\delta\varepsilon_{xz})}{\partial x} \right) dv \\ &= \int_L \left(N\delta\frac{\partial u}{\partial x} + M\delta\frac{\partial \varphi}{\partial x} + Q\delta\frac{\partial w}{\partial x} + Q\delta\varphi \right) dx + \left[N^{(1)}\delta\frac{\partial u}{\partial x} + M^{(1)}\delta\frac{\partial \varphi}{\partial x} + Q^{(1)}\delta\frac{\partial w}{\partial x} + Q^{(1)}\delta\varphi \right]_0^L. \end{aligned} \tag{15}$$

Here we consider the following stress resultant:

$$\begin{aligned} N &= \int_A t_{xx}\,dA, \qquad M = \int_A z t_{xx}\,dA, \qquad Q = k_s \int_A t_{xz}\,dA, \\ N^{(1)} &= \int_A \sigma_{xx}^{(1)}\,dA, \quad M^{(1)} = \int_A z\sigma_{xx}^{(1)}\,dA, \quad Q^{(1)} = k_s \int_A \sigma_{xz}^{(1)}\,dA, \end{aligned} \tag{16}$$

where $k_s = \frac{5}{6}$ is the shear correction factor; δV is the variation of the work by thermal expansion:

$$\delta V = -\int_V E(T,z)\,\alpha(T,z)(T-T_0)\frac{\partial w}{\partial x}\frac{\partial}{\partial x}(\delta w)\,dv = -\int_0^L \left(N^T \frac{\partial w}{\partial x}\frac{\partial}{\partial x}(\delta w) \right) dx, \tag{17}$$

where N^T is the thermal resultant:

$$N^T = \int_{-h/2}^{h/2} E(T,z)\,\alpha(T,z)(T-T_0)\,b\,dz, \tag{18}$$

and $T_0 = 300\,\mathrm{K}$ is the reference temperature; δK is the virtual kinetic energy:

$$\begin{aligned}\delta K &= \frac{1}{2}\int_v \rho(T,z)\,\delta\left[\left(\frac{\partial q_x}{\partial t}\right)^2 + \left(\frac{\partial q_z}{\partial t}\right)^2 \right] dv \\ &= \int_0^L \left\{ I_0 \left[\frac{\partial u}{\partial t}\delta\left(\frac{\partial u}{\partial t}\right) + \frac{\partial w}{\partial t}\delta\left(\frac{\partial w}{\partial t}\right) \right] + I_1 \left[\frac{\partial \varphi}{\partial t}\delta\left(\frac{\partial u}{\partial t}\right) + \frac{\partial u}{\partial t}\delta\left(\frac{\partial \varphi}{\partial t}\right) \right] + I_2 \frac{\partial \varphi}{\partial t}\delta\left(\frac{\partial \varphi}{\partial t}\right) \right\} dx, \end{aligned} \tag{19}$$

where the mass moments of inertia are defined as

$$(I_0, I_1, I_2) = \int_A (1, z, z^2)\,\rho(z,T)\,dA. \tag{20}$$

By substituting (15), (17) and (19) into (14), using integration by parts and setting the coefficients of δu, δw, $\delta\varphi$ to zero, one obtains the following governing equations of motion based on the Timoshenko beam theory

$$\delta u\text{:}\ \frac{\partial N}{\partial x} = I_0\frac{\partial^2 u}{\partial t^2} + I_1\frac{\partial^2 \varphi}{\partial t^2}, \tag{21}$$

$$\delta w\text{:}\ \frac{\partial Q}{\partial x} - N^T\frac{\partial^2 w}{\partial x^2} = I_0\frac{\partial^2 w}{\partial t^2}, \tag{22}$$

$$\delta\varphi\text{:}\ \frac{\partial M}{\partial x} - Q = I_1\frac{\partial^2 u}{\partial t^2} + I_2\frac{\partial^2 \varphi}{\partial t^2}, \tag{23}$$

with the classical boundary conditions (at $x = 0$ or $x = L$)

$$\delta u\colon N = 0, \qquad \text{or } u = 0, \tag{24}$$

$$\delta w\colon Q - N^T \frac{\partial w}{\partial x} = 0, \quad \text{or } w = 0, \tag{25}$$

$$\delta \varphi\colon M = 0, \qquad \text{or } \varphi = 0, \tag{26}$$

and the nonclassical boundary conditions (at $x = 0$ or $x = L$)

$$\delta \frac{\partial u}{\partial x}\colon N^{(1)} = 0, \quad \text{or } \frac{\partial u}{\partial x} = 0, \tag{27}$$

$$\delta\left(\frac{\partial w}{\partial x} + \varphi\right)\colon Q^{(1)} = 0, \quad \text{or } \frac{\partial w}{\partial x} + \varphi = 0, \tag{28}$$

$$\delta \frac{\partial \varphi}{\partial x}\colon M^{(1)} = 0, \quad \text{or } \frac{\partial \varphi}{\partial x} = 0. \tag{29}$$

Considering the above and integrating (7) and (8) over the beam's cross-section, the force-strain and moment-strain relation can be obtained as

$$\left(1 - \mu_1 \frac{\partial^2}{\partial x^2}\right)\left(1 - \mu_0 \frac{\partial^2}{\partial x^2}\right) N = A_{xx}\left[\left(1 - \mu_1 \frac{\partial^2}{\partial x^2}\right) - l^2\left(1 - \mu_0 \frac{\partial^2}{\partial x^2}\right)\frac{\partial^2}{\partial x^2}\right]\frac{\partial u}{\partial x} + B_{xx}\left[\left(1 - \mu_1 \frac{\partial^2}{\partial x^2}\right) - l^2\left(1 - \mu_0 \frac{\partial^2}{\partial x^2}\right)\frac{\partial^2}{\partial x^2}\right]\frac{\partial \varphi}{\partial x}, \tag{30}$$

$$\left(1 - \mu_1 \frac{\partial^2}{\partial x^2}\right)\left(1 - \mu_0 \frac{\partial^2}{\partial x^2}\right) M = B_{xx}\left[\left(1 - \mu_1 \frac{\partial^2}{\partial x^2}\right) - l^2\left(1 - \mu_0 \frac{\partial^2}{\partial x^2}\right)\frac{\partial^2}{\partial x^2}\right]\frac{\partial u}{\partial x} + D_{xx}\left[\left(1 - \mu_1 \frac{\partial^2}{\partial x^2}\right) - l^2\left(1 - \mu_0 \frac{\partial^2}{\partial x^2}\right)\frac{\partial^2}{\partial x^2}\right]\frac{\partial \varphi}{\partial x}, \tag{31}$$

$$\left(1 - \mu_1 \frac{\partial^2}{\partial x^2}\right)\left(1 - \mu_0 \frac{\partial^2}{\partial x^2}\right) Q = C_{xz}\left[\left(1 - \mu_1 \frac{\partial^2}{\partial x^2}\right) - l^2\left(1 - \mu_0 \frac{\partial^2}{\partial x^2}\right)\frac{\partial^2}{\partial x^2}\right]\left(\frac{\partial w}{\partial x} + \varphi\right), \tag{32}$$

in which the cross-sectional rigidities are

$$(A_{xx}, B_{xx}, D_{xx}) = \int_A (1, z, z^2)\, E(z, T)\, dA, \quad C_{xz} = k_s \int_A G(z, T)\, dA. \tag{33}$$

We introduce the following dimensionless parameters

$$\xi = \frac{x}{L}, \quad U(\xi, \tau) = \frac{u(x, t)}{L}, \quad W(\xi, \tau) = \frac{w(x, t)}{L}, \quad \tau = \frac{t}{L^2}\sqrt{\frac{E_c(T_c) I}{\rho_c(T_c) A}}, \tag{34}$$

where $E_c(T_c)$ and $\rho_c(T_c)$ are Young's modulus and the mass density of ceramic Si_3N_4 at the temperature T_c, $I = \frac{1}{12} bh^3$ is the moment of inertia of the rectangular cross-section of the beam and $A = bh$. The explicit relation of the nonlocal normal force, bending moment and shear force can be derived by

substituting the second and fourth derivative of these values from (21)÷(23) into (30)÷(32) as

$$N = A_{xx}\left\{\mathcal{L}_{(3)}\left[\frac{\partial U}{\partial \xi}+k_B\frac{\partial \varphi}{\partial \xi}\right]+k_I\mathcal{L}_{(2)}\left[k_{I0}\frac{\partial^3 U}{\partial \xi\,\partial \tau^2}+k_{I1}\frac{\partial^3 \varphi}{\partial \xi\,\partial \tau^2}\right]\right\}, \tag{35}$$

$$M = A_{xx}L\left\{\mathcal{L}_{(3)}\left[k_B\frac{\partial U}{\partial \xi}+k_D\frac{\partial \varphi}{\partial \xi}\right]+\mathcal{L}_{(2)}\left[k_N\frac{\partial^2 W}{\partial \xi^2}+k_Ik_{I0}\frac{\partial^2 W}{\partial \tau^2}+k_Ik_{I1}\frac{\partial^3 U}{\partial \xi\,\partial \tau^2}+k_Ik_{I2}\frac{\partial^3 \varphi}{\partial \xi\,\partial \tau^2}\right]\right\}, \tag{36}$$

$$Q = A_{xx}\left\{k_C\mathcal{L}_{(3)}\left[\frac{\partial W}{\partial \xi}+\varphi\right]+\mathcal{L}_{(2)}\left[k_Ik_{I0}\frac{\partial^3 W}{\partial \xi\,\partial \tau^2}+k_N\frac{\partial^3 W}{\partial \xi^3}\right]\right\}, \tag{37}$$

where the linear differential operators are

$$\begin{gathered}\mathcal{L}_{(0)} = 1-k_{\mu 0}\nabla^2, \quad \mathcal{L}_{(1)} = 1-k_{\mu 1}\nabla^2, \quad \mathcal{L}_{(2)} = (k_{\mu 0}+k_{\mu 1})-k_{\mu 0}k_{\mu 1}\nabla^2,\\ \mathcal{L}_{(3)} = \mathcal{L}_{(1)}-k_l\mathcal{L}_{(0)}\nabla^2 = 1-(k_{\mu 1}+k_l)\nabla^2+k_{\mu 0}k_l\nabla^4, \quad \nabla = \frac{\partial}{\partial \xi},\end{gathered} \tag{38}$$

and the marks are

$$\begin{gathered}k_B = \frac{B_{xx}}{A_{xx}L}, \quad k_C = \frac{C_{xz}}{A_{xx}}, \quad k_D = \frac{D_{xx}}{A_{xx}L^2}, \quad k_N = \frac{N^T}{A_{xx}},\\ k_I = \frac{I}{AL^2}, \quad k_{I0} = \frac{E_c(T_c)\,I_0}{\rho_c(T_c)\,A_{xx}}, \quad k_{I1} = \frac{E_c(T_c)\,I_1}{\rho_c(T_c)\,A_{xx}\,L}, \quad k_{I2} = \frac{E_c(T_c)\,I_2}{\rho_c(T_c)A_{xx}\,L^2},\\ k_l = \frac{l^2}{L^2}, \quad k_{\mu 0} = \frac{\mu_0}{L^2}, \quad k_{\mu 1} = \frac{\mu_1}{L^2}.\end{gathered} \tag{39}$$

Substituting the derivative for N, M and Q from (35)÷(37) into (21)÷(23), the nonlocal governing equations of the Timoshenko FG nanobeam can be derived as

$$\mathcal{L}_{(3)}\left[\frac{\partial^2 U}{\partial \xi^2}+k_B\frac{\partial^2 \varphi}{\partial \xi^2}\right]-k_I\mathcal{L}_{(4)}\left[k_{I0}\frac{\partial^2 U}{\partial \tau^2}+k_{I1}\frac{\partial^2 \varphi}{\partial \tau^2}\right] = 0, \tag{40}$$

$$\mathcal{L}_{(3)}\left[k_B\frac{\partial^2 U}{\partial \xi^2}+k_D\frac{\partial^2 \varphi}{\partial \xi^2}-k_C\left(\frac{\partial W}{\partial \xi}+\varphi\right)\right]-k_I\mathcal{L}_{(4)}\left[k_{I1}\frac{\partial^2 U}{\partial \tau^2}+k_{I2}\frac{\partial^2 \varphi}{\partial \tau^2}\right] = 0, \tag{41}$$

$$k_C\mathcal{L}_{(3)}\left[\frac{\partial^2 W}{\partial \xi^2}+\frac{\partial \varphi}{\partial \xi}\right]-k_N\mathcal{L}_{(4)}\left[\frac{\partial^2 W}{\partial \xi^2}\right]-k_Ik_{I0}\mathcal{L}_{(4)}\left[\frac{\partial^2 W}{\partial \tau^2}\right] = 0, \tag{42}$$

where the linear differential operator is $\mathcal{L}_{(4)} = \mathcal{L}_{(0)}\mathcal{L}_{(1)} = 1-(k_{\mu 0}+k_{\mu 1})\nabla^2+k_{\mu 0}k_{\mu 1}\nabla^4$.

2.4. ***Temperature rise.*** In the case of a uniform temperature rise (UTR), the temperature of the FG beam uniformly rises by ΔT. Since the temperature is constant in the z-direction, then

$$T(z) = T_0+\Delta T = \text{const.} \tag{43}$$

In the case of a linear temperature rise (LTR), the temperature of the FG beam varies linearly along the thickness of the beam

$$T(z) = T_m+\Delta T\left(\frac{1}{2}+\frac{z}{h}\right), \tag{44}$$

where the temperature of the top and the bottom surface of the nanobeam are

$$T_c = T(h/2), \quad T_m = T(-h/2), \tag{45}$$

where $\Delta T = T_c - T_m$. In this paper, it is assumed that the temperature of the bottom surface is $T_m = T_0 + 5 = 305\,\mathrm{K}$.

In the case of heat conduction across the thickness, the temperature of the FG nanobeam varies nonlinearly (NLTR) along the thickness of the beam. The one-dimensional steady state heat conduction problem can be formulated by a differential equation [Fu et al. 2012]

$$\frac{d}{dz}\left(\kappa(z,T)\frac{dT(z)}{dz}\right) = 0, \tag{46}$$

where the known temperature boundary conditions on the bottom and the top surface are given as in (45). In order to present an analytical solution for (46), it is common to assume that thermal conductivity $\kappa = \kappa(z)$ is independent of temperature. Taking this into account, the solution of (46) can be obtained in a power series as

$$T(z) = T_m + \frac{\Delta T}{\lambda}\sum_{i=0}^{n}\frac{1}{ki+1}\left(\frac{1}{2}+\frac{z}{h}\right)^{ki+1}\left(\frac{\kappa_m-\kappa_c}{\kappa_m}\right)^{i}, \tag{47}$$

where

$$\lambda = \sum_{i=0}^{n}\frac{1}{ki+1}\left(\frac{\kappa_m-\kappa_c}{\kappa_m}\right)^{i}. \tag{48}$$

2.5. ***Solution procedures.*** This section presents the analytical solutions for the vibration problem described by equations (40)÷(42). The Navier solution approach will be used to determine the analytical solutions of vibration frequencies and critical buckling temperature for simply supported boundary conditions. In the case of simply supported boundary conditions, one should specify the classical boundary conditions

$$N = 0, \quad w = 0, \quad \text{and} \quad M = 0, \quad (\text{at } \xi = 0 \text{ and } \xi = 1). \tag{49}$$

As stated above, we consider the nonclassical boundary conditions in the case of the Timoshenko beam

$$\frac{\partial u}{\partial x} = 0, \quad Q^{(1)} = 0, \quad \text{and} \quad \frac{\partial \varphi}{\partial x} = 0, \quad (\text{at } \xi = 0 \text{ and } \xi = 1). \tag{50}$$

By using (6), (9) and (12), $Q^{(1)}$ can be obtained in the displacement form

$$Q^{(1)} = A_{xx}\left\{k_C\left[\frac{k_{\mu 1}^2}{k_{\mu 0}-k_{\mu 1}}\mathcal{L}_{(0)}\mathcal{L}_{(3)} - \frac{k_{\mu 1}^2 - k_l^2(k_{\mu 0}-k_{\mu 1})}{k_{\mu 0}-k_{\mu 1}}\left(1 - \frac{k_{\mu 0}k_{\mu 1}k_l^2}{k_{\mu 1}^2 - k_l^2(k_{\mu 0}-k_{\mu 1})}\nabla^2\right)\right]\left(\frac{\partial^2 W}{\partial \xi^2} + \frac{\partial \varphi}{\partial \xi}\right)\right.$$
$$\left. + \frac{k_{\mu 1}^2}{k_{\mu 0}-k_{\mu 1}}\mathcal{L}_{(1)}\mathcal{L}_{(2)}\left(k_I k_{I0}\frac{\partial^3 W}{\partial \xi\, \partial \tau^2} + k_N \frac{\partial^3 W}{\partial \xi^3}\right)\right\}. \tag{51}$$

The displacement functions can be assumed to be periodic in time in the form

$$U(\xi,\tau)=\sum_{n=1}^{\infty}U_n\cos(n\pi\xi)\,e^{i\omega_n\tau}, \tag{52}$$

$$W(\xi,\tau)=\sum_{n=1}^{\infty}W_n\sin(n\pi\xi)\,e^{i\omega_n\tau}, \tag{53}$$

$$\varphi(\xi,\tau)=\sum_{n=1}^{\infty}\varphi_n\cos(n\pi\xi)\,e^{i\omega_n\tau}, \tag{54}$$

where $i=\sqrt{-1}$, U_j, W_j, φ_j $(j=1,2,\ldots,n)$ are the unknown Fourier coefficients to be determined for each n value and ω_n is the frequency of vibration. It can be checked that the series solution (52)÷(54) satisfies the classical boundary conditions (24)÷(26) and nonclassical boundary conditions (27)÷(29).

Eliminating U and φ from (40)÷(42), the governing differential equation becomes

$$\mathcal{L}_{(8)}\big(\mathcal{L}_{(5)}\mathcal{L}_{(7)}-\mathcal{L}_{(6)}^2\big)W+k_C^2\,\mathcal{L}_{(3)}^2\,\mathcal{L}_{(5)}\frac{\partial^2 W}{\partial\xi^2}=0, \tag{55}$$

where the linear differential operators are

$$\mathcal{L}_{(5)}=\mathcal{L}_{(3)}\nabla^2-k_I\,k_{I0}\,\mathcal{L}_{(4)}\frac{\partial^2}{\partial\tau^2}, \qquad \mathcal{L}_{(6)}=k_B\,\mathcal{L}_{(3)}\nabla^2-k_I\,k_{I1}\,\mathcal{L}_{(4)}\frac{\partial^2}{\partial\tau^2}, \tag{56}$$

$$\mathcal{L}_{(7)}=k_D\,\mathcal{L}_{(3)}\nabla^2-k_C\,\mathcal{L}_{(3)}-k_I\,k_{I2}\,\mathcal{L}_{(4)}\frac{\partial^2}{\partial\tau^2}, \quad \mathcal{L}_{(8)}=(k_C\,\mathcal{L}_{(3)}-k_N\,\mathcal{L}_{(4)})\nabla^2-k_I\,k_{I0}\,\mathcal{L}_{(4)}\frac{\partial^2}{\partial\tau^2}. \tag{57}$$

Substituting (53) into (55) and neglecting the coefficient of ω_n^6, we get the following characteristic equation

$$\alpha_4^2A_\omega\,\omega_n^4+\alpha_3\,\alpha_4B_\omega\,\omega_n^2+\alpha_3^2C_\omega=0, \tag{58}$$

where

$$\begin{aligned}
A_\omega&=-k_I^2\big[(\alpha_1\alpha_6+\alpha_3\alpha_5\,k_{I0})\,n^2\pi^2+\alpha_3\,k_C\,k_{I0}^2\big],\\
B_\omega&=k_I[(\alpha_2\alpha_3\,k_{I0}+\alpha_1\alpha_5)\,n^4\pi^4-k_C\,k_{I0}(\alpha_3-k_N\,\alpha_4)]\,n^2\pi^2,\\
C_\omega&=k_C\,k_N\,\alpha_4\,n^4\pi^4-\alpha_1\alpha_2\,n^6\pi^6,\\
\alpha_1&=k_C\,\alpha_3-k_N\,\alpha_4,\\
\alpha_2&=k_D-k_B^2,\\
\alpha_3&=1+(k_{\mu1}+k_l)\,n^2\pi^2+k_{\mu0}\,k_l\,n^4\pi^4,\\
\alpha_4&=1+(k_{\mu0}+k_{\mu1})\,n^2\pi^2+k_{\mu0}\,k_{\mu1}\,n^4\pi^4,\\
\alpha_5&=k_{I2}-2k_B\,k_{I1}+k_D\,k_{I0},\\
\alpha_6&=k_{I0}\,k_{I2}-k_{I1}^2.
\end{aligned} \tag{59}$$

The smaller root (the eigenvalue $\lambda_n = \omega_n^2$) of (58) is

$$\omega_n^2 = \frac{\alpha_3}{\alpha_4}\,\frac{-B_\omega + \sqrt{B_\omega^2 - 4A_\omega C_\omega}}{2A_\omega}. \tag{60}$$

By setting the fundamental frequency ω_1 to zero, we find the critical buckling temperature $\Delta T_{\rm cr}$ (for $n = 1$). This condition is satisfied if the coefficient $C_\omega = 0$. After a simple transformation, we come to a relation among the parameters of the system that meets the required condition

$$k_l = \frac{1 + k_{\mu 1}\, n^2\pi^2}{1 + k_{\mu 0}\, n^2\pi^2}\,\frac{k_N(1 + k_{\mu 0}\, n^2\pi^2)(k_C + \alpha_2\, n^2\pi^2) - k_C\,\alpha_2\, n^2\pi^2}{k_C\,\alpha_2\, n^4\pi^4}. \tag{61}$$

It is interesting that the parameters of the system (59) can be simplified to certain interesting cases:

Case 1 (Eringen's nonlocal continuum theory). In the case where the strain gradient length scale ($l = 0$) and the nonlocal parameter ($\mu_1 = 0$) are zero, the parameters of system (59) are

$$\begin{aligned}
A_\omega &= -k_I^2\big\{k_C\, k_{I0}^2 + n^2\pi^2[k_{I0}\,\alpha_5 + k_C\,\alpha_6 - k_N\,\alpha_6(1 + k_{\mu 0}\, n^2\pi^2)]\big\},\\
B_\omega &= k_I\, n^2\pi^2[k_C\, k_{I0} + n^2\pi^2(k_{I0}\,\alpha_2 + k_C\,\alpha_5) - k_N(1 + k_{\mu 0}\, n^2\pi^2)(k_C\, k_{I0} + \alpha_5\, n^2\pi^2)],\\
C_\omega &= n^4\pi^4[k_N(1 + k_{\mu 0}\, n^2\pi^2)(k_C + \alpha_2\, n^2\pi^2) - k_C\,\alpha_2\, n^2\pi^2],\\
\frac{\alpha_3}{\alpha_4} &= \frac{1}{1 + k_{\mu 0}\, n^2\pi^2}.
\end{aligned} \tag{62}$$

By setting the strain gradient length scale ($l = 0$) and the nonlocal parameter ($\mu_1 = 0$) to zero we can find the critical temperature $\Delta T_{\rm cr}$ from (61) as

$$k_{\mu 0} = \frac{\alpha_2\, n^2\pi^2(k_C - k_N) - k_C k_N}{k_N\, n^2\pi^2(k_C + \alpha_2\, n^2\pi^2)}. \tag{63}$$

Case 2 (classical continuum theory). In the case where the strain gradient length scale ($l = 0$) and the nonlocal parameters ($\mu_0 = 0,\ \mu_1 = 0$) are zero, the parameters of the system are

$$\begin{aligned}
A_\omega &= -k_I^2\{k_C\, k_{I0}^2 + n^2\pi^2[k_{10}\,\alpha_5 + \alpha^6(k_C - k_N)]\},\\
B_\omega &= k_I\, n^2\pi^2\{k_C\, k_{I0}(1 - k_N) + n^2\pi^2[k_{I0}\,\alpha_2 + \alpha_5(k_C - k_N)]\},\\
C_\omega &= n^4\pi^4[k_C\, k_N - \alpha_2\, n^2\pi^2(k_C - k_N)],\\
\frac{\alpha_3}{\alpha_4} &= 1.
\end{aligned} \tag{64}$$

In a special case of the homogenous beam, based on expressions (20), (33) and (39), one can obtain

$$k_{I0} = 1, \quad k_{I1} = 0, \quad k_{I2} = k_I, \quad k_B = 0, \quad k_C = \frac{k_s}{2(1 + \nu)}, \quad k_D = k_I. \tag{65}$$

Based on expressions (60), (64) and (65), the frequencies of the beam can be derived as

$$\omega_n^2 = \frac{1}{2k_I^2}\,\frac{k_s k_I\, n^2\pi^2(1 - k_N) + 2k_I^2 n^4\pi^4[1 + \nu + k_s - 2k_N(1 + \nu)] - k_I\, n^2\pi^2\sqrt{D}}{k_s + k_I\, n^2\pi^2[k_s + 2(1 + \nu)(2 - k_N)]}, \tag{66}$$

where

$$D=[k_s(1+k_N)+2k_I n^2\pi^2(1+\nu)]^2+8k_N k_I n^2\pi^2(1+\nu)[k_s+2k_I n^2\pi^2(1+\nu)]-8k_s k_I^2 n^4\pi^4(1+\nu). \quad (67)$$

Finally, in the case when the homogenous beam is without a thermal environment ($k_N = 0$), the frequencies of the beam can be derived as

$$\omega_n^2=\frac{1}{2k_I^2}\frac{k_s k_I n^2\pi^2+2k_I^2 n^4\pi^4(1+\nu+k_s)-k_I n^2\pi^2\sqrt{[k_s+2k_I n^2\pi^2(1+\nu)]^2-8k_s k_I^2 n^4\pi^4(1+\nu)}}{k_s+k_I n^2\pi^2[k_s+4(1+\nu)]}. \quad (68)$$

Case 3. In the case where the strain gradient length scale ($l = 0$) is zero, the parameters of the system are

$$\begin{aligned}
A_\omega &= -k_I^2(1+k_{\mu 1}n^2\pi^2)\left\{k_C k_{I0}^2 - n^2\pi^2[k_N\alpha_6(1+k_{\mu 0}n^2\pi^2)-k_C\alpha_6-k_{I0}\alpha_5]\right\},\\
B_\omega &= k_I n^2\pi^2(1+k_{\mu 1}n^2\pi^2)[k_C k_{I0}+k_{I0}\alpha_2 n^2\pi^2+k_C\alpha_5 n^2\pi^2-k_N(1+k_{\mu 0}n^2\pi^2)(k_C k_{I0}+\alpha_5 n^2\pi^2)],\\
C_\omega &= n^4\pi^4(1+k_{\mu 1}n^2\pi^2)[k_N(1+k_{\mu 0}n^2\pi^2)(k_C+\alpha_2 n^2\pi^2)-k_C\alpha_2 n^2\pi^2],\\
\frac{\alpha_3}{\alpha_4} &= \frac{1}{1+k_{\mu 0}n^2\pi^2}.
\end{aligned} \quad (69)$$

It is noticeable that in this case the natural frequency does not depend on the nonlocal parameters μ_1, but only on the parameter μ_0. By setting the strain gradient length scale ($l = 0$) to zero we can find the critical temperature $\Delta T_{\rm cr}$ from (61) as

$$k_{\mu 0}=\frac{\alpha_2 n^2\pi^2(k_C-k_N)-k_C k_N}{k_N n^2\pi^2(k_C+\alpha_2 n^2\pi^2)}. \quad (70)$$

It is noticeable that in this case the critical temperature $\Delta T_{\rm cr}$ does not depend on the nonlocal parameters μ_1, but only on the parameter μ_0, and is the same as the one we can determine from conditions (63) in Case 1.

Case 4 (lower-order nonlocal strain gradient theory). In the case where the nonlocal parameters are equal ($\mu_1 = \mu_0$) the parameters of the system are

$$\begin{aligned}
A_\omega &= -k_I^2(1+k_{\mu 0}n^2\pi^2)\{(1+k_l n^2\pi^2)[k_C k_{I0}^2+n^2\pi^2(k_C\alpha_6+k_{I0}\alpha_5)]-k_N\alpha_6 n^2\pi^2(1+k_{\mu 0}n^2\pi^2)\},\\
B_\omega &= k_I n^2\pi^2(1+k_{\mu 0}n^2\pi^2)\{(1+k_l n^2\pi^2)[k_C k_{I0}+n^2\pi^2(k_{I0}\alpha_2+k_C\alpha_5)]\\
&\qquad -k_N(1+k_{\mu 0}n^2\pi^2)[k_C k_{I0}+\alpha_5 n^2\pi^2]\},\\
C_\omega &= n^4\pi^4(1+k_{\mu 0}n^2\pi^2)\{k_N(1+k_{\mu 0}n^2\pi^2)(k_C+\alpha_2 n^2\pi^2)-k_C\alpha_2 n^2\pi^2(1+k_l n^2\pi^2)\},\\
\frac{\alpha_3}{\alpha_4} &= \frac{1+(k_{\mu 0}+k_l)n^2\pi^2+k_{\mu 0}k_l n^4\pi^4}{1+2k_{\mu 0}n^2\pi^2+k_{\mu 0}^2 n^4\pi^4}.
\end{aligned} \quad (71)$$

By setting $\mu_1 = \mu_0$ we can find the critical temperature $\Delta T_{\rm cr}$ from (61) as

$$k_l=\frac{k_N(1+k_{\mu 0}n^2\pi^2)(k_C+\alpha_2 n^2\pi^2)-k_C\alpha_2 n^2\pi^2}{k_C\alpha_2 n^4\pi^4}. \quad (72)$$

In this case, when the ratio is $l_\mu = l^2/\mu_0 = l^2/\mu_1 = 1$, the parameters of the system are

$$\begin{aligned} A_\omega &= -k_I^2(1+k_{\mu 0}\,n^2\pi^2)^2\{k_C\,k_{I0}^2 + n^2\pi^2[k_{I0}\,\alpha_5 + \alpha_6(k_C - k_N)]\},\\ B_\omega &= k_I\,n^2\pi^2(1+k_{\mu 0}\,n^2\pi^2)^2\{k_C\,k_{I0}(1-k_N) + n^2\pi^2[k_{I0}\,\alpha_2 + \alpha_5(k_C - k_N)]\},\\ C_\omega &= n^4\pi^4(1+k_{\mu 0}\,n^2\pi^2)^2\,[k_C\,k_N - \alpha_2\,n^2\pi^2(k_C - k_N)],\\ \frac{\alpha_3}{\alpha_4} &= 1, \end{aligned} \tag{73}$$

and the natural frequency does not depend on the nonlocal parameters μ_0 and μ_1, but also not on the strain gradient length scale l. The natural frequencies of the system are equal to the frequencies for the case of the classical continuum theory.

Case 5 (strain gradient theory). In the case where the nonlocal parameters are zero ($\mu_1 = \mu_0 = 0$) the parameters of the system are

$$\begin{aligned} A_\omega &= -k_I^2\{(1+k_l\,n^2\pi^2)[k_C\,k_{I0}^2 + n^2\pi^2(k_C\,\alpha_6 + k_{I0}\,\alpha_5)] - k_N\,\alpha_6\,n^2\pi^2\},\\ B_\omega &= k_I\,n^2\pi^2\{(1+k_l\,n^2\pi^2)[k_C\,k_{I0} + n^2\pi^2(k_{I0}\,\alpha_2 + k_C\,\alpha_5)] - k_N[k_C\,k_{I0} + \alpha_5\,n^2\pi^2]\},\\ C_\omega &= n^4\pi^4\{k_N(k_C + \alpha_2\,n^2\pi^2) - k_C\,\alpha_2\,n^2\pi^2(1+k_l\,n^2\pi^2)\},\\ \frac{\alpha_3}{\alpha_4} &= 1 + k_l\,n^2\pi^2. \end{aligned} \tag{74}$$

By setting $\mu_1 = \mu_0 = 0$ we can find the critical temperature $\Delta T_{\rm cr}$ from (61) as

$$k_l = \frac{k_N(k_C + \alpha_2\,n^2\pi^2) - k_C\,\alpha_2\,n^2\pi^2}{k_C\,\alpha_2\,n^4\pi^4}. \tag{75}$$

3. Results and discussion

This section examines the influence of temperature change, FG distribution and small-scale effect on the nondimensional natural frequencies. Varying amounts of small-scale parameters are observed and the variations of the critical buckling temperature and nondimensional natural frequencies with respect to the variations of small-scale parameters are discussed. The functionally graded nanobeam is composed of metal (SUS 304) and ceramic (Si_3N_4), where its bottom surface is pure metal and top surface is pure ceramic nitride. The considered beam has the following dimensions: length $L = 10\,\text{nm}$, width $b = 1\,\text{nm}$ and thickness h varies.

The validity of the proposed method is confirmed by comparing the obtained results with those from the literature [Thai 2012; Rahmani and Pedram 2014]. First, for this purpose, the same parameters are used as in [Thai 2012]. A comparison of the fundamental nondimensional natural frequency for the SS nanobeam is shown in Table 2 for different values of $k_{\mu 0} = 0$, 0.01, 0.02, 0.03 and for ratios $L/h = 5$, 10, 20, 100. The results that are compared are derived from expression (52) for parameter values (62), (65) and $k_N = 0$.

Similarly, a comparison of the results for the FG simply supported nanobeam is given in Table 2 for different values of $k_{\mu 0} = 0$, 0.01, 0.02, 0.03, ratio $L/h = 50$ and the power-law exponent $p = 0$, 0.5, 1, 5. The results that are compared are derived from expression (60) for parameter values (62) and $k_N = 0$. The

	L/h			
$k_{\mu 0}$	5	10	20	100
0	9.274405 (9.2740)	9.707484 (9.7075)	9.828127 (9.8281)	9.867933 (9.8679)
0.01	8.848045 (8.8477)	9.261214 (9.2612)	9.376311 (9.3763)	9.414286 (9.4143)
0.02	8.475550 (8.4752)	8.871325 (8.8713)	8.981576 (8.9816)	9.017953 (9.0179)
0.03	8.663606 (8.6636)	6.799808 (6.7998)	6.141394 (6.1414)	5.216644 (5.2166)

Table 2. Comparison with [Thai 2012] of the nondimensional fundamental frequency for a SS FG nanobeam with various nonlocal parameters μ_0 and ratios L/h.

	p			
$k_{\mu 0}$	0	0.5	1	5
0	9.863157 (9.8631)	7.741301 (7.7413)	6.991723 (6.9917)	5.938935 (5.9389)
0.01	9.409730 (9.4097)	7.385419 (7.3854)	6.670301 (6.6703)	5.665911 (5.6659)
0.02	9.013589 (9.0136)	7.074500 (7.0745)	6.389487 (6.3895)	5.427381 (5.4274)
0.03	8.663606 (8.6636)	6.799808 (6.7998)	6.141394 (6.1414)	5.216644 (5.2166)

Table 3. Comparison with [Rahmani and Pedram 2014] of the nondimensional fundamental frequency for a SS FG nanobeam with various nonlocal parameters μ_0 and power-law indices p when ratio $L/h = 50$.

same parameters of functionally graded material constituents (steel and alumina) are used as in [Rahmani and Pedram 2014].

Furthermore, in order to validate the results of the present work, equation (63) is solved by considering $l = 0$ and $\mu_1 = 0$, and the results of the critical buckling temperature are compared with the literature [Ebrahimi and Salari 2016] and tabulated in tables 4–6. The influence of the gradient indices p and nonlocal parameter μ_0 on the critical buckling temperature ΔT_{cr} and nondimensional natural frequencies for the simply supported FG nanobeam is considered in detail in [Ebrahimi and Salari 2016]. Here, the effects of different parameters such as the higher-order nonlocal parameter μ_1 and the strain gradient length scale l on the thermal buckling of the FG nanobeam are investigated.

Tables 4–6 present the critical buckling temperature of the simply supported FG nanobeam for various values of the nonlocal parameters and strain gradient scale ($\mu_0 = 0, 1, 2, 3$; $\mu_1 = 0, 1, 2, 3$; $l^2 = 0, 1, 2, 3$) based on the present method, for UTR, LTR and NLTR. It can be concluded from the results in tables 4–6 that an increase in the strain gradient length scale leads to an increase in the critical buckling temperature. Therefore, it can be concluded that an increase in the nonlocal scale parameters μ_0 and the higher-order nonlocal scale parameter μ_1 leads to a decrease in the critical buckling temperature. Variations of the critical buckling temperature ΔT_{cr} of the simply supported FG nanobeam with respect to the nonlocal parameter μ_0 for different values of the power-law index (Eringen's nonlocal continuum theory, $l = 0$, $\mu_1 = 0$) are presented in Figure 2. Examining this figure, it can be concluded that an increase in the nonlocal parameter μ_0 leads to a decrease in the critical buckling temperature. In addition, it can be seen that ΔT_{cr} decreases with the increasing power-law index.

		l^2 (nm^2)			
μ_0 (nm^2)	μ_1 (nm^2)	0	1	2	3
0	0	28.5602 (29.1086)	31.3219	34.0737	36.8153
	1	28.5602	31.0742	33.5801	36.0777
	2	28.5602	30.8673	33.1675	35.4608
	3	28.5602	30.6919	32.8176	34.9375
1	0	26.0379 (26.4938)	28.8087	31.5695	34.3207
	1	26.0379	28.5602	31.0742	33.5802
	2	26.0379	28.3526	30.6603	32.9612
	3	26.0379	28.1766	30.3093	32.4362
2	0	23.9251 (24.3100)	26.7035	29.4718	32.2301
	1	23.9251	26.4543	28.9752	31.4878
	2	23.9251	26.2462	28.5602	30.8672
	3	23.9251	26.0697	28.2082	30.3408
3	0	22.1296 (22.4588)	24.9144	27.6892	30.4538
	1	22.1296	24.6646	27.1914	29.7098
	2	22.1296	24.6228	26.7754	29.0878
	3	22.1296	24.2791	26.4226	28.5602

Table 4. Nonlocality parameters and strain gradient length scale effects on the ΔT_{cr} (K) of the SS FG nanobeam in the UTR case when $p = 1$ and $L/h = 50$.

		l^2 (nm^2)			
μ_0 (nm^2)	μ_1 (nm^2)	0	1	2	3
0	0	49.0533 (50.4274)	54.7761	60.4733	66.1440
	1	49.0533	54.2631	59.4516	64.6183
	2	49.0533	53.8345	58.5977	63.3430
	3	49.0533	53.4710	57.8734	62.2606
1	0	43.8219 (44.9580)	49.5684	55.2889	60.9846
	1	43.8219	49.0533	54.2631	59.4520
	2	43.8219	48.6229	53.4057	58.1707
	3	43.8219	48.2579	52.6784	57.0837
2	0	39.4363 (40.3903)	45.2027	50.9429	56.6569
	1	39.4363	44.6858	49.9135	55.1196
	2	39.4363	44.2539	49.0533	53.8343
	3	39.4363	43.8877	48.3235	52.7436
3	0	35.7065 (36.5182)	41.4901	47.2472	52.9776
	1	35.7065	40.9716	46.2148	51.4360
	2	35.7065	40.5385	45.3520	50.1470
	3	35.7065	40.1712	44.6201	49.0533

Table 5. Nonlocality parameters and strain gradient length scale effects on the ΔT_{cr} (K) of the SS FG nanobeam in the LTR case when $p = 1$ and $L/h = 50$.

μ_0 (nm^2)	μ_1 (nm^2)	l^2 (nm^2) 0	1	2	3
0	0	50.8666 (52.0963)	56.8402	62.7871	68.7142
	1	50.8666	56.3045	61.7195	67.1184
	2	50.8666	55.8581	60.8287	65.7855
	3	50.8666	55.4810	60.0705	64.6536
1	0	45.4148 (46.4459)	51.4038	57.3710	63.3165
	1	45.4148	50.8666	56.3006	61.7162
	2	45.4148	50.4179	55.4061	60.3786
	3	45.4148	50.0375	54.6474	59.2440
2	0	40.8519 (41.7270)	46.8540	52.8351	58.7987
	1	40.8519	46.3160	51.7616	57.1936
	2	40.8519	45.8665	50.8666	55.8520
	3	40.8519	45.4853	50.1042	54.7138
3	0	36.9746 (37.7267)	42.9889	49.3428	54.9579
	1	36.9746	42.4489	47.9091	53.3495
	2	36.9746	41.9978	47.0107	52.0053
	3	36.9746	41.6153	46.2487	50.8666

Table 6. Nonlocality parameters and strain gradient length scale effects on the ΔT_{cr} (K) of the SS FG nanobeam in the NLTR case when $p = 1$ and $L/h = 50$.

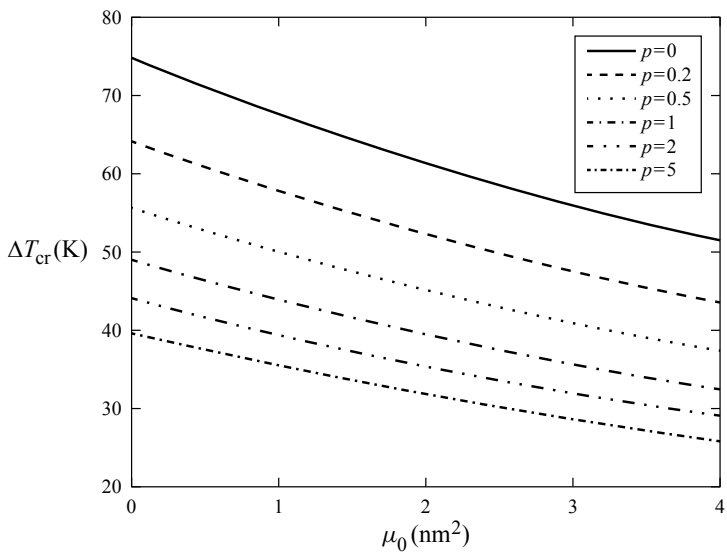

Figure 2. Variation of the critical buckling temperature of the SS FG nanobeam with respect to the nonlocal parameter μ_0 for different values of the power-law index and LNR ($p = 1\ \ L/h = 50,\ \mu_1 = 0,\ l^2 = 0$).

It can be further concluded from tables 4–6 that a decrease in the strain gradient scale l and an increase in the higher-order nonlocal scale parameter μ_1 lead to a decrease in the critical buckling temperature. With the increasing strain gradient scale l, the effect of increasing the higher-order nonlocal parameter μ_1 is compared with the effect of increasing the nonlocal parameter μ_0. It can still be concluded that at small values of the strain gradient scale l, increasing the nonlocal parameter μ_0 has more effects on decreasing the critical buckling temperature than increasing the higher-order nonlocal parameter μ_1. In cases where the strain gradient length scale is zero (see (70)), variations on the higher-order nonlocal parameter μ_1 will have no effect on the critical buckling temperature. To have a better understanding of this issue, variations of the critical buckling temperature of the FG nanobeam are plotted in Figure 3 with respect to increasing the strain length scale and different values of the nonlocal parameters μ_0 and μ_1. For the same reason, Figure 4 presents variations of the critical buckling temperature $\Delta T_{\rm cr}$ with respect to the new scale factor

$$l_\mu = \frac{l^2}{\mu}, \tag{76}$$

for different values of the nonlocal parameter where $\mu = \mu_0 = \mu_1$. It can be concluded that the critical buckling temperature is smaller than the result of the classical solution when the nonlocal parameter is smaller than the strain length scale ($l_\mu < 1$); the critical buckling temperature is larger than the result of the classical solution when the nonlocal parameter is larger than the strain gradient length scale ($l_\mu > 1$). When the nonlocal parameter is equal to the strain gradient length scale $l_\mu = 1$, the critical buckling temperature is equal to that of the classical solution. Also, when $l_\mu = 0$, the results are equal to those from the nonlocal elasticity theory.

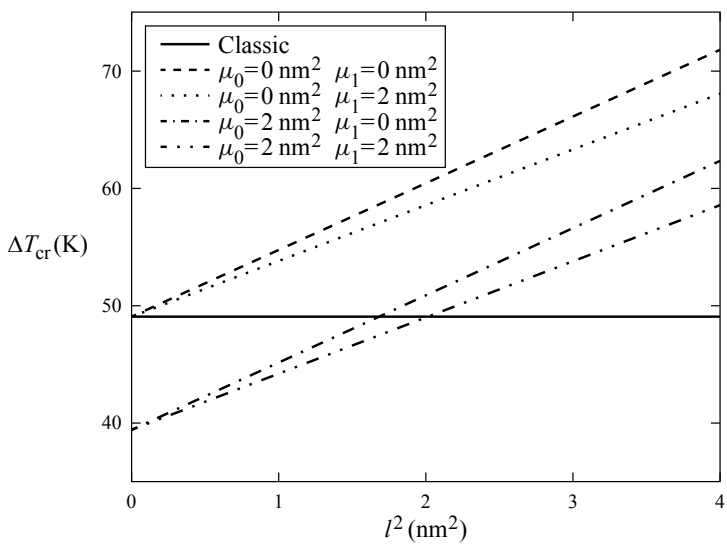

Figure 3. Variation of the critical buckling temperature of the SS FG nanobeam with respect to the strain length scale for different values of the nonlocal parameters and LNR ($p = 1$ $L/h = 50$).

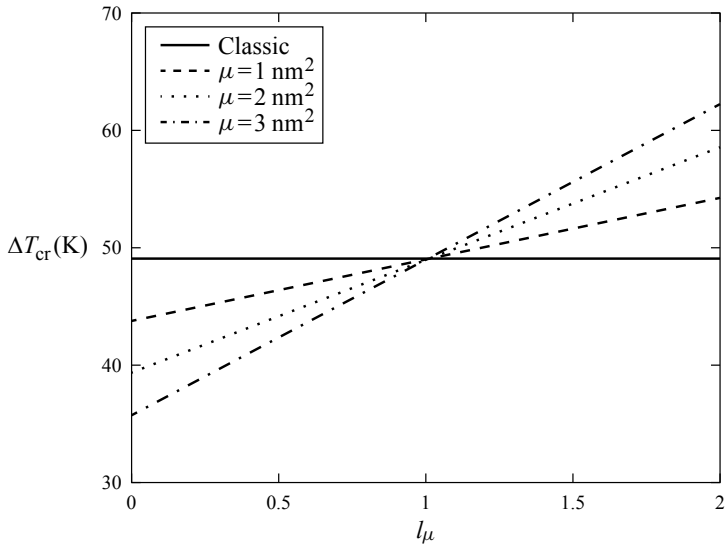

Figure 4. Variation of the critical buckling temperature of the SS FG nanobeam with respect to ratio l_μ, strain length scale for different values of the nonlocal parameters and LNR ($p = 1$ $L/h = 50$ $\mu_0 = \mu_1 = \mu$).

In order to investigate the vibration characteristics of the simply supported FG nanobeam, the first three nondimensional frequencies are presented in tables 7–15. Tables 7–9 present the natural frequencies of the simply supported FG nanobeam subjected to a uniform temperature rise for various values of the nonlocal parameters and the strain gradient length scale parameter ($\mu_0 = 0, 1, 2, 3$; $\mu_1 = 0, 1, 2, 3$; $l^2 = 0, 1, 2, 3$) based on the present method. Also, tables 10–12 and tables 13–15 present the natural frequencies of the simply supported FG nanobeam subjected to a linear and a nonlinear temperature rise, respectively. It can be concluded from the results given in these tables that an increase in the strain gradient length scale l leads to an increase in the nondimensional frequency. On the other hand, an increase in the nonlocal scale parameters μ_0 and the higher-order nonlocal scale parameter μ_1 leads to a decrease in the nondimensional natural frequency. It can still be concluded that at small values of the strain gradient scale l, increasing the nonlocal parameter μ_0 has more effects on decreasing the nondimensional frequency than increasing the higher-order nonlocal parameter μ_1. With the increasing strain gradient scale l, increasing the nonlocal parameter μ_1 has more effects on decreasing the nondimensional frequency than increasing the higher-order nonlocal parameter μ_0. To have a better understanding of this issue, variations of the frequency ratio

$$k_{\omega n} = \frac{\omega_n}{\omega_{nc}}, \tag{77}$$

are plotted in figures 5–7 with respect to the nonlocal scale parameters μ_0 for different values of the strain length scale l and the nonlocal parameter μ_1, where ω_n is the nondimensional frequency calculated using the nonlocal theory (for the parameters of system (59)) and ω_{nc} is the nondimensional frequency calculated using the classical local theory (for the parameters of system (64)). This frequency ratio serves as an index to quantitatively estimate the effects of the nonlocal parameters μ_0 and μ_1, and the

		l^2 (nm^2)			
μ_0 (nm^2)	μ_1 (nm^2)	0	1	2	3
0	0	5.4110 (5.4110)	5.7233	6.0195	6.3018
	1	5.4110	5.6960	5.9674	6.2270
	2	5.4110	5.6730	5.9235	6.1638
	3	5.4110	5.6535	5.8860	6.1097
1	0	5.1101 (5.1102)	5.4398	5.7506	6.0454
	1	5.1101	5.4110	5.6960	5.9674
	2	5.1101	5.3868	5.6500	5.9014
	3	5.1101	5.3663	5.6107	5.8449
2	0	4.8446 (4.8446)	5.1911	5.5159	5.8226
	1	4.8446	5.1609	5.4500	5.7416
	2	4.8446	5.1356	5.4110	5.6730
	3	4.8446	5.1140	5.3700	5.6142
3	0	4.6075 (4.6075)	4.9706	5.3089	5.6269
	1	4.6075	4.9391	5.2497	5.5430
	2	4.6075	4.9126	5.1998	5.4720
	3	4.6075	4.8900	5.1571	5.4110

Table 7. Nonlocality parameters and strain gradient length scale effects on the first nondimensional frequency ω_1 in the UTR case when $p = 1,\ L/h = 20,\ \Delta T = 30\,\mathrm{K}$.

strain length scale l on the vibration solution. It can be clearly seen from the figures that the frequency ratio is less than unity when $l = 0$, regardless of the values of the nonlocal parameters μ_0 and μ_1. The frequency ratio has higher values for higher frequencies. It is observed that increasing the nonlocal parameters will decrease the frequency ratio and decreasing the strain gradient length scale will decrease the frequency ratio. With an increase in the order of frequency, the greatest influence on the frequency ratio is exterted by the nonlocal parameter μ_1. In the cases where the strain gradient length scale is zero (see (70)), variations of the nonlocal parameter μ_1 will have no effect on the frequency ratio. In the case when $l^2 = \mu_0 = \mu_1$, the frequency ratio is one for all orders of frequency and all values of the nonlocal parameters μ_0 and μ_1 and the strain length scale l.

4. Conclusions

This paper investigates the thermal buckling and vibration of the FG nanobeam subjected to different temperature distributions in the through-thickness direction (UTR, LNR and NLTR). By using the variational approach, the equations of motion are obtained based on the Timoshenko beam theory within the framework of the higher-order nonlocal strain gradient theory. The effect of the nonlocal parameters and strain gradient length scale on the critical buckling temperature and nondimensional frequency is observed. Numerical results are presented for certain characteristics of the rectangular cross-section of the beam. It is concluded that an increase in the nonlocal parameters will decrease the critical buckling temperature and nondimensional frequency, while a decrease in the strain gradient length scale will lead to a decrease in the critical buckling temperature and nondimensional natural frequency. For small values

μ_0 (nm^2)	μ_1 (nm^2)	l^2 (nm^2) 0	1	2	3
0	0	22.9433 (22.9447)	27.2682	30.9954	34.3203
	1	22.9433	26.1168	28.9445	31.5195
	2	22.9433	25.4508	27.7325	29.8402
	3	22.9433	25.0162	26.9301	28.7166
1	0	19.2535 (19.2547)	24.2458	28.3729	31.9716
	1	19.2535	22.9433	26.1168	28.9445
	2	19.2535	22.1821	24.7668	27.1062
	3	19.2535	21.6821	23.8649	25.8641
2	0	16.8433 (16.8443)	22.3799	26.7959	30.5807
	1	16.8433	20.9617	24.3944	27.4004
	2	16.8433	20.1257	22.9433	25.4508
	3	16.8433	19.5733	21.9666	24.1236
3	0	15.1044 (15.1054)	21.1022	25.7384	29.6585
	1	15.1044	19.5918	23.2279	26.3672
	2	15.1044	18.6947	21.6988	24.3349
	3	15.1044	18.0986	20.6634	22.9433

Table 8. Nonlocality parameters and strain gradient length scale effects on the second nondimensional frequency ω_2 in the UTR case when $p = 1,\ L/h = 20,\ \Delta T = 30\,\mathrm{K}$.

μ_0 (nm^2)	μ_1 (nm^2)	l^2 (nm^2) 0	1	2	3
0	0	51.2311 (51.2374)	70.7310	85.9135	98.7896
	1	51.2311	62.3227	71.7190	80.0194
	2	51.2311	59.0016	65.8615	72.0715
	3	51.2311	57.2152	62.6300	67.6126
1	0	36.9478 (36.9524)	61.1833	78.2409	92.1949
	1	36.9478	51.2311	62.3227	71.7190
	2	36.9478	47.1349	55.4820	62.7280
	3	36.9478	44.8786	51.6046	57.5498
2	0	30.1914 (30.1952)	57.3565	75.2863	89.7010
	1	30.1914	46.5941	58.5705	68.4835
	2	30.1914	42.0485	51.2311	59.0016
	3	30.1914	39.5027	47.0044	53.4636
3	0	26.0345 (26.0379)	55.2815	73.7177	88.3886
	1	26.0345	44.0146	56.5400	66.7553
	2	26.0345	39.1708	48.8969	56.9865
	3	26.0345	36.4244	44.4487	51.2311

Table 9. Nonlocality parameters and strain gradient length scale effects on the third nondimensional frequency ω_3 in the UTR case when $p = 1,\ L/h = 20,\ \Delta T = 30\,\mathrm{K}$.

μ_0 (nm^2)	μ_1 (nm^2)	l^2 (nm^2) 0	1	2	3
0	0	5.6111 (5.6105)	5.9136	6.2013	6.4763
	1	5.6111	5.8871	6.1506	6.4033
	2	5.6111	5.8648	6.1080	6.3418
	3	5.6111	5.8459	6.0716	6.2891
1	0	5.3209 (5.3204)	5.6390	5.9400	6.2265
	1	5.3209	5.6111	5.8871	6.1506
	2	5.3209	5.5878	5.8425	6.0865
	3	5.3209	5.5679	5.8044	6.0316
2	0	5.0659 (5.0654)	5.3989	5.7126	6.0100
	1	5.0659	5.3699	5.6576	5.9313
	2	5.0659	5.3455	5.6111	5.8648
	3	5.0659	5.3247	5.5715	5.8078
3	0	4.8391 (4.8388)	5.1868	5.5126	5.8201
	1	4.8391	5.1565	5.4555	5.7389
	2	4.8391	5.1311	5.4073	5.6701
	3	4.8391	5.1094	5.3662	5.6111

Table 10. Nonlocality parameters and strain gradient length scale effects on the first nondimensional frequency ω_1 in the LTR case when $p = 1,\ L/h = 20,\ \Delta T = 30\,\mathrm{K}$.

μ_0 (nm^2)	μ_1 (nm^2)	l^2 (nm^2) 0	1	2	3
0	0	23.1537 (23.1492)	27.4544	31.1673	34.4827
	1	23.1537	26.3086	29.1237	31.6897
	2	23.1537	25.6460	27.9167	30.016
	3	23.1537	25.2138	27.1178	28.8967
1	0	19.4947 (19.4913)	24.4479	28.5544	32.1404
	1	19.4947	23.1537	26.3086	29.1237
	2	19.4947	22.3979	24.9658	27.2931
	3	19.4947	21.9017	24.0692	26.0571
2	0	17.1127 (17.1100)	22.5942	26.9843	30.7540
	1	17.1127	21.1871	24.5956	27.5860
	2	17.1127	20.3585	23.1537	25.6460
	3	17.1127	19.8113	22.1840	24.3264
3	0	15.4002 (15.3980)	21.3265	25.9321	29.8350
	1	15.4002	19.8296	23.4363	26.5577
	2	15.4002	18.9417	21.9183	24.5364
	3	15.4002	18.3523	20.8914	23.1537

Table 11. Nonlocality parameters and strain gradient length scale effects on the second nondimensional frequency ω_2 in the LTR case when $p = 1,\ L/h = 20,\ \Delta T = 30\,\mathrm{K}$.

μ_0 (nm^2)	μ_1 (nm^2)	l^2 (nm^2) 0	1	2	3
0	0	51.4739 (51.4699)	70.9453	86.1214	98.9978
	1	51.4739	62.5454	71.9325	80.2287
	2	51.4739	59.229	66.0801	72.2847
	3	51.4739	57.4455	62.8523	67.8294
1	0	37.2452 (37.2400)	61.4074	78.4509	92.4024
	1	37.2452	51.4739	62.5454	71.9325
	2	37.2452	47.3889	55.7155	62.9502
	3	37.2452	45.1401	51.8464	57.7795
2	0	30.5377 (30.5340)	57.5866	75.4976	89.9086
	1	30.5377	46.8499	58.7985	68.6995
	2	30.5377	42.3209	51.4739	59.229
	3	30.5377	39.7866	47.2589	53.7012
3	0	26.4253 (26.4225)	55.5154	73.9299	88.5962
	1	26.4253	44.2793	56.7716	66.9729
	2	26.4253	39.4563	49.1458	57.2172
	3	26.4253	36.7249	44.7118	51.4739

Table 12. Nonlocality parameters and strain gradient length scale effects on the third nondimensional frequency ω_3 in the LTR case when $p = 1,\ L/h = 20,\ \Delta T = 30\,\mathrm{K}$.

μ_0 (nm^2)	μ_1 (nm^2)	l^2 (nm^2) 0	1	2	3
0	0	5.6220 (5.6135)	5.9239	6.2112	6.4857
	1	5.6220	5.8974	6.1605	6.4129
	2	5.6220	5.8752	6.118	6.3514
	3	5.6220	5.8563	6.0816	6.2988
1	0	5.3324 (5.3246)	5.6498	5.9503	6.2363
	1	5.3324	5.6220	5.8974	6.1605
	2	5.3324	5.5987	5.8529	6.0965
	3	5.3324	5.5789	5.8149	6.0418
2	0	5.0778 (5.0707)	5.4102	5.7233	6.0201
	1	5.0778	5.3812	5.6683	5.9416
	2	5.0778	5.3568	5.6220	5.8752
	3	5.0778	5.3361	5.5824	5.8183
3	0	4.8516 (4.8450)	5.1985	5.5236	5.8306
	1	4.8516	5.1683	5.4666	5.7495
	2	4.8516	5.1429	5.4186	5.6808
	3	4.8516	5.1213	5.3775	5.6220

Table 13. Nonlocality parameters and strain gradient length scale effects on the first nondimensional frequency ω_1 in the NLTR case when $p = 1,\ L/h = 20,\ \Delta T = 30\,\mathrm{K}$.

		l^2 (nm^2)			
μ_0 (nm^2)	μ_1 (nm^2)	0	1	2	3
0	0	23.1647 (23.1233)	27.4639	31.1759	34.4906
	1	23.1647	26.3184	29.1327	31.6982
	2	23.1647	25.6560	27.9260	30.0249
	3	23.1647	25.2240	27.1274	28.9058
1	0	19.5075 (19.4735)	24.4583	28.5636	32.1488
	1	19.5075	23.1647	26.3184	29.1327
	2	19.5075	22.4092	24.9761	27.3027
	3	19.5075	21.9133	24.0799	26.0670
2	0	17.1272 (17.0980)	22.6054	26.9939	30.7626
	1	17.1272	21.1990	24.6060	27.5955
	2	17.1272	20.3708	23.1647	25.6560
	3	17.1272	19.8239	22.1954	24.3369
3	0	15.4161 (15.3906)	21.3383	25.9420	29.8439
	1	15.4161	19.8422	23.4472	26.5674
	2	15.4161	18.9549	21.9299	24.5469
	3	15.4161	18.3659	20.9034	23.1647

Table 14. Nonlocality parameters and strain gradient length scale effects on the second nondimensional frequency ω_2 in the NLTR case when $p = 1,\ L/h = 20,\ \Delta T = 30\,\mathrm{K}$.

		l^2 (nm^2)			
μ_0 (nm^2)	μ_1 (nm^2)	0	1	2	3
0	0	51.4858 (51.3939)	70.9549	86.1302	99.0061
	1	51.4858	62.5557	71.942	80.2377
	2	51.4858	59.2397	66.0901	72.2942
	3	51.4858	57.4565	62.8626	67.8393
1	0	37.2606 (37.1957)	61.4179	78.4600	92.4109
	1	37.2606	51.4858	62.5557	71.9420
	2	37.2606	47.4016	55.7267	62.9605
	3	37.2606	45.1532	51.8582	57.7905
2	0	30.5561 (30.5042)	57.5976	75.5069	89.9172
	1	30.5561	46.8626	58.8094	68.7093
	2	30.5561	42.3347	51.4858	59.2397
	3	30.5561	39.8012	47.2715	53.7127
3	0	26.4462 (26.4025)	55.5267	73.9393	88.6049
	1	26.4462	44.2926	56.7826	66.9828
	2	26.4462	39.4710	49.1581	57.2282
	3	26.4462	36.7405	44.725	51.4858

Table 15. Nonlocality parameters and strain gradient length scale effects on the third nondimensional frequency ω_3 in the NLTR case when $p = 1,\ L/h = 20,\ \Delta T = 30\,\mathrm{K}$.

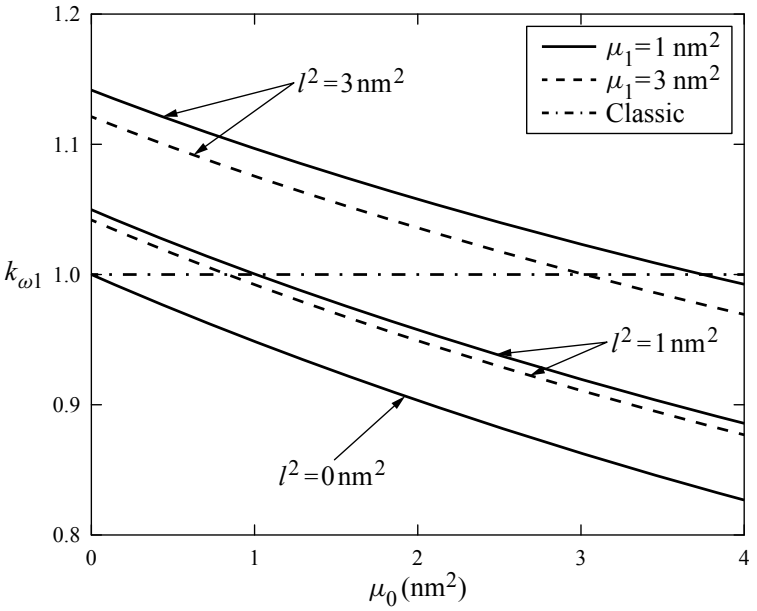

Figure 5. Variation of the frequency ratio for the first nondimensional frequency of the SS FG nanobeam with respect to the nonlocal parameter μ_0 for different values of μ_1 and l^2 and LNR ($p = 1,\ L/h = 50$).

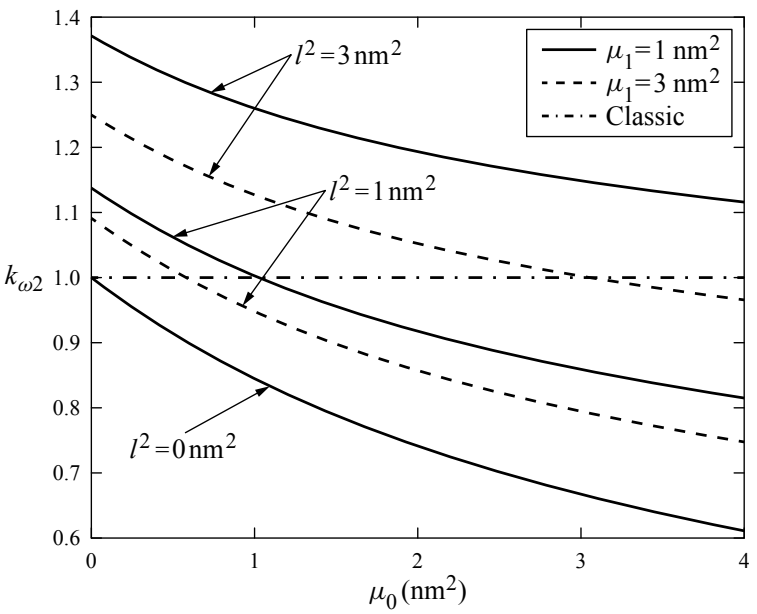

Figure 6. Variation of the frequency ratio for the second nondimensional frequency of the SS FG nanobeam with respect to the nonlocal parameter μ_0 for different values of μ_1 and l^2 and LNR ($p = 1,\ L/h = 50$).

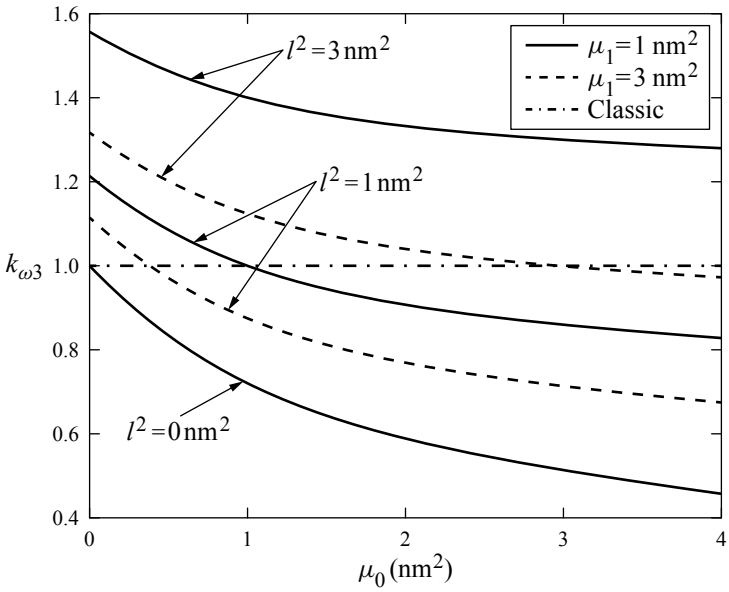

Figure 7. Variation of the frequency ratio for the third nondimensional frequency of the SS FG nanobeam with respect to the nonlocal parameter μ_0 for different values of μ_1 and l^2 and LNR ($p = 1,\ L/h = 50$).

of the strain gradient scale, the dominant influence is exerted by the nonlocal parameter, while for higher values, the dominant influence is shown by the higher-order nonlocal parameter. If nonlocal parameters are equal, then for the values of the strain gradient scale that are smaller than the nonlocal parameter, the critical buckling temperature and nondimensional frequency are lower than in the classical solution, and for the values of the strain gradient scale that are higher than the nonlocal parameter, the critical buckling temperature and nondimensional frequency are higher than in the classical solution. In the case when the strain gradient length scale is zero, the higher-order nonlocal parameters practically have no effect on the critical buckling temperature and nondimensional frequency.

Acknowledgement

This research was supported by the research grant of the Serbian Ministry of Science and Environmental Protection under the number OI 174011.

References

[Aifantis 1992] E. C. Aifantis, "On the role of gradients in the localization of deformation and fracture", *Int. J. Eng. Sci.* **30**:10 (1992), 1279–1299.

[Al-shujairi and Mollamahmutoğlua 2018] M. Al-shujairi and Ç. Mollamahmutoğlua, "Buckling and free vibration analysis of functionally graded sandwich micro-beams resting on elastic foundation by using nonlocal strain gradient theory in conjunction with higher order shear theories under thermal effect", *Compos. B Eng.* **154** (2018), 292–312.

[Alshehri and Hill 2017] M. H. Alshehri and J. M. Hill, "Suction energy for double-stranded DNA inside single-walled carbon nanotubes", *Quart. J. Mech. Appl. Math.* **70**:4 (2017), 387–400.

[Chen et al. 2019] W. Chen, L. Wang, and H.-L. Dai, "Nonlinear free vibration of nanobeams based on nonlocal strain gradient theory with the consideration of thickness-dependent size effect", *J. Mech. Mater. Struct.* **14**:1 (2019), 119–137.

[Ebrahimi and Haghi 2017] F. Ebrahimi and P. Haghi, "Wave propagation analysis of rotating thermoelastically-actuated nanobeams based on nonlocal strain gradient theory", *Acta Mech. Solida Sin.* **30**:6 (2017), 647–657.

[Ebrahimi and Salari 2015a] F. Ebrahimi and E. Salari, "Thermal buckling and free vibration analysis of size dependent Timoshenko FG nanobeams in thermal environments", *Compos. Struct.* **128** (2015), 363–380.

[Ebrahimi and Salari 2015b] F. Ebrahimi and E. Salari, "Nonlocal thermo-mechanical vibration analysis of functionally graded nanobeams in thermal environment", *Acta Astronaut.* **113** (2015), 29–50.

[Ebrahimi and Salari 2016] F. Ebrahimi and E. Salari, "Effect of various thermal loadings on buckling and vibrational characteristics of nonlocal temperature-dependent functionally graded nanobeams", *Mech. Adv. Mater. Struct.* **23**:12 (2016), 1379–1397.

[Eringen 1983] A. C. Eringen, "On differential equations of nonlocal elasticity and solutions of screw dislocation and surface waves", *J. Appl. Phys.* **54**:9 (1983), 4703–4710.

[Eringen 2002] A. C. Eringen, *Nonlocal continuum field theories*, Springer, New York, NY, 2002.

[Fu et al. 2012] Y. Fu, J. Wang, and Y. Mao, "Nonlinear analysis of buckling, free vibration and dynamic stability for the piezoelectric functionally graded beams in thermal environment", *Appl. Math. Model.* **36**:9 (2012), 4324–4340.

[Ghazavi et al. 2018] M. R. Ghazavi, H. Molki, and A. Ali Beigloo, "Nonlinear analysis of the micro/nanotube conveying fluid based on second strain gradient theory", *Appl. Math. Model.* **60** (2018), 77–93.

[Li et al. 2016] L. Li, X. Li, and Y. Hu, "Free vibration analysis of nonlocal strain gradient beams made of functionally graded material", *Int. J. Eng. Sci.* **102** (2016), 77–92.

[Li et al. 2018] L. Li, H. Tang, and Y. Hu, "The effect of thickness on the mechanics of nanobeams", *Int. J. Eng. Sci.* **123** (2018), 81–91.

[Lim et al. 2015] C. W. Lim, G. Zhang, and J. N. Reddy, "A higher-order nonlocal elasticity and strain gradient theory and its applications in wave propagation", *J. Mech. Phys. Solids* **78** (2015), 298–313.

[Lu et al. 2017] L. Lu, X. Guo, and J. Zhao, "Size-dependent vibration analysis of nanobeams based on the nonlocal strain gradient theory", *Int. J. Eng. Sci.* **116** (2017), 12–24.

[Mindlin 1964] R. D. Mindlin, "Micro-structure in linear elasticity", *Arch. Ration. Mech. Anal.* **16**:1 (1964), 51–78.

[Neek-Amal and Peeters 2010] M. Neek-Amal and F. M. Peeters, "Graphene nanoribbons subjected to axial stress", *Phys. Rev. B* **82**:8 (2010), 085432.

[Pavlović et al. 2019a] I. R. Pavlović, R. Pavlović, and G. Janevski, "Dynamic stability and instability of nanobeams based on the higher-order nonlocal strain gradient theory", *Quart. J. Mech. Appl. Math.* **72**:2 (2019), 157–178.

[Pavlović et al. 2019b] I. R. Pavlović, R. Pavlović, and G. Janevski, "Mathematical modeling and stochastic stability analysis of viscoelastic nanobeams using higher-order nonlocal strain gradient theory", *Arch. Mech.* **71**:2 (2019), 137–153.

[Rahmani and Pedram 2014] O. Rahmani and O. Pedram, "Analysis and modeling the size effect on vibration of functionally graded nanobeams based on nonlocal Timoshenko beam theory", *Int. J. Eng. Sci.* **77** (2014), 55–70.

[Şimşek and Yurtcu 2013] M. Şimşek and H. H. Yurtcu, "Analytical solutions for bending and buckling of functionally graded nanobeams based on the nonlocal Timoshenko beam theory", *Compos. Struct.* **97** (2013), 378–386.

[Tang et al. 2019] H. Tang, L. Li, Y. Hu, W. Meng, and K. Duan, "Vibration of nonlocal strain gradient beams incorporating Poisson's ratio and thickness effects", *Thin-Walled Struct.* **137** (2019), 377–391.

[Thai 2012] H.-T. Thai, "A nonlocal beam theory for bending, buckling, and vibration of nanobeams", *Int. J. Eng. Sci.* **52** (2012), 56–64.

[Touloukian 1967] Y. S. Touloukian (editor), *Thermophysical properties of high temperature solid materials*, vol. 1: Elements, Macmillan, New York, 1967.

[Trinh et al. 2016] L.-C. Trinh, T. P. Vo, H.-T. Thai, and T.-K. Nguyen, "An analytical method for the vibration and buckling of functionally graded beams under mechanical and thermal loads", *Compos. B Eng.* **100** (2016), 152–163.

[Xu et al. 2017] X.-J. Xu, X.-C. Wang, M.-L. Zheng, and Z. Ma, "Bending and buckling of nonlocal strain gradient elastic beams", *Compos. Struct.* **160** (2017), 366–377.

[Yang et al. 2018] Y. Yang, J. Wang, and Y. Yu, "Wave propagation in fluid-filled single-walled carbon nanotubes on the nonlocal strain gradient theory", *Acta Mech. Solida Sin.* **31**:4 (2018), 484–492.

Received 17 Jul 2019. Revised 5 Dec 2019. Accepted 14 Dec 2019.

GORAN JANEVSKI: gocky.jane@gmail.com
Department of Mechanical Engineering, University of Niš, Univerzitetski trg 2, 18000 Niš, Serbia

IVAN PAVLOVIĆ: ivanp79@gmail.com
Department of Mechanical Engineering, University of Niš, 18000 Niš, Serbia

NIKOLA DESPENIĆ: ndespa91@gmail.com
Department of Mechanical Engineering, University of Niš, 18000 Niš, Serbia

JOURNAL OF MECHANICS OF MATERIALS AND STRUCTURES
Vol. 15, No. 1, 2020
dx.doi.org/10.2140/jomms.2020.15.135

A NEW ANALYTICAL APPROACH FOR SOLVING EQUATIONS OF ELASTO-HYDRODYNAMICS IN QUASICRYSTALS

VALERY YAKHNO

The dynamic equations for quasicrystals are written as time-dependent partial differential equations of the second order relative to phonon and phason displacements. In these equations phonons describe the dynamics of wave propagation and phasons describe diffusion process in quasicrystals. A new approach for deriving a solution (phonon and phason displacements) of the initial value problem is proposed. In this approach the Fourier transform with respect to 3D space variable of the given phonon, phason forces and initial displacements are assumed to be vector functions with components which have finite supports with respect to Fourier parameters for every fixed time variable. The equations for the Fourier images of displacements are reduced to a vector integral equation of the Volterra-type depending on Fourier parameters. The solution of the obtained vector integral equation is solved by successive approximations. Finally, phonon and phason displacements are derived by matrix transformations and the inverse Fourier transform to the solution of the vector integral equation.

1. Introduction

The icosahedral quasicrystal structure was discovered in Al-Mn alloys [Shechtman et al. 1984]. After that quasicrystals (QCs) have become the focus of theoretical and experimental studies [Levine et al. 1985; Wang et al. 1987; De and Pelcovits 1987; Ding et al. 1993; Ovidko 1992; Edagawa and So 2007; Fan and Fan 2008; Li et al. 2009]. The properties of quasicrystalline materials are surprising and could be remarkably useful. Most of these properties combine effectively to give technologically interesting applications which have been protected recently by several patents [van Blaaderen 2009; Dubois 2000]. For instance, the combination of such properties as high hardness, low friction and corrosive resistance of quasicrystals gives almost ideal materials for motor-car engines. The application of QCs in motor-car engines would be undoubtedly result in reduced air pollution and increased engine lifetimes. The same set of associated properties (hardness, low friction, corrosive resistance) combined with biocompatibility is also very promising for introducing QCs in surgical applications as parts used for bone repair and prosthetic applications [van Blaaderen 2009; Dubois 2005]. The description of the dynamical processes in quasicrystals essentially depends on processes which describe phonons and phasons. For example, in [Gao and Zhao 2006; Rochal and Lorman 2002] both phonons and phasons describe the dynamics of the wave propagation in quasicrystals. There is another opinion, given in [Levine et al. 1985; Li and Fan 2016], that phonons describe the dynamics of wave propagation and phasons describe diffusion. The computation of the Green's function and the theoretical study of the existence and uniqueness of solutions of dynamical differential equations, describing the dynamics of the wave propagation in quasicrystals

MSC2010: 74F10, 35Q74.
Keywords: quasicrystals, mechanics of materials, phonon, phason, elastohydrodynamics, analytical method.

with the general structure of anisotropy without diffusion, has been done in [Yakhno and Çerdik Yaslan 2011a; Yakhno and Çerdik Yaslan 2011b; Çerdik Yaslan 2013; Çerdik Yaslan 2019]. Several interesting examples of solving problems for equations of elasto-hydrodynamics when phonon and phason displacements do not depend on one space variable have been described in [Fan et al. 2009; Li and Fan 2016]: the problem of a moving screw dislocation in an icosahedral quasicrystal was studied by a combination of the perturbation method and variational method in [Fan et al. 2009]; a general solution of equations of elasto-hydrodynamics in two-dimensional quasicrystals was derived in [Li 2011]; the dynamic crack problem in three dimensional icosahedral quasicrystals was solved by finite difference method in [Fan 2013; Li and Fan 2016]. We note that the derivation and computation of phonon and phason displacements by solving initial value and initial boundary value problems for dynamic equations in QCs with the general structure of anisotropy, when phonons describe the dynamics of wave propagation and phasons describe diffusion, have not been developed so far.

In the present paper a new analytical approach for derivation of a solution (phonon and phason displacements) of the initial value problem for differential equations of elasto-hydrodynamics in QCs with the general structure of anisotropy is described. In this approach the Fourier transform with respect to 3D space variable of the given phonon and phason forces and initial displacements are assumed to be vector functions with components which have finite supports with respect to Fourier parameters for every fixed time variable. The equations for the Fourier images of displacements are reduced to a vector integral equation of the Volterra type depending on Fourier parameters. The solution of the obtained vector integral equation is solved by successive approximations. Finally, phonon and phason displacements are derived by matrix transformations and the inverse Fourier transform to the solution of the vector integral equation.

2. Basic equations of elasto-hydrodynamics for quasicrystals

2A. ***Hook's law.*** Let us consider a quasicrystal (QC) with three dimensional quasiperiodic structure. Let $x = (x_1, x_2, x_3) \in R^3$ be a space variable, $t \in R$ be a time variable. According to the generalized elasticity theory of 3D QCs [Ding et al. 1993; Hu et al. 2000], the equations of the deformation are

$$\varepsilon_{kl} = \frac{1}{2}\left(\frac{\partial u_k}{\partial x_l} + \frac{\partial u_l}{\partial x_k}\right), \quad \omega_{kl} = \frac{\partial w_k}{\partial x_l}, \quad k, l = 1, 2, 3, \tag{2-1}$$

and the generalized Hooke's law of three dimensional quasicrystals is given by

$$\sigma_{ij} = \sum_{k,l=1}^{3} (C_{ijkl}\varepsilon_{kl} + R_{ijkl}\omega_{kl}), \quad H_{ij} = \sum_{k,l=1}^{3} (R_{klij}\varepsilon_{kl} + K_{ijkl}\omega_{kl}). \tag{2-2}$$

Here $i, j = 1, 2, 3$, u_i and w_i are components of phonon and phason displacements $\boldsymbol{u} = (u_1, u_2, u_3)$, $\boldsymbol{w} = (w_1, w_2, w_3)$; σ_{ij} and H_{ij} are phonon and phason stresses, $\varepsilon_{ij}(x, t)$, $\omega_{ij}(x, t)$ are phonon and phason strains, respectively.

C_{ijkl} represent the phonon elastic modules (phonon elastic properties of QC), K_{ijkl} are the phason elastic modules (phason elastic properties of CQ), R_{ijkl} are the phonon-phason coupling elastic modules (phonon-phason coupling properties of QC). The following properties for the interchange of indices are

satisfied (see, for example, [Hu et al. 2000]):

$$C_{ijkl} = C_{jikl} = C_{ijlk} = C_{klij}, \quad K_{ijkl} = K_{klij}, \quad R_{ijkl} = R_{jikl}. \tag{2-3}$$

We assume that these properties are satisfied. Moreover the positivity of the elastic strain energy density implies that for any strains ε_{ij} and ω_{ij} that are not zero entirely, the following inequalities are satisfied (see [Hu et al. 2000] and Appendix A):

$$\sum_{j,l,i,k=1}^{3} C_{ijkl}\varepsilon_{ij}\varepsilon_{kl} > 0, \qquad \sum_{j,l,i,k=1}^{3} K_{ijkl}\omega_{ij}\omega_{kl} > 0. \tag{2-4}$$

2B. ***Dynamic equations of elasto-hydrodynamics for quasicrystals.*** According to the arguments of Lubebskey et al. [1985] (see also [Fan et al. 2009; Fan 2013; Li and Fan 2016]) phason modes in quasicrystals correspond to diffusion and for phonon modes Newton's second law must be fulfilled. Hence we have

$$\rho\frac{\partial^2 u_i(x,t)}{\partial t^2} = \sum_{j=1}^{3}\frac{\partial \sigma_{ij}(x,t)}{\partial x_j} + f_i(x,t), \tag{2-5}$$

$$\kappa\frac{\partial w_i(x,t)}{\partial t} = \sum_{j=1}^{3}\frac{\partial H_{ij}(x,t)}{\partial x_j} + g_i(x,t), \quad i = 1,2,3,\ x \in R^3,\ t \in R, \tag{2-6}$$

where $\rho > 0$ is the mass density of QC; $\kappa = 1/\Gamma_w$ is the diffusion coefficient, Γ_w is the kinetic coefficient of the phason field, describing the relaxation of the motion; $f_i(x,t)$ and $g_i(x,t)$, $i = 1,2,3$ are components of body forces $\boldsymbol{f}$ (phonon) and $\boldsymbol{g}$ (phason), respectively; u_i and w_i are components of phonon and phason displacements $\boldsymbol{u} = (u_1, u_2, u_3)$, $\boldsymbol{w} = (w_1, w_2, w_3)$; σ_{ij} and H_{ij} are phonon and phason stresses, which used in (2-1) and (2-2). Using (2-2), equations (2-5), (2-6) can be presented in the form

$$\rho\frac{\partial^2 u_i(x,t)}{\partial t^2} = \sum_{j,k,l=1}^{3} C_{ijkl}\frac{\partial^2 u_k(x,t)}{\partial x_j \partial x_l} + \sum_{j,k,l=1}^{3} R_{ijkl}\frac{\partial^2 w_k(x,t)}{\partial x_j \partial x_l} + f_i(x,t), \tag{2-7}$$

$$\kappa\frac{\partial w_i(x,t)}{\partial t} = \sum_{j,k,l=1}^{3} R_{klij}\frac{\partial^2 u_k(x,t)}{\partial x_j \partial x_l} + \sum_{j,k,l=1}^{3} K_{ijkl}\frac{\partial^2 w_k(x,t)}{\partial x_j \partial x_l} + g_i(x,t). \tag{2-8}$$

Equations (2-7), (2-8) can be written as vector equations in the following form:

$$\rho\frac{\partial^2 \boldsymbol{u}(x,t)}{\partial t^2} = \sum_{j,l=1}^{3}\mathcal{C}_{jl}\frac{\partial^2 \boldsymbol{u}(x,t)}{\partial x_j \partial x_l} + \sum_{j,l=1}^{3}\mathcal{R}_{jl}\frac{\partial^2 \boldsymbol{w}(x,t)}{\partial x_j \partial x_l} + \boldsymbol{f}(x,t), \tag{2-9}$$

$$\kappa\frac{\partial \boldsymbol{w}(x,t)}{\partial t} = \sum_{j,l=1}^{3}\mathcal{K}_{jl}\frac{\partial^2 \boldsymbol{w}(x,t)}{\partial x_j \partial x_l} + \sum_{j,l=1}^{3}\mathcal{R}^T_{jl}\frac{\partial^2 \boldsymbol{u}(x,t)}{\partial x_j \partial x_l} + \boldsymbol{g}(x,t), \tag{2-10}$$

where

$$\mathcal{C}_{jl}=\frac{1}{2}\begin{bmatrix} C_{1j1l}+C_{1l1j} & C_{1j2l}+C_{1l2j} & C_{1j3l}+C_{1l3j} \\ C_{2j1l}+C_{2l1j} & C_{2j2l}+C_{2l2j} & C_{2j3l}+C_{2l3j} \\ C_{3j1l}+C_{3l1j} & C_{3j2l}+C_{3l2j} & C_{3j3l}+C_{3l3j} \end{bmatrix}, \tag{2-11}$$

$$\mathcal{R}_{jl}=\frac{1}{2}\begin{bmatrix} R_{1j1l}+R_{1l1j} & R_{1j2l}+R_{1l2j} & R_{1j3l}+R_{1l3j} \\ R_{2j1l}+R_{2l1j} & R_{2j2l}+R_{2l2j} & R_{2j3l}+R_{2l3j} \\ R_{3j1l}+R_{3l1j} & R_{3j2l}+R_{3l2j} & R_{3j3l}+R_{3l3j}, \end{bmatrix}, \tag{2-12}$$

$$\mathcal{K}_{jl}=\frac{1}{2}\begin{bmatrix} K_{1j1l}+K_{1l1j} & K_{1j2l}+K_{1l2j} & K_{1j3l}+K_{1l3j} \\ K_{2j1l}+K_{2l1j} & K_{2j2l}+K_{2l2j} & K_{2j3l}+K_{2l3j} \\ K_{3j1l}+K_{3l1j} & K_{3j2l}+K_{3l2j} & K_{3j3l}+K_{3l3j} \end{bmatrix}, \tag{2-13}$$

$\mathcal{R}_{jl}^T$ is the matrix transpose of $\mathcal{R}_{jl}$.

3. Initial value problem (IVP) for dynamic equations of elasto-hydrodynamics for quasicrystals

Let us consider the problem of finding vector functions $\boldsymbol{u}$, $\boldsymbol{w}$ satisfying (2-9), (2-10) and the following initial conditions:

$$\boldsymbol{u}(x,0)=\boldsymbol{u}^0(x), \quad \frac{\partial}{\partial t}\boldsymbol{u}(x,t)|_{t=0}=\boldsymbol{u}^1(x), \tag{3-1}$$

$$\boldsymbol{w}(x,0)=\boldsymbol{w}^0(x), \tag{3-2}$$

where $\boldsymbol{u}^0(x)$, $\boldsymbol{u}^1(x)$, $\boldsymbol{w}^0(x)$, $\boldsymbol{f}(x,t)$, $\boldsymbol{g}(x,t)$ are given vector functions with three components depending of x and x,t, respectively; $\mathcal{C}_{jl}$, $\mathcal{R}_{jl}$, $\mathcal{R}_{jl}^T$, $\mathcal{K}_{jl}$ are matrices given by (2-11)–(2-13).

We assume that C_{ijkl}, R_{ijkl}, K_{ijkl}, appearing in (2-11)–(2-13), satisfy (2-3) and (2-4).

Remark 3.1. Note that the initial data (3-1), (3-2), where

$$\boldsymbol{u}^0(x)=0, \quad \boldsymbol{u}^1(x)=0, \quad \boldsymbol{w}^0(x)=0,$$

describe the fact that there are no vibrations and there are no sources of perturbations at the initial moment of time. The initial data (3-1), (3-2) have a physical interpretation of the disturbance at the initial instant of time. Moreover these initial data together with phonon and phason forces $\boldsymbol{f}(x,t)$ and $\boldsymbol{g}(x,t)$ are equivalent to the external forces whose densities are described by (see, for example, [Vladimirov 1971, pp. 172–174, 197–198])

$$\vec{F}=\boldsymbol{u}^0(x)\delta'(t)+\boldsymbol{u}^1(x)\delta(t)+\theta(t)\boldsymbol{f}(x,t), \quad \vec{G}=\boldsymbol{w}^0(x)\delta(t)+\theta(t)\boldsymbol{g}(x,t),$$

where $\delta(t)$ is the Dirac delta function, $\delta'(t)$ is the derivative of $\delta(t)$, $\theta(t)$ is the Heaviside step function (the discontinuous function whose values are zero for negative arguments and are equal to one for nonnegative arguments).

3A. ***IVP in terms of the Fourier transform with respect to space variables.*** Let

$$\tilde{\boldsymbol{f}}(\nu,t)=(\tilde{f}_1(\nu,t),\tilde{f}_2(\nu,t),\tilde{f}_3(\nu,t)), \quad \tilde{\boldsymbol{g}}(\nu,t)=(\tilde{g}_1(\nu,t),\tilde{g}_2(\nu,t),\tilde{g}_3(\nu,t)),$$

be the Fourier images of $\boldsymbol{f}(x,t)$, $\boldsymbol{g}(x,t)$ with respect to $x=(x_1,x_2,x_3)\in R^3$, i.e.,

$$\tilde{f}_j(\nu,t)=\int_{-\infty}^{\infty}\int_{-\infty}^{\infty}\int_{-\infty}^{\infty} f_j(x,t)e^{ix\cdot\nu}\,dx_1\,dx_2\,dx_3,$$
$$\tilde{g}_j(\nu,t)=\int_{-\infty}^{\infty}\int_{-\infty}^{\infty}\int_{-\infty}^{\infty} g_j(x,t)e^{ix\cdot\nu}\,dx_1\,dx_2\,dx_3,$$

where

$$\nu=(\nu_1,\nu_2,\nu_3)\in R^3,\quad x\cdot\nu=x_1\nu_1+x_2\nu_2+x_3\nu_3,\quad i^2=-1,\quad j=1,2,3.$$

Let

$$\tilde{\boldsymbol{u}}^0(\nu)=(\tilde{u}_1^0(\nu),\tilde{u}_2^0(\nu),\tilde{u}_3^0(\nu)),\quad \tilde{\boldsymbol{u}}^1(\nu)=(\tilde{u}_1^1(\nu),\tilde{u}_2^1(\nu),\tilde{u}_3^1(\nu)),\quad \tilde{\boldsymbol{w}}^0(\nu)=(\tilde{w}_1^0(\nu),\tilde{w}_2^0(\nu),\tilde{w}_3^0(\nu))$$

be the Fourier transform of $\boldsymbol{u}^0(x,t)$, $\boldsymbol{u}^1(x,t)$, $\boldsymbol{w}^0(x,t)$ and functions

$$\tilde{u}_j^0(\nu),\ \tilde{u}_j^1(\nu),\ \tilde{w}_j^0(\nu),\ \tilde{f}_j(\nu,t),\ \tilde{g}_j(\nu,t)\quad j=1,2,3$$

have finite supports with respect to ν for every fixed $t>0$.

Problem (2-9), (2-10) can be written in terms of the Fourier transform images as follows

$$\rho\frac{d^2\tilde{\boldsymbol{u}}(\nu,t)}{dt^2}+\mathcal{C}(\nu)\tilde{\boldsymbol{u}}(\nu,t)+\mathcal{R}(\nu)\tilde{\boldsymbol{w}}(\nu,t)=\tilde{\boldsymbol{f}}(\nu,t),\quad t>0, \tag{3-3}$$
$$\kappa\frac{d\tilde{\boldsymbol{w}}(\nu,t)}{dt}+\mathcal{K}(\nu)\tilde{\boldsymbol{w}}(\nu,t)+\mathcal{R}^T(\nu)\tilde{\boldsymbol{u}}(\nu,t)=\tilde{\boldsymbol{g}}(\nu,t),\quad t>0, \tag{3-4}$$
$$\tilde{\boldsymbol{u}}(\nu,0)=\tilde{\boldsymbol{u}}^0(\nu),\quad \frac{d}{dt}\tilde{\boldsymbol{u}}(\nu,t)|_{t=0}=\tilde{\boldsymbol{u}}^1(\nu), \tag{3-5}$$
$$\tilde{\boldsymbol{w}}(\nu,0)=\tilde{\boldsymbol{w}}^0(\nu). \tag{3-6}$$

Here

$$\mathcal{C}(\nu)=\sum_{j,l=1}^{3}\mathcal{C}_{jl}\nu_j\nu_l, \tag{3-7}$$
$$\mathcal{K}(\nu)=\sum_{j,l=1}^{3}\mathcal{K}_{jl}\nu_j\nu_l, \tag{3-8}$$
$$\mathcal{R}(\nu)=\sum_{j,l=1}^{3}\mathcal{R}_{jl}\nu_j\nu_l. \tag{3-9}$$

Remark 3.2. We note that $\mathcal{C}(0)=\mathcal{K}(0)=\mathcal{R}(0)=0$. Taking into account the properties (2-3) and (2-4) we find that $\mathcal{C}(\nu)$, $\mathcal{K}(\nu)$ are symmetric positive definite matrices for $\nu\neq 0$ (see Appendix B). Moreover a solution of (3-3)–(3-6) for $\nu=0$ is given by the following formulas:

$$\tilde{\boldsymbol{u}}(0,t)=\tilde{\boldsymbol{u}}^0(0)+\tilde{\boldsymbol{u}}^1(0)t+\frac{1}{\rho}\int_0^t(t-\tau)\tilde{\boldsymbol{f}}(0,\tau)\,d\tau,\quad \tilde{\boldsymbol{w}}(0,t)=\tilde{\boldsymbol{w}}^0(0)+\frac{1}{\kappa}\int_0^t\tilde{\boldsymbol{g}}(0,\tau)\,d\tau.$$

The construction of the solution of IVP (3-3)–(3-6) for $\nu \neq 0$ are described in the next subsections. Since matrices $\mathcal{C}(\nu)$ and $\mathcal{K}(\nu)$ are real symmetric positive definite for $\nu \neq 0$ (see Appendix B) then $\mathcal{C}(\nu)$ and $\mathcal{K}(\nu)$ are congruent to diagonal matrices of their eigenvalues. That is, there exists orthogonal matrices $\mathcal{T}(\nu)$ and $\mathcal{Z}(\nu)$ such that

$$\mathcal{T}^{-1}(\nu)\mathcal{C}(\nu)\mathcal{T}(\nu) = \mathcal{D}(\nu), \quad \mathcal{Z}^{-1}(\nu)\mathcal{K}(\nu)\mathcal{Z}(\nu) = \mathcal{E}(\nu), \tag{3-10}$$

where $\mathcal{T}^{-1}(\nu)$, $\mathcal{Z}^{-1}(\nu)$ are the inverse matrices to $\mathcal{T}(\nu)$, $\mathcal{Z}(\nu)$; $\mathcal{D}(\nu) = \mathrm{diag}(d_1(\nu), d_2(\nu), d_3(\nu))$, $\mathcal{E}(\nu) = \mathrm{diag}(e_1(\nu), e_2(\nu), e_3(\nu))$ are diagonal matrices with real valued positive diagonal elements for $\nu \neq 0$.

3B. ***Reduction of problem (3-3)–(3-6) to the vector integral equation of the Volterra type.*** Let further $\nu = (\nu_1, \nu_2, \nu_3) \in R^3$ and $\nu \neq 0$. Let us consider vector functions $V(\nu, t)$, $S(\nu, t)$ such that

$$\tilde{\boldsymbol{u}}(\nu, t) = \mathcal{T}(\nu)V(\nu, t), \quad \tilde{\boldsymbol{w}}(\nu, t) = \mathcal{Z}(\nu)S(\nu, t). \tag{3-11}$$

IVP (3-3)–(3-6) can be written in terms of $V(\nu, t)$, $S(\nu, t)$ vector functions as follows:

$$\rho\mathcal{T}(\nu)\frac{d^2V(\nu, t)}{dt^2} + \mathcal{C}(\nu)\mathcal{T}(\nu)V(\nu, t) + \mathcal{R}(\nu)\mathcal{Z}(\nu)S(\nu, t) = \tilde{\boldsymbol{f}}(\nu, t), \quad t > 0, \tag{3-12}$$

$$\kappa\mathcal{Z}(\nu)\frac{dS(\nu, t)}{dt} + \mathcal{K}(\nu)\mathcal{Z}(\nu)S(\nu, t) + \mathcal{R}^T(\nu)\mathcal{T}(\nu)V(\nu, t) = \tilde{\boldsymbol{g}}(\nu, t), \quad t > 0, \tag{3-13}$$

$$\mathcal{T}(\nu)V(\nu, 0) = \tilde{\boldsymbol{u}}^0(\nu), \quad \mathcal{T}(\nu)\frac{d}{dt}V(\nu, t)|_{t=0} = \tilde{\boldsymbol{u}}^1(\nu), \tag{3-14}$$

$$\mathcal{Z}(\nu)S(\nu, 0) = \tilde{\boldsymbol{w}}^0(\nu). \tag{3-15}$$

Multiplying equalities (3-12), (3-14) by $\mathcal{T}^{-1}(\nu)$ and (3-13), (3-15) by $\mathcal{Z}^{-1}(\nu)$ and using (3-10), (3-11) we find

$$\frac{d^2V(\nu, t)}{dt^2} + \frac{1}{\rho}\mathcal{D}(\nu)V(\nu, t) + \mathcal{M}(\nu)S(\nu, t) = \tilde{\boldsymbol{h}}(\nu, t), \quad t > 0, \tag{3-16}$$

$$\frac{dS(\nu, t)}{dt} + \frac{1}{\kappa}\mathcal{E}(\nu)S(\nu, t) + \mathcal{N}(\nu)V(\nu, t) = \tilde{\boldsymbol{p}}(\nu, t), \quad t > 0, \tag{3-17}$$

$$V(\nu, 0) = V^0(\nu), \quad \frac{d}{dt}V(\nu, t)|_{t=0} = V^1(\nu), \tag{3-18}$$

$$S(\nu, 0) = S^0(\nu), \tag{3-19}$$

where matrices $\mathcal{M}(\nu)$, $\mathcal{N}(\nu)$, and vector functions $\tilde{\boldsymbol{h}}(\nu, t)$, $\tilde{\boldsymbol{p}}(\nu, t)$, $V^0(\nu)$, $V^1(\nu)$, $S^0(\nu)$ are defined by

$$\mathcal{M}(\nu) = \frac{1}{\rho}\mathcal{T}^{-1}(\nu)\mathcal{R}(\nu)\mathcal{T}(\nu), \quad \mathcal{N}(\nu) = \frac{1}{\kappa}\mathcal{Z}^{-1}(\nu)\mathcal{R}^T(\nu)\mathcal{Z}(\nu), \tag{3-20}$$

$$\tilde{\boldsymbol{h}}(\nu, t) = \frac{1}{\rho}\mathcal{T}^{-1}(\nu)\tilde{\boldsymbol{f}}(\nu, t), \quad \tilde{\boldsymbol{p}}(\nu, t) = \frac{1}{\kappa}\mathcal{Z}^{-1}(\nu)\tilde{\boldsymbol{g}}(\nu, t), \tag{3-21}$$

$$V^0(\nu) = \mathcal{T}^{-1}(\nu)\tilde{\boldsymbol{u}}^0(\nu), \quad V^1(\nu) = \mathcal{T}^{-1}(\nu)\tilde{\boldsymbol{u}}^1(\nu), \quad S^0(\nu) = \mathcal{T}^{-1}(\nu)\tilde{\boldsymbol{w}}^0(\nu). \tag{3-22}$$

Equations (3-16), (3-17) with conditions (3-18), (3-19) are equivalent to the following system of integral equations of the Volterra-type:

$$V(\nu,t) = \boldsymbol{h}^1(\nu,t) + \int_0^t (\boldsymbol{K}^1 S)(\nu,t,\tau)\,d\tau \tag{3-23}$$

$$S(\nu,t) = \boldsymbol{h}^2(\nu,t) + \int_0^t (\boldsymbol{K}^2 V)(\nu,t,\tau)\,d\tau, \tag{3-24}$$

where

$$\boldsymbol{h}^1(\nu,t) = \cos\left(\frac{1}{\sqrt{\rho}}\mathcal{D}^{1/2}(\nu)\,t\right) V^0(\nu) + \sqrt{\rho}\mathcal{D}^{-1/2}(\nu)\,\sin\left(\frac{1}{\sqrt{\rho}}\mathcal{D}^{1/2}(\nu)\,t\right) V^1(\nu) + \sqrt{\rho}\int_0^t \mathcal{D}^{-1/2}(\nu)\sin\left(\frac{1}{\sqrt{\rho}}\mathcal{D}^{1/2}(\nu)\,(t-\tau)\right)\tilde{\boldsymbol{h}}(\nu,\tau)\,d\tau, \tag{3-25}$$

$$\boldsymbol{h}^2(\nu,t) = \exp\left(-\frac{1}{\kappa}\mathcal{E}(\nu)\,t\right) S^0(\nu) + \int_0^t \exp\left(-\frac{1}{\kappa}\mathcal{E}(\nu)\,(t-\tau)\right)\tilde{\boldsymbol{p}}(\nu,\tau)\,d\tau, \tag{3-26}$$

$$(\boldsymbol{K}^1 S)(\nu,t,\tau) = -\sqrt{\rho}\mathcal{D}^{-1/2}(\nu)\sin\left(\frac{1}{\sqrt{\rho}}\mathcal{D}^{1/2}(\nu)\,(t-\tau)\right)\mathcal{M}(\nu)S(\nu,\tau), \tag{3-27}$$

$$(\boldsymbol{K}^2 V)(\nu,t,\tau) = -\exp\left(-\frac{\mathcal{E}(\nu)}{\kappa}\,(t-\tau)\right)\mathcal{N}(\nu)V(\nu,\tau). \tag{3-28}$$

The system of integral equations (3-23), (3-24) can be written in the form of one vector integral equation as follows:

$$\boldsymbol{U}(\nu,t) = \boldsymbol{h}(\nu,t) + \int_0^t (\boldsymbol{K}\boldsymbol{U})(\nu,t,\tau)\,d\tau, \tag{3-29}$$

where $\boldsymbol{h}(\nu,t)$ is the vector function with six components whose the first three components are components of $\boldsymbol{h}^1(\nu,t)$ and the last three components are components of $\boldsymbol{h}^2(\nu,t)$ ($\boldsymbol{h}^1(\nu,t)$ and $\boldsymbol{h}^2(\nu,t)$ are defined by (3-25), (3-26)); $\boldsymbol{U}(\nu,t) = (V(\nu,t), S(\nu,t))$ is the vector function with six components whose the first three components are components of $V(\nu,t)$ and the last three components are components of $S(\nu,t)$; $\boldsymbol{K}$ is the vector operator with 6 components defined by the following formula

$$(\boldsymbol{K}\boldsymbol{U})(\nu,t,\tau) = ((\boldsymbol{K}^1 S)(\nu,t,\tau), (\boldsymbol{K}^2 V)(\nu,t,\tau)) \tag{3-30}$$

for any vector function $\boldsymbol{U}(\nu,t) = (V(\nu,t), S(\nu,t))$ with six components. Here the vector operators $(\boldsymbol{K}^1 S)(\nu,t,\tau)$ and $(\boldsymbol{K}^2 V)(\nu,t,\tau)$ are determined by (3-27), (3-28).

3C. ***Properties of the kernel of the vector integral equation.*** The operator $\boldsymbol{K}$, defined by (3-27), (3-28), (3-30), satisfies the following properties.

Property 3.3. Let T, ω, Ω be given positive constants ($\omega \le \Omega$);

$$\Delta(T,\omega,\Omega) = \{(\nu,t) \mid \nu = (\nu_1,\nu_2,\nu_3) \in R^3,\ \omega \le |\nu| \le \Omega,\ 0 \le t \le T\};$$

$V(\nu,t) = (V_1(\nu,t), V_2(\nu,t), V_3(\nu,t))$, $S(\nu,t) = (S_1(\nu,t), S_2(\nu,t), S_3(\nu,t))$ be vector functions such that $V_j(\nu,t)$, $S_j(\nu,t)$, $j = 1,2,3$ are continuous in the region $\Delta(T,\Omega)$; $\boldsymbol{U}(\nu,t) = (V(\nu,t), S(\nu,t))$

be the vector function whose the first three components are components of $V(\nu, t)$, and the last three components are components of $S(\nu, t)$. Then all components of the vector function

$$\int_0^t (\boldsymbol{K}\boldsymbol{U})(\nu, t, \tau)\, d\tau$$

are continuous on $\Delta(T, \omega, \Omega)$ and the first three components of them are twice continuously differentiable on $\Delta(T, \omega, \Omega)$ and the last three components are one time continuously differentiable on $\Delta(T, \omega, \Omega)$.

Property 3.4. Let T, ω, Ω be given positive constants; $\Delta(T, \omega, \Omega)$, $V(\nu, t) = (V_1(\nu, t),\ V_2(\nu, t),\ V_3(\nu, t))$, $S(\nu, t) = (S_1(\nu, t),\ S_2(\nu, t),\ S_3(\nu, t))$, $\boldsymbol{U}(\nu, t) = (V(\nu, t),\ S(\nu, t))$ be the region and vector functions defined in Property 3.3; $(\boldsymbol{K}^1 S)_j(\nu, t, \tau)$, $(\boldsymbol{K}^2 S)_j(\nu, t, \tau)$, $j = 1, 2, 3$ be components of vector functions $(\boldsymbol{K}^1 S)(\nu, t, \tau)$ and $(\boldsymbol{K}^2 V)(\nu, t, \tau)$ defined by (3-27), (3-28). Then for any $(\nu, t) \in \Delta(T, \omega, \Omega)$ and $0 \le \tau \le t$ the following inequalities are satisfied:

$$|(\boldsymbol{K}^1 S)_j(\nu, t, \tau)| \le \frac{(t-\tau)}{\rho}\, \Omega^2\, \Upsilon\, \|\boldsymbol{U}(\nu, \tau)\|_2, \tag{3-31}$$

$$|(\boldsymbol{K}^2 V)_j(\nu, t, \tau)| \le \frac{1}{\kappa}\, \Omega^2\, \Upsilon\, \|\boldsymbol{U}(\nu, \tau)\|_2. \tag{3-32}$$

Here the positive constants ρ and κ are introduced in the beginning of Section 2B (after (2-5), (2-6)); the constant Υ is defined by the equality

$$\Upsilon = \sum_{j,l=1}^{3} \|\mathcal{R}_{jl}\|_2, \tag{3-33}$$

where $\|\mathcal{R}_{jl}\|_2$ is the operator norm of the matrix $\mathcal{R}_{jl}$ defined by (2-12),

$$\|\boldsymbol{U}(\nu, \tau)\|_2 = \sqrt{\|V(\nu, \tau)\|_2^2 + \|S(\nu, \tau)\|_2^2},$$
$$\|V(\nu, \tau)\|_2^2 = V_1^2(\nu, \tau) + V_2^2(\nu, \tau) + V_3^2(\nu, \tau),$$
$$\|S(\nu, \tau)\|_2^2 = S_1^2(\nu, \tau) + S_2^2(\nu, \tau) + S_3^2(\nu, \tau).$$

Proof. Let $\mathcal{T}(\nu)$, $\mathcal{Z}(\nu)$ be orthogonal matrices and $\mathcal{D}(\nu)$, $\mathcal{E}(\nu)$ be diagonal matrices with positive diagonal elements for $\nu \ne 0$ defined by (3-10), and $\mathcal{M}(\nu)$, $\mathcal{N}(\nu)$ be matrices defined by (3-20). Then, applying properties of the operator norm of matrix, we find the following inequalities:

$$\left\| \sqrt{\rho}\mathcal{D}^{-1/2}(\nu) \sin\left(\frac{1}{\sqrt{\rho}} \mathcal{D}^{1/2}(\nu)\, (t-\tau) \right) \right\|_2 \le (t-\tau), \tag{3-34}$$

$$\left\| \exp\left(-\frac{\mathcal{E}(\nu)}{\kappa} (t-\tau) \right) \right\|_2 \le 1, \tag{3-35}$$

$$\|\mathcal{M}(\nu)\|_2 \le \frac{1}{\rho} \|\mathcal{T}^{-1}(\nu)\|_2 \|\mathcal{R}(\nu)\|_2 \|\mathcal{T}(\nu)\|_2 = \frac{1}{\rho} \|\mathcal{R}(\nu)\|_2, \tag{3-36}$$

$$\|\mathcal{N}(\nu)\|_2 \le \frac{1}{\kappa} \|\mathcal{Z}^{-1}(\nu)\|_2 \|\mathcal{R}^T(\nu)\|_2 \|\mathcal{Z}(\nu)\|_2 = \frac{1}{\kappa} \|\mathcal{R}^T(\nu)\|_2. \tag{3-37}$$

Using (3-9) we find

$$\|\mathcal{R}(\nu)\|_2 \le |\nu|^2 \sum_{j,l=1}^{3} \|\mathcal{R}_{jl}\|_2 = |\nu|^2\, \Upsilon, \tag{3-38}$$

$$\|\mathcal{R}^T(\nu)\|_2 \le |\nu|^2 \sum_{j,l=1}^{3} \|\mathcal{R}^T_{jl}\|_2 = |\nu|^2\, \Upsilon, \tag{3-39}$$

where Υ is defined by (3-33). Using (3-27), (3-28) and (3-34)–(3-39) we find (3-31), (3-32). □

3D. ***The solution of the vector integral equation (3-29) by successive approximations.*** Let T, ω, Ω be given positive constants ($\omega \le \Omega$) and $\Delta(T, \omega, \Omega)$ be the region defined in Property 3.3. We assume that vector functions $\tilde{\boldsymbol{u}}^0(\nu)$, $\tilde{\boldsymbol{u}}^1(\nu)$, $\tilde{\boldsymbol{w}}^0(\nu)$, appearing in (3-5), (3-6) are continuous for $|\nu| \le \Omega$ and vector functions $\tilde{\boldsymbol{f}}(\nu, t)$, $\tilde{\boldsymbol{g}}(\nu, t)$, appearing in (3-3), (3-4) are continuous for $|\nu| \le \Omega$, $0 \le t \le T$. Moreover vector functions $\tilde{\boldsymbol{u}}^0(\nu)$, $\tilde{\boldsymbol{u}}^1(\nu)$, $\tilde{\boldsymbol{w}}^0(\nu)$ $\tilde{\boldsymbol{f}}(\nu, t)$, $\tilde{\boldsymbol{g}}(\nu, t)$ are supposed to be zero for $|\nu| > \Omega$, $0 \le t \le T$. It follows from (3-21), (3-22) and (3-25), (3-26) that components of vector function $\boldsymbol{h}(\nu, t)$ defined after (3-29) are continuous on $\Delta(T, \Omega)$ and are equal to zero for any (ν, t) satisfying $\nu > \Omega$, $0 \le t \le T$. Moreover the first three components of $\boldsymbol{h}(\nu, t)$ are twice continuously differentiable with respect to t and the last three components are one time continuously differentiable with respect to t in the region $\Delta(T, \omega, \Omega)$.

To find a solution $\boldsymbol{U}(\nu, t)$ of (3-29) for $0 \le t \le T$ and a fixed $\nu \in R^3$, $\nu \ne 0$, we apply the successive approximations

$$\boldsymbol{U}^{(0)}(\nu, t) = \boldsymbol{h}(\nu, t), \tag{3-40}$$

$$\boldsymbol{U}^{(n)}(\nu, t) = \int_0^t (\boldsymbol{K}\boldsymbol{U}^{(n-1)})(\nu, t, \tau)\, d\tau, \quad n = 1, 2, 3, \ldots \tag{3-41}$$

Remark 3.5. Equalities (3-40), (3-41) can be written in a component form as follows:

$$V_j^{(0)}(\nu, t) = H_j^1(\nu, t), \qquad S_j^{(0)}(\nu, t) = H_j^2(\nu, t),$$

$$V_j^{(n)}(\nu, t) = \int_0^t (\boldsymbol{K}^1 S_j^{(n-1)}(\nu, \tau))\, d\tau, \quad S_j^{(n)}(\nu, t) = \int_0^t (\boldsymbol{K}^2 V_j^{(n-1)}(\nu, \tau))\, d\tau,$$

$$n = 1, 2, 3, \ldots; \; j = 1, 2, 3.$$

Here $\boldsymbol{u}^{(n)}(\nu, t)$ is the vector function with the following six components:

$$V_1^{(n)}(\nu, \tau), \quad V_2^{(n)}(\nu, \tau), \quad V_3^{(n)}(\nu, \tau)(\nu, t), \quad S_1^{(n)}(\nu, \tau),$$
$$S_2^{(n)}(\nu, \tau), \quad S_3^{(n)}(\nu, \tau)); \quad H_j^1(\nu, t), \quad H_j^2(\nu, t), \quad j = 1, 2, 3$$

are components of vector functions $\boldsymbol{h}^1(\nu, t)$, $\boldsymbol{h}^2(\nu, t)$ defined by (3-23), (3-24).

Remark 3.6. Since all components of $\boldsymbol{h}(\nu, t)$ are equal to zero for $|\nu| > \Omega$, $0 \le t \le T$ then $\boldsymbol{U}^{(n)}(\nu, t) = 0$ for $|\nu| > \Omega$, $0 \le t \le T$. Moreover $\boldsymbol{U}(\nu, t) = 0$ is a solution of (3-29) for $|\nu| > \Omega$, $0 \le t \le T$.

The goal of this section is to show that for any $j = 1, 2, 3$ the series

$$\sum_{n=0}^{\infty} V_j^{(n)}(\nu, t), \quad \sum_{n=0}^{\infty} S_j^{(n)}(\nu, t),$$

converge uniformly on $\Delta(T, \omega, \Omega)$ to some continuous functions $V_j(\nu, \tau)$, $S_j(\nu, \tau)$, $j = 1, 2, 3$, and then, if

$$V(\nu, \tau) = (V_1(\nu, \tau), V_2(\nu, \tau), V_3(\nu, \tau)), \quad S(\nu, \tau) = (S_1(\nu, \tau), S_2(\nu, \tau), S_3(\nu, \tau))$$

are vector functions with found components then the vector function $\boldsymbol{U}(\nu, t) = (V(\nu, \tau), S(\nu, \tau))$ is a solution of (3-29).

Indeed, we find from (3-40), (3-41) and the properties of Section 3C that vector functions $\boldsymbol{U}^{(n)}(\nu, t)$, $n = 0, 1, 2, 3, \ldots$ have continuous components on $\Delta(T, \omega, \Omega)$ and

$$|V_j^{(n)}(\nu, t)| = \left| \int_0^t (\boldsymbol{K}^1 S_j^{(n-1)}(\nu, \tau))\, d\tau \right| \le B \int_0^t \|\boldsymbol{U}^{(n-1)}(\nu, \tau)\|_2, \tag{3-42}$$

$$|S_j^{(n)}(\nu, t)| = \left| \int_0^t (\boldsymbol{K}^2 V_j^{(n-1)}(\nu, \tau))\, d\tau \right| \le B \int_0^t \|\boldsymbol{U}^{(n-1)}(\nu, \tau)\|_2, \tag{3-43}$$

$$n = 1, 2, 3, \ldots; \quad j = 1, 2, 3,$$

where B is the constant defined by

$$B = \Omega^2 \gamma \max\Big(\frac{1}{\kappa}, \frac{T}{\rho}\Big). \tag{3-44}$$

Using (3-42), (3-43) we find the following inequality:

$$\|\boldsymbol{U}^{(n-1)}(\nu, t)\|_2 \le \sqrt{6}\|\boldsymbol{U}^{(n-1)}(\nu, t)\|_\infty \le \sqrt{6} B \int_0^t \|\boldsymbol{U}^{(n-2)}(\nu, \tau)\|_2\, d\tau, \tag{3-45}$$

where

$$\|\boldsymbol{U}^{(n-1)}(\nu, t)\|_\infty = \max\{\max_{j=1,2,3} |V_j^{(n-1)}(\nu, t)|, \max_{j=1,2,3} |S_j^{(n-1)}(\nu, t)|\}.$$

We have from (3-42), (3-43), (3-45):

$$\|\boldsymbol{U}^{(n-1)}(\nu, t)\|_2 \le \frac{(\sqrt{6}\, B\, t)^{n-1}}{(n-1)!} G, \tag{3-46}$$

$$|V_j^{(n)}(\nu, t)| \le \frac{(\sqrt{6}\, B\, t)^n}{(n)!} \frac{G}{\sqrt{6}}, \tag{3-47}$$

$$|S_j^{(n)}(\nu, t)| \le \frac{(\sqrt{6}\, B\, t)^n}{(n)!} \frac{G}{\sqrt{6}}, \tag{3-48}$$

$$n = 1, 2, 3, \ldots; \quad j = 1, 2, 3,$$

where

$$G = \max_{(\nu,t)\in\Delta(T,\omega,\Omega)} \|\boldsymbol{h}(\nu, t)\|_2.$$

Using (3-46)–(3-48) and the first theorem of Weierstrass [Apostol 1961, p. 425] we find that there are continuous functions $V_j(\nu, t)$, $S_j(\nu, t)$ on the region $\Delta(T, \Omega)$ that the series

$$\sum_{n=0}^{\infty} V_j^{(n)}(\nu, t), \quad \sum_{n=0}^{\infty} S_j^{(n)}(\nu, t)$$

converge uniformly and absolutely on $\Delta(T, \omega, \Omega)$ to $V_j(\nu, t)$, $S_j(\nu, t)$, $j = 1, 2, 3$. Let

$$V(\nu, \tau) = (V_1(\nu, \tau), V_2(\nu, \tau), V_3(\nu, \tau)), \quad S(\nu, \tau) = (S_1(\nu, \tau), S_2(\nu, \tau), S_3(\nu, \tau)),$$

where $V_j(\nu, t)$ and $S_j(\nu, t)$, $j = 1, 2, 3$ are sums of above mentioned series. We want to show now that $\boldsymbol{U}(\nu, t) = (V(\nu, \tau), S(\nu, \tau))$ is a solution of (3-29). Let us consider the vector function $\boldsymbol{U}^{(n)}(\nu, t) = (V^{(n)}(\nu, \tau), S^{(n)}(\nu, \tau))$ defined by (3-40), (3-41). Summing the right and left sides of (3-41) with respect to n from 1 to N we have

$$\sum_{n=1}^{N} \boldsymbol{U}^{(n)}(\nu, t) = \sum_{n=0}^{N-1} \int_0^t (\boldsymbol{K}\boldsymbol{U}^{(n-1)})(\nu, t, \tau)\, d\tau, \tag{3-49}$$

where

$$\sum_{n=1}^{N} \boldsymbol{U}^{(n)}(\nu, t) = \left(\sum_{n=1}^{N} V^{(n)}(\nu, t), \sum_{n=1}^{N} S^{(n)}(\nu, t) \right),$$

$$\sum_{n=1}^{N} V^{(n)}(\nu, t) = \left(\sum_{n=1}^{N} V_1^{(n)}(\nu, t), \sum_{n=1}^{N} V_2^{(n)}(\nu, t), \sum_{n=1}^{N} V_3^{(n)}(\nu, t) \right),$$

$$\sum_{n=1}^{N} S^{(n)}(\nu, t) = \left(\sum_{n=1}^{N} S_1^{(n)}(\nu, t), \sum_{n=1}^{N} S_2^{(n)}(\nu, t), \sum_{n=1}^{N} S_3^{(n)}(\nu, t) \right).$$

Adding the vector function $\boldsymbol{h}(\nu, t)$ to both sides of (3-49) we find

$$\sum_{n=0}^{N} \boldsymbol{U}^{(n)}(\nu, t) = \boldsymbol{h}(\nu, t) + \int_0^t \left(\boldsymbol{K} \sum_{n=0}^{N-1} \boldsymbol{U}^{(n-1)} \right)(\nu, t, \tau)\, d\tau. \tag{3-50}$$

Letting N tend to infinity and using the second Weierstrass theorem [Apostol 1961, p. 426], we find that the vector function $\boldsymbol{U}(\nu, t) = (V(\nu, t), S(\nu, t))$ satisfies (3-29) for $(\nu, t) \in \Delta(T, \omega, \Omega)$. Since ω is an arbitrary positive number such that $\omega \le \Omega$ then the vector function $\boldsymbol{U}(\nu, t) = (V(\nu, t), S(\nu, t))$ has continuous components for $|\nu| \le \Omega$ $(\nu \ne 0)$, $0 \le t \le T$ and the vector function $\boldsymbol{U}(\nu, t) = (V(\nu, t), S(\nu, t))$ is a solution of (3-29) for $|\nu| \le \Omega$ $(\nu \ne 0)$, $0 \le t \le T$.

3E. ***Properties of the solution of the integral equation (3-29).*** Let T, ω, Ω be given positive constants $(\omega \le \Omega)$ and

$$\Delta(T, \Omega) = \{(\nu, t) \mid \nu = (\nu_1, \nu_2, \nu_3) \in R^3,\ \nu \ne 0,\ |\nu| \le \Omega,\ 0 \le t \le T\}.$$

The vector functions $\tilde{\boldsymbol{u}}^0(\nu)$, $\tilde{\boldsymbol{u}}^1(\nu)$, $\tilde{\boldsymbol{w}}^0(\nu)$, $\tilde{\boldsymbol{f}}(\nu, t)$, $\tilde{\boldsymbol{g}}(\nu, t)$, $\boldsymbol{h}(\nu, t)$ satisfy assumptions described in the beginning of Section 3A.

Property 3.7. Let $\boldsymbol{K}^1$, $\boldsymbol{K}^2$, $\boldsymbol{K}$ be operator defined by (3-27), (3-28), (3-30); $\boldsymbol{u}(\nu,t)=(V(\nu,t),S(\nu,t))$ be a solution of (3-29) whose components are continuous on $\Delta(T,\Omega)$. Then

$$\frac{\partial V(\nu,t)}{\partial t},\quad \frac{\partial S(\nu,t)}{\partial t},\quad \frac{\partial^2 V(\nu,t)}{\partial t^2}$$

are continuous on $\Delta(T,\Omega)$.

Proof. Under conditions of Property 3.7 the vector functions

$$\boldsymbol{h}^1(\nu,t),\quad \boldsymbol{h}^2(\nu,t),\quad \frac{\partial \boldsymbol{h}^1(\nu,t)}{\partial t},\quad \frac{\partial \boldsymbol{h}^2(\nu,t)}{\partial t},\quad \frac{\partial^2 \boldsymbol{h}^1(\nu,t)}{\partial t^2}$$

are continuous on $\Delta(T,\omega,\Omega)$ and the vector functions $V(\nu,t)$, $S(\nu,t)$ satisfy equalities (3-23), (3-24). Differentiating (3-23), (3-24) with respect to t we find

$$\frac{\partial V(\nu,t)}{\partial t}=\frac{\partial \boldsymbol{h}^1(\nu,t)}{\partial t}-\int_0^t \cos\Big(\frac{1}{\sqrt{\rho}}\mathcal{D}^{1/2}(\nu)(t-\tau)\Big)\mathcal{M}(\nu)S(\nu,\tau)\,d\tau,$$

$$\frac{\partial^2 V(\nu,t)}{\partial t^2}=\frac{\partial^2 \boldsymbol{h}^1(\nu,t)}{\partial t^2}+\mathcal{M}(\nu)S(\nu,t)+\int_0^t \sqrt{\rho}\mathcal{D}^{1/2}(\nu)\,\sin\Big(\frac{1}{\sqrt{\rho}}\mathcal{D}^{1/2}(\nu)(t-\tau)\Big)\mathcal{M}(\nu)S(\nu,\tau)\,d\tau,$$

$$\frac{\partial S(\nu,t)}{\partial t}=\frac{\partial \boldsymbol{h}^2(\nu,t)}{\partial t}-\mathcal{N}(\nu)V(\nu,t)+\int_0^t \frac{\mathcal{E}(\nu)}{\kappa}\exp\Big(-\frac{\mathcal{E}(\nu)}{\kappa}(t-\tau)\Big)\mathcal{N}(\nu)V(\nu,\tau)\,d\tau.$$

Since the right sides of the obtained equations are continuous functions on $\Delta(T,\omega,\Omega)$ then the left sides are also continuous on $\Delta(T,\omega,\Omega)$. Therefore

$$\frac{\partial V(\nu,t)}{\partial t},\quad \frac{\partial S(\nu,t)}{\partial t},\quad \frac{\partial^2 V(\nu,t)}{\partial t^2}$$

are continuous on $\Delta(T,\omega,\Omega)$. Since ω is an arbitrary positive number such that $\omega\le\Omega$ then the vector functions

$$\frac{\partial V(\nu,t)}{\partial t},\quad \frac{\partial S(\nu,t)}{\partial t},\quad \frac{\partial^2 V(\nu,t)}{\partial t^2}$$

are continuous on $\Delta(T,\Omega)$. □

Property 3.8. Let $\boldsymbol{K}^1$, $\boldsymbol{K}^2$, $\boldsymbol{K}$ be operators defined by (3-27), (3-28), (3-30). Then the solution $\boldsymbol{U}(\nu,t)=(V(\nu,t),S(\nu,t))$ of (3-29) is unique in the class of continuous function on $\Delta(T,\Omega)$.

Proof. Let $\boldsymbol{U}(\nu,t)=(V(\nu,t),S(\nu,t))$ and $\boldsymbol{U}^*(\nu,t)=(V^*(\nu,t),S^*(\nu,t))$ be two solutions of (3-29) whose components are continuous on $\Delta(T,\Omega)$. Setting $\hat{V}(\nu,t)=V(\nu,t)-V^*(\nu,t)$, $\hat{S}(\nu,t)=S(\nu,t)-S^*(\nu,t)$, $\hat{\boldsymbol{u}}(\nu,t)=(\hat{V}(\nu,t),\hat{S}(\nu,t))$ we find from (3-29)

$$\hat{V}(\nu,t)=\int_0^t(\boldsymbol{K}^1\hat{S}(\nu,\tau))\,d\tau, \tag{3-51}$$

$$\hat{S}(\nu,t)=\int_0^t(\boldsymbol{K}^2\hat{V}(\nu,\tau))\,d\tau. \tag{3-52}$$

Using Property 3.4 we obtain from (3-51), (3-52)

$$\|\hat{\boldsymbol{u}}(\nu, t)\|_2 \le \sqrt{6}B \int_0^t \|\hat{\boldsymbol{u}}(\nu, \tau)\|_2 \, d\tau, \tag{3-53}$$

where B is the constant defined by (3-44). Applying Gronwall's lemma to (3-53) we find $\|\hat{\boldsymbol{u}}(\nu, t)\|_2 = 0$ for $(\nu, t) \in \Delta(T, \Omega)$. Using the continuity of $\hat{\boldsymbol{u}}(\nu, t)$ we conclude that

$$\hat{\boldsymbol{u}}(\nu, t) = (\hat{V}(\nu, t), \hat{S}(\nu, t)) = (V(\nu, t) - V^*(\nu, t), S(\nu, t) - S^*(\nu, t)) = 0$$

for $(\nu, t) \in \Delta(T, \Omega)$. This means that $\boldsymbol{U}(\nu, t) = \boldsymbol{U}^*(\nu, t)$ for $(\nu, t) \in \Delta(T, \Omega)$. □

Property 3.9. Let $\boldsymbol{U}(\nu, t) = (V(\nu, t), S(\nu, t))$ be a solution of (3-29) for $(\nu, t) \in \Delta(T, \Omega)$. Then the vector functions $\tilde{\boldsymbol{u}}(\nu, t)$, $\tilde{\boldsymbol{w}}(\nu, t)$, with components given by (3-11), are a unique solution of the initial value problem (3-3)–(3-6) in the class of vector functions for which

$$\tilde{\boldsymbol{u}}(\nu, t), \quad \tilde{\boldsymbol{w}}(\nu, t), \quad \frac{\partial \tilde{\boldsymbol{u}}(\nu, t)}{\partial t}, \quad \frac{\partial \tilde{\boldsymbol{w}}(\nu, t)}{\partial t}, \quad \frac{\partial^2 \tilde{\boldsymbol{u}}(\nu, t)}{\partial t^2}$$

are continuous on $\Delta(T, \Omega)$.

Proof. Using Properties 3.7 and 3.8 we conclude that the solution of integral equations (3-23), (3-24) (or the vector integral Equation (3-29)) is equivalent to the solution of the initial value problem (3-16)–(3-19). Moreover the initial value problem (3-16)–(3-19) can be written in the form of (3-3)–(3-6). Therefore if $\boldsymbol{u}(\nu, t) = (V(\nu, t), S(\nu, t))$ is a solution of (3-29) for $(\nu, t) \in \Delta(T, \Omega)$ then the vector functions $\tilde{\boldsymbol{u}}(\nu, t)$, $\tilde{\boldsymbol{w}}(\nu, t)$, with components given by (3-11), are a unique solution of the initial value problem (3-3)–(3-6) in the class of vector functions whose components

$$V(\nu, t), \quad S(\nu, t), \quad \frac{\partial V(\nu, t)}{\partial t}, \quad \frac{\partial S(\nu, t)}{\partial t}, \quad \frac{\partial^2 V(\nu, t)}{\partial t^2}$$

are continuous on $\Delta(T, \Omega)$. □

3F. ***The solution of initial value problem (2-9), (2-10), (3-1), (3-2).*** Let T, Ω be given positive constants and

$$\mathcal{D}(\Omega) = \{\nu = (\nu_1, \nu_2, \nu_3) \in R^3 \mid |\nu| \le \Omega\};$$

$C_\Omega(R^3)$ be a class of continuous functions whose components belong to $\mathcal{D}(\Omega)$; $PW_\Omega(R^3)$ be the class which is the inverse Fourier transform image of the class $C_\Omega(R^3)$;

Remark 3.10. $PW_\Omega(R^3)$ is called the Paley–Wiener class (see, for example, [Andersen 2004])

We assume further that conditions of Section 3A on vector functions $\tilde{\boldsymbol{u}}^0(\nu)$, $\tilde{\boldsymbol{u}}^1(\nu)$, $\tilde{\boldsymbol{w}}^0(\nu)$, $\tilde{\boldsymbol{f}}(\nu, t)$, $\tilde{\boldsymbol{g}}(\nu, t)$ are satisfied. Using Properties 3.7, 3.8 and Remark 3.5 we find that the solution $\tilde{\boldsymbol{u}}(\nu, t)$, $\tilde{\boldsymbol{w}}(\nu, t)$ of (3-3)–(3-6) has components which are continuous together with components of

$$\frac{\partial \tilde{\boldsymbol{u}}(\nu, t)}{\partial t}, \quad \frac{\partial \tilde{\boldsymbol{w}}(\nu, t)}{\partial t}, \quad \frac{\partial^2 \tilde{\boldsymbol{u}}(\nu, t)}{\partial t^2}$$

for $(\nu, t) \in \Delta(T, \Omega)$ and equal to zero for $|\nu| > \Omega$, $[0, T]$. As a result of solving the vector integral equation (3-29) and application of Property 3.9 we determine the Fourier images of the phonon and phason displacements $\tilde{\boldsymbol{u}}(\nu, t)$, $\tilde{\boldsymbol{w}}(\nu, t)$ for $(\nu, t) \in \Delta(T, \Omega)$. The vector functions $\tilde{\boldsymbol{u}}(\nu, t)$, $\tilde{\boldsymbol{w}}(\nu, t)$ satisfy

(3-3)–(3-6). To find unknown phonon and phason displacements $\boldsymbol{u}(x,t)$, $\boldsymbol{w}(x,t)$ satisfying (2-9), (2-10), (3-1), (3-2) we need to derive the inverse Fourier transform of $\tilde{\boldsymbol{u}}(\nu,t)$ and $\tilde{\boldsymbol{w}}(\nu,t)$. Indeed, applying the inverse Fourier transform to $\tilde{\boldsymbol{u}}(\nu,t)$ and $\tilde{\boldsymbol{w}}(\nu,t)$ we find vector functions $\boldsymbol{u}(x,t)$, $\boldsymbol{w}(x,t)$. Since the components of

$$\tilde{\boldsymbol{u}}(\nu,t), \quad \tilde{\boldsymbol{w}}(\nu,t), \quad \frac{\partial\tilde{\boldsymbol{u}}(\nu,t)}{\partial t}, \quad \frac{\partial\tilde{\boldsymbol{w}}(\nu,t)}{\partial t}, \quad \frac{\partial^2\tilde{\boldsymbol{u}}(\nu,t)}{\partial t^2}$$

are continuous for $(\nu,t)\in\Delta(T,\Omega)$ and equal to zero for $|\nu|>\Omega$, $[0,T]$ then the components of $\boldsymbol{u}(x,t)$ belong to the class $C^2([0,T];PW_\Omega(R^3))$ and the components of $\boldsymbol{w}(x,t)$ belong to the class $C^1([0,T];PW_\Omega(R^3))$. Here $C^2([0,T];PW_\Omega(R^3))$ is the class of all two time continuously differentiable mappings of $[0,T]$ into $PW_\Omega(R^3))$ and $C^1([0,T];PW_\Omega(R^3))$ is the class of all one time continuously differentiable mappings of $[0,T]$ into $PW_\Omega(R^3))$. Equalities (3-3)–(3-6) can be written in terms of $\boldsymbol{u}(x,t)$ and $\boldsymbol{w}(x,t)$ as equalities (2-9), (2-10), (3-1), (3-2). This means that we find vector functions $\boldsymbol{u}(x,t)$ and $\boldsymbol{w}(x,t)$ in classes $C^2([0,T];PW_\Omega(R^3))$ and $C^1([0,T];PW_\Omega(R^3))$ which are a solution of (2-9), (2-10), (3-1), (3-2). These vector functions are phonon and phason displacements. We note that the numerical implementation of the inverse Fourier transform can be done by the technique described in [Yakhno and Çerdik Yaslan 2012, §3.5].

4. Example of solving equations of elasto-hydrodynamics in icosahedral quasicrystals

For illustration of the approach we consider the equations of elasto-hydrodynamics in 3D icosahedral quasicrystals. We take the simple case when all functions appearing in equations depend on x_3 and t only. We note that for icosahedral quasicrystals phonon elastic constants (see, for example, [Ding et al. 1993; Hu et al. 2000]) are defined by

$$C_{ijkl}=\lambda\delta_{ij}\delta_{kl}+\mu(\delta_{ik}\delta_{jl}+\delta_{il}\delta_{jk}),$$

where δ_{ij} is the Kronecker delta (i.e., $\delta_{ij}=1$ for $i=j$ and $\delta_{ij}=0$ for $i\neq j$) λ, μ are given constants such that $\mu>0$, $\lambda+2\mu>0$. All nonzero phason, phonon-phason coupling elastic constants are given by the following expressions [Ding et al. 1993; Hu et al. 2000]:

$$\begin{aligned}
K_{1111}=K_{2222}=K_{1212}=K_{2121}&=K_1,\\
K_{1131}=K_{3111}=K_{1113}=K_{1311}=K_{2213}=K_{1322}=K_{2312}=K_{1223}&=K_2,\\
K_{2231}=K_{3122}=K_{2321}=K_{2123}=K_{1232}=K_{3312}=K_{3221}=K_{2132}&=-K_2,\\
K_{3333}&=K_1+K_2,\\
K_{2323}=K_{3131}=K_{3232}=K_{1313}&=K_1-K_2;\\
R_{1111}=R_{1122}=R_{1133}=R_{1113}=R_{2233}=R_{2332}=R_{3111}=R_{3131}&=R,\\
R_{1221}=R_{3232}=R_{1311}=R_{1331}=R_{2121}&=R,\\
R_{2211}=R_{2222}=R_{2213}=R_{2312}=R_{2321}=R_{3122}=R_{1223}=R_{1212}&=-R,\\
R_{3212}=R_{3221}=R_{1322}=R_{1321}=R_{2123}=R_{2112}&=-R,\\
R_{3333}&=-2R.
\end{aligned}$$

Here K_1, K_2, R are given constants such that $K_1 > 0$, $K_2 > 0$, $K_1 - K_2 > 0$.

Using this presentation of phonon, phason, and phono-phason coupling constants and the fact that components of vector functions $\boldsymbol{u} = (u_1, u_2, u_3)$ and $\boldsymbol{w} = (w_1, w_2, w_3)$ depend on x_3, t only, equations of elasto-hydrodynamics (2-9), (2-10) can be written in the form

$$\rho \frac{\partial^2 \boldsymbol{u}(x_3,t)}{\partial t^2} = \mathcal{C}_{33} \frac{\partial^2 \boldsymbol{u}(x_3,t)}{\partial x_3^2} + \mathcal{R}_{33} \frac{\partial^2 \boldsymbol{w}(x_3,t)}{\partial x_3^2} + \boldsymbol{f}(x_3,t), \tag{4-1}$$

$$\kappa \frac{\partial \boldsymbol{w}(x_3,t)}{\partial t} = \mathcal{K}_{33} \frac{\partial^2 \boldsymbol{w}(x_3,t)}{\partial x_3^2} + \mathcal{R}_{33} \frac{\partial^2 \boldsymbol{u}(x_3,t)}{\partial x_3^2} + \boldsymbol{g}(x_3,t), \tag{4-2}$$

where

$$\mathcal{C}_{33} = \begin{bmatrix} \mu & 0 & 0 \\ 0 & \mu & 0 \\ 0 & 0 & \lambda + 2\mu \end{bmatrix}, \quad \mathcal{R}_{33} = \begin{bmatrix} 0 & 0 & 0 \\ 0 & 0 & 0 \\ 0 & 0 & -2R \end{bmatrix},$$

$$\mathcal{K}_{33} = \begin{bmatrix} K_1 - K_2 & 0 & 0 \\ 0 & K_1 - K_2 & 0 \\ 0 & 0 & K_1 + K_2, \end{bmatrix},$$

Let us consider, for simplicity, the case $\boldsymbol{f}(x_3,t) = 0$, $\boldsymbol{g}(x_3,t) = 0$. The initial value problem for equations (4-1), (4-2) consists of finding the vector functions $\boldsymbol{u}(x_3,t)$ and $\boldsymbol{w}(x_3,t)$ satisfying (4-1), (4-2) and initial data

$$u_j(x,0) = 0, \quad \frac{\partial}{\partial t} u_j(x,t)|_{t=0} = \delta_{j3}\, \delta_\Omega(x_3), \tag{4-3}$$

$$w_j(x,0) = 0, \quad j = 1,2,3; \tag{4-4}$$

where for a given positive constant Ω the function $\delta_\Omega(x_3)$ of the variable x_3 is defined by

$$\delta_\Omega(x_3) = \frac{\sin(\Omega x_3)}{\pi x_3} \ (x_3 \neq 0), \quad \delta_\Omega(0) = \frac{\Omega}{\pi}. \tag{4-5}$$

Remark 4.1. We note that the Fourier transform of $\delta_\Omega(x_3)$ is the rectangular function $\Pi_\Omega(\nu_3)$ which is equal to 1 for $\nu_3 \in [-\Omega, \Omega]$ and equal to zero for $|\nu_3| > \Omega$ (see formula (C-4) in Appendix C).

Equations (4-1)–(4-4) are written in terms of Fourier images with respect to the space variable x_3 as follows:

$$\rho \frac{d^2 \tilde{\boldsymbol{u}}(\nu_3,t)}{dt^2} + \mathcal{C}(\nu_3)\tilde{\boldsymbol{u}}(\nu_3,t) + \mathcal{R}(\nu_3)\tilde{\boldsymbol{w}}(\nu_3,t) = 0, \quad t > 0, \tag{4-6}$$

$$\kappa \frac{d \tilde{\boldsymbol{w}}(\nu_3,t)}{dt} + \mathcal{K}(\nu_3)\tilde{\boldsymbol{w}}(\nu_3,t) + \mathcal{R}(\nu_3)\tilde{\boldsymbol{u}}(\nu_3,t) = 0, \quad t > 0, \tag{4-7}$$

$$\tilde{u}_j(\nu,0) = 0, \quad \frac{d}{dt}\tilde{u}_j(\nu,t)|_{t=0} = \delta_{3j}\Pi_\Omega(\nu_3), \tag{4-8}$$

$$\tilde{w}_j(\nu_3,0) = 0, \tag{4-9}$$

where

$$\mathcal{C}(\nu_3) = \operatorname{diag}(\mu\nu_3^2, \mu\nu_3^2, (\lambda+2\mu)\nu_3^2),$$
$$\mathcal{K}(\nu_3) = \operatorname{diag}((K_1-K_2)\nu_3^2, (K_1-K_2)\nu_3^2, (K_1+K_2)\nu_3^2),$$
$$\mathcal{R}(\nu_3) = \begin{bmatrix} 0 & 0 & 0 \\ 0 & 0 & 0 \\ 0 & 0 & -2R\nu_3^2 \end{bmatrix},$$

Applying the reasonings of Section 3 we reduce equations (4-6)–(4-7) with data (4-8)–(4-9) to the system of integral equations of the form (3-23), (3-24), where

$$V(\nu_3,t) = (V_1(\nu_3,t), V_2(\nu_3,t), V_3(\nu_3,t)), \quad S(\nu_3,t) = (S_1(\nu_3,t), S_2(\nu_3,t), S_3(\nu_3,t)),$$
$$V_j(\nu_3,t) \equiv \tilde{u}_j(\nu_3,t), \quad S_j(\nu_3,t) \equiv \tilde{w}_j(\nu_3,t), \quad j=1,2,3;$$
$$\boldsymbol{h}^1(\nu_3,t) = \begin{pmatrix} 0 \\ 0 \\ \Pi_\Omega(\nu_3)\sin(c_p|\nu_3|t)/(c_p|\nu_3|) \end{pmatrix}, \quad \boldsymbol{h}^2(\nu_3,t) = \begin{pmatrix} 0 \\ 0 \\ 0 \end{pmatrix},$$
$$(\boldsymbol{K}^1 S)(\nu_3,t,\tau) = \begin{pmatrix} 0 \\ 0 \\ 2R|\nu_3|\sin(c_p|\nu_3|(t-\tau))S_3(\nu_3,\tau)/(\rho c_p) \end{pmatrix},$$
$$(\boldsymbol{K}^2 V)(\nu_3,t,\tau) = \begin{pmatrix} 0 \\ 0 \\ 2R|\nu_3|^2\exp(-a^2|\nu_3|^2(t-\tau))V_3(\nu_3,\tau)/\kappa \end{pmatrix}.$$

Here

$$c_p = \frac{\lambda+2\mu}{\rho}, \quad a = \frac{K_1+K_2}{\kappa}.$$

It follows from the obtained integral equations that

$$V_k(\nu_3,t) \equiv \tilde{u}_k(\nu_3,t) = 0, \quad S_k(\nu_3,t) \equiv \tilde{w}_k(\nu_3,t) = 0, \quad k=1,2;$$

and functions $V_3(\nu_3,t) \equiv \tilde{u}_3(\nu_3,t)$, $S_3(\nu_3,t) \equiv \tilde{w}_3(\nu_3,t)$ satisfy the following integral equations

$$V_3(\nu_3,t) = \frac{1}{c_p|\nu_3|}\sin(c_p|\nu_3|t)\Pi_\Omega(\nu_3) + \frac{2R|\nu_3|}{\rho c_p}\int_0^t \sin(c_p|\nu_3|(t-\tau))S_3(\nu_3,\tau)\,d\tau, \tag{4-10}$$
$$S_3(\nu_3,t) = \frac{2R\,|\nu_3|^2}{\kappa}\int_0^t \exp(-a^2\,|\nu_3|^2\,(t-\tau))V_3(\nu_3,\tau)\,d\tau. \tag{4-11}$$

As a result, we find a solution $V_3(\nu_3,t)$, $S_3(\nu_3,t)$ of (4-10), (4-11) in the form

$$V_3(\nu_3,t) = \sum_{n=0}^{\infty} V_3^{(n)}(\nu_3,t), \quad S_3(\nu_3,t) = \sum_{n=0}^{\infty} S_3^{(n)}(\nu_3,t), \tag{4-12}$$

where

$$V_3^{(0)}(\nu_3, t) = \frac{1}{c_p\,|\nu_3|}\sin(c_p\,|\nu_3|\,t)\Pi_\Omega(\nu_3), \quad S_3^{(0)}(\nu, t) = 0,$$

$$V_3^{(n)}(\nu_3, t) = \frac{2R\,|\nu_3|}{\rho\,c_p}\int_0^t \sin(c_p\,|\nu_3|\,(t-\tau))S_3^{(n-1)}(\nu_3, \tau)\,d\tau,$$

$$S_3^{(n)}(\nu_3, t) = \frac{2R\,|\nu_3|^2}{\kappa}\int_0^t \exp(-a^2\,|\nu_3|^2\,(t-\tau))V_3^{(n-1)}(\nu_3, \tau)\,d\tau, \quad n = 1, 2, 3, \ldots.$$

Using the reasonings of Section 3 we prove the absolute and uniform convergence of series (4-12) and that functions $V_3(\nu_3, t)$, $S_3(\nu_3, t)$ and their partial derivatives

$$\frac{\partial V_3(\nu_3, t)}{\partial t}, \quad \frac{\partial^2 V_3(\nu_3, t)}{\partial t^2}, \quad \frac{\partial S_3(\nu_3, t)}{\partial t}$$

are continuous on $\Delta_3(T, \Omega) = \{(\nu_3, t) \mid \nu_3 \in R,\ \nu_3 \neq 0,\ |\nu_3| \leq \Omega,\ 0 \leq t \leq T\}$ and equal to zero for $|\nu_3| > \Omega$, $0 \leq t \leq T$. Moreover we show that vector functions $\tilde{\boldsymbol{u}}(\nu_3, t) = (0, 0, V_3(\nu_3, t))$, $\tilde{\boldsymbol{w}}(\nu_3, t) = (0, 0, S_3(\nu_3, t))$ are the solution of (4-6)–(4-9). We note that the inverse Fourier transform with respect to ν_3 of $V_3(\nu_3, t)$, $S_3(\nu_3, t)$ exists and the obtained functions are differentiable. We denote these functions by $u_3(x_3, t)$, $w_3(x_3, t)$. Similar to Section 3 we show that $\boldsymbol{u}(x_3, t) = (0, 0, u_3(x_3, t))$, $\boldsymbol{w}(x_3, t) = (0, 0, w_3(x_3, t))$ are the solution of the initial value problem of elasto-hydrodynamic equations (4-1)–(4-4). Moreover, applying the inverse Fourier transform to (4-12) and using properties of the direct and inverse Fourier transforms (see equalities (C-1)–(C-11) in Appendix C) we find

$$u_3(x_3, t) = \sum_{n=0}^{\infty} u_3^{(n)}(x_3, t), \quad w_3(x_3, t) = \sum_{n=0}^{\infty} w_3^{(n)}(x_3, t), \tag{4-13}$$

where

$$u_3^{(0)}(x_3, t) = \frac{1}{2c_p}\int_{x_3 - c_p t}^{x_3 + c_p t} \delta_\Omega(\xi)\,d\xi, \quad w_3^{(0)}(x_3, t) = 0, \tag{4-14}$$

$$u_3^{(n)}(x_3, t) = -\frac{R}{c_p \rho}\int_0^t \left(\int_{x_3 - c_p(t-\tau)}^{x_3 + c_p(t-\tau)} \frac{\partial^2 w_3^{(n-1)}(\xi, \tau)}{\partial \xi^2}\,d\xi\right) d\tau, \tag{4-15}$$

$$w_3^{(n)}(x_3, t) = -\frac{R}{a\kappa\sqrt{\pi}}\int_0^t \left(\int_{-\infty}^{+\infty} \exp\left(-\frac{(\xi - x_3)^2}{4a^2(t-\tau)}\right)\frac{\partial^2 u_3^{(n-1)}(\xi, \tau)}{\partial \xi^2}\,d\xi\right)\frac{d\tau}{\sqrt{t-\tau}}, \tag{4-16}$$

$$n = 1, 2, 3, \ldots$$

Hence the solution of the initial value problem (4-1)–(4-4) is found by formulas $\boldsymbol{u}(x_3, t) = (0, 0, u_3(x_3, t))$, $\boldsymbol{w}(x_3, t) = (0, 0, w_3(x_3, t))$, where $u_3(x_3, t)$ and $w_3(x_3, t)$ are defined by (4-13)–(4-16).

5. Conclusion

The new approach to solve the initial value problem for differential equations of elasto-hydrodynamics in 3D quasicrystals with the general structure of anisotropy is described in the paper. This approach consists of derivation of phonon and phason displacements by solving the dynamic equations describing the wave

propagation for phonon and diffusion process for phason in quasicrystals with the arbitrary anisotropy. There are the following important steps in this approach. The equations of elasto-hydrodynamics in quasicrystals are written in terms of the Fourier images with respect to 3D space variable. The solution of the obtained initial value problem is reduced to the vector integral equation of the Volterra type depending on 3D Fourier parameter. The vector integral equation is solved by successive approximations. The phonon and phason displacements are found by matrix transformations and the application of the inverse Fourier transform to the solution of the vector integral equation. To make all steps correctly we need the following assumption. The Fourier transform with respect to 3D space variable of the given phonon, phason forces as well as initial displacements have to be vector functions with components which have finite supports with respect to Fourier parameters.

We note that if the image of the Fourier transform of a smooth function with respect to space variables has the finite support $\{\nu = (\nu_1, \nu_2, \nu_3) : |\nu| \le \Omega\}$ then we can apply the inverse Fourier transform to this image and the obtained result is the smooth function which belongs to the Paley–Wiener space (see, for example, [Andersen 2004]). Here $\Omega > 0$ is a given constant. From a physical point of view we make the following constraints on the mathematical model of elasto-hydrodynamics in QCs. We exclude high space frequencies in oscillation which are described by phonon and phason displacements. This means that we exclude some sources of oscillation in our consideration. For example, many mathematical models use a point source (in initial data or inhomogeneous terms of equations) which is described by the Dirac delta function. The Dirac delta function is not a classical function - it is a generalized function (distribution). The Dirac delta function does not belong to the Paley–Wiener space. This means that our approach can not be applied for equations of elasto-hydrodynamics in the case if the Dirac delta function appears in initial data or inhomogeneous terms of equations. However the Dirac delta function can be approximated by functions from Paley–Wiener space. For example, the Dirac delta function of one variable $\delta(x_1)$ can be approximated by

$$\delta_\epsilon(x_1) = \frac{\sin(\epsilon x_1)}{\pi x_1}, \quad x_1 \neq 0; \quad \delta_\epsilon(0) = \frac{\epsilon}{\pi},$$

where $\epsilon > 0$ is the sufficiently large parameter of approximation (regularization). Moreover the inverse Fourier transform of the rectangular function $\Pi_\epsilon(\nu_1)$, which is equal to 1 for $|\nu_1| \le \epsilon$ and equal to zero for $|\nu_1| > \epsilon$, is the function $\delta_\epsilon(x_1)$. Therefore $\delta_\epsilon(x_1)$ belongs to the Paley–Wiener space. Using this remark we can approximate the Dirac delta function of three space variables (if the Dirac delta function appears in the description of the phonon, phason forces or initial displacements) by the function $\delta_\epsilon(x_1)\delta_\epsilon(x_2)\delta_\epsilon(x_3)$ which is from the Paley–Wiener space and then apply our approach to find an approximate solution of the original problem. In Section 4 the approach is illustrated on the example of solving equations of elasto-hydrodynamics for 3D icosahedral quasicrystals in the case when components of phonon and phason displacements depend on x_3 and t variables and one component of phonon initial data $\boldsymbol{u}^1$ contains the function $\delta_\epsilon(x_3)$. Here the image of the Fourier transform of the solution of equations in 3D icosahedral quasicrystals is found by successive approximations and then the application of the inverse Fourier transform has been made analytically. Unfortunately the operation of the inverse Fourier transform can not be made analytically for all quasicrystals with general structure of anisotropy and we need to apply it numerically.

At the end of conclusion we would like to say that the present paper is the first part of the study which is related with the theoretical background of the second part of this study, where we plan to

described the computational methods of the initial value problems solving for differential equations of elasto-hydrodynamics of quasicrystals with the general structure of anisotropy.

Appendix A. Consequence of the positivity of elastic energy for Section 2A

With notation of the work [Hu et al. 2000] the elastic energy is written as follows (see [Hu et al. 2000, Formula 4.17])

$$F = \frac{1}{2}[\varepsilon, \omega]\begin{bmatrix} \boldsymbol{C} & \boldsymbol{R} \\ \boldsymbol{R}^T & \boldsymbol{K} \end{bmatrix}\begin{bmatrix} \varepsilon \\ \omega \end{bmatrix},$$

where $[\varepsilon, \omega]$ is the vector row whose elements are phonon and phason strains ε_{ij}, ω_{ij}, respectively; $\begin{bmatrix} \varepsilon \\ \omega \end{bmatrix}$ is the vector column whose elements are phonon and phason strains ε_{kl}, ω_{kl}; $\boldsymbol{C} = [C_{ijkl}]$ is the matrix of the phonon elastic modules, $\boldsymbol{K} = [K_{ijkl}]$ is the matrix of the phason elastic modules, $\boldsymbol{R} = [R_{ijkl}]$ is the matrix of the phonon-phason coupling elastic modules, $\boldsymbol{R}^T = [R_{klij}]$ is transpose to $\boldsymbol{R}$.

Since the elastic energy F is positive (see [Hu et al. 2000, (5.40)]) then the symmetric matrix

$$\begin{bmatrix} \boldsymbol{C} & \boldsymbol{R} \\ \boldsymbol{R}^T & \boldsymbol{K} \end{bmatrix}$$

is always positive definite. This means that

$$[\varepsilon,\ \omega]\begin{bmatrix} \boldsymbol{C} & \boldsymbol{R} \\ \boldsymbol{R}^T & \boldsymbol{K} \end{bmatrix}\begin{bmatrix} \varepsilon \\ \omega \end{bmatrix} > 0$$

for any $[\varepsilon, \omega] \neq 0$ and in particular for any $[\varepsilon, 0] \neq 0$ or any $[0, \omega] \neq 0$ the last inequality implies

$$[\varepsilon, 0]\begin{bmatrix} \boldsymbol{C} & \boldsymbol{R} \\ \boldsymbol{R}^T & \boldsymbol{K} \end{bmatrix}\begin{bmatrix} \varepsilon \\ 0 \end{bmatrix} = \varepsilon^T \boldsymbol{C}\varepsilon > 0,$$

and

$$[0, \omega]\begin{bmatrix} \boldsymbol{C} & \boldsymbol{R} \\ \boldsymbol{R}^T & \boldsymbol{K} \end{bmatrix}\begin{bmatrix} 0 \\ \omega \end{bmatrix} = \omega^T \boldsymbol{K}\omega > 0.$$

Therefore the positivity of energy implies the positive definiteness of matrices $\boldsymbol{C}$ and $\boldsymbol{K}$ and the last inequalities can be written in the form of inequalities (2-4) of the present paper.

Appendix B. Positive definiteness of $\mathcal{C}(\nu)$ and $\mathcal{K}(\nu)$

Let

$$\alpha = \begin{pmatrix} \alpha_1 \\ \alpha_2 \\ \alpha_3 \end{pmatrix}, \quad \alpha^T = (\alpha_1, \alpha_2, \alpha_3), \quad \nu = (\nu_1, \nu_2, \nu_3), \quad \nu_1^2 + \nu_2^2 + \nu_3^2 \neq 0, \quad \alpha_1^2 + \alpha_2^2 + \alpha_3^2 \neq 0;$$

matrices $\mathcal{C}(\nu)$ and $\mathcal{K}(\nu)$ be defined by (3-7), (3-8), (2-11), (2-13). Using (2-3), (2-11), (2-13), (3-7), (3-8) we find

$$\alpha^T \mathcal{C}(\nu)\alpha = \sum_{j,l,i,k=1}^{3} C_{ijkl}(\alpha_i \nu_j)(\alpha_k \nu_l), \quad \alpha^T \mathcal{K}(\nu)\alpha = \sum_{j,l,i,k=1}^{3} K_{ijkl}(\alpha_i \nu_j)(\alpha_k \nu_l).$$

We note that $\varepsilon_{ij} = \alpha_i \nu_j$ (or $\omega_{ij} = \alpha_i \nu_j$) are not zero entirely. Therefore, using (2-4) we find that

$$\alpha^T \mathcal{C}(\nu)\alpha > 0, \quad \alpha^T \mathcal{K}(\nu)\alpha > 0$$

for $\nu_1^2 + \nu_2^2 + \nu_3^2 \neq 0$ and $\alpha_1^2 + \alpha_2^2 + \alpha_3^2 \neq 0$. This means the positive definiteness of matrices $\mathcal{C}(\nu)$ and $\mathcal{K}(\nu)$ for $\nu \neq 0$.

Appendix C. Formulas of the direct and inverse transforms of some functions used in Section 4

In this section we describe some formulas of the Fourier transform which we use in Section 4. Let $\mathcal{F}$ and $\mathcal{F}^{-1}$ be operators of the direct and inverse transforms defined by

$$\mathcal{F}[\varphi(x_3)](\nu_3) = \int_{-\infty}^{+\infty} \varphi(x_3) \exp(i x_3 \nu_3)\, dx_3, \quad \mathcal{F}^{-1}[\tilde{\varphi}(\nu_3)](x_3) = \frac{1}{2\pi} \int_{-\infty}^{+\infty} \tilde{\varphi}(x_3) \exp(-i \nu_3 x_3)\, d\nu_3$$

for the given piecewise continuous functions $\varphi(x_3)$, $\tilde{\varphi}(\nu_3)$ for which the Fourier transform $\mathcal{F}[\varphi(x_3)](\nu_3)$ and the inverse Fourier transform $\mathcal{F}^{-1}[\tilde{\varphi}(\nu_3)](x_3)$ exist.

Let $c_p > 0$, $t > 0$, $\Omega > 0$ be given constants; $\theta(t)$ be the Heaviside step function (i.e., $\theta(t) = 1$ for $t \geq 0$, $\theta(t) = 0$ for $t < 0$); $\delta_\Omega(x_3)$ be the function defined by (4-5). Then the following formulas take place:

$$\mathcal{F}\left[\frac{1}{2c_p}\theta(c_p t - |x_3|)\right](\nu_3) = \frac{1}{c_p|\nu_3|} \sin(c_p|\nu_3|t). \tag{C-1}$$

Proof.

$$\mathcal{F}\left[\frac{1}{2c_p}\theta(c_p t - |x_3|)\right](\nu_3) = \frac{1}{2c_p} \int_{-c_p t}^{c_p t} \exp(i x_3 \nu_3)\, dx_3 = \frac{1}{c_p|\nu_3|} \sin(c_p|\nu_3|t). \qquad \square$$

$$\mathcal{F}^{-1}\left[\frac{1}{c_p|\nu_3|} \sin(c_p|\nu_3|t)\right](x_3) = \frac{1}{2c_p}\theta(c_p t - |x_3|). \tag{C-2}$$

Proof. Applying the operator $\mathcal{F}$ to (C-1) we obtain (C-2). $\square$

$$\mathcal{F}^{-1}[\Pi_\Omega(\nu_3)](x_3) = \frac{\sin(\Omega x_3)}{\pi x_3} \equiv \delta_\Omega(x_3). \tag{C-3}$$

Proof. $\mathcal{F}^{-1}[\Pi_\Omega(\nu_3)](x_3) = \dfrac{1}{2\pi} \displaystyle\int_{-\Omega}^{\Omega} \exp(-i \nu_3 x_3)\, d\nu_3 = \delta_\Omega(x_3).$ $\square$

$$\mathcal{F}\left[\frac{\sin(\Omega x_3)}{\pi x_3}\right](\nu_3) = \Pi_\Omega(\nu_3). \tag{C-4}$$

Proof. Applying the operator $\mathcal{F}$ to (C-3) we obtain (C-4). $\square$

The next formula and its verification can be found, for example, in [Vladimirov 1971]:

$$\mathcal{F}\left[\int_{-\infty}^{+\infty} \varphi(\xi)\psi(x_3 - \xi)\, d\xi\right](\nu_3) = \mathcal{F}[\varphi(x_3)](\nu_3) \cdot \mathcal{F}[\psi(x_3)](\nu_3) \tag{C-5}$$

for any piecewise continuous functions $\varphi(x_3)$ and $\psi(x_3)$ for which the convolution

$$\int_{-\infty}^{+\infty} \varphi(\xi)\psi(x_3 - \xi)\, d\xi$$

exists and absolutely integrable.

Applying the operator $\mathcal{F}^{-1}$ to formula (C-5) we find

$$\mathcal{F}^{-1}\big[\mathcal{F}[\varphi(x_3)](\nu_3)\cdot\mathcal{F}[\psi(x_3)](\nu_3)\big](x_3)=\int_{-\infty}^{+\infty}\varphi(\xi)\psi(x_3-\xi)\,d\xi. \tag{C-6}$$

The formula (C-6) for $\psi(x_3)=(1/2\pi)\theta(c_pt-|x_3|)$ and $\varphi(x_3)=\delta_\Omega(x_3)$ can be written in the form

$$\begin{aligned}\mathcal{F}^{-1}\left[\frac{1}{c_p|\nu_3|}\sin(c_p|\nu_3|t)\cdot\Pi_\Omega(\nu_3)\right](x_3)&=\int_{-\infty}^{+\infty}\frac{1}{2c_p}\theta(c_pt-|\xi-x_3|)\delta_\Omega(\xi)\,d\xi\\&=\frac{1}{2c_p}\int_{x_3-c_pt}^{x_3+c_pt}\delta_\Omega(\xi)\,d\xi.\end{aligned} \tag{C-7}$$

$$\mathcal{F}^{-1}[\exp(-a^2\,\nu_3^2\,(t-\tau))](x_3)=\frac{1}{2a\sqrt{\pi(t-\tau)}}\exp\left(-\frac{x_3^2}{4a^2\,(t-\tau)}\right). \tag{C-8}$$

Proof.

$$\begin{aligned}\mathcal{F}^{-1}[\exp(-a^2\nu_3^2(t-\tau))](x_3)&=\frac{1}{2\pi}\int_{-\infty}^{+\infty}\exp(-a^2\nu_3^2(t-\tau))\exp(-i\,\nu_3x_3)\,d\nu_3\\&=\frac{1}{\pi}\int_0^{+\infty}\exp(-a^2\,\nu_3^2\,(t-\tau))\cos(\nu_3x_3)\,d\nu_3\\&=\frac{1}{2a\sqrt{\pi(t-\tau)}}\exp\left(-\frac{x_3^2}{4a^2(t-\tau)}\right).\end{aligned}$$

□

The next formula and its proof can be found in [Vladimirov 1971]:

$$\mathcal{F}^{-1}[\nu_3^2\tilde{\varphi}(\nu_3)](x_3)=-\frac{\partial^2\varphi(x_3)}{\partial x_3^2}. \tag{C-9}$$

Using formulas (C-6), (C-8) and (C-9) for

$$\psi(x_3)=\frac{1}{2a\sqrt{\pi(t-\tau)}}\exp(-\frac{x_3^2}{4a^2\,(t-\tau)})$$

we find

$$\mathcal{F}^{-1}[\exp(-a^2\nu_3^2(t-\tau))\nu_3^2\tilde{\varphi}(\nu_3)](x_3)=-\frac{1}{2a\sqrt{\pi(t-\tau)}}\int_{-\infty}^{+\infty}\exp\left(-\frac{(\xi-x_3)^2}{4a^2(t-\tau)}\right)\frac{\partial^2\varphi(\xi)}{\partial\xi^2}\,d\xi. \tag{C-10}$$

Using formulas (C-2), (C-6) and (C-9) for $\psi(x_3)=(1/(2c_p))\theta(c_pt-|x_3|)$ we have

$$\mathcal{F}^{-1}\left[\frac{1}{c_p|\nu_3|}\sin(c_p|\nu_3|(t-\tau))\nu_3^2\tilde{\varphi}(\nu_3)\right](x_3)=-\frac{1}{2c_p}\int_{x_3-c_p(t-\tau)}^{x_3+c_p(t-\tau)}\frac{\partial^2\varphi(\xi)}{\partial\xi^2}\,d\xi. \tag{C-11}$$

References

[Andersen 2004] N. B. Andersen, "Real Paley–Wiener theorems for the inverse Fourier transform on a Riemannian symmetric space", *Pac. J. Math.* **213**:1 (2004), 1–13.

[Apostol 1961] T. M. Apostol, *Calculus, I: Introduction, with vectors and analytic geometry*, Blaisdell, Waltham, MA, 1961.

[van Blaaderen 2009] A. van Blaaderen, "Quasicrystals from nanocrystals", *Nature* **461** (2009), 892–893.

[Çerdik Yaslan 2013] H. Çerdik Yaslan, "Equations of anisotropic elastodynamics in 3D quasicrystals as a symmetric hyperbolic system: deriving the time-dependent fundamental solutions", *Appl. Math. Model.* **37**:18-19 (2013), 8409–8418.

[Çerdik Yaslan 2019] H. Çerdik Yaslan, "On three-dimensional elastodynamic problems of one-dimensional quasicrystals", *Waves Random Complex Media* **29**:4 (2019), 614–630.

[De and Pelcovits 1987] P. De and R. A. Pelcovits, "Linear elasticity theory of pentagonal quasicrystals", *Phys. Rev. B* **35**:13 (1987), 8609–8620.

[Ding et al. 1993] D.-H. Ding, W. Yang, C. Hu, and R. Wang, "Generalized elasticity theory in quasicrystals", *Phys. Rev. B* **48**:10 (1993), 7003–7010.

[Dubois 2000] J.-M. Dubois, "New prospects from potential applications of quasicrystalline materials", *Mater. Sci. Eng. A* **294-296** (2000), 4–9.

[Dubois 2005] J.-M. Dubois, *Useful quasicrystals*, World Sci., London, 2005.

[Edagawa and So 2007] K. Edagawa and Y. G. So, "Experimental evaluation of phonon-phason coupling in icosahedral quasicrystals", *Philos. Mag.* **87**:1 (2007), 77–95.

[Fan 2013] T. Y. Fan, "Mathematical theory and methods of mechanics of quasicrystalline materials", *Engineering* **5**:4 (2013), 407–448.

[Fan and Fan 2008] T. Y. Fan and L. Fan, "Plastic fracture of quasicrystals", *Philos. Mag.* **88**:4 (2008), 523–535.

[Fan et al. 2009] T. Y. Fan, X. F. Wang, W. Li, and A. Y. Zhu, "Elasto-hydrodynamics of quasicrystals", *Philos. Mag.* **89**:6 (2009), 501–512.

[Gao and Zhao 2006] Y. Gao and B.-S. Zhao, "A general treatment of three-dimensional elasticity of quasicrystals by an operator method", *Phys. Status Solidi B* **243**:15 (2006), 4007–4019.

[Hu et al. 2000] C. Hu, R. Wang, and D.-H. Ding, "Symmetry groups, physical property tensors, elasticity and dislocations in quasicrystals", *Rep. Prog. Phys.* **63**:1 (2000), 1–39.

[Levine et al. 1985] D. Levine, T. C. Lubensky, S. Ostlund, S. Ramaswamy, P. J. Steinhardt, and J. Toner, "Elasticity and dislocations in pentagonal and icosahedral quasicrystals", *Phys. Rev. Lett.* **54**:14 (1985), 1520–1523.

[Li 2011] X.-F. Li, "A general solution of elasto-hydrodynamics of two-dimensional quasicrystals", *Philos. Mag. Lett.* **91**:4 (2011), 313–320.

[Li and Fan 2016] W. Li and T. Fan, "Elasto-dynamics of quasicrystals", *Crystals* **6**:11 (2016), art. id. 152.

[Li et al. 2009] W. Li, T. Y. Fan, and Y. L. Wu, "Plastic analysis of crack problems in three-dimensional icosahedral quasicrystalline material", *Philos. Mag.* **89**:31 (2009), 2823–2831.

[Lubensky et al. 1985] T. C. Lubensky, S. Ramaswamy, and J. Toner, "Hydrodynamics of icosahedral quasicrystals", *Phys. Rev. B* **32**:11 (1985), 7444–7452.

[Ovidko 1992] I. A. Ovidko, "Plastic deformation and decay of dislocations in quasi-crystals", *Mater. Sci. Eng. A* **154**:1 (1992), 29–33.

[Rochal and Lorman 2002] S. B. Rochal and V. L. Lorman, "Minimal model of the phonon-phason dynamics in icosahedral quasicrystals and its application to the problem of internal friction in the i-AlPdMn alloy", *Phys. Rev. B* **66**:14 (2002), art. id. 144204.

[Shechtman et al. 1984] D. Shechtman, I. Blech, D. Gratias, and J. W. Cahn, "Metallic phase with long-range orientational order and no translational symmetry", *Phys. Rev. Lett.* **53**:20 (1984), 1951–1954.

[Vladimirov 1971] V. S. Vladimirov, *Equations of mathematical physics*, Pure Appl. Math. **3**, Dekker, New York, 1971.

[Wang et al. 1987] N. Wang, H. Chen, and K. H. Kuo, "Two-dimensional quasicrystal with eightfold rotational symmetry", *Phys. Rev. Lett.* **59**:9 (1987), 1010–1017.

[Yakhno and Çerdik Yaslan 2011a] V. G. Yakhno and H. Çerdik Yaslan, "Computation of the time-dependent Green's function of three dimensional elastodynamics in 3D quasicrystals", *Comput. Model. Eng. Sci.* **81**:4 (2011), 295–309.

[Yakhno and Çerdik Yaslan 2011b] V. G. Yakhno and H. Çerdik Yaslan, "Three dimensional elastodynamics of 2D quasicrystals: the derivation of the time-dependent fundamental solution", *Appl. Math. Model.* **35**:6 (2011), 3092–3110.

[Yakhno and Çerdik Yaslan 2012] V. G. Yakhno and H. Çerdik Yaslan, "Approximate fundamental solutions and wave fronts for general anisotropic materials", *Int. J. Solids Struct.* **49**:6 (2012), 853–864.

Received 10 Aug 2019. Revised 11 Dec 2019. Accepted 16 Dec 2019.

VALERY YAKHNO: valery.yakhno@deu.edu.tr
Electrical and Electronics Engineering Department, Dokuz Eylul University, Izmir, Turkey

JOURNAL OF MECHANICS OF MATERIALS AND STRUCTURES
Vol. 15, No. 1, 2020
dx.doi.org/10.2140/jomms.2020.15.159

EXPANSION-CONTRACTION BEHAVIOR OF A PRESSURIZED POROHYPERELASTIC SPHERICAL SHELL DUE TO FLUID REDISTRIBUTION IN THE STRUCTURE WALL

VAHID ZAMANI AND THOMAS J. PENCE

Spherical shells with porohyperelastic walls that contain mobile liquid are examined for the purpose of determining how the in-wall liquid distribution affects the overall mechanical response. Attention is restricted to spherical symmetry and to Mooney–Rivlin type material models that are generalized so as to incorporate swelling. In this setting, different distributions of the same amount of liquid are examined for their effect on the sphere's pressure-expansion behavior. Liquid distributions that are essentially uniform are found to give the most compliant response. In contrast, nonuniform liquid distributions that concentrate liquid near either the inner or outer wall are found to stiffen the overall behavior. Liquid redistribution can also alter the basic monotonicity properties of the resulting inflation graphs, possibly leading to various limited burst events.

1. Introduction

Liquid infused soft solids, ranging from gels to biological tissue, exhibit complex mechanical and physical behavior as the liquid content varies. The underlying chemical and microstructural phenomena can be modeled at the continuum mechanics level [Drozdov 2013; Drozdov et al. 2018], and such modeling aids the development of soft material actuators [Stuart et al. 2010; Liu et al. 2018]. The focus of the present work is on how the specific liquid distribution influences the amount of deformation in a soft solid system that responds to mechanical load. In particular, we examine how a soft solid structure or mechanism with a *fixed liquid content* can undergo significant deformation simply by having the fixed amount of liquid redistributed in a different fashion within the system.

For this purpose we consider an internally pressurized spherical cell with "gel-type" cell walls, namely the walls consist of a liquid infused porohyperelastic material. This corresponds to a spherical balloon or bladder with liquid infused walls. The overall amount of liquid is fixed, but may redistribute itself within the bladder wall. Attention is restricted to spherically symmetric liquid distributions in order to permit a treatment that exploits spherical symmetry. At issue is how the liquid distribution affects the amount of overall expansion that is due to an internal pressurization.

We follow a continuum mechanical treatment that tracks change in the local liquid content in terms of the associated material volume change. Both the base soft porous ground substance and the mobile liquid constituent are regarded as incompressible. This causes the local amount of swelling v to be a proxy for the amount of mobile liquid that is currently resident. Prior to any settled equilibrium — meaning that there is still active liquid migration through the porous material — the description of the liquid seepage requires the consideration of the driving action of pore pressure gradients, osmotic pressure,

Keywords: swelling, liquid redistribution, shell stiffness, burst, porohyperelastic.

electrochemistry, and other factors. It also requires the consideration of the resistance between the liquid and solid constituents as they mechanically interact. Continuum mechanical treatments for this interactive seepage include well known and now classical works such as [Truesdell 1962; Bowen 1980] that remain highly recommended. More recent contributions that are also of a comprehensive nature include [Duda et al. 2010; Chester and Anand 2010; Pence 2012].

Because the present considerations restrict attention to equilibrated states where any liquid migration has ceased, the type of finite deformation treatment of swelling presented in [Tsai et al. 2004] may be applied. This type of treatment was employed in [Pence and Tsai 2006] for the study of swelling induced cavitation in spherical geometries. Here it is to be mentioned that the treatment of swelling in [Tsai et al. 2004; Pence and Tsai 2006] is, in certain aspects of its mathematical description, connected to treatments of growth and remodeling. Related work on cavitation under swelling/growth and its extension to include the effect of inclusions include [Goriely et al. 2010; Duda et al. 2011; Yavari and Goriely 2013; van der Sman 2015].

Balloon-like problems that make use of the constitutive models in [Tsai et al. 2004; Pence and Tsai 2006] for treating a spherical shell type wall were the focus of [Zamani and Pence 2017] where, among other things, a swelling induced abrupt burst phenomenon was examined. This burst phenomenon, like swelling induced cavitation, can be viewed as a more general example of swelling induced instability (see [Amar and Ciarletta 2010] for the effect of constraint on such instabilities). Recent related work on inflation instabilities and broader issues for spherical geometry problems that have connection to the treatment here are given in [Selvadurai and Suvorov 2018; Mihai et al. 2019; Cheng et al. 2019].

The continuum mechanical framework is presented in Section 2, including the formulation of the spherical inflation boundary value problem and a summary of the key results from [Zamani and Pence 2017] which was restricted to the consideration of uniform swelling. This section can also serve as a quick review of previous results. Section 3 gives the necessary modifications so as to treat nonuniform swelling distributions, and in particular introduces the class of harmonic swelling distributions. Section 4 then investigates the central question, which is how liquid redistribution affects the pressure-inflation behavior. It is found that, among other things, redistribution can lead to an overall change in the structural compliance. It can also change the basic monotonicity behavior of the pressure versus inflation graph. The consequences of these findings as it relates to possible expansion/contraction at fixed pressure, solely by liquid redistribution in the shell wall, are elaborated in Section 5. The final Section 6 places our findings in a broader perspective and discusses some of the main limitations in the overall approach.

2. Preliminaries

Swelling due to the infusion of liquid gives a local increase in volume. Because of this, the usual incompressiblity condition of volume preservation, $\det \boldsymbol{F} = 1$, where $\boldsymbol{F}$ is the deformation gradient, is generalized because of the volume change due to swelling. This yields

$$\det \boldsymbol{F} = v, \tag{1}$$

where v is the *swelling field*. Locations with $v = 1$ are unswollen (because no additional liquid is present), in which case the usual incompressibility constraint is recovered. Locations where $v > 1$ are swollen due to the presence of additional liquid whereupon v gives the new natural free volume (relative to the

unswollen reference state). It is to be remarked that the incompressible porous ground substance base constituent may itself contain irretrievably bound liquid in its fine microstructure. In such a case the liquid referred to in this treatment is in fact the free liquid (potentially mobile liquid), and the reference configuration then describes the porous base material with its bound liquid constituent (see e.g., [van der Sman 2015]).

As demonstrated in [Fang et al. 2008] in the context of polymer gels, and discussed in [Gou and Pence 2016] in the context of biological tissue, a treatment that employs (1) as a constraint, meaning that v as a function of location is specified, is appropriate when electrochemical effects (including osmotic pressure) dominate mechanical forces in the determination of equilibrium when an incompressible liquid constituent causes swelling in an otherwise incompressible porous ground substance constituent.

2.1. ***Hyperelastic stored energy.*** The material's mechanical response, both prior to swelling and after any swelling has occurred, is treated as hyperelastic. Let W be the elastic energy density as measured with respect to the unswollen reference configuration. As in hyperelasticity without swelling, this W is a function of the deformation gradient where frame invariance requires this dependence to be in terms of the right Cauchy–Green deformation tensor $\boldsymbol{C} = \boldsymbol{F}^T\boldsymbol{F}$. In addition, W will now also depend upon the liquid volume fraction as indicated in terms of the local amount of swelling v. This gives $W = W(\boldsymbol{C}, v)$. In the absence of body forces the equilibrium equation is $\operatorname{div}\boldsymbol{T} = 0$ where $\boldsymbol{T}$ is the Cauchy stress tensor:

$$\boldsymbol{T} = \frac{2}{v}\boldsymbol{F}\frac{\partial W}{\partial \boldsymbol{C}}\boldsymbol{F}^T - p\boldsymbol{I}. \tag{2}$$

Here p is the reactive stress associated with the constraint (1). It is a pure pressure contribution as in the conventional incompressible theory that is now generalized to include the liquid swelling effect.

We consider isotropic materials, in which case the dependence of W upon $\boldsymbol{C}$ is through the invariants of $\boldsymbol{C}$,

$$I_1 = \operatorname{tr}\boldsymbol{C}, \quad I_2 = \tfrac{1}{2}\big((\operatorname{tr}\boldsymbol{C})^2 - \operatorname{tr}\boldsymbol{C}^2\big). \tag{3}$$

The third isotropic invariant $I_3 = \det\boldsymbol{C} = v^2$ by virtue of (1). Consequently, $W = W(I_1, I_2, v)$ and this causes the $\boldsymbol{T}$ in (2) to take the form

$$\boldsymbol{T} = \frac{2}{v}\left(\frac{\partial W}{\partial I_1} + I_1\frac{\partial W}{\partial I_2}\right)\boldsymbol{B} - \frac{2}{v}\frac{\partial W}{\partial I_2}\boldsymbol{B}^2 - p\boldsymbol{I}. \tag{4}$$

Here $\boldsymbol{B} = \boldsymbol{F}\boldsymbol{F}^T$ is the left Cauchy–Green deformation tensor.

The particular constitutive model that we shall employ here takes the well known Mooney–Rivlin model in the classical incompressible theory and extends it to include the swelling effect [Treloar 1975]. For our purposes this motivates the form

$$W(I_1, I_2, v) = \frac{1}{2}\alpha\mu v^{q_1}\left(\frac{I_1}{v^{2/3}} - 3\right) + \frac{1}{2}(1-\alpha)\mu v^{q_2}\left(\frac{I_2}{v^{4/3}} - 3\right), \tag{5}$$

that was used in [Zamani and Pence 2017]. Here $\mu > 0$ is the infinitesimal shear modulus in the absence of swelling and α obeying $0 \le \alpha \le 1$ is the Mooney–Rivlin parameter that distinguishes between the I_1 and I_2 content of the material. The exponents q_1 and q_2 provide for a possible swelling sensitivity in the

I_1 to I_2 content ratio. Note that the conventional Mooney–Rivlin form is recovered upon setting $v = 1$. The neo-Hookean form is obtained by making the additional specialization $\alpha = 1$.

2.2. ***Spherical inflation.*** Using the above framework we consider a finite thickness spherical shell with inner radius $R_i > 0$ and outer radius $R_o > R_i$ prior to any loading or any swelling. Attention is restricted to radially symmetric swelling $v = v(R)$. The loading is taken to consist of applied pressures P_i and P_o on the inner and outer boundaries. These symmetric conditions motivate the consideration of the symmetric deformation for *radial inflation*

$$r = r(R), \quad \theta = \Theta, \quad \phi = \Phi, \tag{6}$$

on $R_i \le R \le R_o$, $0 \le \Theta < 2\pi$, $0 \le \Phi \le \pi$ where the radial inflation function $r(R)$ is to be determined. Thus (6) is a map from reference spherical coordinates (R, Θ, Φ) to deformed spherical coordinates (r, θ, ϕ). Let $\{\boldsymbol{e}_R, \boldsymbol{e}_\Theta, \boldsymbol{e}_\Phi\}$ and $\{\boldsymbol{e}_r, \boldsymbol{e}_\theta, \boldsymbol{e}_\phi\}$ represent unit basis vectors in the spherical coordinate system of the respective reference and deformed configurations. It follows from (6) that the deformation gradient is given by

$$\boldsymbol{F} = r'(\boldsymbol{e}_r \otimes \boldsymbol{e}_R) + \lambda(\boldsymbol{e}_\theta \otimes \boldsymbol{e}_\Theta + \boldsymbol{e}_\phi \otimes \boldsymbol{e}_\Phi), \tag{7}$$

with $r' = dr/dR$ and $\lambda = r/R$. Here λ is the azimuthal stretch, meaning that it is the stretch along spherical surfaces. Because of the spherical symmetry, the stretch λ is the same in all directions upon each spherical surface. However, λ will vary through the thickness of the shell. The swelling condition (1) becomes $v = \det \boldsymbol{F} = \lambda^2 r' = r^2 r'/R^2$, making $r' = v/\lambda^2$, and thus yielding

$$I_1 = \frac{v^2}{\lambda^4} + 2\lambda^2, \quad I_2 = \lambda^4 + 2\frac{v^2}{\lambda^2}. \tag{8}$$

Also, because $v = v(R)$, condition (1) in the form $r^2\, dr = vR^2\, dR$ integrates to

$$r^3 = r_i^3 + 3\int_{R_i}^{R} v(\zeta)\, \zeta^2\, d\zeta, \tag{9}$$

where $r_i = r(R_i)$ and ζ is a dummy integration variable. More generally (9) provides the map $r = r(R)$ in terms of the single parameter r_i which still needs to be determined.

It also follows from (4), (7) and the first of (8) that the Cauchy stress tensor takes the form

$$\boldsymbol{T} = T_{rr}(\boldsymbol{e}_r \otimes \boldsymbol{e}_r) + T_{\theta\theta}(\boldsymbol{e}_\theta \otimes \boldsymbol{e}_\theta + \boldsymbol{e}_\phi \otimes \boldsymbol{e}_\phi), \tag{10}$$

with

$$T_{rr} = -p + \frac{2v}{\lambda^4}\frac{\partial W}{\partial I_1} + \frac{4v}{\lambda^2}\frac{\partial W}{\partial I_2}, \tag{11}$$

$$T_{\theta\theta} = -p + \frac{2\lambda^2}{v}\frac{\partial W}{\partial I_1} + \left(\frac{2v}{\lambda^2} + \frac{2\lambda^4}{v}\right)\frac{\partial W}{\partial I_2}. \tag{12}$$

The specified pressures P_i and P_o at the inner and outer surfaces yield the boundary conditions

$$T_{rr}|_{r_i} = -P_i, \quad T_{rr}|_{r_o} = -P_o, \tag{13}$$

where $r_o = r(R_o)$. It is readily verified that the radial symmetry condition $p = p(R)$ leads to the satisfaction of the equilibrium equation along the θ and ϕ coordinate directions, leaving the radial equation

$$\frac{dT_{rr}}{dr} + \frac{2}{r}(T_{rr} - T_{\theta\theta}) = 0, \tag{14}$$

which is formally an ordinary differential equation for $p(R)$ because $d/dr = (1/r')d/dR = (r^2/vR^2)d/dR$. Because of (9) this first order differential equation contains the parameter r_i and for this reason is able to accommodate the two boundary conditions (13) by proper choice of that parameter. One is easily led to the equation for r_i by performing the relevant substitutions, integrating, and applying the boundary conditions.

In the absence of swelling, so that pressure is the only agent driving the deformation, this problem has a long and storied history in hyperelasticity going back at least to the work of Green and Shield [1950]. To make contact with that work set $v \equiv 1$ whereupon r_i is determined solely from the pressure difference between the interior and the exterior of the sphere:

$$\Delta P = P_i - P_o.$$

Much of the reason for the interest in that problem is that *inflation curves* of ΔP as a function of r_i may then exhibit nonmonotone behavior, even though the energy function W obeys relations, such as the Baker–Ericksen inequality, that are typically regarded as sufficient for physically realistic response. This leads to inflation instabilities, and there is a vast literature on the subject. A particularly elegant exposition is found in the work of Carroll [1987]. Generalizing that work to address the swelling effect in terms of the field variable v was one of the principal aims of [Zamani and Pence 2017].

For our purposes a useful and elegant procedure is obtained by rewriting $W(I_1, I_2, v)$ as $w(\lambda, v)$ upon making use of (8). Then note that

$$\frac{\partial w}{\partial \lambda} = \frac{\partial W}{\partial I_1}\frac{\partial I_1}{\partial \lambda} + \frac{\partial W}{\partial I_2}\frac{\partial I_2}{\partial \lambda} = 4\left(\lambda - \frac{v^2}{\lambda^5}\right)\frac{\partial W}{\partial I_1} + 4\left(\lambda^3 - \frac{v^2}{\lambda^3}\right)\frac{\partial W}{\partial I_2} = 2\frac{v}{\lambda}(T_{\theta\theta} - T_{rr}) = \frac{vr}{\lambda}\frac{dT_{rr}}{dr}, \tag{15}$$

where the last two steps employed first the pair (11) and (12) and then (14). The boundary conditions (13) now give

$$\Delta P = \int_{r_i}^{r_o} \frac{dT_{rr}}{dr}\, dr = \int_{R_i}^{R_o} \frac{\lambda}{vr}\frac{\partial w}{\partial \lambda}\frac{dr}{dR}\, dR, \tag{16}$$

whereupon again using $r' = v/\lambda^2$ and $\lambda = r/R$ we thus obtain

$$\Delta P = \int_{R_i}^{R_o} \frac{R}{r^2}\frac{\partial w}{\partial \lambda}\, dR. \tag{17}$$

An alternative form follows by noting that $R\, d\lambda/dR = -\lambda + v/\lambda^2$ which enables one to transform (17) into

$$\Delta P = \int_{\lambda_i}^{\lambda_o} \frac{1}{v - \lambda^3}\frac{\partial w}{\partial \lambda}\, d\lambda, \tag{18}$$

where $\lambda_i = r_i/R_i$ and $\lambda_o = r_o/R_o$ are the stretches at the inner and outer surface, respectively. All of these forms revert back to well known formulas in the absence of swelling ($v = 1$) and, just as in

those nonswelling treatments, alternative elegant means can be utilized to obtain these formulas, such as starting from a principal stretch formulation or pursuing an energy treatment.

Calculating the derivative $\partial w/\partial\lambda$ for the Mooney–Rivlin-type model (5) and inserting that form into (17) now provides

$$\frac{\Delta P}{\mu} = 2\int_{R_i}^{R_o} \frac{R}{r^2}\left[\alpha v^{q_1}\left(\frac{r}{Rv^{2/3}} - \frac{R^5 v^{4/3}}{r^5}\right) + (1-\alpha)v^{q_2}\left(\frac{r^3}{R^3 v^{4/3}} - \frac{R^3 v^{2/3}}{r^3}\right)\right] dR. \tag{19}$$

Here $v = v(R)$ is regarded as given and thus the general form of $r = r(R)$ follows from $v(R)$ using (9). This general form for $r(R)$ contains r_i as a parameter. As the parameter r_i is varied the integral (19) generates different values for the pressure difference ΔP. In this way the *pressure-inflation graph* for the given swelling field is determined.

2.3. ***Pressure-inflation relation in the absence of swelling.*** In the absence of swelling, the problem under consideration is a classical one that has been widely studied within the theory of incompressible finite hyperelasticity, i.e., with the constraint $\det \boldsymbol{F} = 1$. A radially symmetric spherical inflation is then possible in every isotropic homogeneous incompressible hyperelastic material. This gives rise to inflation graphs that follow from formulae such as (19) by simply taking $v \equiv 1$. The expectation that there is no inflation if $\Delta P = 0$ follows by noting that the integral (19) vanishes upon setting $v = 1$ and taking $r = R$. Thus inflation graphs in the absence of swelling "start" at $(r_i, \Delta P) = (R_i, 0)$.

As r_i increases from R_i it may be that the graph simply increases monotonically. This is called type-(a) behavior. However, the graph may also increase to a maximum and then monotonically decrease to zero; this is type-(b) behavior. Finally, the graph may first increases to a local maximum, then decrease to a local positive minimum before again monotonically increasing; this is type-(c) behavior. All three types of behavior can occur for the classical Mooney-Rivlin model energy (5) in the absence of swelling, as illustrated in Figure 1. In particular, for (5) with $v = 1$ this behavior is determined as follows: if $\alpha = 1$ then type-(b) behavior is ensured (this is the well known neo-Hookean material behavior). If $0 \le \alpha < 0.823$ then type-(a) behavior is ensured. With $0.823 < \alpha < 1$, type-(a) behavior occurs if the shell is thick, but type-(c) occurs if the shell is thin. Here thick and thin is determined in terms of the *shell thickness ratio* $\xi \equiv R_i/R_o$. There is a function $\xi_{a/c} = \xi_{a/c}(\alpha)$ that is monotonically decreasing on the interval $0.823 < \alpha < 1$ such that $\xi_{a/c}(0.823) = 1$ and $\xi_{a/c}(1) = 0$. For values $0.823 < \alpha < 1$, type-(a) behavior occurs if $R_i/R_o < \xi_{a/c}(\alpha)$ and type-(c) behavior occurs if $R_i/R_o > \xi_{a/c}(\alpha)$. Because $\xi_{a/c}(\alpha)$ is monotone, its inverse graph is also monotone, and the overall behavior can be summarized as shown in Figure 2.

Rivlin's experiments on gum rubber in the 1940s, which suggested that $\alpha \approx 7/8$ (for what was then known simply as the Mooney energy), in conjunction with nearly everybody's common experience in blowing up a party balloon, has mades this an intriguing (and well known) result in the theory of nonlinear elasticity. A balloon is thin walled (R_i/R_o close to one) and the common experience is that in blowing up a balloon there is first a clear amount of inflation resistance. However, at a certain pressure of blowing the previous inflation resistance suddenly gives way to an interval of easy inflation prior to a resumption of inflation resistance similar to the initial one. Connecting this abrupt and limited burst of inflation (not bursting in the sense of ultimate rupture, which is the balloon's sad fate if the pressure is increased

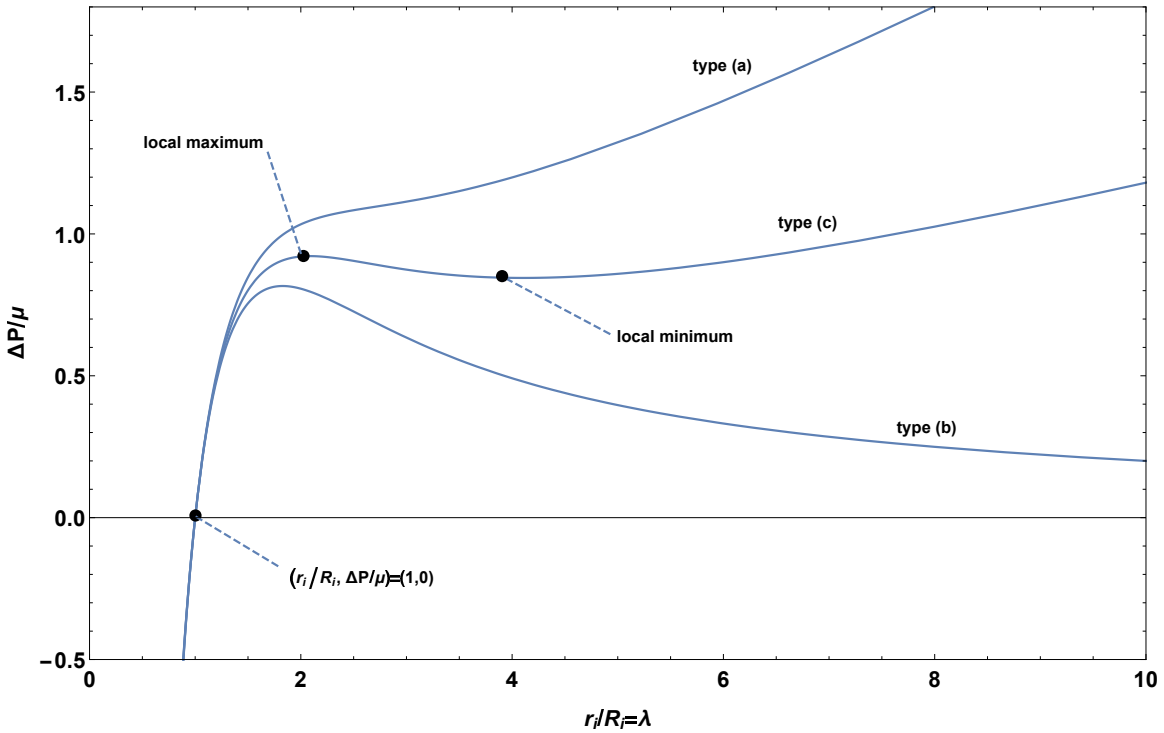

Figure 1. Inflation graphs showing three qualitatively different types of behavior (a)-(c) when there is no swelling ($v = 1$). These particular graphs correspond to W in (5), all with thickness ratio $R_i/R_o = 0.5$. The differences are due to the value of α. Here: $\alpha = 0.8$ (top curve); $\alpha = 0.9$ (middle curve); and $\alpha = 1$ (bottom curve).

too much) to the multivaluedness of r_i as a function of ΔP for type-(c) behavior, has generated an extensive literature — both experimental and theoretical (see e.g., [Müller and Strehlow 2004]).

A simple analtyical characterization of the equation describing the function $\xi_{a/c}(\alpha)$ in Figure 2 is not straight forward. Carroll [1987] has elegantly described the mathematical conditions that define this function for general hyperelastic stored energy functions $W(I_1, I_2)$. This permits an analytical characterization in terms of multiple functions and equations that we now briefly summarize. First define two functions $G(\eta)$ and $H(\eta, \xi)$ as

$$G(\eta) = \frac{1}{2}\eta^{2/3}\frac{\partial w}{\partial \lambda}\bigg|_{\lambda=\eta^{-1/3}}, \qquad H(\eta, \xi) = G(x)|_{x=\eta/(\xi^3+\eta(1-\xi^3))}. \tag{20}$$

Here the function $w(\lambda)$ is as described above just before (15) with the additional specialization of taking $v = 1$ since Carroll [1987] did not seek to treat swelling. The condition for a value ξ to be on the transition curve (the curve labelled $\xi_{a/c}$ in Figure 2) is that it gives the simultaneous satisfaction of the two equations

$$G(\eta) = H(\eta, \xi), \qquad \frac{\partial G}{\partial \eta} = \frac{\partial H}{\partial \eta}. \tag{21}$$

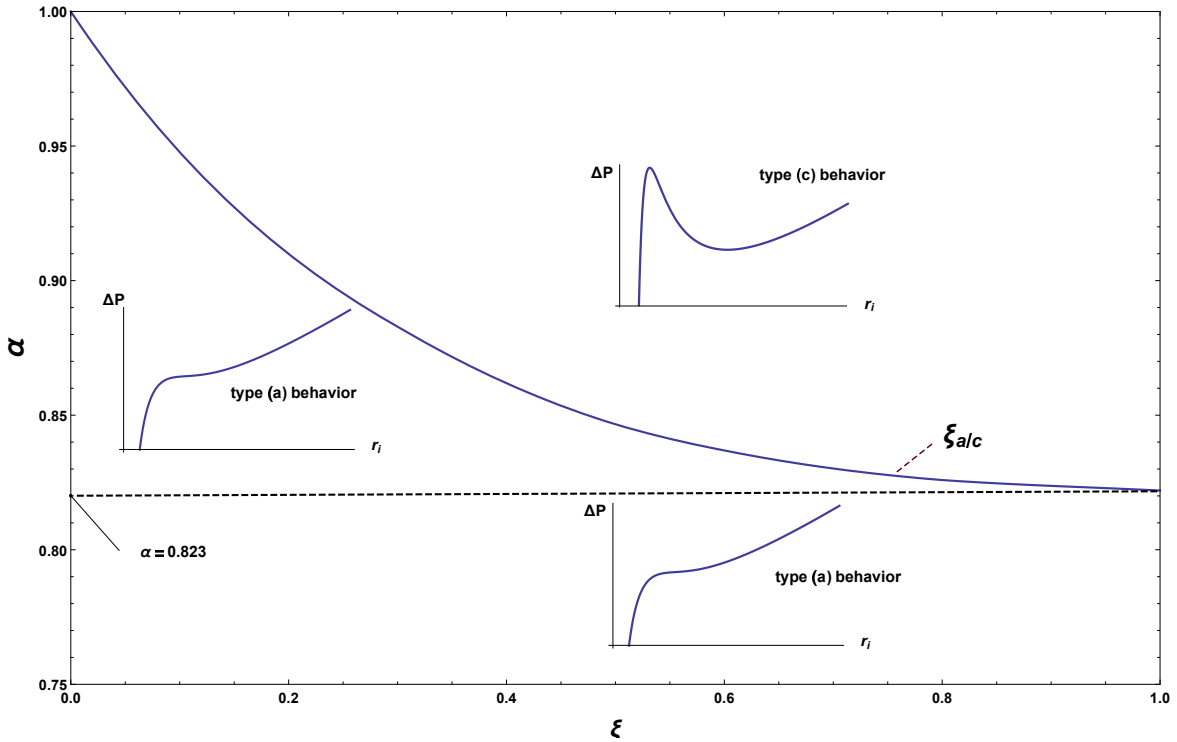

Figure 2. Qualitative behavior of the inflation graph for the Mooney–Rivlin model W given by (5) in the absence of swelling ($v = 1$). The curve $\xi = \xi_{a/c}$ provides a transition between type-(c) and type-(a) behaviors.

For the Mooney–Rivlin energy the function $G(\eta)$ is given by

$$G(\eta) = \mu\big[\alpha\big(\eta^{1/3} - \eta^{7/3}\big) + (1-\alpha)\big(\eta^{-1/3} - \eta^{5/3}\big)\big].$$

The $\xi_{a/c}$ curve in Figure 2 can then be constructed numerically by ranging through the values of ξ in the interval $0 < \xi < 1$ and in each case eliminating η between the two equations in (21) while solving for α.

For type-(c) behavior, because the first monotonically increasing "branch" of the graph terminates at the local maximum, an increasing ΔP then necessitates some kind of "branch transition" (again, the party balloon). There is an interval of ΔP on which this transition (i.e., jump) can in principle take place, and different physically based criteria can select different transition values of ΔP. In particular, a maximum delay criterion (which invokes the jump when the current branch "runs out") is suggested by energy minimization with respect to weak variations. Alternatively, the "Maxwell line" convention, based on the equal area rule with respect to the inflation graph, is suggested by energy minimization with respect to strong variations. Other conventions are also possible (based, for example, on thermodynamic fluctuations, or additional physical effects that may enter). We return to these considerations later in Section 5.

2.4. ***Pressure-inflation relation for uniform swelling.*** Building on the analysis of [Carroll 1987] our work [Zamani and Pence 2017] considered various aspects of uniform swelling as it relates to this problem

of spherical inflation. This means that v is independent of R. One of the main issues addressed in [Zamani and Pence 2017] was the inflation behavior as this uniform v varied with time in a quasistatic fashion. Thus, ΔP and v served as independent load-type parameters. Attention was restricted to $v \geq 1$, since "de-swelling" (or dessication) would generally lead to various wrinkling type instabilities that were not in the scope of that work. Also, because v was uniform, the relation (18) was relatively easy to use, and it became a central focus of the analysis in [Zamani and Pence 2017].

The pressure-inflation graphs remain a useful tool, as does the (a)–(c) classification type for those graphs. Now the graphs depend upon v. In other words, *there is a separate graph for each* $v \geq 1$. Note then that the homogeneous deformation of uniform expansion $r = v^{1/3}R$ makes $\Delta P = 0$ as can be verified directly from (19) and which also can be shown to follow from (18). Thus we have the intuitive result that uniform swelling gives uniform expansion when $\Delta P = 0$. In other words, the pressure inflation graphs for uniform swelling v now "start" at $(r_i, \Delta P) = (v^{1/3}R_i, 0)$.

Much of the technical analysis in [Zamani and Pence 2017] is based on a swelling generalization of Carroll's treatment in terms of an appropriate generalization of the G and H functions that appear in (20). One of the main results from that treatment is that if $q_1 = q_2$ in (5) then the value of v does not affect the behavior type (a)–(c). Thus, Figure 2 continues to indicate the qualitative form of the inflation graph for any uniform v provided that $q_1 = q_2$. On the other hand, it was also established that if $q_1 \neq q_2$ then the behavior type could vary with v. Thus, if $q_1 \neq q_2$, an unswollen inflation graph might have type-(a) behavior, whereas uniform wall swelling $v > 1$ might cause the inflation graph to become one with type-(c) behavior. This has obvious consequences for swelling induced instability phenomena. Qualitatively describing and quantitatively characterizing those consequences was a major focus in [Zamani and Pence 2017]. In fact, as described in that work, it is also possible to get limited burst type instability phenomena from swelling, even if the graph type did not change with v (e.g., even if $q_1 = q_2$). A rather complete mathematical framework for addressing the various possibilities was presented in [Zamani and Pence 2017], where, again, only uniform swelling was considered.

3. Nonuniform harmonic swelling fields

Turning to the main new issue of interest, we wish to consider the effect of nonuniform swelling fields. As previously mentioned, the spherical symmetry is maintainable so long as $v = v(R)$. For each such $v(R)$ the determination of the inflation graph continues as a key consideration, and it remains useful to classify their behavior according to the (a)–(c) scheme. However, when v is nonuniform, any use of the relation (18) necessitates expressing v as a function of λ. In the event that such a function is not single valued, then the integral must be split up into various λ ranges. For this reason, it is simpler to work directly with (19) which is the course followed for the rest of this paper.

On this basis, as we establish in the remainder of this paper, the behavior type according to the (a)–(c) scheme does not as directly correlate with the parameters in W as it did for the case of uniform swelling. For example, whereas W in (5) with $q_1 = q_2$ allowed for the continued use of Figure 2 for uniform swelling, Figure 2 will no longer determine the behavior type if $v(R)$ is not uniform even if $q_1 = q_2$.

Since our interest is in different nonuniform swelling fields $v(R)$, all of which correspond to the same amount of movable liquid, it is useful to introduce ΔV the *added swelling volume* associated with the

swelling field $v(R)$. Thus

$$\Delta V = 4\pi \int_{R_i}^{R_o} (v(R) - 1) R^2 \, dR. \tag{22}$$

In particular, because the swelling is due to an original soft hyperelastic ground substance having imbibed a certain amount of incompressible liquid, it follows that ΔV represents the combined volume of all of this free and potentially movable liquid. In the mathematical treatment, it is then natural to encounter the nondimensionalized quantity $\Delta V / R_i^3$.

The interpretation of ΔV in terms of the added mass of an incompressible fluid swelling agent gives rise to the key question of the present study: what changes in mechanical behavior take place if the same amount of liquid simply redistributes itself within the shell wall in different ways? Examining this question serves as the guiding principle for the remainder of this inquiry.

On this basis, we seek to consider various functions $v(R)$, all of which have a common $\Delta V > 0$. Even with this restriction, the problem remains rather general and so attention is further restricted to functions $v(R)$ of the special form

$$v(R) = \frac{A}{R} + B, \tag{23}$$

where A and B are constants. The form (23) is chosen here because this makes $v(R)$ the general spherically symmetric solution to $\nabla^2 v = 0$. From a physical perspective, one may then contemplate a variety of physical mechanisms that might suggest such a "harmonic form". For example, chemical potential regulation at the inner and outer radii for the purpose of establishing an osmotic pressure gradient might possibly suggest such a scenario, although we do not here seek to tie the ensuing results to this or any other particular mechanism.

Entering (22) with (23) one obtains

$$\frac{\Delta V}{R_i^3} = \frac{2\pi}{R_i}(\xi^{-2} - 1)A + \frac{4\pi}{3}(\xi^{-3} - 1)(B - 1), \tag{24}$$

where ξ obeying $0 < \xi < 1$ continues to be the ratio R_i / R_o. In working with (23) and (24) let

$$v_i \equiv v(R_i) = \frac{A}{R_i} + B, \quad v_o \equiv v(R_o) = \frac{A}{R_o} + B, \tag{25}$$

which means that v_i is the local swelling amount at $R = R_i$ and v_o is the local swelling amount at $R = R_o$. It then follows that

$$A = \frac{v_o - v_i}{1/R_o - 1/R_i}, \quad B = \frac{v_o R_o - v_i R_i}{R_o - R_i}. \tag{26}$$

It will be convenient to characterize the distributions (23) in terms of ΔV and the parameter v_i, instead of A and B. To this end, enter (24) with (26) and solve for v_o, which gives

$$v_o = \frac{3\Delta V}{2\pi R_i^3}\left(\frac{\xi^3}{(1-\xi)(2+\xi)}\right) - \frac{\xi(1+2\xi)}{2+\xi} v_i + \frac{2(1+\xi+\xi^2)}{2+\xi}, \tag{27}$$

whereupon

$$A = \left[-\frac{3\Delta V}{2\pi R_i^3}\left(\frac{\xi^3}{2-3\xi+\xi^3}\right) + v_i\left(\frac{2(1-\xi^3)}{2-3\xi+\xi^3}\right) - \frac{2(1-\xi^3)}{2-3\xi+\xi^3}\right] R_i,$$
$$B = \frac{3\Delta V}{2\pi R_i^3}\left(\frac{\xi^3}{2-3\xi+\xi^3}\right) - v_i\left(\frac{3\xi(1-\xi^2)}{2-3\xi+\xi^3}\right) + \frac{2(1-\xi^3)}{2-3\xi+\xi^3}. \tag{28}$$

Thus for a given $\Delta V > 0$, R_i, and $R_o = R_i\,\xi^{-1}$ we may view (23) with A and B given by (28) as a family of harmonic swelling fields, each with the same overall free liquid content but with different distributions of that liquid as determined by the single "tuning parameter" v_i. As v_i changes, the same overall added mass ΔV due to the fixed amount of liquid swelling agent is distributed through the spherical shell in different ways.

We restrict considerations to swelling fields (23) such that $v(R) \geq 1$ at all locations. This will be the case if both $v_i \geq 1$ and $v_o \geq 1$. Setting $v_o = 1$ in (27) and solving for v_i yields

$$v_i|_{v_o=1} = 1 + \frac{3\Delta V}{2\pi R_i^3}\left(\frac{\xi^2}{1+\xi-2\xi^2}\right) \equiv v_i^{\max}. \tag{29}$$

Thus, (23) with A and B given by (28) is parameterized by v_i on the interval $1 \leq v_i \leq v_i^{\max}$.

If $v_o = v_i$, then $A = 0$ and we retrieve a uniform distribution of the kind studied in [Zamani and Pence 2017]. For a given ΔV the uniform distribution is associated with the v_i value that is found by substituting $v_i = v_o = v_{\text{uni}}$ in (27) and solving for the special value v_{uni}. This gives

$$v_{\text{uni}} = 1 + \frac{3\Delta V}{4\pi R_i^3}\left(\frac{\xi^3}{1-\xi^3}\right). \tag{30}$$

If for a given added volume ΔV, the value v_i is exactly v_{uni} in (30), then the distribution is uniform and all of the results from [Zamani and Pence 2017] apply for the given added mass ΔV. Inverting (30):

$$\frac{\Delta V}{R_i^3} = \frac{4}{3}\pi(v_{\text{uni}}-1)\frac{1-\xi^3}{\xi^3}, \tag{31}$$

and substituting from this result into (29) gives $v_i^{\max}$ in terms of v_{uni} as

$$v_i^{\max} = 1 + 2(v_{\text{uni}}-1)\frac{1+\xi+\xi^2}{\xi(1+2\xi)}. \tag{32}$$

Consequently, it follows that

- if $v_{\text{uni}} < v_i \leq v_i^{\max}$ then the added mass is more concentrated at the inner surface, and
- if $1 \leq v_i < v_{\text{uni}}$ then the added mass is more concentrated near the outer surface.

Figure 3 shows such a family of harmonic swelling distributions, all with the same overall added mass, which in this case is 30 percent of the original volume. Consequently, $v_{\text{uni}} = 1.3$. The value of $v_i^{\max}$ is dependent on ξ by virtue of (32). For Figure 3 we take the moderately thick wall $R_i = R_o/2$ or $\xi = 0.5$, which in turn makes $v_i^{\max} = 2.05$.

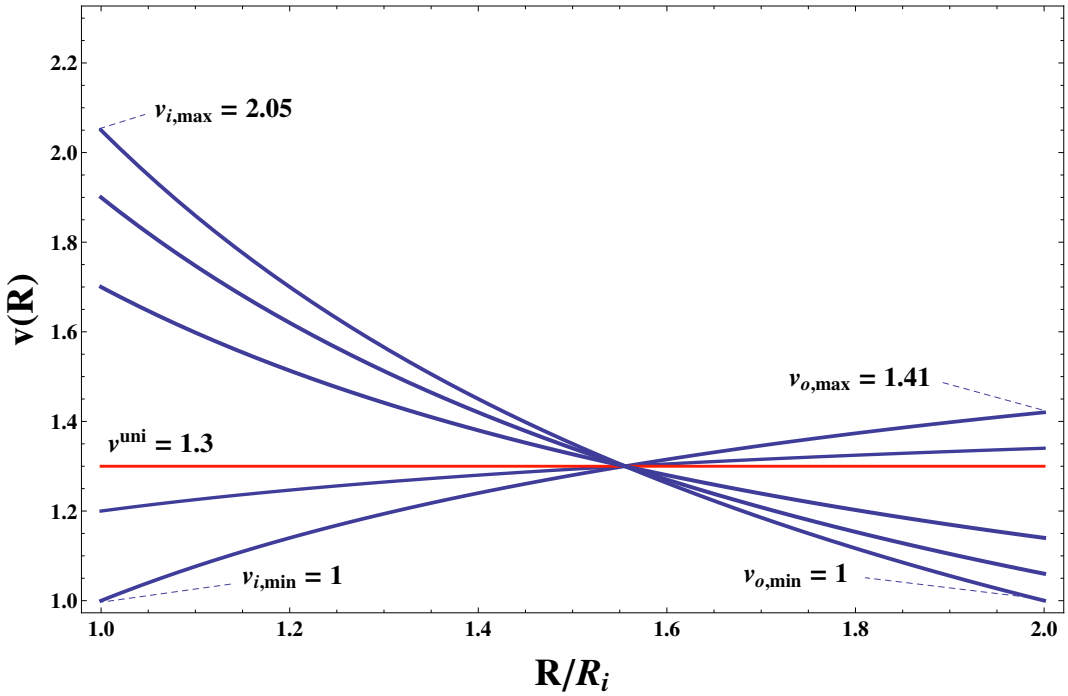

Figure 3. The family of harmonic swelling distributions (23) with constants (28) that are parameterized with respect to v_i such that $v(R) \geq 1$. Here $\xi = 0.5$. All distributions have the same amount of overall added mass associated with $v_{\text{uni}} = 1.3$ (30% increase in wall volume from the reference configuration that contains no free liquid).

4. Behavior under nonuniform swelling

The relations (29) and (30) show that the dependence of both $v_i^{\max}$ and v_{uni} upon $\Delta V/R_i^3$ is linear; also the resulting curve for $v_i^{\max}$ is above that for v_{uni}. Figure 4 shows these curves when $\xi = 0.9$. Vertical line segments in Figure 4 between $v_i = 1$ and $v_i = v_i^{\max}$ correspond to different harmonic swelling distributions for the same ΔV. In other words *each point on the vertical segment represents a harmonic swelling field, and the vertical segment itself encompasses all harmonic swelling fields for the fixed* ΔV. Consequently, the vertical line segment represents *a family of harmonic swelling fields*, and each member of the family involves a different distribution of the given amount of swelling agent.

The question now arises as to how the inflation graphs vary — if at all — as the swelling field changes within any such family. The physical significance is that if the inflation graphs are found to vary, then liquid redistribution will alter the inflation response.

The development thus far is capable of addressing a wide range of hyperelastic swelling material constitutive models; for material model (5) this range is characterized by choices for μ, α, q_1 and q_2. The development also addresses spherical shells of different wall thickness ratios $\xi = R_i/R_o$. For the purpose of illustrating the rich range of behaviors that can occur we provide results in the context of the material model (5) with $\alpha = 0.85$, $q_1 = q_2 = 0$ and a spherical shell with $\xi = 0.9$. The value $\alpha = 0.85$ is motivated by the previously indicated Rivlin experiments and the values $q_1 = q_2 = 0$ are

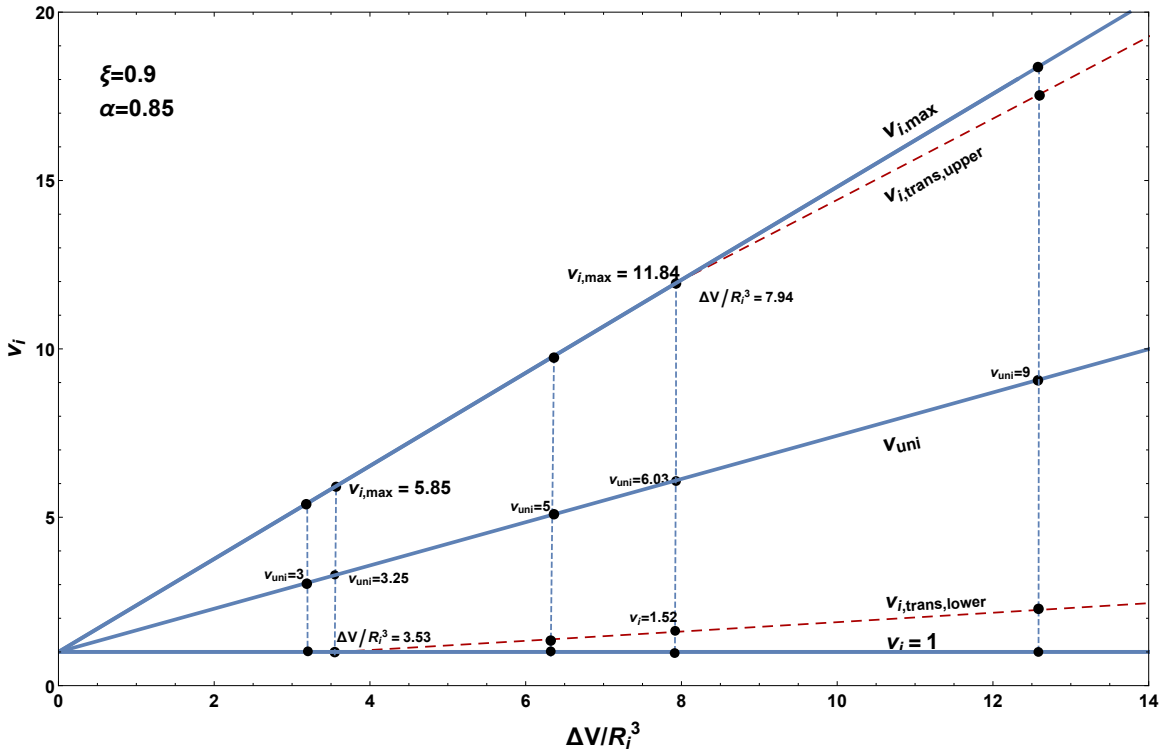

Figure 4. The value v_i on the interval $1 \le v_i \le v_i^{\max}$ parameterizes harmonic swelling fields, all of which have the same added mass content ΔV. For a given value of ΔV each of these parameterized families correspond to a vertical line segment on this figure, which here is for $\xi = 0.9$. The significance of the other curves is developed throughout the text narrative of Section 4.

broadly consistent with Treloar's remarks on swelling in [Treloar 1975]. The value $\xi = R_i/R_o$ gives a moderately thin bladder wall, but one in which internal redistribution of liquid would seem possible. Summarizing, we present results for

$$\frac{1}{\mu} W(I_1, I_2, v) = 0.425 \frac{I_1}{v^{2/3}} + 0.075 \frac{I_2}{v^{4/3}} - 1.5, \qquad R_i = 0.9 R_o. \tag{33}$$

The shear modulus parameter μ then remains the scale parameter for the pressure. In this context, different amounts ΔV of liquid swelling agent are considered. Each value of ΔV gives rise to its own harmonic family of swelling fields, each of which is characterized by a different value of v_{uni} and $v_i^{\max}$ on the basis of (30) and (29) using $\xi = 0.9$.

Figures 5 and 6 show that the inflation graphs do indeed vary within a family. These two figures are for the case $\Delta V/R_i^3 = 3.20$, which makes $v_{\text{uni}} = 3$ and $v_i^{\max} = 5.3$. Figure 5 displays the inflation graphs for all values v_i on the interval $1 \le v_i \le 3.21$, whereas Figure 6 is for the remaining interval $3.21 \le v_i \le 5.3 = v_i^{\max}$. Each inflation graph in both figures is of type-(c). For Figure 5 we find that the uppermost inflation graph is that associated with $v_i = 1$. Then as v_i increases the graphs become

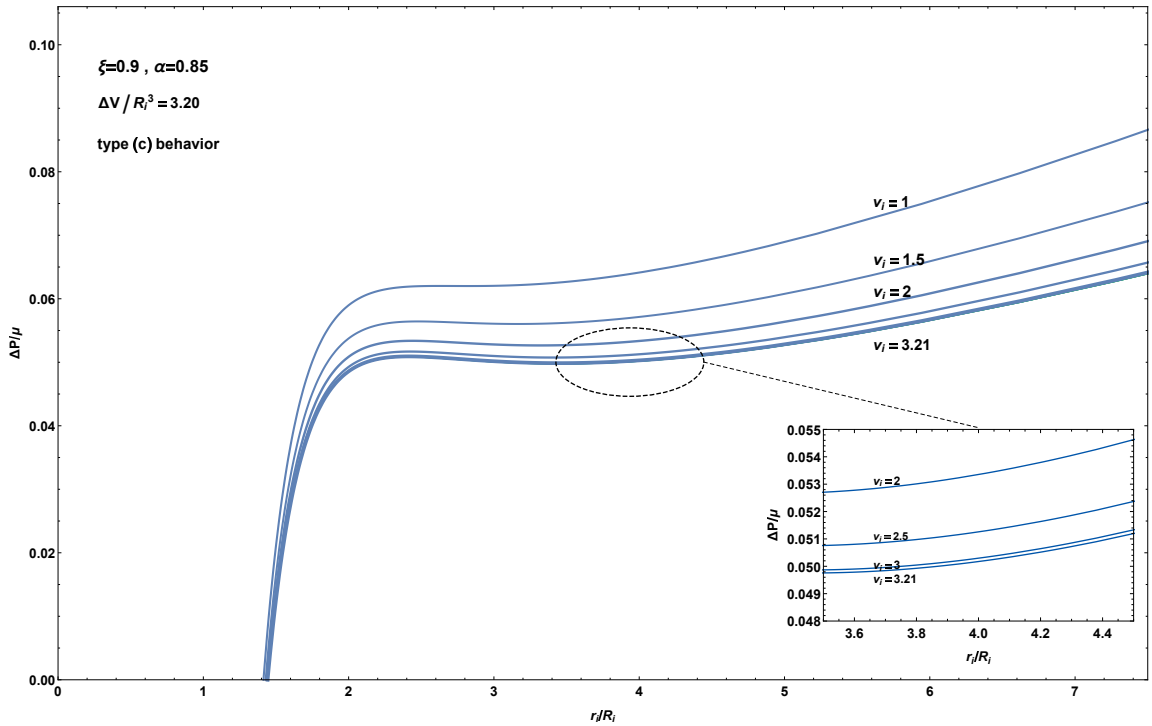

Figure 5. Inflation graphs for (33) with $\Delta V/R_i^3 = 3.20$ (which makes $v_{\text{uni}} = 3.0$ and $v_i^{\max} = 5.3$). The graphs here correspond to $1 \le v_i < 3.21$ which is the subfamily (of the overall family $1 \le v_i \le 5.3$) for which the graphs become lower as v_i increases.

progressively lower until reaching the lowermost graph corresponding to $v_i = 3.21$, thereby finishing Figure 5. Further increase in v_i then results in inflation graphs that become progressively higher as v_i continues to increase, all the way to the value $v_i^{\max} = 5.3$. These are shown in Figure 6. Thus the family of inflation graphs is effectively divided into two subfamilies: one for $1 \le v_i < 3.21$ and another for $3.21 < v_i \le 5.3 = v_i^{\max}$.

The lowest of all the graphs is found to occur when $v_i = 3.21$ which is close to the value $v_{\text{uni}} = 3$ where the swelling agent is uniformly distributed. It is to be noted from Figure 5 that the graph for the two curves $v_i = 3$ and $v_i = 3.21$ are quite close, so that it is not completely clear how numerical sensitivity might be a factor in this finding. In any event, the uniform distribution generates what is essentially the lowest graph in the overall family. Consequently, if the same amount of added mass is distributed in a highly nonuniform fashion, then to obtain the same inflation r_i requires a greater amount of pressure. In this sense an essentially uniform distribution of the swelling agent gives the most compliant response. By shifting more and more of the swelling agent to the wall extremities, one makes the response increasingly stiff. The stiffest response occurs when the mass is maximally concentrated at the outer surface of the wall (i.e., $v_i = 1$). By maximally concentrated, we mean within the class of harmonic swelling distributions that make $v(R) \ge 1$ for all R.

Figures 5 and 6 represented the family of inflation graphs for the particular added mass amount $\Delta V/R_i^3 = 3.20$. We now inquire into whether these graphs are representative when one considers other

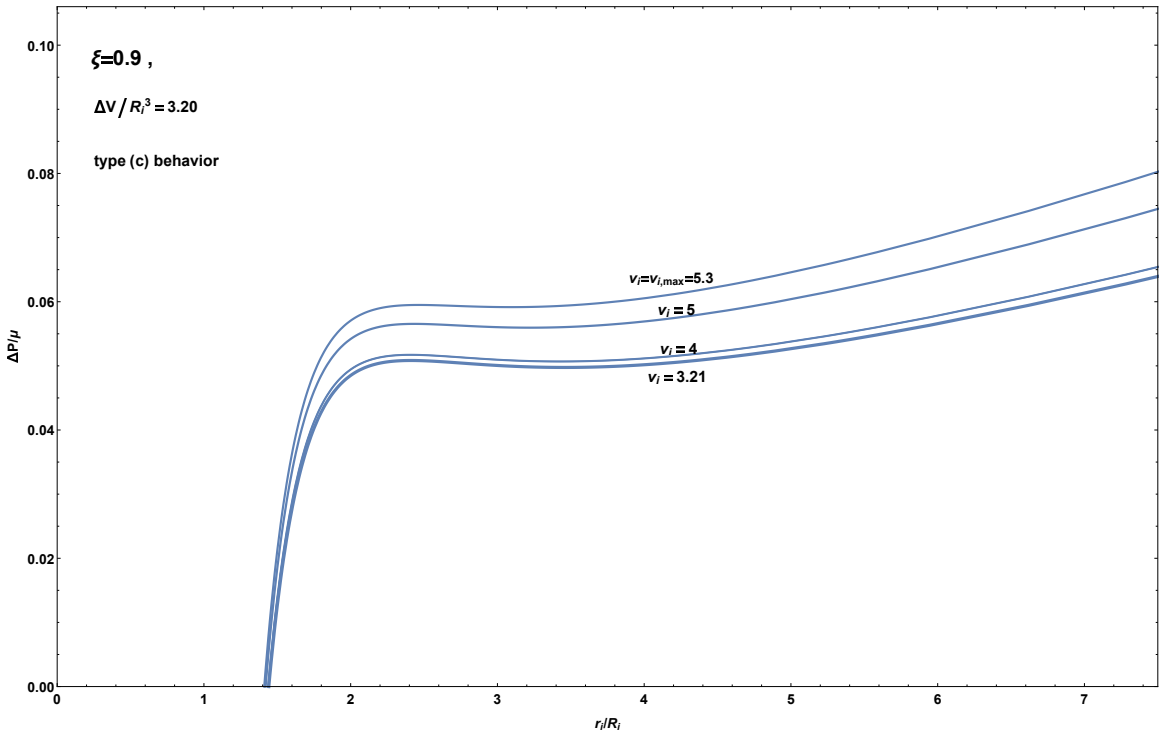

Figure 6. Subfamily of inflation graphs for (33) with $\Delta V/R_i^3 = 3.20$ corresponding to $3.21 < v_i \leq 5.3 = v_i^{\max}$. The complete family of inflation graphs $1 \leq v_i \leq v_i^{\max}$ is accounted for by combining these graphs with those from Figure 5.

values of $\Delta V/R_i^3$. In other words, we ask whether the general family behavior indicated in Figures 5 and 6 persists when one considers different vertical line segments in Figure 4? A partial answer to this question is provided by Figure 7 which corresponds to $\Delta V/R_i^3 = 6.36$ (making $v_{\text{uni}} = 5$ and $v_i^{\max} = 9.60$). Now we show the full family of graphs $1 \leq v_i \leq v_i^{\max}$ on the same figure. The lowest graph in Figure 7 is for $v_i = 5.43$ and it is again the case that the overall family is split into two subfamilies: the subfamily $1 \leq v_i < 5.43$ where the graphs become progressively lower, and the subfamily $5.43 < v_i \leq 9.60 = v_i^{\max}$ where they become progressively higher. As was the case for Figures 5 and 6, near the lowermost v_i-graph one finds that the nearby graphs become highly bunched together. Indeed the determination of the specific v_i-value of the lowest graph is sensitive to the numerical algorithm. Also, v_{uni} is again in the bunched region (see the inset in Figure 7).

As we examine other families (i.e., other values of $\Delta V/R_i^3$) we find that this general ordering behavior persists, namely there is a subfamily where the graphs become progressively lower followed by a rising subfamily. The lowermost graphs are highly bunched together near v_{uni}. Because of possible numerical sensitivity in this extreme bunching region, we shall henceforth regard v_{uni} as representative of the lowermost graph in the overall harmonic family of distributions.

Turning now from the graph ordering to the graph behavior in Figure 7 we find that the lowermost graph is again of type-(c). For the full family of graphs as parameterized by v_i on $1 \leq v_i \leq 9.60 = v_i^{\max}$,

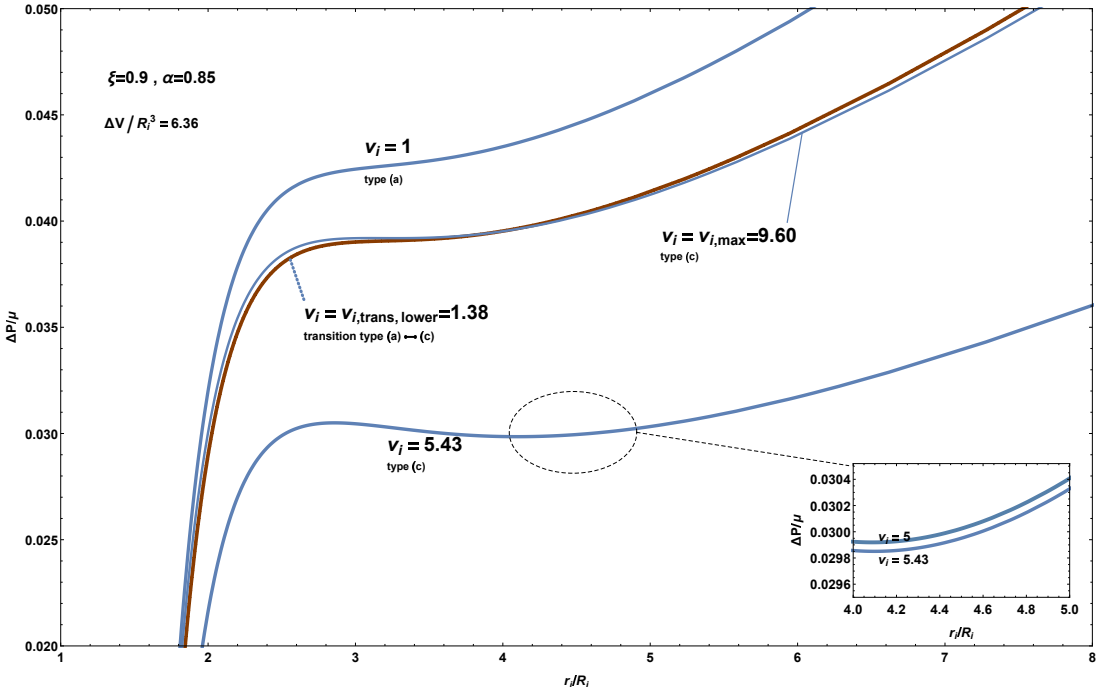

Figure 7. The family of inflation graphs for (33) with $\Delta V/R_i^3 = 6.36$ (which makes $v_{\text{uni}} = 5.0$ and $v_i^{\max} = 9.60$). Some remain type-(c) but others are now type-(a). The transition between the two behaviors is the particular inflation graph for $v_i = v_{i,\text{trans,lower}}$ which is shown in red.

we find that the bounding values $v_i = 1$ and $v_i = v_i^{\max}$ give different graph type behavior. Specifically, it is found that the graph for $v_i = v_i^{\max}$ is of type-(c), whereas the graph for $v_i = 1$ is of type-(a). All of the inflation graphs for $5.43 \leq v_i \leq v_{i,\max}$ are type-(c). As regards the range $1 \leq v_i < 5.43$ we find that that there is a special value of v_i in this range — which we here denote by the name $v_{i,\text{trans,lower}}$ — such that the inflation graph is of type-(a) for $1 \leq v_i < v_{i,\text{trans,lower}}$ and is of type-(c) for $v_{i,\text{trans,lower}} < v_i \leq v_{i,\max}$. In particular we find that $v_{i,\text{trans,lower}} = 1.38$.

Because figures 5 and 6 for $\Delta V/R_i^3 = 3.20$ show all type-(c) behavior whereas Figure 7 for $\Delta V/R_i^3 = 6.36$ shows both type-(c) and type-(a) behavior, we enquire into the transition between these two different sorts of families. In doing so we find that the special value $\Delta V/R_i^3 = 3.53$ provides the transition. For $\Delta V/R_i^3 < 3.53$ every member of the response curve family exhibits type-(c) behavior, whereas for $\Delta V/R_i^3 > 3.53$ both type-(c) and type-(a) behavior are found to occur. Figure 8 shows the family of inflation graphs for $\Delta V/R_i^3 = 3.53$. With the exception of the inflation graph for $v_i = 1$, all of the inflation graphs give type-(c) behavior and so have two locations with zero slope. For $v_i = 1$ in Figure 8 these two zero slope locations have coalesced giving a single zero slope location that is also an inflection point, which is the hallmark for the transition between the two different behavior types. In other words the value $v_{i,\text{trans,lower}}$ emerges from the value $v_i = 1$ when $\Delta V/R_i^3 = 3.53$.

Figure 4 also shows the vertical line corresponding to this transition family $\Delta V/R_i^3 = 3.53$. We then show the line in Figure 4 corresponding to $v_i = v_{i,\text{trans,lower}}$ for all $\Delta V/R_i^3 > 3.53$.

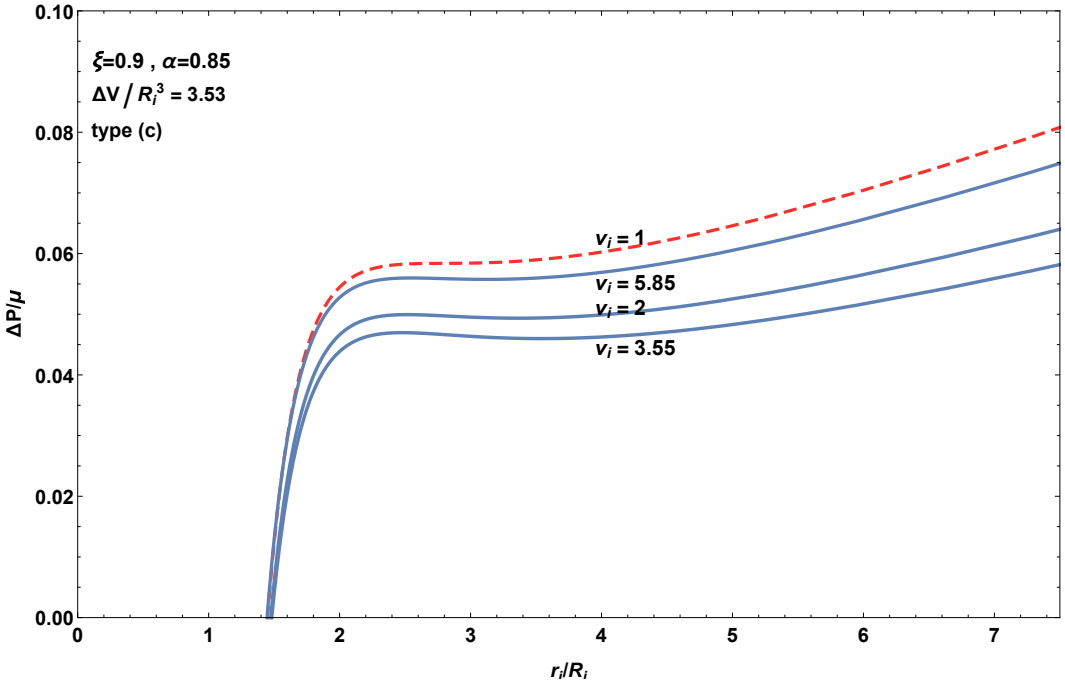

Figure 8. The family of inflation graphs for (33) with $\Delta V/R_i^3 = 3.53$ (which makes $v_{\text{uni}} = 3.25$ and $v_i^{\max} = 5.85$). The value $\Delta V/R_i^3 = 3.53$ provides the transition between the family type shown in figures 5 and 6 (always type-(c)) and the family type shown in Figure 7 (sometimes type-(c) and sometimes type-(a)).

This might seem to provide a full resolution to the issue of how the different inflation graph families for $\xi = 0.9$ and $\alpha = 0.85$ vary with overall swelling matter content ΔV. However, the consideration of even larger values of ΔV indicate that there is more to the story. Figure 9 shows the family of inflation graphs for $\Delta V/R_i^3 = 12.58$ (or $v_{\text{uni}} = 9$). As for all of the previous values of ΔV, the lowest inflation graph is either at or near the uniform distribution and this graph is of type-(c). Also, as in Figure 7, values of v_i sufficiently close to $v_i = 1$ give inflation graphs with type-(a) behavior. Now, however, it is also found that values of v_i sufficiently close to $v_i = v_{i,\max}$ also give type-(a) behavior. In other words, there are now (at least) two transitions away from the type-(c) behavior of the uniform distribution; one (or more) occurring for $v_i < v_{\text{uni}}$ and one (or more) occurring for $v_i > v_{\text{uni}}$. In fact, we find that there is one transition on each side of v_{uni}. The one for $v_i < v_{\text{uni}}$ is the previously found transition that occurs at $v_i = v_{i,\text{trans,lower}}$. The one for $v_i > v_{\text{uni}}$ is new and is now denoted by $v_{i,\text{trans,upper}}$. For the case of Figure 9, where $v_{\text{uni}} = 9$ and $v_i^{\max} = 18.2$, it is found that $v_{i,\text{trans,lower}} = 2.23$ and $v_{i,\text{trans,upper}} = 17.54$. The inflation graphs at both $v_{i,\text{trans,lower}}$ and $v_{i,\text{trans,upper}}$ have a single location with zero slope that is also an inflection point.

For all of the cases of very large ΔV that we have examined for $\xi = 0.9$ and $\alpha = 0.85$, we find that the general properties within the family of inflation curves qualitatively reflect that just described for the case of $\Delta V/R_i^3 = 12.58$ as depicted in Figure 9. The demarcation between the qualitative behavior of Figure 9 and the earlier qualitative behavior of Figure 7 (where there was only one transition between

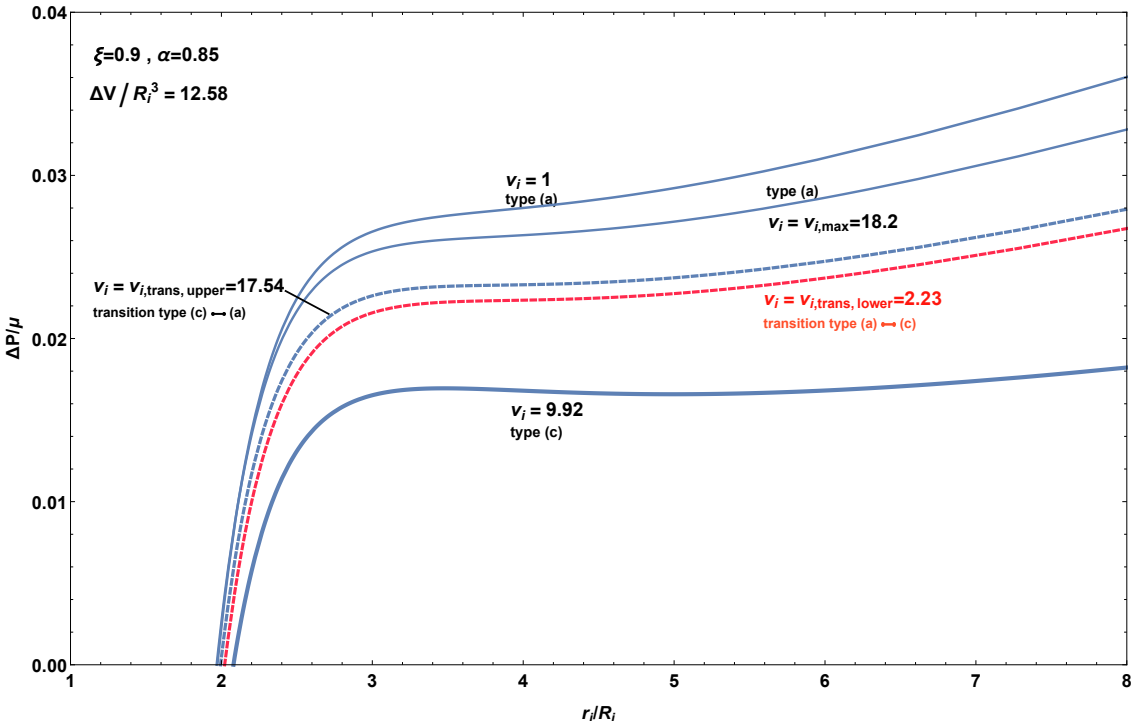

Figure 9. The family of inflation graphs for (33) with $\Delta V/R_i^3 = 12.58$ (which makes $v_{\text{uni}} = 9.0$ and $v_i^{\max} = 18.2$). Now the behavior is type-(c) for v_i near v_{uni} but type-(a) both near $v_i = 1$ and near $v_i = v_i^{\max}$.

type-(c) and type-(a) behavior) is found to occur at $\Delta V/R_i^3 = 7.94$. The corresponding family of inflation graphs for $\Delta V/R_i^3 = 7.94$ is depicted in Figure 10. This gives a case where $v_{i,\text{trans,upper}}$ first makes an appearance. Now, however, the emergence of this transition value occurs from $v_i = v_{i,\max}$ and not from $v_i = 1$ as was the case with the emergence of $v_{i,\text{trans,lower}}$. The emergence of $v_{i,\text{trans,upper}}$ from $v_{i,\max}$ is also depicted in Figure 4.

Based on all of the above considerations, Figure 4 now provides a complete picture of how the various type-(c) and type-(a) behaviors are organized. The swelling distributions as parameterized by v_i give rise to the region between the curves $v_i = 1$ and $v_i = v_{i,\max}$. The uniform distribution curve runs through the middle of this region. Above the uniform distribution curve, the swelling agent is more concentrated near the inner surface of the shell wall. Below the uniform distribution curve, the swelling agent is more concentrated near the outer surface of the shell wall. Type-(a) behavior occurs in two regions of Figure 4, one of which corresponds to a heavy concentration near the inner surface and the other of which corresponds to a heavy concentration near the outer surface. The central portion of the region containing the uniform distribution curve gives type-(c) behavior.

How can we so definitively assert that the uniform distribution curve is always in the type-(c) region of Figure 4? Alternatively stated, how do we know that both the curves for $v_{i,\text{trans,lower}}$ and $v_{i,\text{trans,upper}}$ remain bounded away from the uniform distribution curve? This is a consequence of a mathematical result obtained in [Zamani and Pence 2017]. That paper was solely devoted to uniform swelling distributions.

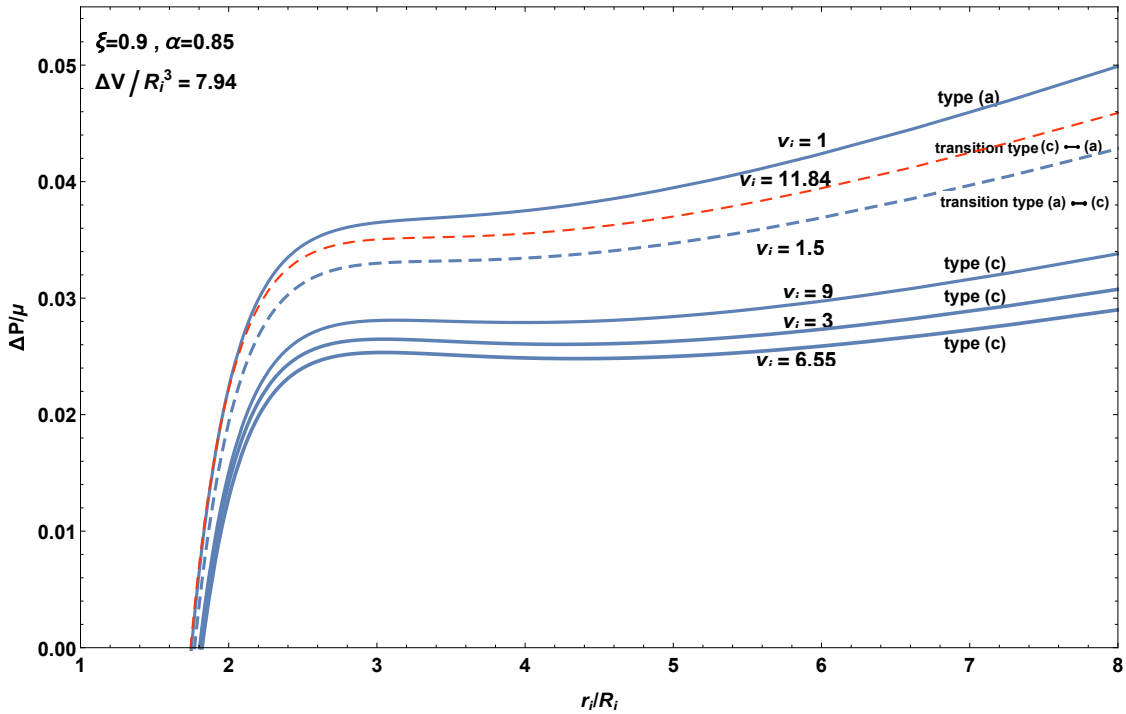

Figure 10. The family of inflation graphs for (33) with $\Delta V/R_i^3 = 7.94$ (which makes $v_{\text{uni}} = 6.03$ and $v_i^{\max} = 11.84$). The value $\Delta V/R_i^3 = 7.94$ provides the transition between the family types shown in figures 7 and 9.

As alluded to in Section 2.4, a key result of that work (see also [Pence and Tsai 2006]) was that a uniform swelling distribution does not alter the behavior type from that which is found in the treatment when no swelling is present. This rather general result ensures that the v_{uni} line in Figure 4 is always associated with type-(c) behavior.

5. Inflation-deflation behavior due to swelling agent redistribution at a fixed pressure

The findings of the previous Section 4 have immediate and interesting consequences for inflating and deflating a spherical shell simply by altering the distribution of the fixed added mass swelling agent without changing the pressure. For the purposes of this continuing discussion, we continue with the material and structure characterized by (33). In addition, we also now limit attention to $\Delta V/R_i^3 = 3.20$. Together this gives the family of inflation graphs depicted in figures 5 and 6.

Using these figures suppose that the sphere is pressurized with $\Delta P = 0.08\mu$ and that this level of pressurization is maintained as swelling agent is redistributed. This redistribution, which amounts to varying v_i, corresponds to then shifting between the various inflation graphs in figures 5 and 6 at the height determined by $\Delta P/\mu = 0.08\mu$. This will generate changes in r_i/R_i. The least value is $r_i/R_i = 6.78$ which occurs on the inflation graph for $v_i = 1$. The largest value is $r_i/R_i = 10.31$ which occurs on the inflation graph for $v_i = 3.21$. Figure 11 shows r_i/R_i as a function of v_i for $\Delta P = 0.08\mu$.

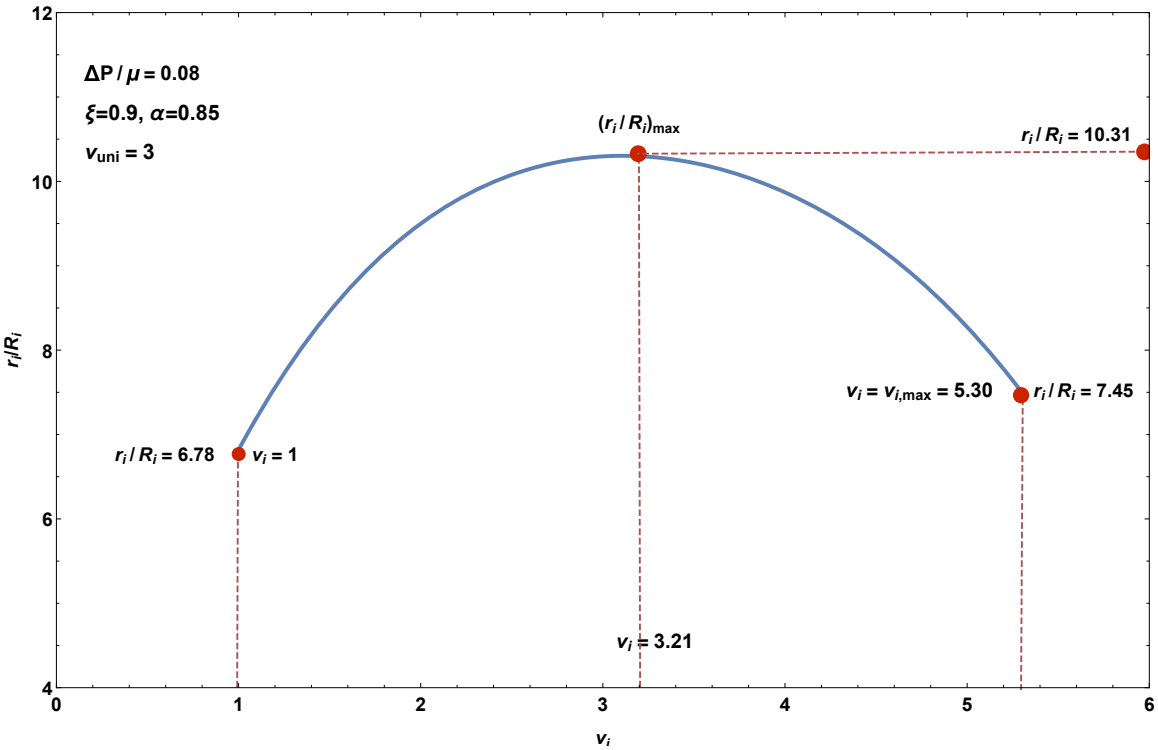

Figure 11. Inflation in terms of r_i/R_i as a function of v_i for (33) with $\Delta V/R_i^3 = 3.20$, which correspond to the sequence of inflation graphs in figures 5 and 6. This specific figure corresponds to $\Delta P = 0.08\mu$. The graph is well behaved, first monotonically increasing (where the correlation is with Figure 5) and then monotonically decreasing (correlated with Figure 6).

The graph in Figure 11 can be generated by moving in figures 5 and 6 along the horizontal line $\Delta P/\mu = 0.08\mu$. Starting at $v_i = 1$ one first moves to the right along this line in Figure 5 whereupon one passes through a sequence of inflation graphs corresponding to continuously increasing v_i until encountering the rightmost inflation graph along that line, which in this case is that for $v_i = 3.21$. This rightmost inflation graph gives the distribution with the maximum inflation for that value of ΔP. All of this generates the first portion of Figure 11 which shows its monotonic increase to $(r_i/R_i)_{\max}$. Note that the just-described construction using Figure 5 passes through all the inflation graphs corresponding to $1 \leq v_i \leq 3.21$ in a one-to-one fashion. We now come back along the same horizontal line, but now using Figure 6 in order to pass through the remaining inflation graphs, namely those corresponding to $3.21 < v_i \leq v_i^{\max}$. This also happens in a one-to-one fashion with increasing v_i during this leftward traversal. Now, because r_i decreases as v_i increases, one generates the rest of Figure 11, namely the part with the monotonic decrease.

As shown by Figure 11 the maximum inflation occurs when $v_i = 3.21$ which is close to the value v_{uni} where the swelling agent is dispersed in a uniform fashion throughout the shell wall. As the swelling agent is increasingly concentrated toward either the inner or outer boundary of the wall, then the radius

decreases. The fact that r_i/R_i in Figure 11 is a single-valued function of v_i is because the height corresponding to $\Delta P = 0.08\mu$ in figures 5 and 6 gives a single encounter with each inflation graph during the right and leftward traversals along the associated horizontal line. Alternatively stated, the type-(c) behavior of the inflation graphs, even with their nonmonotone behavior, has no effect on the process when $\Delta P = 0.08\mu$ because that is well above the graph locations where the nonmonotonicity takes place.

The situation is more complicated if the value of $\Delta P/\mu$ corresponds to a height in either Figure 5 or Figure 6 where the nonmonotonicity of the inflation graphs comes into play. Take $\Delta P/\mu = 0.055$ for which the graph of r_i/R_i versus v_i is shown in Figure 12. To understand why the graph in Figure 12 does not correspond to a single valued function of v_i, note that the value $\Delta P/\mu = 0.055$ now puts one squarely in a region of both Figure 5 and Figure 6 where certain inflation graphs are encountered three times along the horizontal segment: first on an ascending branch, then on its descending branch, and then on the other ascending branch. For the rightward traversal using Figure 5 beginning at $v_i = 1$ this gives rise to the S-shaped graph portion of Figure 12 prior to the maximum inflation at $(r_i/R_i)_{\max}$. As regards the maximum inflation itself, it corresponds to the rightmost inflation graph for $\Delta P/\mu = 0.055$, again this is $v_i = 3.21$. After the maximum in Figure 12, the remaining portion of the graph is generated by the leftward motion along the $\Delta P/\mu = 0.055$ line in Figure 6, meaning that now v_i increases from $v_i = 3.21$ to $v_i^{\max}$. A similar triple intersection phenomena occurs in this leftward traversal, and so there is a corresponding reentrant (doubling-back) portion to Figure 12 after the maximum inflation location.

The two portions of Figure 12 shown in red correspond to points on decreasing portions of the inflation graphs in figures 5 and 6. In the context of a single fixed pressure-inflation graph, increasing graph portions are classically stable. However decreasing graph portions are classically unstable [Ericksen 1975]. To be more precise, a location on an increasing graph portion corresponds to a local energy minimum, whereas a location on a decreasing graph portion corresponds to a local energy maximum. Consequently, from the perspective of energy minimization, should the system ever find itself with an inflation amount corresponding to a location on an unstable branch, the system can lower its energy while maintaining the same pressurization by transitioning to either of the two other equilibrium positions, namely those associated with the two increasing branches. Both of these alternatives are locally stable because they are local minima of energy, although one will involve a lower overall energy (the global minimum). Without belaboring the local versus global minimum distinction, the broader point is that, from a stability perspective, the red portions of Figure 12 will be avoided altogether as the swelling agent is redistributed through the system, i.e., as v_i varies.

Let us consider the consequences by contrasting the two cases of figures 11 and 12 which correspond to the same system at two different pressures. For both pressures we have that $1 \le v_i \le 5.30 = v_i^{\max}$ parameterizes a continuous family of harmonic swelling distributions (23); this means that the same amount of swelling agent is redistributed in a continuous fashion. This in turn leads to changes in the overall inflation, in fact very large changes. For $\Delta P = 0.08\mu$ this inflation change occurs in a continuous fashion as shown in Figure 11. However, for $\Delta P = 0.055\mu$ avoiding the unstable portions of Figure 12 does not allow the same type of continuous inflation. Instead, it is necessary to discontinuously transition (i.e., jump) between the various graph portions of Figure 12. This leads to transition regions as shown in Figure 13. Continuous redistribution of swelling agent corresponding to v_i fully traversing either $1.63 \le v_i \le 1.70$ or $4.79 \le v_i \le 4.89$ are interpreted as requiring jump transitions on Figure 13 that correspond to abrupt change in inflation (without altering $v(R)$, the swelling agent distribution).

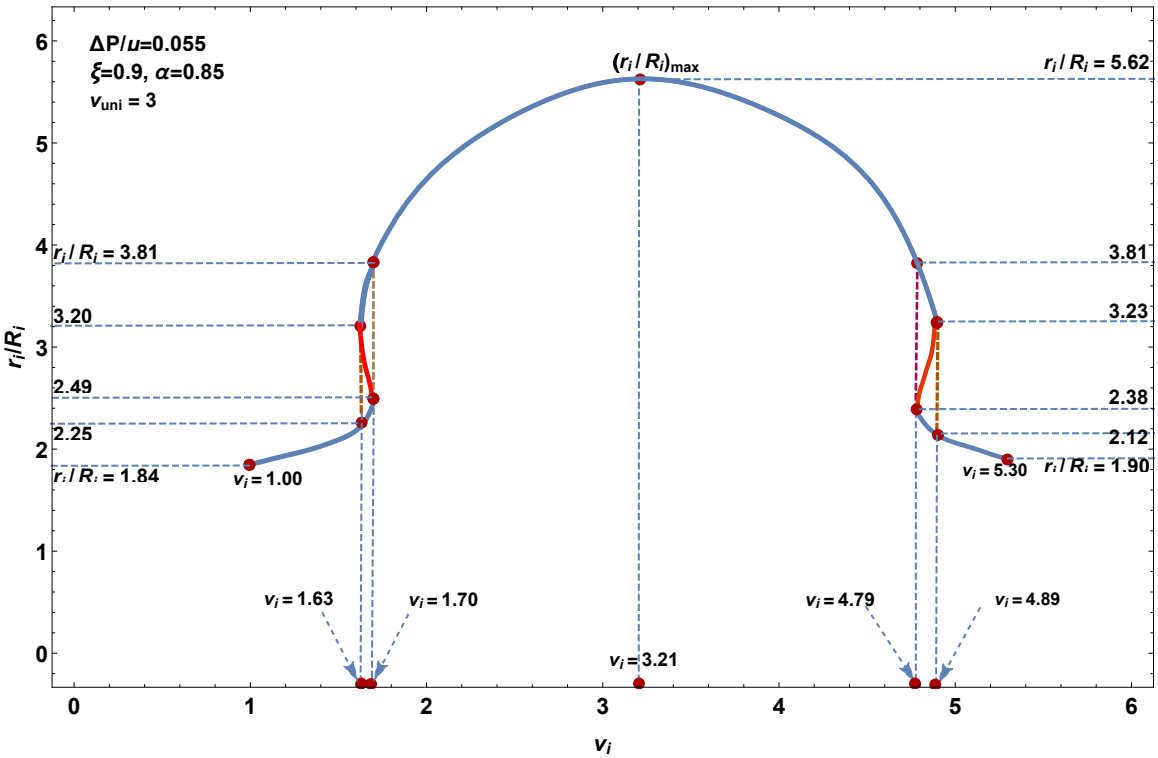

Figure 12. Inflation in terms of r_i/R_i as v_i varies for (33) with $\Delta V/R_i^3 = 3.20$, which again corresponds to the inflation graphs in figures 5 and 6. Here $\Delta P/\mu = 0.055\mu$. In contrast to Figure 11, the graph is not a single valued function of v_i.

The obvious next question that arises is how to determine the jump locations in Figure 13? Ultimately, that is an issue that requires broadening the analysis framework so as to include a specific stability criterion. Any such broadening must address the connection to the underlying physical considerations (e.g., what is the nature of local perturbations that may disrupt equilibrium at a local minimum so as to invoke a transition to the global minimum?). For a case where equilibrium at a local minimum can persist until the local minimum itself vanishes, one obtains a maximum delay type of convention, and this is indicated by the red arrows in Figure 13. Consequently, under such a criterion one obtains a classical hysteresis behavior. On the other hand, there is certainly a particular value in each of the intervals $1.63 \leq v_i \leq 1.70$ and $4.79 \leq v_i \leq 4.89$ where the two local energy values happen to coincide. At that particular value the global minima switches from being on the first stable branch to the second stable branch. Taking that as an alternative stability criterion locates an intermediate value in each of the hysteresis regions in Figure 13 where a common directionally independent transition would occur. The intermediate value on $1.63 \leq v_i \leq 1.70$ would correspond to the particular inflation graph in Figure 5 that causes the horizontal pressure line to correspond to the classical Maxwell line (equal area) construction [Ericksen 1975]. Similarly, the intermediate value on $4.79 \leq v_i \leq 4.89$ would correspond to the particular inflation graph in Figure 6 that also causes the horizontal pressure line to correspond to this same sort of equal area construction.

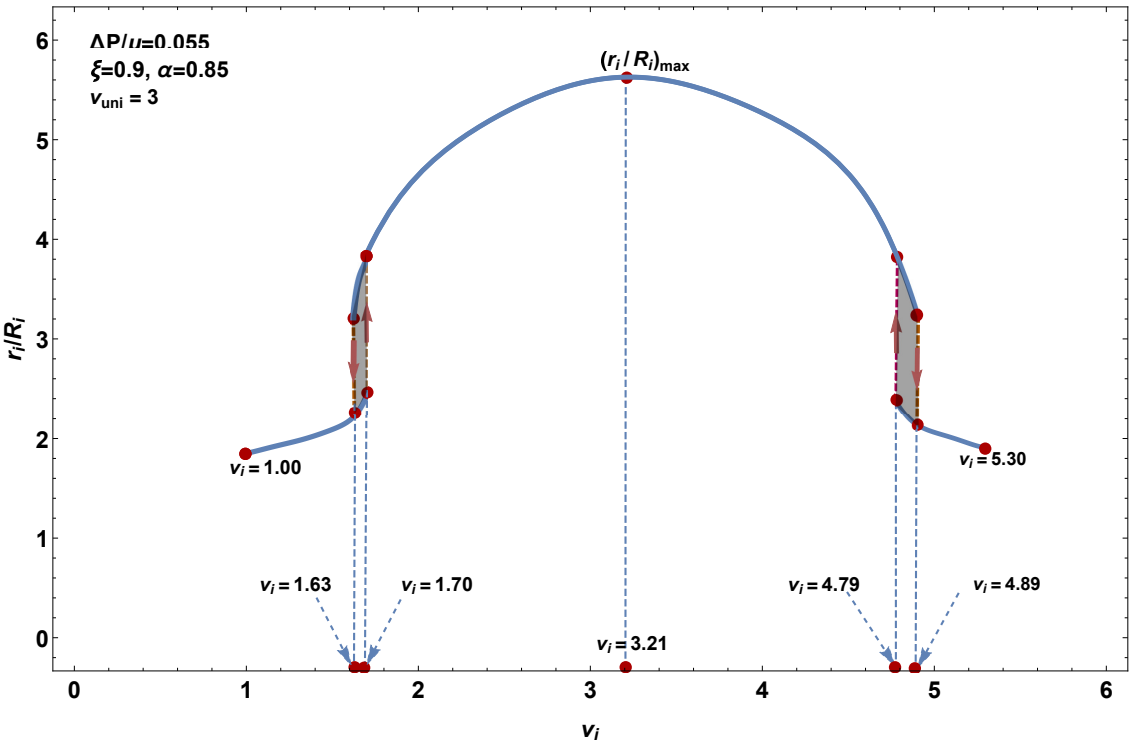

Figure 13. Because the graph in Figure 12 does not establish r_i as a single valued function of v_i, the swelling agent redistribution involves abrupt jumps (limited bursts of inflation). These are restricted to the transition regions as shown. One possibility is the classical hysteresis behavior that involves jumps at the endpoints of the transition regions (red arrows).

For our present purposes we do not wish for these interesting albeit finer stability distinctions to obscure the broader point, which is that the unstable graph portions of Figure 12 give rise to jump-like transitions in inflation as the swelling agent redistributes itself in a completely smooth fashion. For the example corresponding to Figure 12 these jump transitions, or limited inflation bursts, occur in relatively narrow windows of the overall swelling agent redistribution as indicated by the jump regions of Figure 13.

6. Final remarks including study limitations and connection to broader issues

The mechanical properties of porous soft matter are generally dependent upon the amount of liquid that is locally present. As liquid enters (or exits) it causes the material to swell (deswell) and this can lead to unexpected types of deformation. In addition to the local volume change due to the liquid redistribution, there is also the possibly altered structural load response. In this work we have examined these issues in the context of a classical spherical shell.

Specifically, we have considered a spherical shell whose walls are composed of a porous ground substance hyperelastic material that contains a fixed amount of mobile liquid swelling agent. We consider the effect of liquid redistribution in this context, where the redistribution is always radially symmetric.

This preserves the radial symmetry so that the shell is always spherical. Both ground substance and mobile liquid are regarded as individually incompressible. It is presumed that there are no voids in the wall material. Thus the volume of the shell wall is a constant. It is a soft material wall that surrounds the interior spherical region, and the interior spherical region can expand or contract as determined by the shell wall stiffness that provides resistance to any internal pressurization.

Formulating and examining the boundary value problem for modeling this spherical inflation was the object of this paper where the focus was on the combined affect of internal pressure and swelling agent redistribution within the shell wall. Among our findings was that the redistribution of the fixed amount of liquid swelling agent could significantly change the overall expansion. For a fixed pressurization the most expansion was found to occur when the liquid was uniformly distributed throughout the shell wall. Altering the distribution so that the swelling agent was highly concentrated near either the inner or the outer wall surface was found to give less expansion. Thus an active redistribution of liquid within the wall was found to significantly modulate the overall volume.

These findings were obtained in the context of a specific example — meaning a specific choice of structural and material model. The simple spherical geometry essentially rendered the structural model as one described by two degrees of freedom: (1) the wall thickness in the reference state when no free liquid is present and no pressure is applied, and (2) the amount of swelling agent that is then introduced. The first of these degrees of freedom is described by the parameter ξ and the second by the parameter ΔV.

The liquid swelling agent is treated as an incompressible fluid and the ground substance is treated as an incompressible porous hyperelastic material. The resulting state of mixture is described by the field variable v which gives the local volume change from the original ground substance reference state ($v = 1$). Thus v also serves as a direct proxy for the liquid volume fraction. Attention was restricted to equilibrium situations, meaning that any liquid migration has ceased and the liquid has settled into a specific distribution. The resulting equilibrated material was treated as hyperelastic with a stored energy density W that depends on both deformation gradient $\boldsymbol{F}$ (as in conventional hyperelasticity) and the swelling field v. In the absence of additional liquid ($v = 1$) this W was taken to reduce to a conventional Mooney–Rivlin form described in terms of the material parameter α. The extension to include swelling maintained the Mooney–Rivlin model form, while introducing possible swelling sensitivity via q_1 and q_2. The different liquid distributions were described in terms of a simple model expression that we referred to as harmonic. A single variable v_i served to parameterize a complete family of distributions for a fixed amount of swelling agent (described by ΔV). The internal pressure P was the single load parameter. Thus, by virtue of these modeling choices, the resulting problem was described by two structure parameters (ξ, ΔV), three material parameters (α, q_1, q_2), one normalized load parameter P/μ, and one liquid distribution parameter v_i.

Among the limitations of the present work is that only one choice for (α, q_1, q_2, ξ) was examined in any deep way, namely the well motivated values $(\alpha, q_1, q_2, \xi) = (0.85, 0, 0, 0.9)$. As seen from Figure 2, the corresponding (α, ξ) point is in the type-(c) region for behavior in the absence of swelling ($\Delta V = 0$) which also makes it the behavior for any $\Delta V > 0$ so long as the liquid swelling agent is uniformly distributed. Importantly, the point $(\alpha, \xi) = (0.85, 0.9)$ in Figure 2 is near the boundary of the type-(c) to type-(a) transition for uniform swelling distributions.

Along with $q_1 = q_2 = 0$ the focus on $(\alpha, \xi) = (0.85, 0.9)$ allowed us to consider the detailed affect of the remaining three parameters ΔV, v_i and P/μ. In this context a rich variety of behaviors was observed.

Some attempt to codify our behavior findings led to the diagram displayed in Figure 4 which may be viewed as a type of *liquid redistribution structural response map* for the particular pair (α, ξ) that was the focus of our developed example.

Among the issues not treated in the present work are how the response might alter for the consideration of other (α, ξ) pairs. In other words, viewing Figure 2 as a sort of *global phase diagram*, each point of that phase diagram would itself generate a liquid redistribution structural response map akin to that displayed in Figure 4. The possible variation in these response maps would seem to be of some interest. The question arises as to the effect of alternative constitutive models beyond that of the relatively well known Mooney–Rivlin form that is the focus of this paper. Even more general issues concern any possible compressibility in the individual constituents as well as the consideration of alternative deformation modes not connected to spherical symmetry. For this purpose, [Tsai et al. 2004] is of some possible relevance in view of its discussion on the contrasting roles of compressibility versus incompressibility in a case of swelling induced bending for a boundary value problem that can be viewed in terms of a cantilevered beam.

Finally, the issue of the physics behind the liquid agent redistribution was not treated. In particular, v_i was regarded as a control variable that was at our disposal. One might consider either passive or active mechanisms for achieving such control and thus redistributing the fixed amount of liquid. Their detailed consideration would most likely encounter important questions related to the broader thermodynamics of the envisaged process. In this regard, the present study has chosen to focus on the specific modeling issues associated solely with the mechanics of materials and structures portion of any such broader analysis.

Acknowledgment

This work is made possible by NPRP grant nos. 4-1333-1-214 and 8-2424-1-477 from the Qatar National Research Fund (a member of Qatar Foundation). The statements made herein are solely the responsibility of the authors.

References

[Amar and Ciarletta 2010] M. B. Amar and P. Ciarletta, "Swelling instability of surface-attached gels as a model of soft tissue growth under geometric constraints", *J. Mech. Phys. Solids* **58**:7 (2010), 935–954.

[Bowen 1980] R. M. Bowen, "Incompressible porous medium models by the use of the theory of mixtures", *Int. J. Eng. Sci.* **18** (1980), 1129–1148.

[Carroll 1987] M. M. Carroll, "Pressure maximum behavior in inflation of incompressible elastic hollow spheres and cylinders", *Quart. Appl. Math.* **XLV**:1 (1987), 141–154.

[Cheng et al. 2019] J. Cheng, Z. Jia, H. Guo, Z. Nie, and T. Li, "Delayed burst of a gel balloon", *J. Mech. Phys. Solids* **124** (2019), 143–158.

[Chester and Anand 2010] S. A. Chester and L. Anand, "A coupled theory of fluid permeation and large deformations for elastomeric materials", *J. Mech. Phys. Solids* **58**:11 (2010), 1879–1906.

[Drozdov 2013] A. D. Drozdov, "Finite elasticity of nanocomposite hydrogels", *Compos. Interfaces* **20**:9 (2013), 673–692.

[Drozdov et al. 2018] A. D. Drozdov, J. Christiansen, and J. deClaville, "Time-dependent response of hydrogels under multi-axial deformation accompanied by swelling", *Acta Mech.* **229** (2018), 5067–5092.

[Duda et al. 2010] F. P. Duda, A. C. Souza, and E. Fried, "A theory for species migration in a finitely strained solid with application to polymer network swelling", *J. Mech. Phys. Solids* **58**:4 (2010), 515–529.

[Duda et al. 2011] F. P. Duda, A. C. Souza, and E. Fried, "Solvent uptake and cavitation", *J. Mech. Phys. Solids* **59**:11 (2011), 2341–2354.

[Ericksen 1975] J. L. Ericksen, "Equilibrium of bars", *J. Elasticity* **5**:3 (1975), 191–201.

[Fang et al. 2008] Y. Fang, T. J. Pence, and X. Tan, "Nonlinear elastic modeling of differential expansion in trilayer conjugated polymer actuators", *Smart Mater. Struct.* **17**:6 (2008), 065020.

[Goriely et al. 2010] A. Goriely, D. E. Moulton, and R. Vandiver, "Elastic cavitation, tube hollowing, and differential growth in plants and biological tissues", *EPL* **91**:1 (2010), 18001.

[Gou and Pence 2016] K. Gou and T. J. Pence, "Hyperelastic modeling of swelling in fibrous soft tissue with application to tracheal angioedema", *J. Math. Biol.* **72** (2016), 499–526.

[Green and Shield 1950] A. E. Green and R. T. Shield, "Finite elastic deformation of incompressible isotropic bodies", *Proc. R. Soc. A* **202**:1070 (1950), 407–419.

[Liu et al. 2018] S. L. Z. Liu, E. Boatti, K. Bertoldi, and R. Kramer-Bottiglio, "Stimuli-induced bi-directional hydrogel unimorph actuators", *Extreme Mech. Lett.* **21** (2018), 35–43.

[Mihai et al. 2019] L. A. Mihai, D. Fitt, T. E. Woolley, and A. Goriely, "Likely equilibria of stochastic hyperelastic spherical shells and tubes", *Math. Mech. Solids* **24**:7 (2019), 2066–2082.

[Müller and Strehlow 2004] I. Müller and P. Strehlow, *Rubber and rubber balloons: paradigms of thermodynamics*, vol. 637, Springer, 2004.

[Pence 2012] T. J. Pence, "On the formulation of boundary value problems with the incompressible constituents constraint in finite deformation poroelasticity", *Math. Methods Appl. Sci.* **35** (2012), 1756–1783.

[Pence and Tsai 2006] T. J. Pence and H. Tsai, "Swelling-induced cavitation of elastic spheres", *Math. Mech. Solids* **11**:5 (2006), 527–551.

[Selvadurai and Suvorov 2018] A. P. S. Selvadurai and A. P. Suvorov, "On the development of instabilities in an annulus and a shell composed of a poro-hyperelastic material", *Proc. R. Soc. A* **474**:2218 (2018), 20180239.

[van der Sman 2015] R. G. M. van der Sman, "Hyperelastic models for hydration of cellular tissue", *Soft Matter* **11**:38 (2015), 7579–7591.

[Stuart et al. 2010] M. A. C. Stuart, W. T. S. Huck, J. Genzer, M. Müller, C. Ober, M. Stamm, G. B. Sukhorukov, I. Szleifer, V. V. Tsukruk, M. Urban, et al., "Emerging applications of stimuli-responsive polymer materials", *Nat. Mater.* **9**:2 (2010), 101–113.

[Treloar 1975] L. R. G. Treloar, *The physics of rubber elasticity*, Oxford University Press, 1975.

[Truesdell 1962] C. Truesdell, "Mechanical basis of diffusion", *J. Chem. Phys.* **37** (1962), 2336–2334.

[Tsai et al. 2004] H. Tsai, T. J. Pence, and E. Kirkinis, "Swelling induced finite strain flexure in a rectangular block of an isotropic elastic material", *J. Elasticity* **75**:1 (2004), 69–89.

[Yavari and Goriely 2013] A. Yavari and A. Goriely, "Nonlinear elastic inclusions in isotropic solids", *Proc. R. Soc. A* **469**:2160 (2013), 20130415.

[Zamani and Pence 2017] V. Zamani and T. J. Pence, "Swelling, inflation, and a swelling-burst instability in hyperelastic spherical shells", *Int. J. Solids Struct.* **125** (2017), 134–149.

Received 20 Aug 2019. Revised 31 Dec 2019. Accepted 10 Jan 2020.

VAHID ZAMANI: zamaniva@msu.edu
Department of Mechanical Engineering, Michigan State University, Engieering Building, East Lansing, MI 48824-1226, United States

THOMAS J. PENCE: pence@egr.msu.edu
Department of Mechanical Engineering, Michigan State University, Engineering Building, East Lansing, MI 48824-1226, United States

SUBMISSION GUIDELINES

ORIGINALITY

Authors may submit manuscripts in PDF format online at the Submissions page. Submission of a manuscript acknowledges that the manuscript is original and has neither previously, nor simultaneously, in whole or in part, been submitted elsewhere. Information regarding the preparation of manuscripts is provided below. Correspondence by email is requested for convenience and speed. For further information, write to contact@msp.org.

LANGUAGE

Manuscripts must be in English. A brief abstract of about 150 words or less must be included. The abstract should be self-contained and not make any reference to the bibliography. Also required are keywords and subject classification for the article, and, for each author, postal address, affiliation (if appropriate), and email address if available. A home-page URL is optional.

FORMAT

Authors can use their preferred manuscript-preparation software, including for example Microsoft Word or any variant of TEX. The journal itself is produced in LATEX, so accepted articles prepared using other software will be converted to LATEX at production time. Authors wishing to prepare their document in LATEX can follow the example file at www.jomms.net (but the use of other class files is acceptable). At submission time only a PDF file is required. After acceptance, authors must submit all source material (see especially Figures below).

REFERENCES

Bibliographical references should be complete, including article titles and page ranges. All references in the bibliography should be cited in the text. The use of BibTEX is preferred but not required. Tags will be converted to the house format (see a current issue for examples); however, for submission you may use the format of your choice. Links will be provided to all literature with known web locations; authors can supply their own links in addition to those provided by the editorial process.

FIGURES

Figures must be of publication quality. After acceptance, you will need to submit the original source files in vector format for all diagrams and graphs in your manuscript: vector EPS or vector PDF files are the most useful. (EPS stands for Encapsulated PostScript.)

Most drawing and graphing packages—Mathematica, Adobe Illustrator, Corel Draw, MATLAB, etc.—allow the user to save files in one of these formats. Make sure that what you're saving is vector graphics and not a bitmap. If you need help, please write to graphics@msp.org with as many details as you can about how your graphics were generated.

Please also include the original data for any plots. This is particularly important if you are unable to save Excel-generated plots in vector format. Saving them as bitmaps is not useful; please send the Excel (.xls) spreadsheets instead. Bundle your figure files into a single archive (using zip, tar, rar or other format of your choice) and upload on the link you been given at acceptance time.

Each figure should be captioned and numbered so that it can float. Small figures occupying no more than three lines of vertical space can be kept in the text ("the curve looks like this:"). It is acceptable to submit a manuscript with all figures at the end, if their placement is specified in the text by means of comments such as "Place Figure 1 here". The same considerations apply to tables.

WHITE SPACE

Forced line breaks or page breaks should not be inserted in the document. There is no point in your trying to optimize line and page breaks in the original manuscript. The manuscript will be reformatted to use the journal's preferred fonts and layout.

PROOFS

Page proofs will be made available to authors (or to the designated corresponding author) at a Web site in PDF format. Failure to acknowledge the receipt of proofs or to return corrections within the requested deadline may cause publication to be postponed.

Journal of Mechanics of Materials and Structures

Volume 15, No. 1 January 2020